Frontiers of Biomechanics 3

Damien Lacroix · Marzia Brunelli
Cécile Perrault · Adrien Baldit
Maryam Shariatzadeh
Ana Campos Marin · Andre Castro
Sara Barreto

Multiscale Mechanobiology in Tissue Engineering

Springer

Frontiers of Biomechanics

Volume 3

Series Editors
Taiji Adachi, Department of Biosystems Science, Institute for Frontier Life and Medical Sciences, Kyoto University, Kyoto, Japan
Damien Lacroix, INSIGNEO Institute for in silico Medicine, The University of Sheffield, Sheffield, United Kingdom
Christopher R. Jacobs, Department of Biomedical Engineering, Columbia University, New York, New York, USA

Associate Series Editor
Hiromi Miyoshi, Faculty of System Design, Tokyo Metropolitan University, Tokyo, Japan

Aims and Scope:

Biomechanics is a rapidly expanding field that focuses on exploring the mechanics of structure–function relationships underlying the functionality of living systems with the aim of gaining insights for medical applications. The field cuts across diverse disciplines: physics, biology, medicine, mechanical engineering, and biomedical engineering, and incorporates principles and concepts from these fields in the study of living systems and their dynamics.

A major objective of this series is to pioneer new frontiers of biomechanics by including concepts and ideas from new research frontiers yet to be addressed within the existing paradigm of biomechanics. The series highlights the role of mechanics in the realization of multicomponent and hierarchical interactions that characterize living systems, based on the context of open systems. The series also presents in-depth coverage of cutting-edge research in frontiers of biomechanics that explores fundamental concepts of what constitutes life, based on mechanics as an entity of energy principles and information science. It is hoped that this series will develop as an open system (analogous to living systems) that is admissible of future research dynamics and expansion in the field of biomechanics.

Distinctive features of the series:

- Each volume will cover core topics in the frontiers of biomechanics.
- The series will be multidisciplinary in that it will consist of volumes written by authors who are at the forefront of research in diverse fields including physics, mechanical engineering, biology, and medicine.
- Each volume will place emphasis on not only providing readers with new knowledge and techniques in biomechanics, but also presenting the underlying concepts and principles concisely and precisely so that the readers are able to discern unresolved and challenging problems in biomechanics.
- The series aims to contribute to further expansion and development of the field of biomechanics by including concepts and ideas from new research frontiers yet to be addressed within the existing paradigm of biomechanics.

More information about this series at http://www.springer.com/series/13453

Damien Lacroix • Marzia Brunelli
Cécile Perrault • Adrien Baldit
Maryam Shariatzadeh • Ana Campos Marin
Andre Castro • Sara Barreto

Multiscale Mechanobiology in Tissue Engineering

Springer

Damien Lacroix
INSIGNEO Institute for in silico Medicine
The University of Sheffield
Sheffield, UK

Marzia Brunelli
INSIGNEO Institute for in silico Medicine
The University of Sheffield
Sheffield, UK

Cécile Perrault
INSIGNEO Institute for in silico Medicine
The University of Sheffield
Sheffield, UK

Adrien Baldit
INSIGNEO Institute for in silico Medicine
The University of Sheffield
Sheffield, UK

Maryam Shariatzadeh
INSIGNEO Institute for in silico Medicine
The University of Sheffield
Sheffield, UK

Ana Campos Marin
INSIGNEO Institute for in silico Medicine
The University of Sheffield
Sheffield, UK

Andre Castro
INSIGNEO Institute for in silico Medicine
The University of Sheffield
Sheffield, UK

Sara Barreto
INSIGNEO Institute for in silico Medicine
The University of Sheffield
Sheffield, UK

ISSN 2199-8515 ISSN 2199-8523 (electronic)
Frontiers of Biomechanics
ISBN 978-981-10-8074-6 ISBN 978-981-10-8075-3 (eBook)
https://doi.org/10.1007/978-981-10-8075-3

Library of Congress Control Number: 2018950839

© Springer Nature Singapore Pte Ltd. 2019
This work is subject to copyright. All rights are reserved by the Publisher, whether the whole or part of the material is concerned, specifically the rights of translation, reprinting, reuse of illustrations, recitation, broadcasting, reproduction on microfilms or in any other physical way, and transmission or information storage and retrieval, electronic adaptation, computer software, or by similar or dissimilar methodology now known or hereafter developed.
The use of general descriptive names, registered names, trademarks, service marks, etc. in this publication does not imply, even in the absence of a specific statement, that such names are exempt from the relevant protective laws and regulations and therefore free for general use.
The publisher, the authors, and the editors are safe to assume that the advice and information in this book are believed to be true and accurate at the date of publication. Neither the publisher nor the authors or the editors give a warranty, express or implied, with respect to the material contained herein or for any errors or omissions that may have been made. The publisher remains neutral with regard to jurisdictional claims in published maps and institutional affiliations.

Printed on acid-free paper

This Springer imprint is published by the registered company Springer Nature Singapore Pte Ltd.
The registered company address is: 152 Beach Road, #21-01/04 Gateway East, Singapore 189721, Singapore

Preface

This book focuses on the mechanobiological principles in tissue engineering with a particular emphasis on the multiscale aspects of the translation of mechanical forces from bioreactors down to the cellular level. It aims to contribute to a better understanding on the design and use of bioreactors for tissue engineering and the use of mechanical loading to optimise in vitro cell culture conditions.

It covers experimental and computational approaches and the combination of both to show the benefits that computational modelling can bring to experimentalists when studying in vitro cell culture within a scaffold. With topics from multidisciplinary fields of life sciences, medicine and engineering, the book provides a novel approach to the use of engineering tools for the optimisation of biological processes and its application to regenerative medicine. The research described in this book was based on a European Research Council grant (258321) entitled 'Finite element simulations of mechanobiology in tissue engineering' partially funded by the European Commission.

A review of current state-of-the-art bioreactors is presented in Chap. 1. Spinner flasks, rotating and perfusing bioreactors are extensively reviewed as systems for control over shear stress applied forces and seeding capabilities. Then, bioreactor systems used to apply tension and compression on seeded constructs and the effect of these stimuli on cell differentiation are presented. Finally, the effect of electromagnetic fields on osteogenic differentiation are also presented.

Cell seeding in biomaterial scaffolds is often achieved through a perfusion bioreactor. However, not all scaffolds and perfusion bioreactors are optimised to each other. The scaffold and the bioreactor used to generate the engineered tissue have usually been developed empirically. As the research area is going further and the computational possibilities as well, a virtual physiological human cell tool to improve and optimise this process is presented in Chap. 2. A workflow from a single cell modelling to the bioreactor modelling and the biomaterial scaffold is presented

to create a patient specific implant. Combining experimental measurements with fluid, structure and fluid/structure analysis, we are able to calculate the mechanical stimuli at the cell, scaffold and bioreactor levels in a patient or sample specific manner.

The mechanical properties of a polycaprolactone rapid-prototyping scaffold are examined in Chap. 3 with particular focus on strain/stress curve, relaxation behaviour, apparent elastic modulus and dynamic mechanical analysis. The effect of different scaffold architectures and boundary conditions on mechanical properties are examined and the total error quantified. Then, the necessity for the development of collagen-polycaprolactone scaffolds to transmit mechanical stress to cells are explained and the organisation of the collagen inside the scaffold is shown. The effect of mechanical compression on the polycaprolactone scaffold cell proliferation and differentiation is presented. Results on seeding efficiency, proliferation and differentiation are further discussed and compared with other studies found in literature.

Despite the ability of rapid-prototyping techniques to fabricate regular structures, the consistency with which these regular structures are produced throughout the scaffold and from one scaffold to another needs to be quantified. Small variations at the pore level can affect the local mechanical stimuli sensed by the cells thereby affecting the final tissue properties. Most studies assume rapid prototyping scaffolds as regular structures without quantifying the local mechanical stimuli at the cell level. In Chap. 4, a computational method using a micro-computed tomography-based scaffold geometry is presented to characterise the mechanical stimuli within a real scaffold at the pore level. Five samples from a commercial polycaprolactone scaffold are analysed and computational fluid dynamics analyses are created to compare local velocity and shear stress values at the same scaffold location. The high variability amongst samples is shown. This chapter shows that regular scaffolds need to be thoroughly analysed in order to quantify real cell mechanical stimuli so inspection methods should be included as part of the fabrication process.

Chapter 5 presents a Computational Fluid Dynamics (CFD) simulations combined with micro Particle Image Velocimetry (μPIV) experiments to predict seeding efficiency and optimise experimental parameters. The chapter shows that cells reach all pores inside the scaffold mainly following streamlines with a higher number of cells passing by the centre of the pores where fluid velocities are higher. Since cells do not intercept with scaffold substrate, low cell seeding efficiency was observed and compares well with the CFD model. In this chapter, an experimental approach was developed to investigate cell seeding inside a 3D scaffold, and a computational model was able to predict local fluid dynamics and cell seeding efficiency.

Mechanical forces and 3D topological environment can be used to control differentiation of mesenchymal stem cells. However, the effects of physical and mechanical cues of the microenvironment on cell fate determination have not yet been fully understood. In Chaps. 6 and 7, an investigation and comparison of the

effect of mechanical stimulations on soft cellular microspheres are presented when subjected to dynamic fluid compression in three different in vitro systems: microfluidic chamber, compression bioreactor and orbital shaker. Mechanical forces can stimulate the differentiation of mesenchymal progenitors in microenvironment. Results showed that despite similar cell viability, on average the level of ALP activity in 5 days dynamic compression regime was nearly two times higher than 10 days compression. Also, free floating samples presented the highest cell number and ALP activity compared to other conditions. Application of compression cycles on mesenchymal stem cells could be used as a model to study the effect of mechano-stimulation on osteogenesis.

In Chap. 8, the formulation of poro-viscoelastic behaviour of collagen hydrogels presented in previous chapters is described using different finite element solvers. The computational approach enables to understand better the contribution of collagen on the mechanical stimuli that affects cell behaviour, by modelling a complex system including a scaffold, the collagen medium and cells.

Cell cytoskeleton provides a bridge to transmit information between the extracellular and the intracellular environments. It has been suggested that the cytoskeleton components may have distinct mechanical roles in the cell and that they might form the structure that defines cell rigidity. One approach to studying the mechanosensing processes is to understand the mechanical properties of cells' constitutive components individually. The development of a multi-structural 3D finite element model of a single-adherent cell is described in Chap. 9 to investigate the biophysical differences of the mechanical role of each cytoskeleton component. The multi-structural model not only illustrates that a combination of cytoskeletal structures with their own properties is necessary for a complete description of cellular mechanics, but also clarifies the effects of cytoskeletal heterogeneity on the interpretation of force-deformation measurements.

The ability to predict the mechanical responses of different adherent cell types presents many opportunities to mechanobiology research to further identify changes from cell physiological conditions to disease. Using the multi-structural cell model presented in Chap. 9, the effect of the variation of the material properties of the intracellular components on the cell response after compression and shearing is shown in Chap. 10. A parametric study was performed to understand the key mechanical features from different cell types, focussing on variation of the mechanical properties of specific cytoskeleton components and prestress. The time dependent responses observed were remarkably similar to those reported for a variety of measurements with atomic force microscopy, suggesting this model is a consensus description of the fundamental principles defining cell mechanics.

In Chap. 11, current perspectives are presented to indicate that more efforts need to be put into the development of such advanced studies presented earlier, and a new workflow including the use of computer modelling for the development of new tissue engineering product is proposed.

This unique book provides a valuable resource for researchers and graduate students studying mechanobiology and tissue engineering. It also offers a deep insight of tissue engineering and its use in the design of bioreactors for undergraduate students. This book has been supplemented with extensive references for each chapter to enable the reader to progress through the study of each chapter.

Sheffield, UK

Marzia Brunelli
Cécile Perrault
Adrien Baldit
Ana Campos Marin
Maryam Shariatzadeh
Andre Castro
Sara Barreto
Damien Lacroix

Contents

Chapter 1
A Review of Bioreactors and Mechanical Stimuli

The increased need to accelerate the healing process of critical size defects in the bone led to the study of optimal combination of cells, materials and external stimuli to obtain fully differentiated tissue to the injured site. Bioreactors play a crucial role in the control over the development of functional tissue allowing control over the surrounding chemical and mechanical environment. This chapter aims to review bioreactor systems currently available for monitoring mesenchymal stem cells (MSCs) behaviour under mechanical stimuli and to give an insight of their effect on cellular commitment. Shear stress, mechanical strain and pulsed electromagnetic field bioreactors are presented, and the effect of multiple conditions under varying parameters such as amplitude, frequency or duration of the stimuli on bone progenitor cells differentiation is considered and extensively discussed with particular focus on osteogenic and chondrogenic commitment.

1.1 Introduction to the Tissue Engineering Approach

1.1.1 Mesenchymal Stem Cells and External Environment

Long bone fracture gaps can be repaired through the use of natural and synthetic grafts seeded with cells to enhance tissue formation. For this purpose, the tissue engineering (TE) approach aims to use cells directly harvested from the donor and then expand them in cultures to reach the desired number. Osteoblasts are the most obvious choice for bone TE purposes as they are the main precursors of the bone. Despite this, their low proliferation rate and their fully differentiated state present issues. Moreover, there are problems related to the lack of tissue source and morbidity (Finkemeier 2002). As a consequence, mesenchymal stem cells (MSCs) currently are the next cellular target (Salgado et al. 2004) to satisfy the demand for an increased proliferation rate and a reduced amount of surgical intervention. Indeed, MSCs present high proliferation rates and can also be obtained from several sources such as bone marrow, adipose tissue or cord blood. Their undifferentiated state allows them to differentiate towards diverse lineages such as osteoblasts, chondrocytes, adipocytes or myocytes (Caplan 2007). After expansion and seeding

© Springer Nature Singapore Pte Ltd. 2019

D. Lacroix et al., *Multiscale Mechanobiology in Tissue Engineering*,
Frontiers of Biomechanics 3, https://doi.org/10.1007/978-981-10-8075-3_1

onto the scaffolds, cells usually are stimulated through bioreactors to drive their differentiation towards a defined pathway and to obtain fully differentiated tissue to implant. Applying external stimuli, cells activate biochemical pathways defining the functional properties of the resulting engineered tissue (Hoffman et al. 2011). For example, chemical stimulation was found to be particularly promising. On this regard, fibroblast growth factors (FGFs) showed to increase self-renewal and to maintain cell multi-lineage differentiation potential, transforming growth factors (TGFs) and serum-free medium-induced chondrogenesis; bone morphogenic proteins (BMPs) and dexamethasone were instead the most relevant chemical factors inducing osteogenesis and have already been employed for clinical treatments such as spinal fusion and long bone fractures (Wilson et al. 2005).

Another stimuli having an impact on cells differentiation is the mechanical load. As a matter of fact, the bone is constantly under loading condition arising from the daily activities. Vigorous exercise induces up to 1000 microstrain in human bone, where 1000 microstrain equal to 0.01% change in length compared to the initial length, and are associated with bone mass increase (Klein-Nulend et al. 2012). As many evidences have shown the possibility to influence cell behaviour through mechanical stimulation (Ehrlich and Lanyon 2002; Kelly and Jacobs 2010), the use of external mechanical stimuli on cell differentiation has become an increasingly common practice nowadays.

1.1.2 Mechanical Stimuli and Cell Behaviour

Cell behaviour can be triggered by hydrostatic pressure, fluid shear stress, mechanical strain and electrical fields generated by interstitial flow passing on charged bone crystals. For example, continuous hydrostatic pressure decreases collagen production by osteoblasts, while intermittent compressive forces enhance osteoblast activity and decreased osteoclast resorption (Rubin et al. 2006). Hydrostatic pressure has also shown to play a role on chondrocyte behaviour as a constant stimulus was proved to lead to chondrogenesis, while intermittent strain led to hypertrophy (Rubin et al. 2006). When bone is loaded in tension, compression or torsion, the interstitial fluid is moved towards regions of low pressure to come back when the load is removed, inducing an oscillatory fluid flow of 0.8 Pa up to 3 Pa in vivo. This regime results in a dramatic amplification of local strains in proximity of the osteocyte processes (Klein-Nulend et al. 2012; Klein-Nulend et al. 2005). Osteocytes are able to sense this variation in the interstitial fluid as demonstrated by multiple studies where shear stress was found to trigger mechano-activated biochemical pathways regulating NO production in osteocytes (Vezeridis et al. 2006; Rubin et al. 2006). Osteocytes were found to be more responsive to mechanical stimuli than other cell types and are believed to play a role in regulating the activity of osteoblasts and osteoclasts (Klein-Nulend et al. 1995). Furthermore, mechanical stimuli were shown to regulate calcium deposition with osteoblast cells increasing mineralization as a result of cyclic loading (Sittichockechaiwut et al. 2009; Damaraju et al. 2014).

1.1.3 Cell Mechanotransduction

The effect of mechanical forces on bone cells is currently under investigation aiming to define a relationship between stimuli and differentiation. The key cues to better understand the effect of mechanical stimuli on cell commitment are (1) the forces applied by the cytoskeleton and the contractile components of cells on the surrounding environment, (2) how the stiffness of the surrounding environment influences cells through durotaxis and (3) how external mechanical stimuli generated by gravitational action, muscles and other cells are translated into biochemical processes. In skeletogenesis the differentiation of stem cells towards the osteogenic or chondrogenic pathway is regulated by many external factors (Kelly and Jacobs 2010; Mauck 2003) influencing cytoskeletal organization, shape, motility (Lim et al. 2010; McBeath et al. 2004) as well as the expression of transcriptor factors (Salazar and Ohneda 2012). For example, the Wnt/ß-catenin or Rho/ROCK signalling pathways are known to play a crucial role in controlling cell commitment towards the osteogenic or chondrogenic pathway through the expression of Sox9 and Runx2 at early stage of differentiation (Kelly and Jacobs 2010). Sox9 is put alongside with expression of collagen II, TGFβ and glycosaminoglycan (GAG) genes and identifies differentiation towards the chondrogenic lineage, while Runx2 identifies osteogenic differentiation and induces expression of collagen I and non-collagenous proteins such as alkaline phosphatase (ALP), osteocalcin (OC) and osteopontin (OP). OC and OP are markers for bone mineralization and help in regulating the size of mineral crystals deposited by mature osteoblasts (Clarke 2008).

1.1.4 Bioreactors for Tissue Engineering

To find a correlation between mechanical forces and cell differentiation, complex bioreactors providing a controlled micromechanical environment were developed combining advanced scaffold designs and mechanical conditioning systems (Zhang et al. 2010; Tanaka 1999; Thorpe et al. 2013). Bioreactors facilitate the monitoring and control of biological or biochemical processes undergoing within the scaffold during the bone-forming process. Bioreactors are generally adapted to fit within an incubator that controls the external environment guaranteeing physiological conditions: 37 °C temperature, 5% CO_2 concentration and 99% humidity. A requirement for cell culture bioreactors is inertia to the harsh chemistry of the biological environment preventing corrosion and toxic reactions. Moreover, the diffusion limit and uniform distribution of cells in the scaffolds are key factors to consider in the development of functional tissue. With this purpose, bioreactors aim to maximize the supply of nutrients and oxygen to cells seeded in internal areas exceeding the diffusion limit distance of 100–200 μm (Ratcliffe and Niklason 2002) in order to maintain their viability. Exchange of substances within the scaffold during the seeding can be also used to help increasing seeding efficiency and uniform

distribution of cells (Sobral et al. 2011). For this purpose, current techniques employ convection of medium by perfusion, centrifugation and spinner flasks (Zhang et al. 2010). Moreover, bioreactors can be designed to apply shear strain forces, mechanical strain or pulsed electromagnetic fields with a high control over the stimulation in order to reproduce the biological environment and clarify the relationship between mechanical stimulation and tissue formation.

1.2 Bioreactors for Fluid Flow-Induced Cell Differentiation

A homogeneous cellular distribution and a good exchange of nutrients and oxygen within the scaffolding material are the first step in the development of functional engineered tissue. Due to the three dimensional architecture of novel scaffolds, static seeding is no longer an optimal method as it leads to a low seeding efficiency, cellular inhomogeneous distribution and low diffusion of fluids or gases in the internal regions causing cell apoptosis. In order to overcome these limitations, different systems were considered which are spinner flask (SF), rotating wall vessel (RWV), biaxial rotating (BXR) and perfusion bioreactors. These systems are more efficient compared to the static methods where molecule exchange occurs by diffusion because those novel systems induce a convective flow, enhancing cell attachment, proliferation and differentiation.

1.2.1 Rotating Bioreactors

SF bioreactors consist in a vessel provided with side arms for gas exchange and a stirring mechanism able to create a flow though the culture media (Fig. 1.1a). In order to avoid scaffolds fluctuation, pins are connected to the top lid for allocating samples. SF bioreactors were shown to increase the seeding efficiency compared to static methods (Mauney et al. 2004) and to induce osteogenic differentiation though the expression of ALP and OC and increased calcium deposition (Meinel et al. 2005).

RWV bioreactors consist in a hollow cylinder provided with an external chamber for scaffolds allocation and working as medium reservoir, rotating along the radial axis (Fig. 1.1b). The laminar flow generated by the rotating motion results in low shear stress preventing cell detachment and partially overcome the diffusional limitations characteristic of static and SF seeding methods. Despite this, lower cell number and matrix production were observed compared to SF methods because scaffolds are free to float inside the chamber hitting against the walls of the rotating vessel. Solutions include (1) fixing scaffolds to the cylindrical structure as in rotating

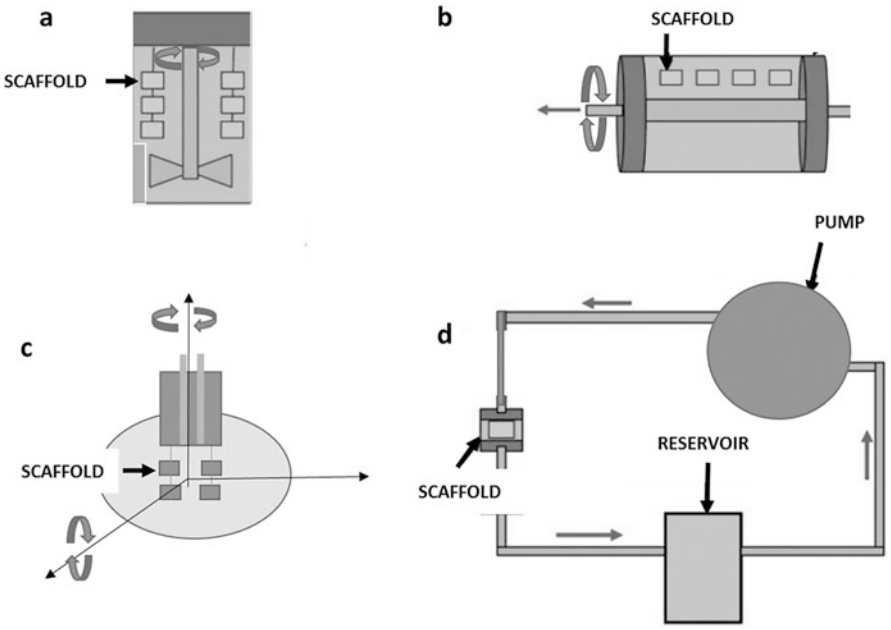

Fig. 1.1 Bioreactors for seeding and differentiation of MSCs due to effect of fluid flow. Spinner flask (**a**) and rotating wall vessel (**b**) bioreactors provide rotation towards an axis, while the biaxial rotating wall vessel (**c**) systems allow rotation in two directions providing homogeneous shear stress distribution in the culture chamber. Closed loop perfusion bioreactor (**d**) scheme employing a serial multichamber configuration. (Figures adjusted from Zhang et al. 2010)

bed bioreactors (Rauh et al. 2011), (2) employing scaffolds with lower density than water (Yeatts and Fisher 2011) or (3) preventing contact with the walls by optimization of the rotation rate (Zhang et al. 2010).

According to a study by Zhang (Zhang et al. 2010), the gold standard seeding performances are given by biaxial rotating bioreactor (BXR). It consists in a spherical chamber equipped with pins for scaffolds allocation, a reservoir for culture media and a perfusion system (Fig. 1.1c). The spherical chamber is able to rotate simultaneously in two perpendicular axes overcoming diffusion problems observed with SF. Moreover, it prevents cell detachment phenomena observed in RWV, thanks to the spaces for scaffold allocation. In summary, BXRs provide all the advantages of the perfusion systems while overcoming the "cell washout" phenomena observed in perfusion bioreactors. Indeed by not allocating the scaffold directly in the flow stream, cell detachment from the side of the scaffold facing the oncoming flow is prevented, resulting in higher homogeneous distribution of cells. BXRs increase considerably cell attachment, proliferation, molecule diffusion and osteogenic differentiation compared to SF, RWV and even perfusion bioreactors working in optimal conditions (Zhang et al. 2010).

1.2.2 *Perfusion Bioreactors*

In the last decade, the attention turned towards perfusion bioreactors (Fig. 1.1d) composed by a chamber fitting the geometry of the scaffold, a medium reservoir for supply of nutrients and a waste reservoir. Some perfusion bioreactors are closed loop and do not use a waste reservoir but nutrients are continuously pumped into the system (Kausar and Kishore 2013). Perfusion bioreactors force the fluid through the entire scaffold allowing cells to reach the interior of the structure and enhancing homogeneous distribution and optimal supply of gases and nutrients. The first challenge developing perfusion systems is related to prevent air bubbles formation as the presence of air is the main cause of local stress variation as it blocks the passage of fluid increasing the local flow rate and inhomogeneous condition inside the culture chamber, which might compromise the seeding process. A similar effect is observed when scaffolds are not completely anchored to the walls of the bioreactor chamber. In this case, void areas arise and become the preferred pathway for fluid to flow. The shear stresses generated by the fluid flowing through the scaffold are not only dependent on the inlet flow rate but also on the scaffold pore size and interconnectivity (Melchels et al. 2011; Porter et al. 2005; Chen et al. 2011). Despite the difficulties in developing efficient perfusion systems, a number of studies have studied the effect of perfusion flow on cell attachment, proliferation, matrix production and differentiation. While turbulent flow caused mainly cell detachment or programmed cell death due to the high shear stress (Cherry 1993), laminar regimes such as continuous, oscillating and pulsating flow led to satisfactory results and increased performances compared to static conditions. The effect of velocity and number of cycles on cell attachment was elucidated by Koch et al. who applied an oscillatory perfusion flow showing that velocities up to 5 mm/s were necessary in order to obtain uniform cell distribution in the interior of the scaffold (Fig. 1.2). He also demonstrated that the main effects on seeding efficiency were elicited by the number of cycles applied rather than the velocity used. Indeed, a lower number of cycles led to higher seeding efficiency. This suggests a dual role of shear stress which promotes cell attachment at the early stages of the seeding process but causes cell detachment if applied for long periods of time. The velocity of fluid flow was also found to significantly affect the viability of cells on the exterior of the scaffold as increased cell apoptosis was found associated to increasing shear stress regime (Fig. 1.3). These outcomes underline the need to define the optimal conditions enhancing uniform cell distribution, high seeding efficiency and cell viability.

Continuous unidirectional flow of cell suspension was also demonstrated to increase cell attachment and distribution (Vunjak-Novakovic et al. 1999; Wendt et al. 2003), ECM production and osteogenic differentiation (Scaglione et al. 2006; Bjerre et al. 2011; Papadimitropoulos et al. 2013; Koch et al. 2010; Sikavitsas et al. 2005). Moreover, a laminar flow oscillating in nature mimics the in vivo conditions applied to bone cells and stimulates calcium production in osteoblast-like cells (Koch et al. 2010) and human bone marrow stromal cells (Li et al. 2004). However, pulsating flow was found to be the most efficient in enhancing mineralization

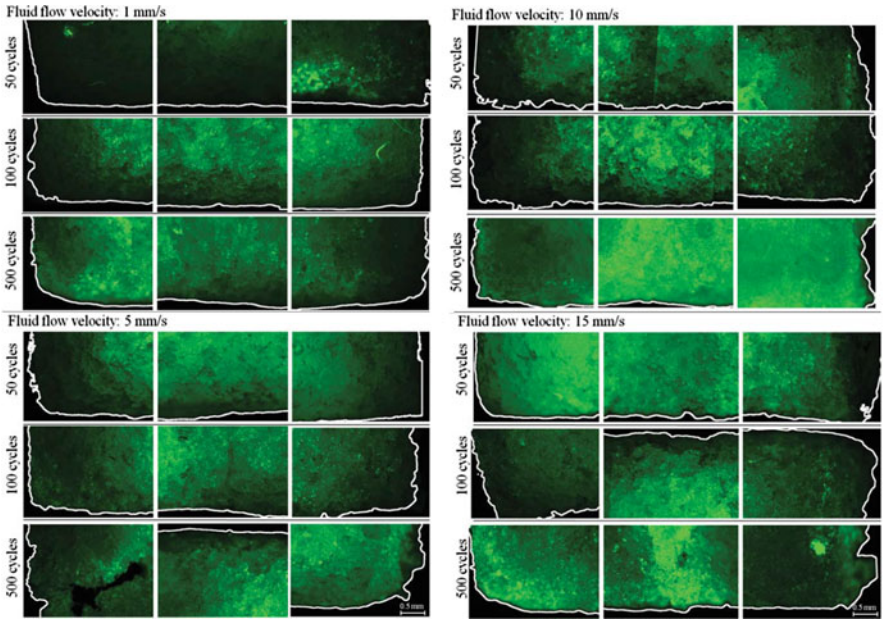

Fig. 1.2 Effect of velocity and number of cycles on cell attachment in the interior of the scaffold. (Koch et al. 2010)

(Jacobs et al. 1998; Bancroft et al. 2002), inhibiting cell apoptosis (Tan et al. 2008) and regulating matrix deposition (Vezeridis et al. 2006; Tan et al. 2007). The main drawback of perfusion bioreactors is the high amount of reagents needed, which has led to the development of perfusion microfluidic systems.

Microfluidic systems are easy to develop, require a low amount of reagents and above all allow to perform parallel experiments (Beebe et al. 2002). The new generation "lab on a chip" microfluidic devices permit repeatability of experimental conditions, testing simultaneously multiple samples. Due to their high versatility, they have already found application in the development of in vitro vascular implants (Khan et al. 2012). Polydimethylsiloxane (PDMS) is the most commonly used material for microfluidic perfusion culture systems since it is non-cytotoxic, autoclavable, gas permeable, flexible and easy to mold. Moreover, PDMS has low autofluorescence, and it is light transparent finding application for fluorescence and optical imaging (Kim et al. 2007). For cellular culture purposes, a glass-PDMS configuration is the preferred choice (Plecis and Chen 2007) as PDMS can be easily covalently bonded to glass substrates by surface activation through gas plasma treatments (Bhattacharya et al. 2005; Millare et al. 2008). Microfluidics systems made of glass-PDMS are currently used as support for 2D and 3D culture studies on the differentiation towards muscular tissue (Tourovskaia et al. 2005); the effect of different flow rates on cell morphology and proliferation (Kim et al. 2006), liver toxicology (Kane et al. 2006), cell seeding and monitoring (Toh et al. 2007); and

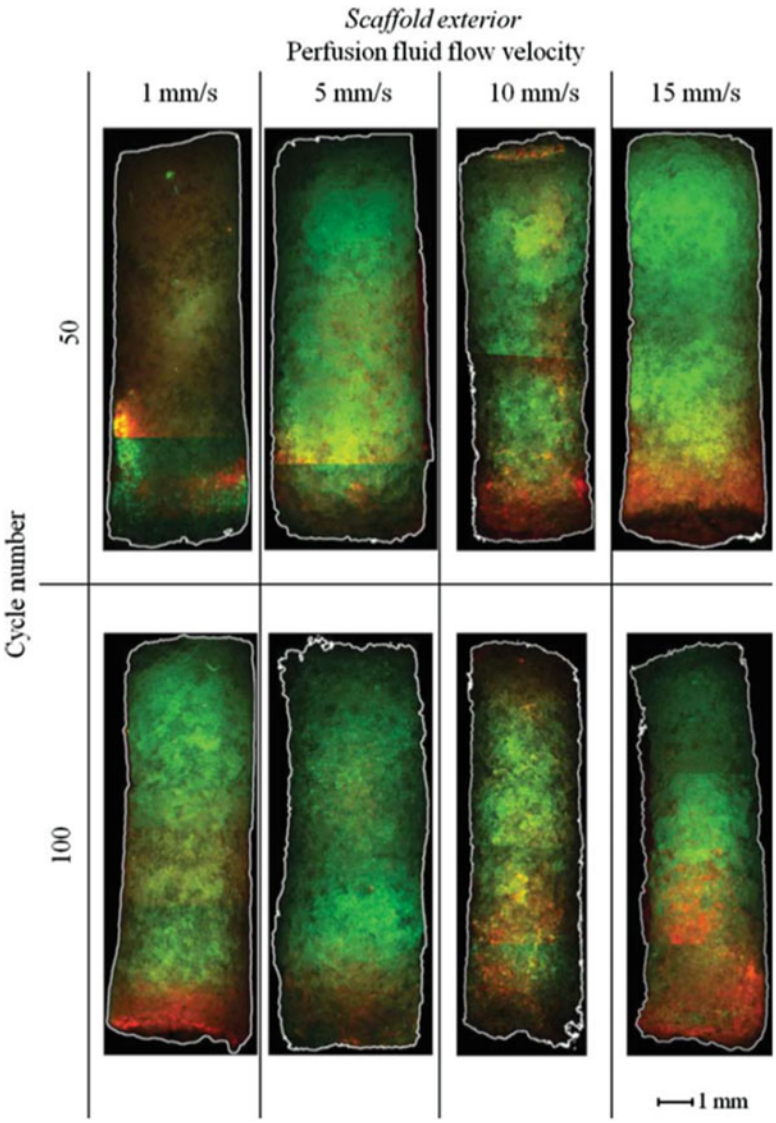

Fig. 1.3 Cell distribution on the exterior of the scaffold employing different velocities and number of cycles. Alive cells are shown in green, while apoptotic/dead cells are shown in red. (Koch et al. 2010)

comparison between cell lineages response to hydrostatic pressure (Park et al. 2012). Creating a robust sealed channel and avoiding bubble formation (Kim et al. 2007) are among the main challenges to currently face in the design of an efficient microfluidic system. In general, the fluid flow in a microfluidic perfusion system defines cell seeding efficiency and nutrients and gases delivery and can be used to transport

molecules probing cells to perform cellular assays to test for cellular activities or viability (Jeon et al. 2000). Normally fluid infusion processes are controlled by external pumps and valves and can employ multiple inputs. Among the applications mentioned above which can be controlled by fluid flow, cell seeding represent a particularly delicate issue as it needs optimization to avoid cells settling due to low shear stresses as well as cell viability and detrimental effects caused instead by high shears. On this matter, cell settling is normally overcome by minimizing the distance between cell reservoir and culture chamber or employing a viscous carrier to decrease the settling rate or by rotating the reservoir (Kim et al. 2007).

1.3 Bioreactors for Mechanically Loaded-Induced Cell Differentiation

1.3.1 Common Bioreactor Types

Common bioreactor systems for mechanical-induced differentiation include a vessel containing the culture media, space to allocate scaffolds and clamping parts aiming to apply tension or compression stimuli through an external computer control. In simple stretching devices, the extremities of the scaffold are anchored to grips connected to external automatic controls and able to move on a plane and transmit the displacement to the structure (Fig. 1.4a). Four-point bending devices (Fig. 1.4b) are another widely used and fairly simple configuration. The working principle consists in placing the structure on two vertical pillars and applying a force perpendicular to the plane of the structure (Mauney et al. 2004). Both setups allow high computed-control over the mechanical stimuli employing load and displacement sensors, actuators and an external control interface. Four-point bending systems equipped with micromanipulators and cameras were extensively used also to transmit tension as well as compression stimuli though the use of a piezoelectric actuators bending when voltage is applied (Tanaka 1999). Applying voltage, a piezoelectric layer shrinks while the other stretches, bending the actuator and transmitting the resulting displacement to the sample (Fig. 1.4c). When the polarity is inverted, the actuator bends on the other direction, allowing to test cell behaviour under both stimuli in 2D collagen layers. The addition of multiple chamber configurations allows high-throughput studies and increases repeatability and reproducibility of the tested conditions (MacQueen et al. 2012). Recently, novel bioreactors are developed to fit in incubators and maximize sterile conditions such as the BOSE ElectroForce® Systems (Fig. 1.4d) already employed in studies on scaffold mechanical characterization (Abrahamsson et al. 2010; Brunelli et al. 2017a), hMSCs differentiation (Thorpe et al. 2013; Brunelli et al. 2017b) and vascularization of bone grafts (Kong et al. 2012). The biodynamic chamber works as a bioreactor providing (1) sterile and isolated environment, (2) samples immersed state preventing drying phenomena, (3) high controlled tension or compression stimuli

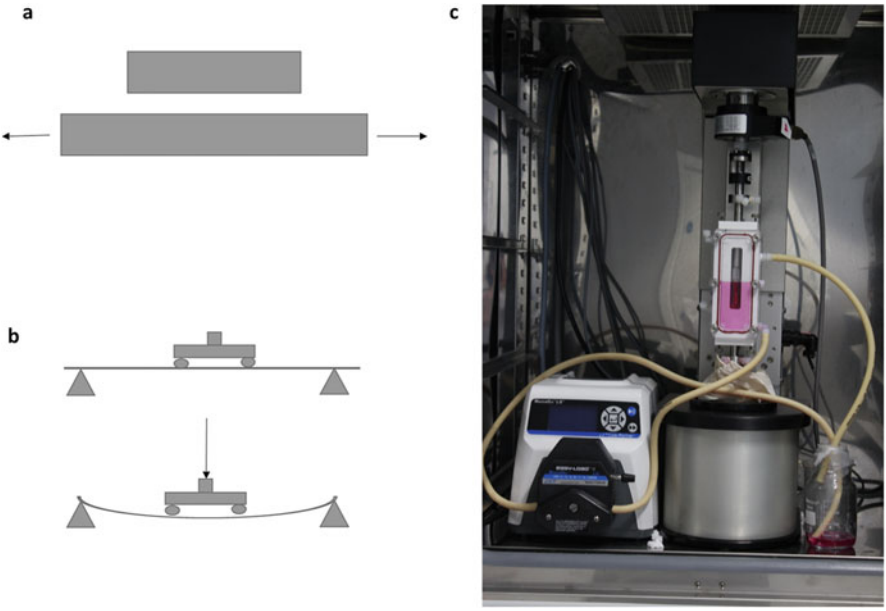

Fig. 1.4 Stretching principle to apply tension stimuli (**a**); four-point bending system (**b**) while applying deformation on 2D-seeded substrates; (**c**) BOSE ElectroForce® equipped with culture chamber forms mechanical stimulation and simultaneous perfusion of media

and simultaneously fluid shear stress by an external pumping system and (4) multiple motor configuration for parallel experiments.

1.3.2 Mechanical Load and Cell Commitment

By employing stretching devices or four-point bending systems, mesenchymal stem cells osteogenic commitment was studied on 2D surfaces or 3D structures (Table 1.1). 2D silicone membranes coated with collagen were considered to study MSCs behaviour under tension, showing increased osteogenic differentiation through synthesis of BMP2 and collagen 1 in multiple studies (Kearney et al. 2010; Rui et al. 2011; Friedl et al. 2007). Haudenshild et al. demonstrated the dual effect of tension and compression on hMSCs seeded in 3D alginate phosphate scaffolds (Haudenschild et al. 2009). Volume, surface area, skeletal length and diameter of cells were quantified by confocal images and revealed variation in cell morphology depending on the stimuli received. Compression stimuli led to round and shorter cells while tension led to more elongated and spread cells compared to controls. Moreover, gene microarray screening and RT-PCR analysis showed upregulation of a wide range of osteogenic genes and downregulation of chondrogenic genes in samples undergoing tension stimuli. The opposite expression

Table 1.1 Comparison between studies on the effect of mechanical forces on skeletogenesis

Cells	Scaffolds	Differentiation media	Parameters	Differentiation	References
Stretching devices					
MSCs	Silicon membrane	–	0.5% strain	Osteogenesis↑	Kearney et al. (2010)
			0.17 Hz		
			4 h/day		
			3 days/week		
		–	4 and 8% strain	Osteogenesis ↑	Rui et al. (2011)
			0.5 Hz		
			4 h/day		
		Osteogenic	0.3% strain	Osteogenesis↑	Friedl et al. (2007)
			1 Hz		
			15 min/day		
			2 or 8% strain	Strain 8%:	Jagodzinski et al. (2004)
			1 Hz	Osteogenesis↑	
			2 h/day		
			3 days/week		
Four-point bending					
BMSCs	Partially demineralized bone	Osteogenic	0.2 mm	Depending on dexamethasone concentration:	Mauney et al. (2004)
			0.2 Hz		
			250 cycles/day	Osteogenesis↑	
Osteoblasts	Collagen gels	–	0.3% strain	Low amplitude,	Tanaka et al. (2003)
			Low VS broad frequencies	High frequencies:	
				Osteogenesis ↑	
MSCs	Collagen gels	–	0.8, 0.9% strain	Chondrogenesis↓	Au-Yeung et al. (2010)
			1, 0.5, 0.1 Hz	Osteogenesis↓	
			1 h/day		

(continued)

Table 1.1 (continued)

Cells	Scaffolds	Differentiation media	Parameters	Differentiation	References
			7 days/week		
Porcine MSCs	Agarose hydrogels	Chondrogenic	10% + 1% strain	Chondrogenesis ↓	Thorpe et al. (2008)
			1 Hz		
			1 h/day		
			5 days/week		
		Chondrogenic VS untreated	10% strain	Supplementing chondrogenic media: Chondrogenesis ↑	Thorpe et al. (2010)
			1 Hz		
			1 h/day		
			5 days/week		
Other systems					
Porcine MSCs	Agarose hydrogels	Chondrogenic	10% strain	Confined compression: Chondrogenesis ↑	Thorpe et al. (2013)
			1 Hz		
			10 sec/day		
			5 days/week		
MSCs	Poly ethylene hydrogels	Chondrogenic VS untreated	10% strain	Chondrogenesis ↑	Terraciano et al. (2007)
			1 Hz		
			1, 2, 2.5, 4 h/day		
	Fibrin polyurethan 3D scaffolds	Chondrogenic	15, 20, 30% strain	High strain, high frequency: chondrogenesis ↑	Li et al. (2010)
			0.1, 1 Hz		
	Poly ethylene hydrogels	–	15% strain	Chondrogenesis↓	Steinmetz and Bryant (2011)
			0.3 Hz	Osteogenesis↓	
			4 h/day		
			14 days		
	Agarose hydrogels	–	9% strain	54, 120 mins: Chondrogenesis ↑	Elder et al. (2001)
			0.03, 0.15,0.33 Hz		
			12, 54, 120 min/day		
			3 days/week		

profile was characteristic in samples undergoing compression. Due to their remarkable properties in terms of biocompatibility, biomimetic, easy molding and transmission of uniform distribution of stresses through the structure, hydrogels were mainly considered as scaffolds for compression studies. Moreover, hydrogels allow accessibility to the core of the structure through fluorescence and optical light, enabling to monitor the conditions of cells placed in the interior volume of seeded scaffolds (Thevenot et al. 2008). For example, collagen gel scaffolds allowed real-time monitoring of cells and fibre alignment in multiple studies. Both static and cyclic loading conditions were shown to affect cell alignment inducing cells to orient parallel to the direction of the applied stress (Au-Yeung et al. 2010). However, collagen orientation, GAG and cellular metabolism variations were absent, suggesting that mechanical loading alone has no effect on the collagen remodelling action performed by hMSCs.

1.3.3 Loading Parameters Affecting Cells Response

Chemical cues have a high impact on the modulation of cellular response to mechanical forces. For example, the osteogenic commitment of bone marrow stromal cells (BMSCs) cultured in demineralized bone scaffolds and undergoing cyclic tension was found to be strictly related to the concentration of dexamethasone, varying ALP and OP expression. Absence as well as high amounts of dexamethasone (100 nM) led to suppression of osteogenic markers. Similar results were obtained investigating compression stimuli. When coupled with chondrogenic media, mechanical compression increased chondrogenesis gene expression (Thorpe et al. 2008), but compression forces alone showed to induce no significant differences in cell phenotype compared to free swelling samples in multiple studies (Terraciano et al. 2007; Thorpe et al. 2010).

Amplitude, frequency and duration of the stimuli can play a role in the activation of mechanotransduction pathways (Mack et al. 2004) and in modulating osteogenic or chondrogenic protein expression. Applying 2% and 8% cyclic tensile strain on MSCs, ALP activity and OC expression were upregulated when 8% strain was applied regardless of the presence of dexamethasone (Jagodzinski et al. 2004). The effect of sinusoidal frequencies (S), broad frequencies (V) and a combination of both (S + V) stimuli was investigated on osteoblasts keeping constant amplitude and varying frequencies of the stimulus. OC was 2.6-fold higher when S+V was applied; other osteogenic markers were upregulated after 4 days from V exposure, but no significant differences were noticed by applying S alone (Tanaka et al. 2003). Varying amplitude and frequency, Li et al. observed increased chondrogenic marker expression of the TGF family as result of high strain and high frequency stimulations (Li et al. 2010). Low-amplitude high-frequency stimuli were shown to produce the same effect as high-amplitude low-frequency stimuli to activate bone formation (Ozcivici et al. 2010). Similar results were obtained in other studies where the duration of the stimuli and its frequency were varied. Long periods of stimulations

have no significant difference in driving cell commitment compared to results obtained by continuous loading with downregulation of both osteogenic and chondrogenic markers (Steinmetz and Bryant 2011). hMSCs are sensitive to accumulation of stress eliciting a stronger chondrogenic commitment to higher frequencies as well as to strain history which enhances chondrogenic differentiation over longer periods of stimulation (54 or 120 min versus 12 min) (Elder et al. 2001). Despite the high amount of studies claiming chondrogenesis commitment as a result of compression, short boosts of compression were found to activate the same response as dexamethasone elicits on matrix mineralization by hMSCs cultured in polyurethane (Sittichokechaiwut et al. 2010) and 3D PCL (Brunelli et al. 2017b) scaffolds. This suggests the possibility to induce osteogenic differentiation by compression forces within polymeric scaffolds.

1.4 Electromagnetic Field Bioreactors and Differentiation

Electromagnetic field (EMF) and pulsed EMF (PEMF) in vivo arise from the piezoelectric effect induced by bone deformation as a consequence of muscular action (Kramarenko and Tan 2003). EMF stimuli arise in vivo in two ways: (1) as a consequence of postural or walking activities causing displacement in the bone and resulting in EMF frequencies ranging between 5 and 30 Hz and (2) when bone fracture occurs giving rise to a negative potential due to accumulation of negative charges at the injured site (Antonsson and Mann 1985). In the recovery process, EMFs and PEMFs have a beneficial effect on patients affected by osteoporosis or non-union fractures, decreasing bone resorption action performed by osteoblasts or accelerating the bone-forming process by osteoblasts (Bassett et al. 1977; Aaron et al. 2004). In order to observe the effect of EMFs and PEMFs on cellular conformational changes, proliferation and differentiation, EMF-based bioreactors were developed. These systems consist of two Helmholtz coins hosting a chamber for scaffold allocation and connected to an external EMF generator (Fig. 1.5). Applying continuous stimuli of PEMF was found to have no effect on osteoblasts or BMSCs proliferation, ALP or calcium content up to day 14 where an increase in calcium deposition occurs in BMSCs at the expense of proliferation (Jansen et al. 2010). In other studies employing short resting periods between consecutive stimulations (8 h), EMF increased hMSCs proliferation, viability and multi-lineage differentiation (Sun et al. 2009). MEF was found to affect bone progenitor cell proliferation rate depending on their bone differentiation stage (BMSCs versus osteoblasts) and the presence of osteogenic media (Sun et al. 2010). BMSCs have a higher proliferation rate compared to untreated controls in presence of osteogenic media whereas previously differentiated osteoblasts decreased in cell number compared to untreated controls. Increased ALP and BMP2 were observed at early stages culturing BMSCs in osteogenic media. Following these findings, studies were performed using mainly BMSCs culture in osteogenic media in order to maximize the osteogenic performance (osteogenic BMSCs). Increased osteogenic markers

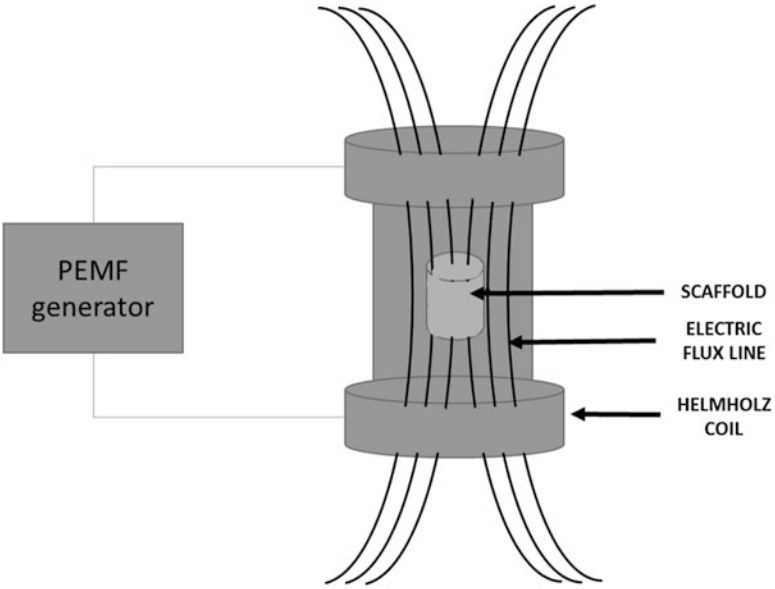

Fig. 1.5 Common design for PEMF bioreactors. (Figure adjusted from Zhang et al. 2010)

expression and proliferation rate were achieved by applying PEMF over shorter periods at low amplitude. Osteogenic BMSCs undergoing 0.13 mT quasi-rectangular pulses at 7.5 Hz for 2 h a day showed higher production of ALP at day 7 and enhanced mineralization at day 28 compared to untreated controls (Tsai et al. 2009). The effect of frequency on BMSCs osteogenic marker expression was further investigated at 1mT of EMF by varying frequencies at 10, 30, 50 and 70 Hz. Enhanced proliferation was observed in samples stimulated at 10 Hz as well as expression of ALP and OC after a week of treatment. Despite this, enhanced cell viability was observed at 50 Hz together with maturation of osteoblasts after 2 weeks of exposure and extensive matrix mineralization (Liu et al. 2013). Similar studies were performed supplementing hMSCs with chondrogenic media and applying 5mT sinusoidal EMF at 15 Hz four times a day (45 min every 8 h) over 21 days demonstrating that sinusoidal low-frequency EMF stimulates and maintains differentiation towards a lineage when supplemented with specific growth factors (Mayer-Wagner et al. 2011).

1.5 Discussion

As reviewed above, mechanical stimuli affect MSCs shape, proliferation, matrix production and gene expression. Perfusion and biaxial rotating systems assist the seeding process at early stage of culture as well as the differentiation at late stage of

culture, by providing either homogeneous distribution of cell or stresses through the scaffold. Microfluidic systems are able to provide the required amount of nutrients preventing waste issues and uniform shear stress stimuli through the seeded structure. Moreover, they are also a support for real-time monitoring of cell activities by building perfusion chambers made of light transparent materials and by setting a system of pumps regulating the flow of different solutions reacting with cells cultured in the bioreactor. Furthermore, the microfluidic approach minimizes the handling of samples and consequently the risk of infections and also provides multichamber configurations allowing to perform parallel experiments and to increase the repeatability of the tested conditions. Microsystems known as "lab on a chip" are also employed for applying tension and compression in a controlled biological environment.

In terms of differentiation following mechanical stimuli, the most relevant effects are observed by fluid flow which demonstrates to induce osteogenic differentiation without the need for osteogenic supplements. A dynamic flow enhances not only cellular attachment but also proliferation and osteogenesis. Pulsing fluid flow is the best condition eliciting osteogenic differentiation as it closely mimics the regime characterizing the interstitial fluid flow caused by physiological movements in vivo. Compression and tension stimuli do not define a clear differentiation pathway as the addition of osteogenic or chondrogenic media was often required in order to investigate their effect on cell commitment. Both stimuli led to enhanced cell differentiation when coupled with specific media formulations: compression led to chondrogenesis differentiation, while tension evoked osteogenesis as largely demonstrated in hydrogels. However, different regimes in terms of amplitude, frequency and duration of the stimuli have a strong impact on the final outcomes, leading to contrasting results. Osteogenesis is enhanced by high-amplitude low frequency as well as by low-amplitude high-frequency regimes, while high-amplitude high-frequency stimuli induce chondrogenesis. The duration of the stimuli as well was found to play a role in the differentiation process. Long period of stimulation seems to prevent differentiation of cells into the bone or cartilage, while short burst of stimulation is more effective in eliciting differentiation. EMF and PEMF can be considered to obtain fully differentiated bone tissue decreasing the amount of time required for the healing process as already demonstrated in vivo on osteoporotic patients. Short bursts of low-amplitude high-frequency stimuli put alongside osteogenic media supplements demonstrate once more to induce proliferation and mineralization in hMSCs.

Mechanical loading stimuli were mainly investigated on hydrogels due to their biocompatibility, accessibility to common imaging methods and their ability in transmitting to cells uniform stress through the whole structure. However, more recently the focus moved to the investigation of cells commitment in 3D porous structures due to the demand for scaffolds able to transmit higher strain amplitudes to cultured cells. Despite this, porous polymeric 3D scaffolds prevent the use of common imaging techniques, and their deformation is not easily predictable as for hydrogels due to their complex geometry and mechanics, hence losing control over the forces sensed by cells. While the distribution of stress in hydrogels is uniform

guaranteeing the same level of stress through all the volume of the scaffold, porous polymeric scaffolds present a complicate architecture whose deformation can lead to local tensile forces in the inner areas of the scaffold as a result, for example, of external compression. In addition, shear stress caused by the fluid flowing in and out of the structure elicits a still unclear synergic action with the external mechanical strain. Microcomputed tomography imaging and computer modelling are recently employed in an increasing number of studies (Van Lenthe et al. 2007; Tuan and Hutmacher 2005; Lacroix et al. 2009) aiming to help defining locally the mechanical environment and correlate it to cells commitment.

1.6 Conclusions

The effect of shear stress, mechanical stimuli and EMF was extensively investigated in the last two decades helping defining the role of different environmental conditions on gene upregulation and proteins expression. Osteogenesis is enhanced or inhibited depending on the regimes applied, the scaffold employed as support for mechanical stimulation and the differentiation stage of cells. Pulsing shear stress is the most promising stimulus to drive cell commitment towards the osteogenic pathway as it closely mimics flow regimes observed in vivo during common activities. The optimal combination of parameters to apply to stem cells in terms of tension, compression and shear stress to obtain fully differentiate tissue is nowadays still ongoing work and needs further optimization, but the need of chemical supplements as support in eliciting cell response as a consequence of mechanical stimuli is becoming more and more prevalent. Multiple chamber bioreactors having small dimensions are increasingly used to provide control over the mechanical environment and experimental conditions and to reduce experimental variability. Studies employing bioreactors put alongside with computer modelling give a good chance to obtain the control needed over external and internal conditions to ultimately obtain well-defined protocols able not only to clarify cell transduction pathways but also to drive differentiation towards functional tissue for TE purposes.

References

Aaron RK, Ciombor D, Simon BJ (2004) Treatment of non-unions with electric and electromagnetic fields. Clin Orthop Relat Res 419:21–29. Available at: http://journals.lww.com/corr/Abstract/2004/02000/Treatment_of_Nonunions_With_Electric_and.5.aspx. Accessed 29 May 2015

Abrahamsson CK et al (2010) Chondrogenesis and mineralization during in vitro culture of human mesenchymal stem cells on three-dimensional woven scaffolds. Tissue Eng A 16 (12):3709–3718. Available at: http://www.pubmedcentral.nih.gov/articlerender.fcgi?artid=2991213&tool=pmcentrez&rendertype=abstract. Accessed 16 Aug 2013

Antonsson EK, Mann RW (1985) The frequency content of gait. J Biomech 18(1):39–47

Au-Yeung KL et al (2010) Development of a micromanipulator-based loading device for mechanoregulation study of human mesenchymal stem cells in three-dimensional collagen constructs. Tissue Eng Part C 16(1):93–107

Bancroft GN et al (2002) Fluid flow increases mineralized matrix deposition in 3D perfusion culture of marrow stromal osteoblasts on a dose-depend manner. Natl Acad Sci 99(20):12600–12605

Bassett CAL, Pilla A, Pawluk R (1977) A non-operative salvage of surgically-resistant pseudarthroses and non-unions by pulsing electromagnetic fields: a preliminary report. Clin Orthop Relat Res 124:128–143. Available at: http://journals.lww.com/corr/Citation/1977/05000/A_Non_Operative_Salvage_of_Surgically_Resistant.17.aspx. Accessed 29 May 2015

Beebe DJ, Mensing GA, Walker GM (2002) Physics and applications of microfluidics in biology. Annu Rev Biomed Eng 4:261–286. Available at: http://www.google.com/search?client=safari&rls=en-us&q=Physics+and+applications+of+microfluidics+in+biology&ie=UTF-8&oe=UTF-8. Accessed 7 Aug 2013

Bhattacharya S et al (2005) Studies on surface wettability of poly (dimethyl) siloxane (PDMS) and glass under oxygen-plasma treatment and correlation with bond strength. J Microelectromech Syst 14(3):590–597

Bjerre L et al (2011) Flow perfusion culture of human mesenchymal stem cells on coralline hydroxyapatite scaffolds with various pore sizes. J Biomed Mater Res A 97(3):251–263. Available at: http://www.ncbi.nlm.nih.gov/pubmed/21442726. Accessed 27 Oct 2014

Brunelli M, Perrault CM, Lacroix D (2017a) Mechanical response of 3D insert® PCL to compression. J Mech Behav Biomed Mater 65:478–489. https://doi.org/10.1016/j.jmbbm.2016.08.038

Brunelli M, Perrault CM, Lacroix D (2017b) Short bursts of cyclic mechanical compression modulates tissue formation in a 3D hybrid scaffold. J Mech Behav Biomed Mater 71:165–174. https://doi.org/10.1016/j.jmbbm.2017.03.008

Caplan AI (2007) Adult mesenchymal stem cells for tissue engineering versus regenerative medicine. J Cell Physiol 213:341–347

Chen Y et al (2011) Characterization and optimization of cell seeding in scaffolds by factorial design: quality by design approach for skeletal tissue engineering. Tissue Eng Part C 17 (12):1211–1221. Available at: http://eutils.ncbi.nlm.nih.gov/entrez/eutils/elink.fcgi?dbfrom=pubmed&id=21895492&retmode=ref&cmd=prlinks. Accessed 14 Sept 2013

Cherry RS (1993) Animal cells in turbulent fluids: details of the physiscal stimulus and the biological response. Biotechnol Adv 11:279–299

Clarke B (2008) Normal bone anatomy and physiology. Clin J Am Soc Nephrol 3:131–139. Available at: http://www.pubmedcentral.nih.gov/articlerender.fcgi?artid=3152283&tool=pmcentrez&rendertype=abstract. Accessed 9 July 2014

Damaraju S et al. (2014) The effect of mechanical stimulation on mineralization in differentiating osteoblasts in collagen-I scaffolds. Tissue Eng Part A 1–12. Available at: http://www.ncbi.nlm.nih.gov/pubmed/24851936. Accessed 19 Sept 2014

Ehrlich PJ, Lanyon LE (2002) Mechanical strain and bone cell function: a review. Osteoporos Int 13:688–700

Elder SH et al (2001) Chondrocyte differentiation is modulated by frequency and duration of cyclic compressive loading. Ann Biomed Eng 29(6):476–482

Finkemeier CG (2002) Bone-Grafting and Bone-Graft Substitutes. J Bone Joint Surg 84A (3):454–463

Friedl G et al (2007) Undifferentiated human mesenchymal stem cells (hMSCs) are highly sensitive to mechanical strain: transcriptionally controlled early osteo-chondrogenic response in vitro. Osteoarthr Cartil 15(11):1293–1300. Available at: http://www.ncbi.nlm.nih.gov/pubmed/17977755. Accessed 1 Oct 2014

Haudenschild AK et al (2009) Pressure and distortion regulate human mesenchymal stem cell gene expression. Ann Biomed Eng 37(3):492–502. Available at: http://www.ncbi.nlm.nih.gov/pubmed/19125331. Accessed 20 Jan 2014

Hoffman BD, Grashoff C, Schwartz MA (2011) Dynamic molecular processes mediate cellular mechanotransduction. Nature 475(7356):316–323

Jacobs CR et al (1998) Differential effect of steady versus oscillating flow on bone cells. J Biomech 31:969–976
Jagodzinski M et al (2004) Effects of cyclic longitudinal mechanical strain and dexamethasone on osteogenic differentiation of human bone marrow stromal cells. Eur Cells Mater 7:35–41
Jansen JH et al (2010) Stimulation of osteogenic differentiation in human osteoprogenitor cells by pulsed electromagnetic fields: an in vitro study. BMC Musculoskelet Disord 11:188–199
Jeon NL et al (2000) Generation of solution and surface gradients using microfluidic systems. Langmuir 16:8311–8316
Kane BJ et al (2006) Liver-specific functional studies in a microfluidic array of primary mammalian hepatocytes. Anal Chem 78(13):4291–4298
Kausar H, Kishore RN (2013) Bone tissue engineering. Int J Pharm Pharm Sci 5(1):30–32
Kearney EM et al (2010) Tensile strain as a regulator of mesenchymal stem cell osteogenesis. Ann Biomed Eng 38(5):1767–1779. Available at: http://www.ncbi.nlm.nih.gov/pubmed/20217480. Accessed 20 Sept 2014
Kelly DJ, Jacobs CR (2010) The role of mechanical signals in regulating chondrogenesis and osteogenesis of mesenchymal stem cells. Birth Defects Res Part C 85(Part C):75–85. Available at: http://www.ncbi.nlm.nih.gov/pubmed/20301221. Accessed 7 Nov 2013
Khan OF, Chamberlain MD, Sefton MV (2012) Toward an in vitro vasculature: differentiation of mesenchymal stromal cells within an endothelial cell-seeded modular construct in a microfluidic flow chamber. Tissue Eng A, 18:744–756. Available at: http://www.pubmedcentral.nih.gov/articlerender.fcgi?artid=3313613&tool=pmcentrez&rendertype=abstract. Accessed 6 Aug 2013
Kim L et al (2006) Microfluidic arrays for logarithmically perfused embryonic stem cell culture. Lab Chip 6(3):394–406. Available at: http://www.ncbi.nlm.nih.gov/pubmed/16511623. Accessed 10 Aug 2013
Kim L, Toh Y, Voldman J (2007) A practical guide to microfluidic perfusion culture of adherent mammalian cells. Lab Chip 7(6):681–694. Available at: http://www.rsc.org/delivery/_ArticleLinking/ArticleLinking.asp?JournalCode=LC&Year=2007&ManuscriptID=b704602b&Iss=Advance_Article. Accessed 20 Aug 2013
Klein-Nulend J et al (1995) Pulsating fluid flow increases nitric oxide (NO) synthesis by osteocytes but not periosteal fibroblasts - correlaation with prostaglandin regulation. Biochem Biophys Res Commun 217(2):640–648
Klein-Nulend J, Bacabac RG, Mullender MG (2005) Mechanobiology of bone tissue. Pathol Biol 53(10):576–580. Available at: http://www.ncbi.nlm.nih.gov/pubmed/16364809. Accessed 23 Sept 2013
Klein-Nulend J, Bacabac R, Bakker A (2012) Mechanical loading and how it affects bone cells: the role of the osteocyte cytoskeleton in maintaining our skeleton. Eur Cells Mater 24:278–291
Koch MA et al (2010) Perfusion cell seeding on large porous PLA/calcium phosphate composite scaffolds in a perfusion bioreactor system under varying perfusion parameters. J Biomed Mater Res A 95(4):1011–1018. Available at: http://www.ncbi.nlm.nih.gov/pubmed/20872752. Accessed 14 Sept 2013
Kong Z et al (2012) Dynamic compression promotes proliferation and neovascular networks of endothelial progenitor cells in demineralized bone matrix scaffold seed. J Appl Physiol 113 (4):619–626. Available at: http://www.ncbi.nlm.nih.gov/pubmed/22723630. Accessed 19 Sept 2014
Kramarenko AV, Tan U (2003) Effects of high-frequency electromagnetic fields on human EEG: a brain mapping study. Int J Neurosci 113:1007–1019
Lacroix D, Planell JA, Prendergast PJ (2009) Computer-aided design and finite-element modelling of biomaterial scaffolds for bone tissue engineering. Philos Transact A Math Phys Eng Sci 367 (1895):1993–2009. Available at: http://www.ncbi.nlm.nih.gov/pubmed/19380322. Accessed 4 Sept 2013
Li YJ et al (2004) Oscillatory fluid flow affects human marrow stromal cell proliferation and differentiation. J Orthop Sci 22:1283–1289

Li Z et al (2010) Chondrogenesis of human bone marrow mesenchymal stem cells in fibrin-polyurethane composites is modulated by frequency and amplitude of dynamic compression and shear stress. Tissue Eng 16(2):575–584

Lim CT, Bershadsky A, Sheetz MP (2010) Mechanobiology. J R Soc Interface 7:291–293. Available at: http://www.pubmedcentral.nih.gov/articlerender.fcgi?artid=2943884&tool=pmcentrez&rendertype=abstract. Accessed 4 Sept 2014

Liu C et al (2013) Effect of 1 mT sinusoidal electromagnetic fields on proliferation and osteogenic differentiation of rat bone marrow mesenchymal stromal cells. Bioelectromagnetics 34 (6):453–464. Available at: http://www.ncbi.nlm.nih.gov/pubmed/23589052

Mack PJ et al (2004) Force-induced focal adhesion translocation: effects of force amplitude and frequency. Am J Physiol 287(4):954–962

MacQueen L et al (2012) Three-dimensional mechanical compression of biomaterials in a microfabricated bioreactor with on-chip strain sensors. In: 16th intern conf miniaturized systems for chemistry and life science, p 1141–43

Mauck R (2003) The role of cell seeding density and nutrient supply for articular cartilage tissue engineering with deformational loading. Osteoarthr Cartil 11(12):879–890. Available at: http://www.sciencedirect.com/science/article/pii/S1063458403002322. Accessed 22 Jan 2014

Mauney JR et al (2004) Mechanical stimulation promotes osteogenic differentiation of human bone marrow stromal cells on 3-D partially demineralized bone scaffolds in vitro. Calcif Tissue Int 74 (5):458–468. Available at: http://www.ncbi.nlm.nih.gov/pubmed/14961210. Accessed 8 Nov 2013

Mayer-Wagner S et al (2011) Effects of low frequency electromagnetic fields on the chondrogenic differentiation of human mesenchymal stem cells. Bioelectromagnetics 32(4):283–290

McBeath R et al (2004) Cell shape, cytoskeletal tension, and RhoA regulate stem cell lineage commitment. Dev Cell 6(4):483–495. Available at: http://www.sciencedirect.com/science/article/pii/S1534580704000759. Accessed 13 Nov 2013

Meinel L et al (2005) The inflammatory responses to silk films in vitro and in vivo. Biomaterials 26 (2):147–155. Available at: http://www.ncbi.nlm.nih.gov/pubmed/15207461. Accessed 27 Aug 2013

Melchels FP et al (2011) The influence of the scaffold design on the distribution of adhering cells after perfusion cell seeding. Biomaterials 32(11):2878–2884. Available at: http://www.ncbi.nlm.nih.gov/pubmed/21288567. Accessed 14 Sept 2013

Millare B et al (2008) Dependence of the quality of adhesion between poly (dimethylsiloxane) and glass surfaces on the conditions of treatment with oxygen plasma. Langmuir 24:13218–13224

Ozcivici E et al (2010) Low-level vibrations retain bone marrow ' s osteogenic potential and augment recovery of trabecular bone during Reambulation. PLoS One 5(6):11178–11188

Papadimitropoulos A et al (2013) A collagen network phase improves cell seeding of open-pore structure scaffolds under perfusion. J Tissue Eng Regen Med 7:183–191

Park S et al (2012) Chip-based comparison of the osteogenesis of human bone marrow- and adipose tissue-derived mesenchymal stem cells under mechanical stimulation. In: Kerkis I (ed) PLoS ONE 7(9); 46689–700. Available at: http://dx.plos.org/10.1371/journal.pone.0046689. Accessed 11 Feb 2014

Plecis A, Chen Y (2007) Fabrication of microfluidic devices based on glass–PDMS–glass technology. Microelectron Eng 84:1265–1269. Available at: http://linkinghub.elsevier.com/retrieve/pii/S0167931707001451. Accessed 9 Aug 2013

Porter B et al (2005) 3-D computational modeling of media flow through scaffolds in a perfusion bioreactor. J Biomech 38(3):543–549. Available at: http://www.ncbi.nlm.nih.gov/pubmed/15652553. Accessed 22 Aug 2013

Ratcliffe A, Niklason LE (2002) Bioreactors and bioprocessing for tissue engineering. Ann N Y Acad Sci 961:210–215

Rauh J et al (2011) Bioreactor systems for bone tissue engineering. Tissue Eng Part B Rev 17 (4):263–280. Available at: http://www.ncbi.nlm.nih.gov/pubmed/21495897. Accessed 27 Octo 2014

Rubin J, Rubin C, Jacobs CR (2006) Molecular pathways mediating mechanical signaling in bone. Gene 367:1–16. Available at: http://www.pubmedcentral.nih.gov/articlerender.fcgi?artid=3687520&tool=pmcentrez&rendertype=abstract. Accessed 23 Sept 2013

Rui YF et al (2011) Mechanical loading increased BMP-2 expression which promoted osteogenic differentiation of tendon-derived stem cells. J Orthop Res 29(3):390–396. Available at: http://www.ncbi.nlm.nih.gov/pubmed/20882582. Accessed Sept 2014

Salazar GT, Ohneda O (2012) Review of biophysical factors affecting osteogenic differentiation of human adult adipose-derived stem cells. Biophys Rev 5(1):11–28. Available at: http://link.springer.com/10.1007/s12551-012-0079-6. Accessed 17 Nov 2013

Salgado AJ, Coutinho OP, Reis RL (2004) Bone tissue engineering: state of the art and future trends. Macromol Biosci 4:743–765

Scaglione S et al (2006) Engineering of osteoinductive grafts by isolation and expansion of ovine bone marrow stromal cells directly on 3D ceramic scaffolds. Biotechnol Bioeng 93(1):181–187. Available at: http://www.ncbi.nlm.nih.gov/pubmed/16245346. Accessed 5 Feb 2015

Sikavitsas VI et al (2005) Flow perfusion enhances the calcified matrix deposition of marrow stromal cells in biodegradable nonwoven fiber mesh scaffolds. Ann Biomed Eng 33(1):63–70

Sittichockechaiwut A et al (2009) Use of rapidly mineralising osteoblasts and short periods of mechanical loading to accelerate matrix maturation in 3D scaffolds. Bone 44(5):822–829. Available at: http://www.sciencedirect.com/science/article/pii/S8756328209000040. Accessed 22 Jan 2014

Sittichokechaiwut A et al (2010) Short bouts of mechanical loading are as effective as dexamethasone at inducing matrix production by human bone marrow mesenchymal stem cells. Eur Cells Mater 20:45–57

Sobral JM et al (2011) Three-dimensional plotted scaffolds with controlled pore size gradients: effect of scaffold geometry on mechanical performance and cell seeding efficiency. Acta Biomater 7(3):1009–1018. Available at: http://www.ncbi.nlm.nih.gov/pubmed/21056125. Accessed 14 Oct 2014

Steinmetz NJ, Bryant SJ (2011) The effects of intermittent dynamic loading on chondrogenic and osteogenic differentiation of human marrow stromal cells encapsulated in RGD-modified poly (ethylene glycol) hydrogels. Acta Biomater 7(11):3829–3840. Available at: http://www.ncbi.nlm.nih.gov/pubmed/21742067. Accessed 10 June 2014

Sun L et al (2009) Effect of pulsed electromagnetic field on the proliferation and differentiation potential of human bone marrow mesenchymal stem cells. Bioelectromagnetics 30(4):251–260

Sun L et al (2010) Pulsed electromagnetic fields accelerate proliferation and osteogenic gene expression in human bone marrow mesenchymal stem cells during osteogenic differentiation. Bioelectromagnetics 31(3):209–219

Tan SD et al (2007) Osteocytes subjected to fluid flow inhibit osteoclast formation and bone resorption. Bone 41(5):745–751. Available at: http://www.ncbi.nlm.nih.gov/pubmed/17855178. Accessed 23 Sept 2013

Tan SD et al (2008) Inhibition of osteocyte apoptosis by fluid flow is mediated by nitric oxide. Biochem Biophys Res Commun 369(4):1150–1154. Available at: http://www.ncbi.nlm.nih.gov/pubmed/18339304. Accessed 23 Sept 2013

Tanaka SM (1999) A new mechanical stimulator for cultured bone cells using piezoelectric actuator. J Biomech 32(4):427–430

Tanaka SM et al (2003) Effects of broad frequency vibration on cultured osteoblasts. J Biomech 36 (1):73–80. Available at: http://www.ncbi.nlm.nih.gov/pubmed/12485640

Terraciano V et al (2007) Differential response of adult and embryonic mesenchymal progenitor cells to mechanical compression in hydrogels. Stem Cells 25:2730–2738

Thevenot P et al (2008) Method to analyze three-dimensional cell distribution and infiltration in degradable scaffolds. Tissue Eng Part C 14(4):319–331. Available at: http://www.pubmedcentral.nih.gov/articlerender.fcgi?artid=2913783&tool=pmcentrez&rendertype=abstract. Accessed 15 Aug 2013

Thorpe SD et al (2008) Dynamic compression can inhibit chondrogenesis of mesenchymal stem cells. Biochem Biophys Res Commun 377(2):458–462. Available at: http://www.sciencedirect.com/science/article/pii/S0006291X08019463. Accessed 7 Nov 2013

Thorpe SD et al (2010) The response of bone marrow-derived mesenchymal stem cells to dynamic compression following TGF-beta3 induced chondrogenic differentiation. Ann Biomed Eng 38 (9):2896–2909. Available at: http://www.ncbi.nlm.nih.gov/pubmed/20458627. Accessed 4 Sept 2014

Thorpe SD et al (2013) Modulating gradients in regulatory signals within mesenchymal stem cell seeded hydrogels: a novel strategy to engineer zonal articular cartilage. PLoS One 8 (4):60764–60777. Available at: http://www.pubmedcentral.nih.gov/articlerender.fcgi?artid=3628868&tool=pmcentrez&rendertype=abstract. Accessed 8 Sept 2014

Toh Y et al (2007) A novel 3D mammalian cell perfusion-culture system in microfluidic channels. Lab Chip 7(3):302–309

Tourovskaia A, Figueroa-Masot X, Folch A (2005) Differentiation-on-a-chip: a microfluidic platform for long-term cell culture studies. Lab Chip 5(1):14–19

Tsai M et al (2009) Modulation of osteogenesis in human mesenchymal stem cells by specific pulsed electromagnetic field stimulation. J Orthop Res 27(9):1169–1174

Tuan HS, Hutmacher DW (2005) Application of micro CT and computation modeling in bone tissue engineering. Comput Aided Des 37(11):1151–1161. Available at: http://linkinghub.elsevier.com/retrieve/pii/S0010448505000369. Accessed 27 Aug 2013

Van Lenthe GH et al (2007) Nondestructive micro-computed tomography for biological imaging and quantification of scaffold-bone interaction in vivo. Biomaterials 28(15):2479–2490. Available at: http://www.ncbi.nlm.nih.gov/pubmed/17258316. Accessed 20 Aug 2013

Vezeridis PS et al (2006) Osteocytes subjected to pulsating fluid flow regulate osteoblast proliferation and differentiation. Biochem Biophys Res Commun 348(3):1082–1088. Available at: http://www.ncbi.nlm.nih.gov/pubmed/16904067. Accessed 23 Sept 2013

Vunjak-Novakovic G et al (1999) Bioreactor cultivation conditions modulate the composition and mechanical properties of tissue-engineered cartilage. J Orthop Res 17(1):130–138

Wendt D et al (2003) Oscillating perfusion of cell suspensions through three-dimensional scaffolds enhances cell seeding efficiency and uniformity. Biotechnol Bioeng 84(2):205–214. Available at: http://www.ncbi.nlm.nih.gov/pubmed/12966577. Accessed 20 Aug 2013

Wilson CJ et al (2005) Mediation of biomaterial – cell interactions by adsorbed proteins: a review. Tissue Eng 11(1):1–18

Yeatts AB, Fisher JP (2011) Bone tissue engineering bioreactors: dynamic culture and the influence of shear stress. Bone 48(2):171–181. Available at: http://www.ncbi.nlm.nih.gov/pubmed/20932947. Accessed 25 Oct 2014

Zhang Z et al (2010) A comparison of bioreactors for culture of fetal mesenchymal stem cells for bone tissue engineering. Biomaterials 31(33):8684–8695. Available at: http://www.ncbi.nlm.nih.gov/pubmed/20739062. Accessed 14 Oct 2014

Chapter 2
Multiscale Simulation of Bioreactor Design and In Vitro Conditions

Tissue grafts obtained from tissue engineering techniques can be developed with the application of cells in a scaffold within a bioreactor. In this chapter we present a multiscale method to simulate a bioreactor design that can adapt to the personalized tissue sought. It includes personalization of the bioreactor design but also personalization of the in vitro conditions. As the research area is going further and the computational possibilities as well, tools must be developed to design patient's cell-specific pair of scaffold and bioreactor, as a virtual physiological human cell tool.

Thanks to a parametric geometry and a computational fluid dynamics model, we are able to design bioreactor chambers relying on the nearest boundary conditions in the bones to apply it to the bone substitute where cells have been seeded. First of all, considering an existing bioreactor chamber, we can design an optimized scaffold knowing the boundary conditions that the bioreactor chamber will impose. On the other hand, knowing the scaffold geometry used, a bioreactor chamber will be designed to reach appropriate environmental conditions at the cell scale.

It allowed testing two different bioreactor geometries showing no major interest within the simulation, but regarding the experimental process, the bubble traps presence is compulsory to avoid cell death. On the other hand, two scaffold geometries were tested highlighting a major difference regarding the local fluid flow within the scaffold pores and therefore on the cell development. Moreover, experimental analyses are required to correctly compare the simulation and improve the strength of the optimization process.

2.1 Introduction

Tissue grafts obtained from tissue engineering techniques can be developed with the application of cells in a scaffold within a bioreactor (see Chap. 1 for a detailed review). Nonetheless those biotechnical progresses remain empirical in practice and mostly based on a trial-and-error approach. Biomechanics used jointly with bioinformatics techniques are able to provide predictive tools to design patient-specific bioreactors. In this chapter we will present a multiscale method to simulate a bioreactor design that can adapt to the personalized tissue sought. It includes

© Springer Nature Singapore Pte Ltd. 2019

D. Lacroix et al., *Multiscale Mechanobiology in Tissue Engineering*,
Frontiers of Biomechanics 3, https://doi.org/10.1007/978-981-10-8075-3_2

personalization of the bioreactor design but also personalization of the in vitro conditions (Chabiniok et al. 2016).

Cell seeding in biomaterial scaffolds is often achieved through a perfusion bioreactor. However, not all scaffolds and perfusion bioreactors are optimized to each other. The scaffold and the bioreactor used to generate the engineered tissue have usually been developed empirically. As the research area is going further and the computational possibilities as well, tools must be developed to design patient's cell-specific pair of scaffold and bioreactor, as a virtual physiological human (VPH) cell tool (Baldit et al. 2014).

Combining experimental measurements with fluid, structure and fluid/structure analysis, we are able to calculate the mechanical stimuli at the cell, scaffold and bioreactor levels in a patient- or sample-specific manner. This chapter is focused on designing bioreactor chamber or scaffold with ideal conditions to generate engineered tissues in optimal conditions. Thanks to a parametric geometry and a computational fluid dynamics (CFD) model, we are able to design bioreactor chambers relying on the nearest boundary conditions in the bones to apply it to the bone substitute where cells have been seeded. This chapter aims to propose a method and workflow to provide to specific selected cells:

1. Boundary conditions for an accurate analysis at the scaffold scale
2. Boundary conditions for fluid perfusion in a bioreactor chamber
3. Mould drafts of chamber and scaffold to be used with a 3D printer, for instance

This multiscale approach enables to simulate the tissue engineering process by predicting the tissue formation that results from a specific environment under given biological, chemical or mechanical conditions.

2.2 The Bioreactor Design Process

2.2.1 The Bioreactor Chamber

As described in Chap. 1, there are many ways to realize a bioreactor (Zhang et al. 2010; Tanaka 1999; Thorpe et al. 2013; Kausar and Kishore 2013; Beebe et al. 2002). It is well known that the cell environment is key to produce the sought tissue.

In order to test a wide range of bioreactor designs and predict the influence of one component of the geometry of the bioreactor, a parametric generator is ideal to design a specific bioreactor. Those designs must be consistent with the usual biological materials used and able to mimic the conditions under which the bioreactor is undergoing.

To be as flexible as possible, microfluidic systems seem to be the easiest way to try and design as many bioreactors as we need to fulfil our objectives. The advantages of this technique are defined in Chap. 1. Nonetheless, it is material (cells, physiological solution, polymers, chemical components) and time-consuming. Therefore a numerical simulation of this technique would only reduce it to a

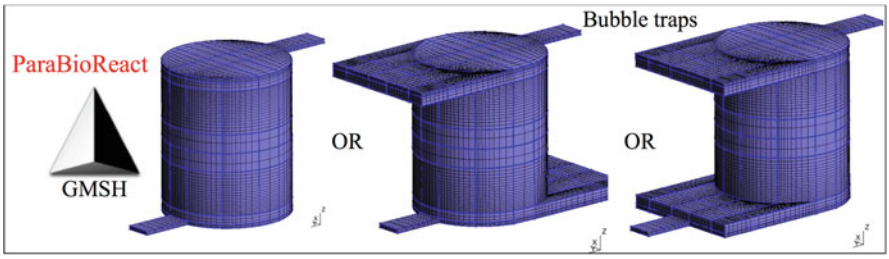

Fig. 2.1 Parametric geometries provided by *ParaBioReact*

computational cost. Moreover, with various simulations with different external stimuli like a pump, a mechanical loading device, a chemical loading through the physiological environment can be probed allowing a huge flexibility of design reducing unexpected experimental discrepancies. Although once a suitable design is obtained, an experimental test is required to ensure the design validity.

2.2.2 A Parametric Bioreactor

A tool was developed to generate various geometries of the bioreactor named *ParaBioReact* for parametric bioreactor. It was done with *GMSH* (Geuzaine and Remacle 2009), and some possibilities are presented in the following part.

2.2.2.1 Geometry Generation

Three geometries are presented in Fig. 2.1. From the left to the right, bioreactor chambers evolve from the simplest one and two configurations including bubble traps to avoid air bubble inside the chamber.

2.2.2.2 Mesh Generation

Mesh density relies on the sought model's accuracy. For instance, it means that this generic tool allows generating a rough mesh to improve the optimization process and find approximate results. Then they will be improved with an accurate mesh to obtain better final results.

Depending on the foreseen resolution method, linear or quadratic meshes can be generated on tetrahedral or hexahedral configuration as presented on Fig. 2.2.

The number of elements depends on the parameterization used and, for instance, the meshes on Fig. 2.2 contain 134,678 and 26,244 elements, respectively, for tetrahedral and hexahedral versions. Obviously the mesh control allows optimizing the mesh pattern reducing the number of element to obtain better simulation results.

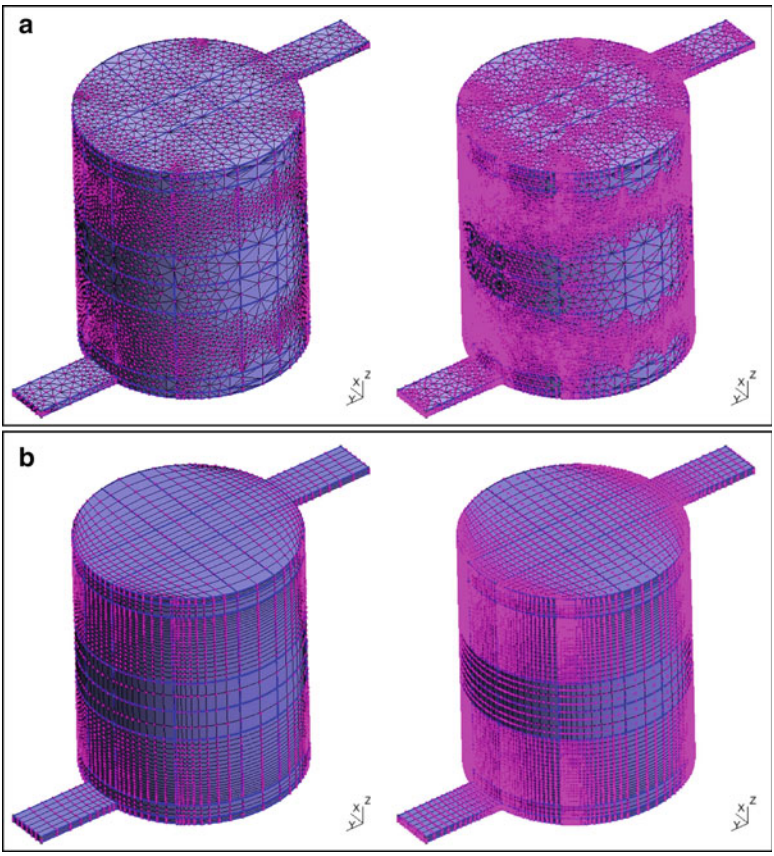

Fig. 2.2 Meshes obtained by *ParaBioReact*. (**a**) Tetrahedral meshes. (**b**) Hexahedral meshes

2.2.3 Optimization Process

To predict the engineered tissue and the needed environment, an optimization loop is required to run numerical simulations. Moreover, the following work is useful through two leading ways as introduced above (1 and 3 because the experimental setup is already designed) and presented on the following Fig. 2.3 to illustrate the third one as an optimization of the bioreactor chamber.

First of all, considering an existing bioreactor chamber, we can design an optimized scaffold knowing the boundary conditions that the bioreactor chamber will impose. On the other hand, knowing the scaffold geometry used, a bioreactor chamber will be designed to reach appropriate environmental conditions at the cell scale. This loop allows treating more or less complex problems. Depending on the fluid flow and the additional element materials, the computations can use CFD analysis and finite element (FE) analysis.

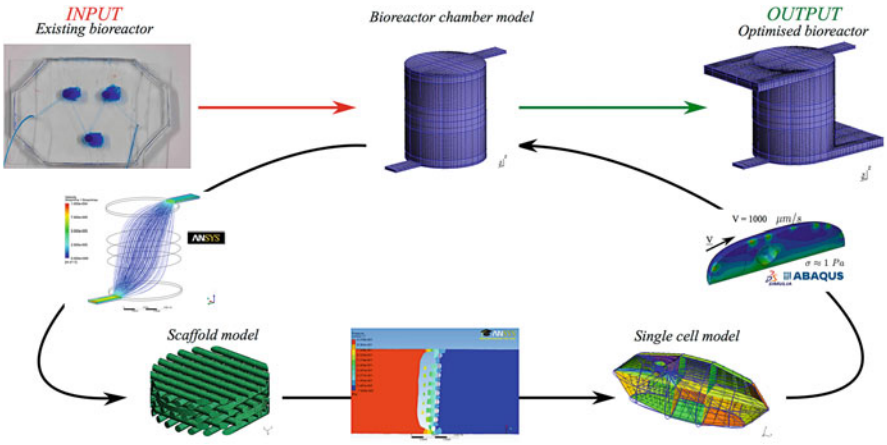

Fig. 2.3 Optimization process scheme

The whole process is divided into four steps: first the acquisition of the geometry; second the modelling of the chamber thanks to a mesher; third the extraction of the inlet conditions and the application of the inlet conditions on the scaffold thanks to a CFD analysis; fourth the application of fluid solicitation on a single cell model thanks to fluid-structure interaction (FSI) analysis; and finally the optimizing loop is stopped to generate a suitable bioreactor design.

2.3 In Vitro Experimental Study

The proposed method is presented based on a commercial scaffold from 3D *BioTek* (New Jersey, USA) that aims to design an adapted bioreactor for the bone and osteochondral applications.

2.3.1 Scaffold

A commonly used scaffold produced by 3D *Biotek* (New Jersey, USA) was taken. Its standard geometry is a disc with a diameter of 5 mm and a thickness of 1.5 mm. The theoretical geometry and the real reconstructed geometry from microCT are shown in Fig. 2.4.

These generic scaffolds are made of polycaprolactone (PCL), and material property values from the literature are summarized in Table 2.1. Each scaffold rod has a diameter close to 0.25 mm, and the final cylindrical shape is obtained by punching a 3D printed scaffold sheet.

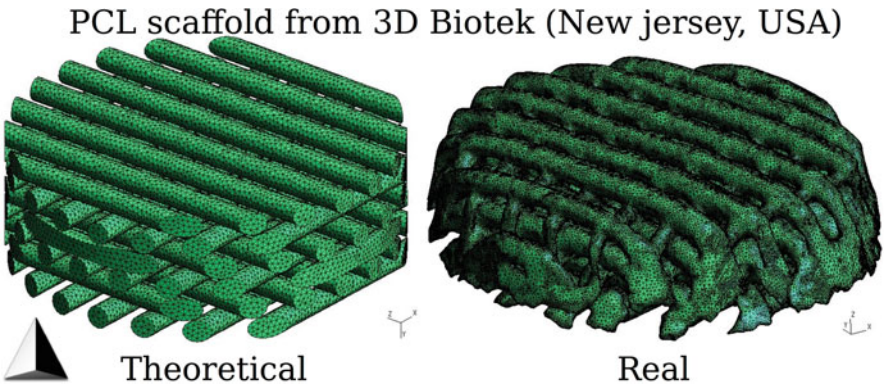

Fig. 2.4 Scaffold geometry: designed and real one obtained by microCT scanning

Table 2.1 Polycaprolactone properties

Materials	Young's modulus [MPa]	Poisson's ratio
PCL	80	0.3

2.3.2 The Bioreactor Chamber

A custom-made bioreactor chamber was used to seed mesenchymal stem cells and grow bone tissue. It is made of polydimethylsiloxane (PDMS) to be biocompatible and easy to produce. A simple chamber geometry was used to fit with the cylindrical shape of the scaffold used. It is a tube with rectangular perpendicular inlet and outlet to be able to add in a row few chambers presented on Fig. 2.5.

Considering the geometry of the chamber, we have a 5 mm diameter tube with a height of 6 mm. The inlet and outlet are provided by rectangular channels of 0.15 mm height, 1 mm width and defined as 2 mm long. On the real geometry, two bubble traps have been added because bubbles were disturbing the cell culture process. These elements consist in two parallelepipeds disposed on the top and on the bottom of the chamber. Their dimensions are $5 \times 5 \times 0.5$ mm^3.

2.3.3 Environment or Boundary Conditions

Physiological conditions are maintained in the chamber, and the only mechanical stimulation applied to the cells is the fluid flow. Therefore, an accurate control of this loading must be reached as explained in Chap. 3.

In the studied case, the contact between the scaffold and the chamber wall was considered as perfect, and there was no relative motions reducing the study to a CFD analysis regarding the bioreactor chamber.

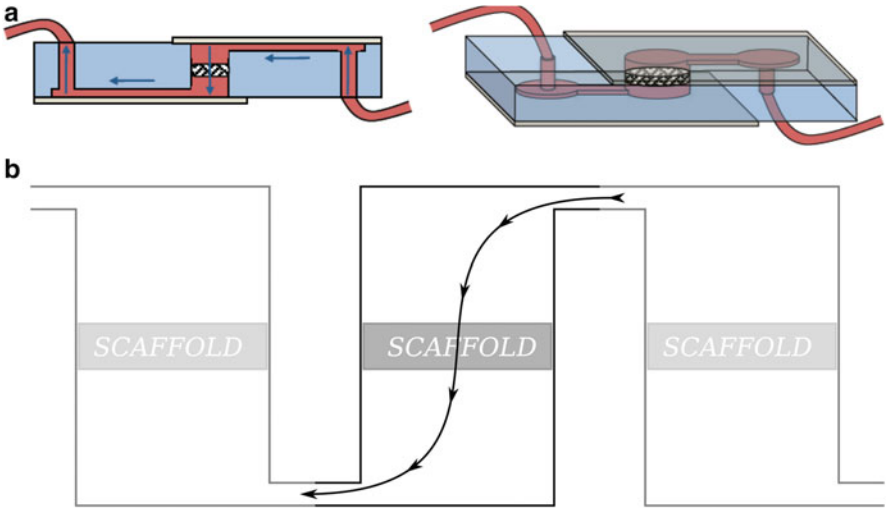

Fig. 2.5 Bioreactor chamber model. (**a**) Chamber geometry. (**b**) Bioreactor geometry

2.4 Simulation Study

2.4.1 Chamber's Boundary Conditions

According to the fluid flow usually applied in bioreactor chambers for chondrocyte cells ($q \approx 2\ mm^3.s^{-1}$) and the presence of a scaffold wherein cells are seeded, an overpressure will appear before the scaffold. The latter depends on the scaffold permeability that has to be computed.

First of all, a CFD analysis was performed to measure local fluid velocities and shear stresses within the scaffold. The influence of the real geometry is noteworthy in terms of variables heterogeneity through the bone substitute, which obviously will affect cells behaviour. Then, a cell-seeding model is implemented to study the cell population behaviour under these conditions.

2.4.2 Scaffold Apparent Permeability

An apparent permeability of real scaffolds was extracted from the CFD analysis performed at the scaffold scale, and the results are presented in Fig. 2.6.

According to Darcy's law with the one-dimensional assumption, the permeability is defined by:

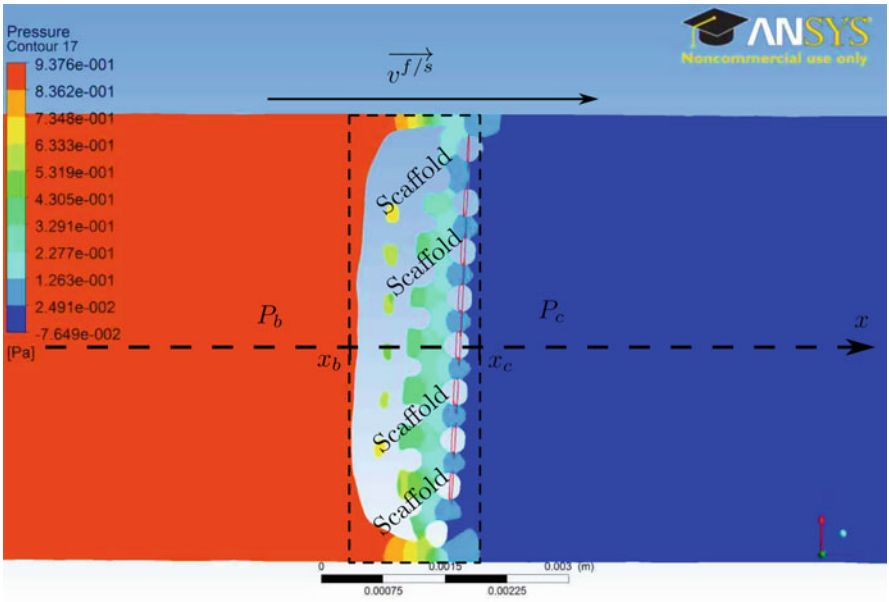

Fig. 2.6 Pressure field along the bioreactor chamber and through the scaffold

$$k = -v^{f/s} \frac{x_c - x_b}{P_c - P_b}$$

The averaged scaffold geometry defined previously was used, the fluid velocity used is 1 mm.s^{-1} and the variation of pressure was extrapolated from CFD results, like the one shown in Fig. 2.6. It leads to the following results:

$$k = -1 \frac{1.5 - 0}{(0 - 0.9376) \times 10^{-6}} = 1.60 \times 10^{-6} \text{ m}^4.\text{N}^{-1}.\text{s}^{-1}$$

Applying this method over a set of six samples, we obtained an averaged value of 1.35×10^{-6} m^4.N^{-1} s^{-1} and a range of $[0.85 - 1.66] \times 10^{-6}$m^4. N^{-1}. s^{-1}. The permeability, k, is related to the intrinsic permeability, $\bar{k}$, and the dynamic viscosity, μ, as the following ratio: $k = \frac{\bar{k}}{\mu}$.

Taking into account the dynamic fluid viscosity (water) equal to 8.90×10^{-4} m^{-2} .N.s, we obtained an intrinsic permeability of 1.20×10^{-9} m^2.

Using the same assumption on Darcy's law to our initial problem with an applied local velocity of $v^{f/s} = 0.1$ mm.s^{-1}, the over pressure is estimated by:

$$P_b = \frac{v^{f/s}}{k}(x_c - x_b) = \frac{0.1}{1.60 \times 10^6}(1.5 - 0) = 0.09 \text{ Pa}$$

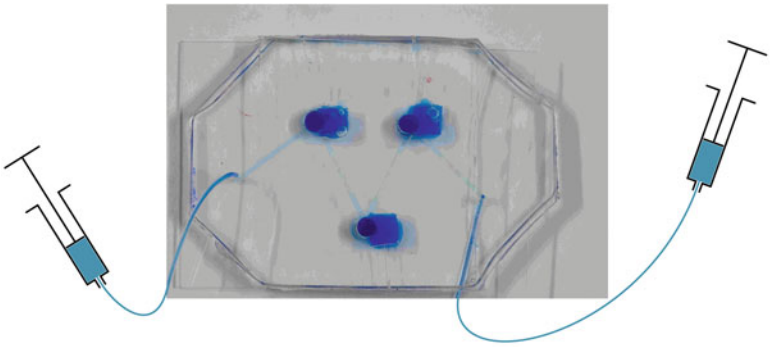

Fig. 2.7 Experimental setup of the bioreactor made of three chambers

Knowing this hydraulic overpressure locally bore by scaffold (≈0.1 Pa), the strain induced on the scaffold is negligible compared to the material properties meaning no deformation will occur on the scaffold due to the fluid flow. This observation allows to fully reducing the problem to a CFD analysis. Experimentally, the inflow used is a constant flow rate of 120 μL.min^{-1} applied with a syringe pump visible in Fig. 2.7.

Based on the chamber geometry, the inlet fluid velocity is around 13.34 mm.s^{-1}, and the outlet condition is assumed to fulfil the mass balance supposing no leaks appear during the perfusion.

2.4.3 *Fluid Flow Analysis in the Bioreactor Chamber*

A CFD analysis was developed to understand the fluid flow present in bioreactor chambers experimentally used. Using the parametric tool described previously (*ParaBioReact*), several configurations and boundary conditions were tested to mimic the real experimental conditions.

Considering the geometry of the chamber, we have a 5 mm diameter tube with a height of 6 mm. The inlet and outlet are provided by rectangular channels of 0.15 mm height, 1 mm width and defined as 2 mm long. On the real geometry, two bubble traps were added because bubbles were disturbing the cell culture process. These elements consist in two parallelepipeds disposed on the top and on the bottom of the chamber. Their dimensions are $5 \times 5 \times 0.5$ mm^3.

We considered a laminar water fluid flow through the chamber to get the results presented in Figs. 2.8 and 2.9. The fluid was described as an incompressible Newtonian fluid with a viscosity of 0.001 kg.m.s^{-1} and a density of 1000 kg.m^{-3}. Non-slip wall condition was modelled.

The gravity was not taken into account because it appears to not have any influence on the results up to now. Even if we orient it to get the lying position of the real chamber, no differences were observed.

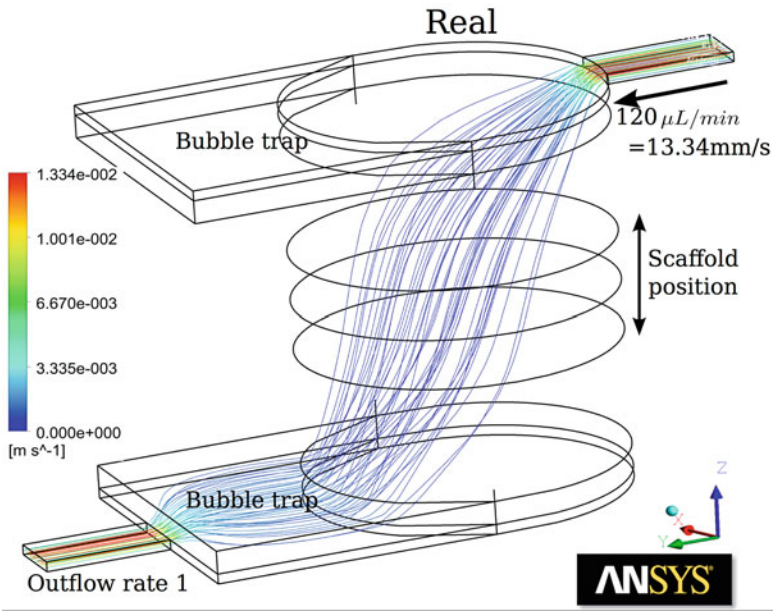

Fig. 2.8 Fluid streamlines through the real geometry of the chamber

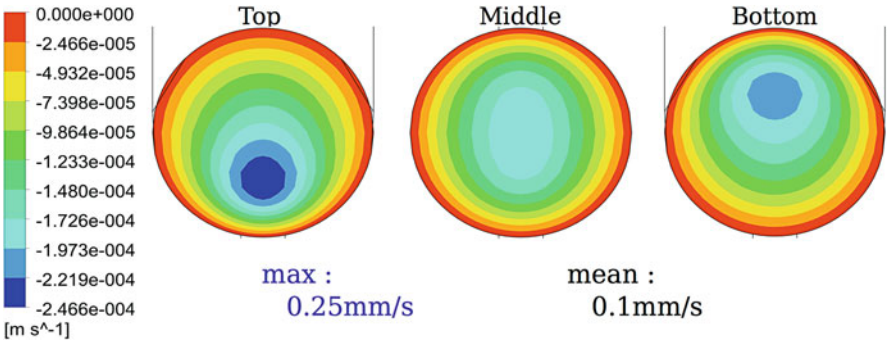

Fig. 2.9 Velocity field inside the scaffold area under real bioreactor conditions

On the other hand, this analysis highlighted the diagonal orientation of the streamlines which lead to a heterogeneous velocity field above the scaffold shown in Fig. 2.9.

Up to now, the cell seeding within the scaffold was not investigated in terms of number of cells by scaffold location. This work in progress may reveal a peculiar behaviour as the high velocity is diagonally observed.

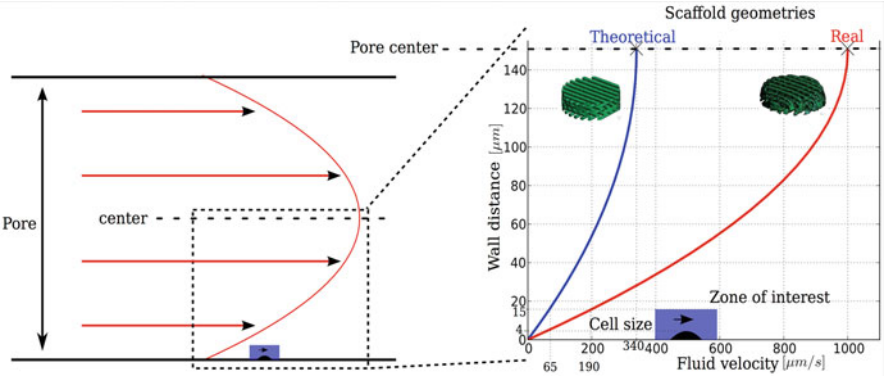

Fig. 2.10 Velocity field within theoretical and real scaffold geometries. On the left the pore considered as infinite is represented with a fluid stream over a single cell. On the right, calculations have been applied for a pore radius of 150 μm and maximal velocities of 340 μm.s^{-1} and 1000 μm.s^{-1}, respectively, for theoretical and real scaffold geometries

2.4.4 Fluid Structure Interaction at Single Cell Scale Seeded in the Scaffold

Fluid velocity maps obtained by CFD analysis at the scaffold scale (Campos and Lacroix 2015) (see Fig. 2.10 where maximal pore velocities are presented) applying an inflow of 0.1 mm.s^{-1} as obtained above by simulation at bioreactor scale (see Chap. 4 for details). Those results were used to extrapolate the local velocities field in a scaffold pore with a maximal velocity in between 0.34 and 1 mm.s^{-1}. The cell was considered seeded on a plane surface and submitted to a constant solicitation due to a fluid flow parallel to the surface (see Fig. 2.10). The fluid velocity field was determined considering that the scaffold pore was an infinite cylinder allowing using the Poiseuille law to get the following velocity definition:

$$v(r) = v_{\max}\left[1 - \left(\frac{r}{R}\right)^2\right]$$

Equally, the shear stress is defined by:

$$\sigma_{rz}(r) = \eta\frac{\mathrm{dv}(r)}{\mathrm{dr}} = -\eta v_{\max}\frac{2r}{R^2}$$

Those boundary conditions were then used in Fluid Structure Interaction (FSI) analysis performed with Abaqus. The fluid was considered as water regarding the viscosity of the physiological solution. Regarding the single cell structure and materials, a sounded model was used (Barreto et al. 2013); see Chap. 9 for details.

The simulation allows observing stress and strain concentration close to the connection between the cytoskeleton and the membrane and also the contact with the cell substrate showed in Fig. 2.11. Due to divergence issues, simulations were run in a range of fluid velocities between 15 and 72 μm.s^{-1}.

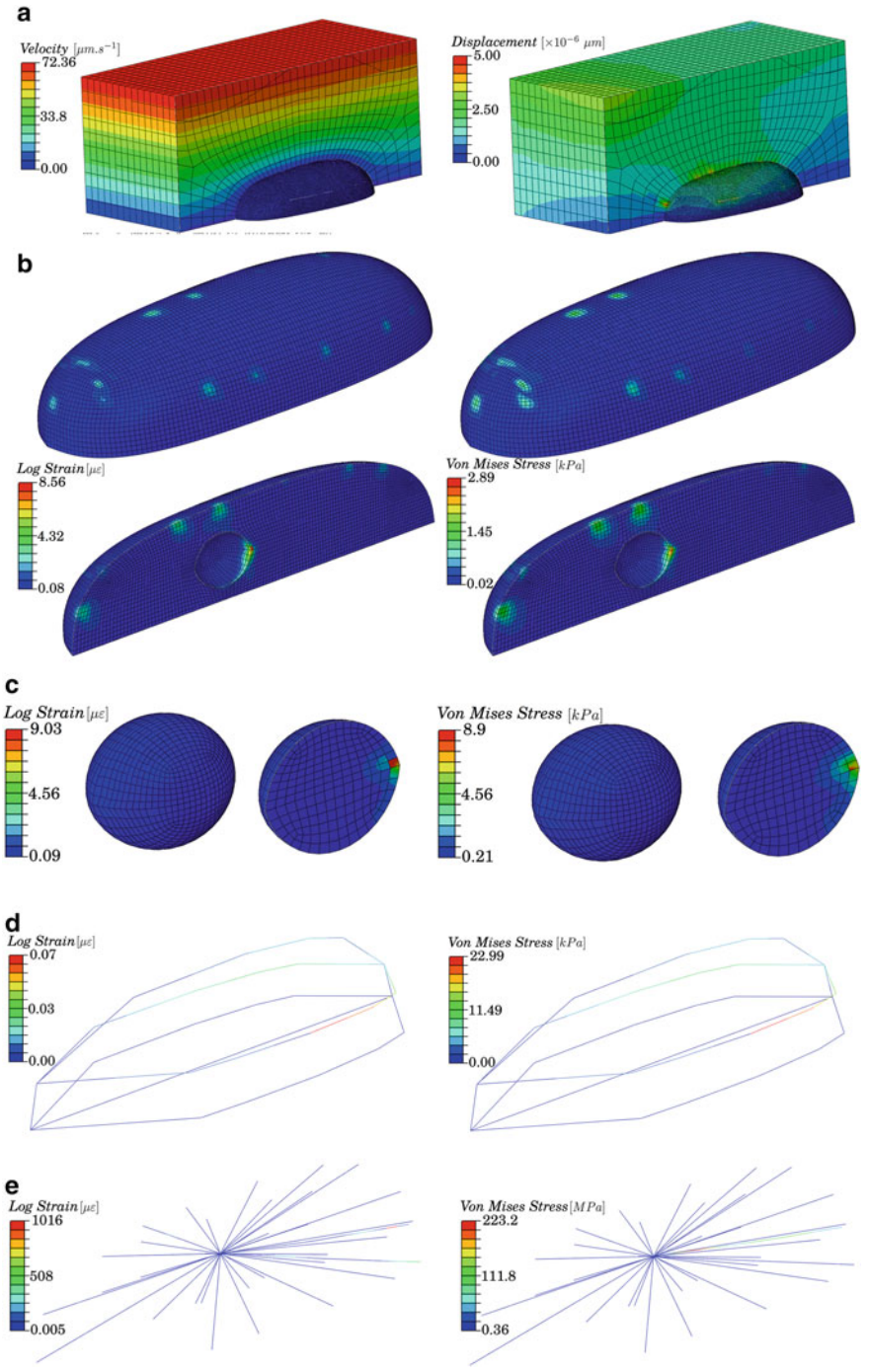

Fig. 2.11 Fluid structure interaction results for an environmental fluid flow of 72 μm.s^{-1}. (**a**) Fluid flow imposed. (**b**) Logarithmic strain and von Mises stress distributions within the cytoplasm. (**c**) Logarithmic strain and von Mises stress distributions within the nucleus. (**d**) Logarithmic strain and

We clearly observed that the cytoskeleton configuration leads to a concentration of mechanical extreme values close to the connection between the cytoskeleton and the cell membrane. The order of magnitude of stress is 100 kPa, and the associate strains are με. Those values are consistent regarding the solicitation that might be physiologically observed.

Compared to the theoretical condition, the maximal fluid velocity leads to similar values and increased linearly due to the linear model used. The cytoskeleton plays a major role under this mechanical condition, and most of the loading is borne by the microtubules.

Using the real scaffold geometry, this work would suggest various cell behaviours through the produced engineered tissue due to heterogeneous mechanical solicitation and biochemical environment which was not took into account in the model. Thanks to the imaging techniques, an experimental analysis of an engineered tissue within a scaffold would allow comparing simulation and reality (see Chap. 3).

The final design of the bioreactor suits cell life development within a theoretical scaffold.

2.5 Conclusions

A general method was presented in this chapter (Sect. 2.2) and applied to the specific design of a scaffold chamber. It allowed testing two different bioreactor geometries (with or without bubble traps) showing no major interest within the simulation, but regarding the experimental process, the bubble traps presence is compulsory to avoid cell death (see Chap. 3). On the other hand, two scaffold geometries have been tested highlighting a major difference regarding the local fluid flow within the scaffold pores and therefore on the cell development (see Chap. 4). Once again those remarks illustrate the fact that the simulation cannot replace the experimentation, but by working simultaneously together, better results are obtained.

Moreover, experimental analyses are required to correctly compare the simulation and improve the strength of the optimization process. As the experimental part, the simulation presents some limits like, for instance, the FSI computation divergence under high fluid velocity. In fact due to such a high stiffness contrast between the cell structure bodies and the fluid, local large strains induced divergences. Those numerical limits have to be solved to extend the method capacity regarding the range of solicitation experimentally applied. The output of the presented method might have a strong interest to be coupled with biocompatible prototyping like 3D printing.

The same method is extendable to more complex bioreactors or cell behaviours. For instance, actual models allow applying mechanical stimuli (Yu et al. 2016) in

Fig. 2.11 (continued) von Mises stress distributions within the cytoskeleton actin fibres. (**e**) Logarithmic strain and von Mises stress distributions within the cytoskeleton microtubules

addition to the conventional perfusion. It would be easy to add in the optimization loop a finite element analysis to take into account deformations in the scaffold to run calculation on the deformed scaffold shape to know the local velocity implied. On the other hand, using more complex description of cell behaviour (Khayyeri et al. 2015) would enhance the local influence of the optimization loop allowing foreseeing cell population development. At the end of those simulations, if the obtained values influence the cell behaviour in the wrong way, the chamber design or the boundary conditions will be changed to reach ideal cell proliferation environment.

References

Baldit A, Campos A, Brunelli M, Perrault C, Lacroix D (2014) Multi-scale modeling in tissue engineering: a virtual physiological approach. Proceeding virtual physiological human conference

Barreto S, Clausen CH, Perrault CM, Fletcher DA, Lacroix D (2013) A multi-structural single cell model of force-induced interactions of cytoskeletal components. Biomaterials 26:6119–6126

Beebe DJ, Mensing GA, Walker GM (2002) Physics and applications of microfluidics in biology. Annu Rev Biomed Eng 4:261–286

Campos MA, Lacroix D (2015) The inter-sample structural variability of regular tissue-engineered scaffolds significantly affects the micromechanical local cell environment. Interface Focus 5 (2):20140097–20140097

Chabiniok R, Wang VY, Hadjicharalambous M, Asner L, Lee J, Sermesant M, Kuhl E, Young AA, Moireau P, Nash MP, Chapelle D, Nordsletten DA (2016) Multiphysics and multiscale modelling, data–model fusion and integration of organ physiology in the clinic: ventricular cardiac mechanics. Interface Focus 6(2)

Geuzaine C, Remacle J-F (2009) Gmsh: a three-dimensional finite element mesh generator with built-in pre- and post-processing facilities. Int J Numer Methods Eng 79(11):1309–1331

Kausar H, Kishore RN (2013) Bone tissue engineering. Int J Pharm Pharm Sci 75:118

Khayyeri H, Barreto S, Lacroix D (2015) Primary cilia mechanics affects cell mechanosensation: a computational study. J Theor Biol 379:38–46

Tanaka SM (1999) A new mechanical stimulator for cultured bone cells using piezoelectric actuator. J Biomech 32(4):427–430

Thorpe SD, Nagel T, Carroll SF, Kelly DJ (2013) Modulating gradients in regulatory signals within mesenchymal stem cell seeded hydrogels: a novel strategy to engineer zonal articular cartilage. PLoS One 8(4):e60764

Yu H-S, Kim J-J, Kim H-W, Lewis MP, Wall I (2016) Impact of mechanical stretch on the cell behaviors of bone and surrounding tissues. J Tissue Eng 7:1

Zhang Z-Y, Teoh SH, Teo EY, Chong MSK, Shin CW, Tien FT, Choolani M a, Chan JKY (2010) A comparison of bioreactors for culture of fetal mesenchymal stem cells for bone tissue engineering. Biomaterials 31(33):8684–8695

Chapter 3
Mechanical Stimulation in a PCL Additive Manufacturing Scaffold

Three-dimensional (3D) scaffolds are increasingly employed as support for studies on cellular activities. They are widely shown to enhance cell survival and are a promising approach to be employed to mimic the in vivo conditions due to their controlled architecture. Moreover, 3D stiff structures fabricated by additive manufacturing are able to bear mechanical stimuli finding a role in the investigation of the effect of mechanical forces on cell proliferation and commitment. With this purpose, we propose a combination of a 3D polycaprolactone (PCL) scaffold and collagen soft gel as support for studying the response of mesenchymal stem cells following mechanical compression. This chapter focuses on the characterization of 3D Insert® PCL scaffolds behaviour under mechanical compression. After defining mechanical properties and variability due to boundary effects, the focus moves on the development of a new composite scaffold made of a stiff PCL structure acting as support for cell activities and able to bear mechanical compression while embedding a soft collagen gel matrix responsible to provide an environment enhancing cellular activities as well as to transmit the stress resulting from the mechanical stimulation from the stiff matrix to the seeded cells. Finally, the last section focuses on the effect of low mechanical strain applied on seeded scaffolds and how the cellular response varies to bursts of compression applied at different time points.

3.1 Introduction to 3D Scaffolds

The tissue engineering (TE) approach aims to closely mimic the biological environment found in the body in order to drive progenitor cells towards a defined differentiation pathway and obtain fully functional tissue as replacement in injured sites. Although the behaviour of several cellular lineages seeded on two dimensional (2D) surfaces is nowadays well defined on a wide range of materials (Engler et al. 2006), it prevents to provide a real replication of the biological environment because of the lack of structure. As a consequence, the first challenge addressed by TE is the use of three-dimensional (3D) structures closely mimicking the geometry and chemistry of the biological environment characterizing the target tissue. For bone regeneration purposes, a basic requirement is for the scaffold to be able to bear

© Springer Nature Singapore Pte Ltd. 2019

D. Lacroix et al., *Multiscale Mechanobiology in Tissue Engineering*,
Frontiers of Biomechanics 3, https://doi.org/10.1007/978-981-10-8075-3_3

mechanical stimuli as the bone is constantly under mechanical forces by the action of muscles and body movements. Gelatine-like scaffolds made by natural polymers such as collagen, fibrin or chitosan represent a good choice to be used in culture studies as they naturally mimic the main components of the extracellular matrix. However, soft matrices lack of mechanical properties preventing their use for bone regeneration purposes. Synthetic materials made by polymerization of lactic acid, glycolic acid or caprolactone often embedding natural proteins were fabricated to develop composite scaffolds able to bear mechanical stimulation and providing at the same time extracellular matrix characteristic of bone tissue (Chen et al. 2002). Among those, polycaprolactone (PCL) is gaining increasing interest as it is a thermoplastic polymer presenting low glass transition and melting temperature. As a consequence, it is easy to mould to the desired shape by temperature dependant processes (Yilgor et al. 2008). Moreover, due to its high degree of crystallinity and hydrophobicity, it showed to be highly biocompatible and presents slow degradation rates tuneable by varying the molecular weight (Yilgor et al. 2008). The second challenge addressed by TE regards the study of how mechanical stimuli affects the bone forming process as the bone undergoes constant mechanical stimulation and remodels itself depending on the sensed forces. The cellular response to tension and compression stimuli has already been clarified on 2D supports or employing 3D soft matrices as extensively reviewed in Chap. 1. Despite of this, how the mechanical stimuli is transmitted, sensed and transduced into the cells employing 3D porous structures made of stiff materials is still an ongoing study. The main challenge employing 3D porous structures for mechanical stimulation regards the assessment of the real stress distribution through the structure. Contrary to soft materials, 3D scaffolds lead to non-uniform distribution of stresses within the specimen as a result of the applied deformation, presenting local areas of tension stimuli in response to compression forces. Another drawback carried by stiff 3D scaffolds is related to their low deformability requiring a step towards the development of composite scaffolds made of a stiff structure bearing the compression and embedding a soft matrix responsible for transmitting the resulting stress to cells.

3.2 Mechanical Response of Starch-Based Scaffolds

3.2.1 Parameters Affecting Mechanical Properties of Starch Materials

Porous biomaterials are mainly characterized under compression stimuli due to the limitation in applying tensile strain related to their structure. The stress/strain curve of such starch biomaterials under mechanical compression shows three different regions characterized, respectively, by an initial linear region from which can be extrapolated the elastic modulus of the structure, a plateau of roughly constant stress

with increasing strain and a final region of densification of the material governed by plastic effects where the stress values increase rapidly with strain (Hutmacher et al. 2001). Starches were characterized in different studies in dry or immersed state in order to better represent the physiological conditions that cells sense in vivo. On this purpose, starches with different architectures were investigated to define how geometrical parameters such as porosity, pore size and offset between fibres affect the mechanical behaviour of materials. For example, Hutmacher et al. (2001) showed the differences in terms of elastic modulus under mechanical compression of PCL scaffolds maintaining the same porosity and pore size and by varying the lay-down pattern at 0/60/120 and 0/72/144/36/108. Young's modulus values related to the three-angle pattern amount to 41.9 ± 3.5 MPa and 29.4 ± 4.0 MPa in dry and immersed state, respectively, while E values up to 20.2 and 21.5 MPa were found testing the five-angle patterned samples under the same conditions. These results demonstrate that a variation in the orientation of fibres has a strong effect on the stiffness of the structure in both dry and immersed state. Furthermore, a decrease of Young's modulus is observed when water surrounds the specimen in the three-angle lay-down patterned scaffold. This behaviour is believed to be associated with the water uptake which was demonstrated in various studies (Lohmann et al. 2000; Slivka 2000) to cause plasticization effects of the structure. Further dynamic analysis on dry PLA scaffolds (Ghosh et al. 2008) defined the influence of pore size and porosity on the mechanical response of scaffold under dynamic compressive forces. Scaffolds in a dry state analysed by DMA at 37 °C showed no significant differences in the viscoelastic properties of the structure over a wide range of frequencies between 0.05 and 50 Hz. These outcomes were justified considering that the working temperature (37 °C) is much lower than the glass transition temperature of the material (60 °C) preventing viscoelastic relaxation to occur. In the same study, pore size and porosity of the scaffold were varied at constant frequency. Low porosity and small size pores led to an increase in the storage modulus. In terms of loss modulus, it was shown that in general values do not correlate with either porosity or pore size. However, tan δ shows an increase for scaffolds presenting higher porosity due to the dissipation mechanism affecting preferentially specimens with large pores. In the same study, experiments performed in an immersed state at 37 °C surprisingly showed a similar behaviour compared to the dry state in terms of storage modulus which was expected to decrease as a consequence of the uptake of water and plasticization effects. This discrepancy was explained by taking into account the fact that water fills the pores leading to difficulties in deforming the scaffold through hydrostatic effect of water in the pores. However, significant differences can be noticed in loss modulus and tan δ. Compared to results obtained testing scaffolds in the dry state, specimens tested in water showed higher values in terms of the loss modulus, while tan δ tends to decrease more rapidly with increasing frequency. This behaviour is believed to be related to the motion of water molecules causing friction forces to arise from the contact between liquid and sample.

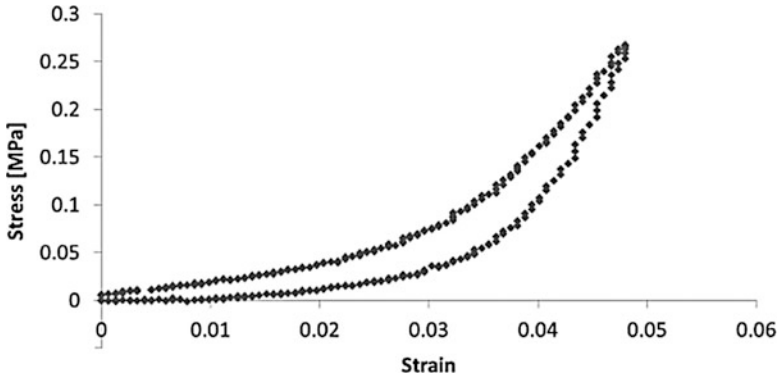

Fig. 3.1 Loading and unloading stress/strain curve on a single PCL sample showing the viscoelastic behaviour of the starch

3.2.2 Elastic Modulus of 3D Insert® PCL Scaffolds

The aim of this study consists in mechanically characterizing the behaviour of 3D Insert® PCL scaffolds in dry state (PCL) undergoing compression stimuli. All experiments were performed at 37 °C unless differently stated conditions controlling the displacement imposed on the PCL with the BOSE Bioreactors 5500. The stress/strain curve was analysed defining the zero position by the eye as close as possible to the sample. Then, a 5% ramp was applied to a specimen, and a stress/strain curve was extrapolated by the data acquired by the WinEst software. The contact position was defined when the load reached 0.1 N.

The stress/strain curve shows the typical behaviour of a viscoelastic material with a hysteresis cycle resulting from the energy loss due to the deformation of the structure (Fig. 3.1). Moreover, applying low strains prevent plastic deformation to occur as the curve returns to the origin and no residual strain is left. The loading curve was further investigated by applying during ten times a 5% strain ramp on the same sample and allowing 10 min rest between one stimulation and the next in order to allow complete recovery of the structure (Fig. 3.2a). The results showed that the same structure responded differently to identical stimuli presenting acceptable variability values ($\sigma < 10\%$) only for strains below 2.5%. This behaviour occurs as a consequence of boundary effects caused by the geometry of the sample used to prevent the uniform propagation of the compressive force through the structure as reviewed in the next session of this chapter. Further observing the loading behaviour in a low strain range (Fig. 3.2b), the graph shows a curvature associated to the initial adaptation of the structure to the compression stimuli. Then, a change in slope occurs at 1% strain followed by a range between 1% and 2.5% strain where the stress varies linearly with strain. Thus, this range was selected for the calculation of apparent elastic modulus (E). E values decrease progressively with temperature up to 2.5 ± 1 MPa at 37 °C (Fig. 3.3). The progressive decrease of E was expected as

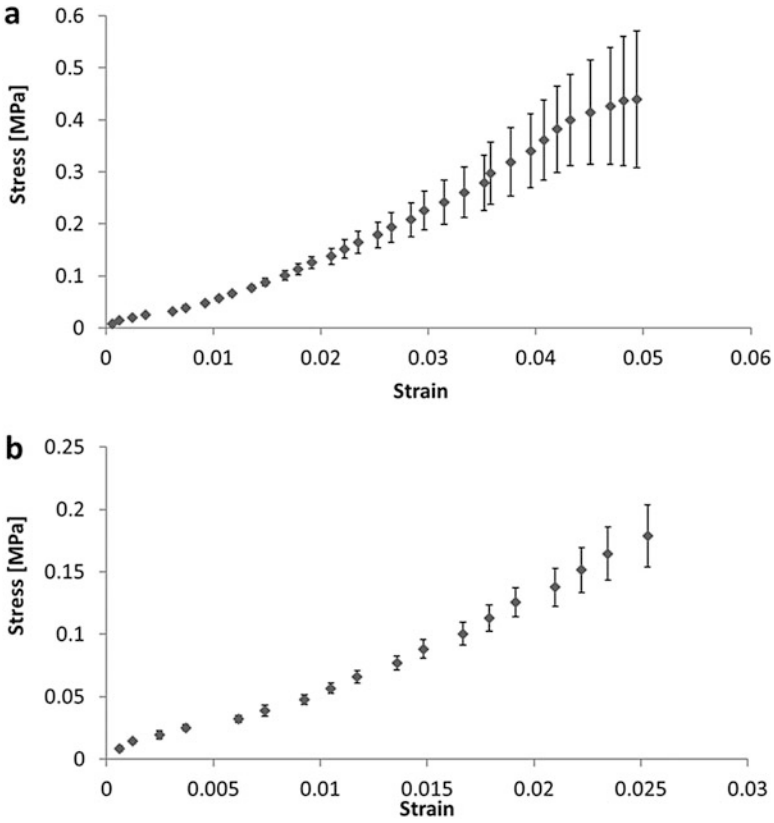

Fig. 3.2 (**a**) Loading curve as average of 12 compressions on a single sample; (**b**) loading stress/strain curve for low strain values

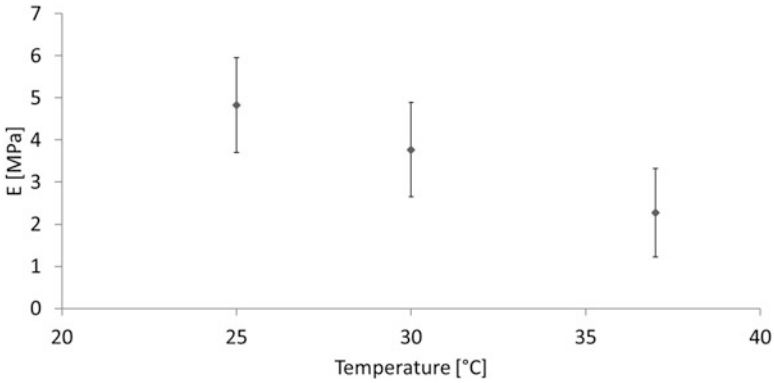

Fig. 3.3 Apparent elastic modulus varying temperature

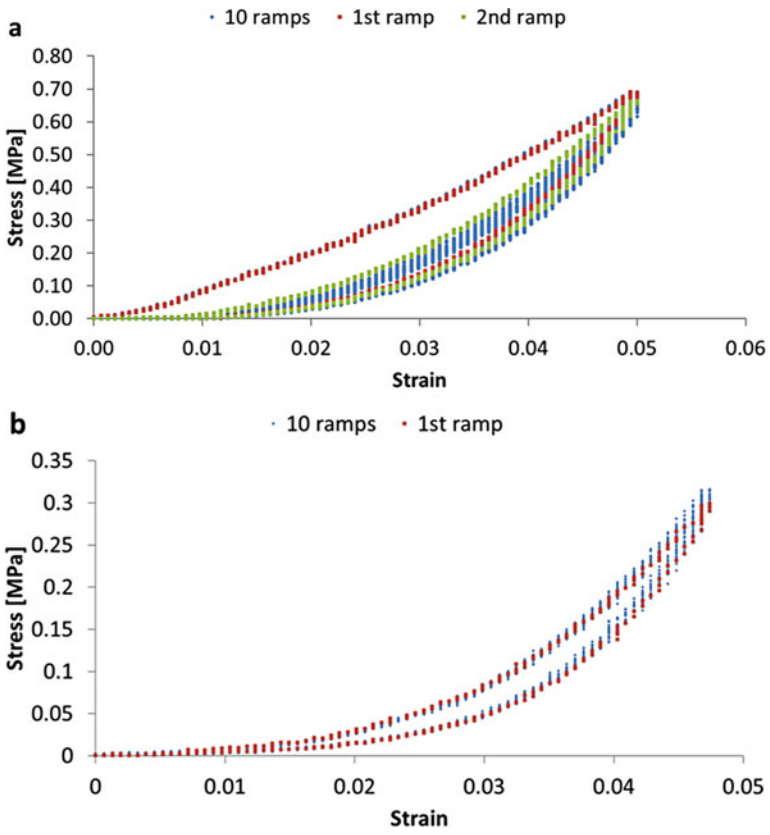

Fig. 3.4 (**a**) Stress/strain curves applying ten loading/unloading ramps on the same scaffold before relaxation (**b**) and after samples underwent relaxation

scaffolds are made of polymeric fibres organized in a 3D structure whose chemical and mechanical properties are temperature dependent (Odusanya et al. 2003).

3.2.3 Response to Dynamic Compression of 3D Insert PCL Scaffolds

Samples were tested under dynamic conditions by applying 5% strain triangle waves for ten cycles at 1 Hz. When scaffolds were not relaxed, viscoelastic behaviour correlated to the deformation of the structure occurs causing a progressive decrease of the loading curve slope with increasing number of ramps applied (Fig. 3.4a). These viscoelastic effects resulting from the relaxation of the structure to the compression can be successfully removed by applying constant deformation on the structure over time. Following relaxation, viscoelastic effects were absent, and

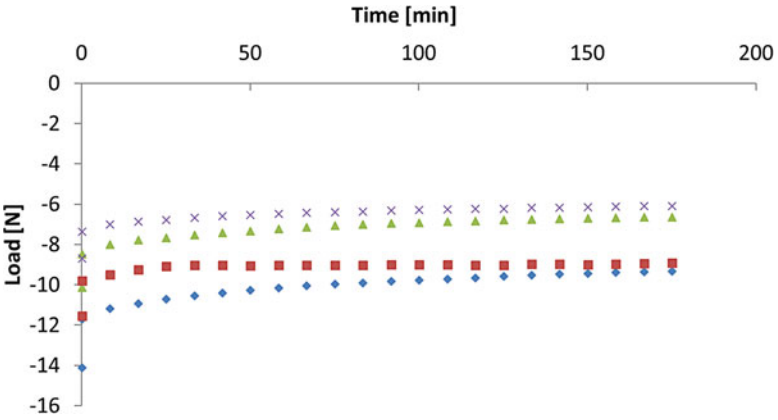

Fig. 3.5 Load distribution over time of PCL scaffold under constant compression

consecutive load of the structure led to overlapping stress/strain curves suggesting improvement in the internal stability of the structure (Fig. 3.4b). An 8% constant strain for 3 h was demonstrated to be sufficient in preventing viscoelastic behaviour to occur during dynamic stimulation as long as the imposed strain is below the value at which structures were relaxed (Fig. 3.5).

However, applying the same level of strain on different samples led to significant differences in the mechanical response of PCL scaffolds as shown by the load pattern registered relaxing four samples (Fig. 3.5). This discrepancy is explained by considering differences among samples in terms of orientation and spacing between fibres which are going to play a fundamental role in the rearrangement of the structure and the resulting mechanical properties.

The behaviour under compression stimuli on relaxed samples was also investigated by dynamic mechanical analyses applying 5% strain sinewaves at 0.5, 1, 5 and 10 Hz in dry or immersed state (Fig. 3.6). Preliminary results that suggest no significant differences can be noticed comparing dry and wet conditions. The storage modulus (E') shows a significant increase ($p < 0.01$) at 5 and 10 Hz compared to lower frequency tested (Fig. 3.6a), while the loss modulus (E'') remains constant (Fig. 3.6b) considering either dry or wet state.

3.2.4 Boundary Effects

Drawbacks associated with the use of 3D Insert PCL scaffolds are related to the small geometry of the structure and the geometrical variability. First, the PCL scaffolds used in this study do not meet the geometrical criteria necessary for a material to be suitable for compression tests where the height is requested to match at least twice the diameter in order to prevent boundary effects (Chen et al. 1999; Gama et al. 2004). It was shown employing a well-known material such as PDMS that

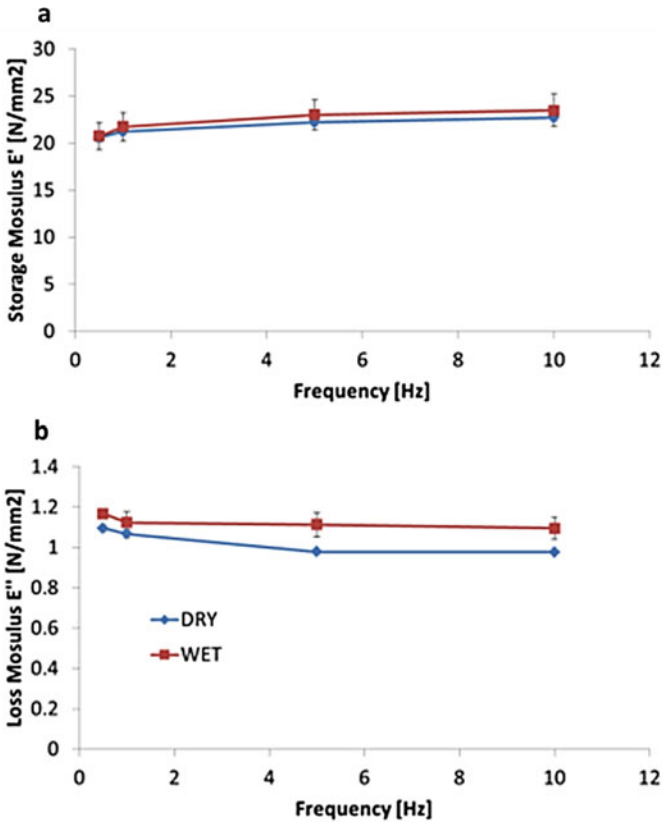

Fig. 3.6 (**a**) Storage modulus (E') and (**b**) loss modulus (E'') varying frequency

when that condition is not met, the resulting elastic modulus is affected by boundary effects leading to an overall error up to 30% (Fig. 3.7a). Applying compressive strain on PDMS 2 mm and 10 mm height on three different samples, the elastic modulus was found to decrease for samples with height measuring less than twice the diameter. However, comparing different samples of the same height, no significant differences are found repositioning the sample between one ramp and the other either at 2 or 10 mm. Varying the velocity used to apply the stimuli from 1 to 10 μm/s did not have any side effect on the mechanical response of the PDMS specimens. The same results were obtained applying the same stimulation on three PCL samples where variation in velocity did not affect the mechanical response of the specimens (Fig. 3.7b). However, higher standard deviation values are obtained compared to the PDMS at the same height in the same conditions, reaching up to 60% error. These differences are due to variation in the pore size, fibre diameter and interconnectivity of scaffolds affecting the stress through different structures. Moreover, 3D Insert PCL has not an even shape but present a bullet-like structure and imperfections resulting from the fabrication process. Therefore, enhanced boundary effects are

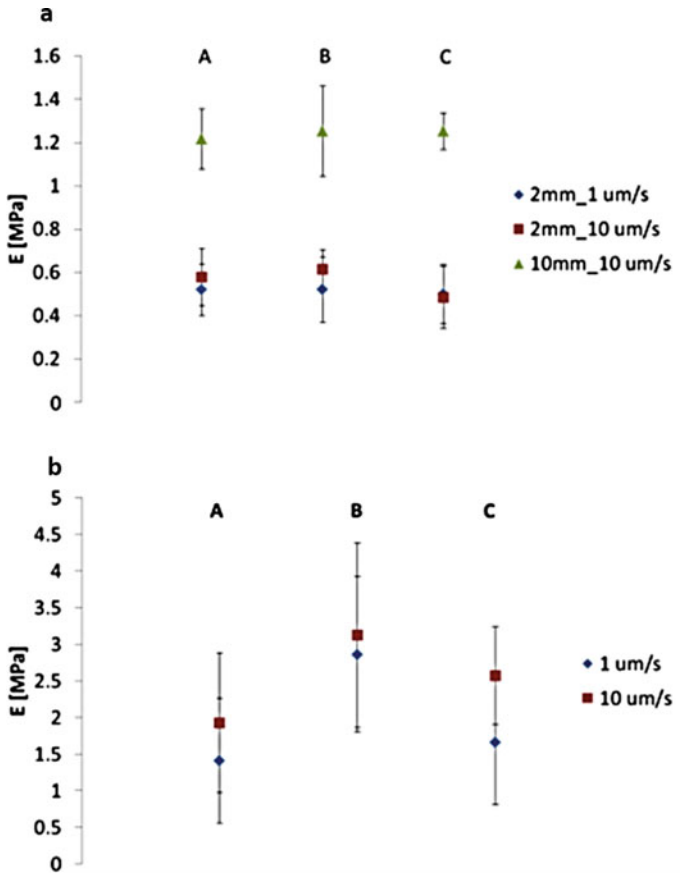

Fig. 3.7 Elastic modulus resulting from compression ramps applied to (**a**) PDMS and (**b**) PCL scaffolds varying height and velocity of the applied compression ramp

observed applying compression on the structure by rotating the structure on the radial plane. Considering a single sample and applying ten loading/unloading ramps at 5% strain and repositioning the sample ($N = 18$) at each stimulation keeping the same orientation inside the machine demonstrate the possibility to decrease the average repositioning error amounting to 60% down to 34%. This variability is due to either minimal difference in the preload applied related to the precision of the machine or the different orientation of the structure when positioned into the bioreactor. In order to distinguish between effects due to systematic error (precision of the machine) or random error (repositioning of the sample), another batch of 18 scaffolds was tested avoiding the repositioning of the sample but setting the zero position at each stimulation, leading to an average error of 19% on the elastic modulus.

3.3 MSCs Differentiation in 3D Insert® PCL Scaffolds Embedding Collagen

3.3.1 Effect of Geometry on Cellular Attachment

The step towards 3D scaffolds goes along with some complications correlated to the geometry of the structure. Porosity and interconnectivity are among the most important parameters to take in account for cell attachment and survival (Hutmacher 2000; Karageorgiou and Kaplan 2005). Indeed, small pores and low interconnectivity lead to non-uniformly seeded scaffolds and difficulties in supplying nutrients and oxygen in the inner portion of the structure. On the other side, large pores may prevent cell attachment due to the low rate of contact between cells and the walls of the scaffold. Pores between 200 and 400 μm are preferred for bone ingrowth, allowing good seeding efficiency and nutrient supply in the construct and osteogenesis in vitro (Karageorgiou and Kaplan 2005). Moreover to be employed for cellular studies, scaffolds must be biocompatible preventing the release of toxic substances and biodegraded compounds in order to enhance replacement by functional bone tissue to be implanted (O'Keefe and Mao 2011). PCL constructs fabricated by additive manufacturing techniques based on the deposition of consecutive layers of fibres are widely employed for studying cell activities. Different architectures were analysed changing pore sizes, including gradients of pores and varying offset between consecutive layers of fibres (Sobral et al. 2011). The best results were obtained when the structure is characterized by open pores and an offset between fibres is present, allowing bridging between cells in the scaffolds and good proliferation potential (Declercq et al. 2013). 3D Insert® PCL are promising scaffolds to be used in the investigation of cell differentiation as their ability in supporting cells activities over long periods of time has already been shown in previous studies investigating endothelial differentiation (Marino et al. 2012) and nerve regeneration (Barbarisi et al. 2014).

3.3.2 Characterization of Stiff 3D Insert PCL Scaffold Embedding Soft Collagen Gel

The first goal of this study consists in obtaining scaffolds with a uniform distribution of collagen though the structure (cPCL). Following air plasma treatment in order to increase surface activity, samples were embedded with collagen by dropping 20 μl volume on the top of the scaffold and let solidify in incubator for 40 min. After solidification, Sirius red staining revealed collagen to form layers bridging consecutive PCL fibres (Fig. 3.8a). Collagen was not uniformly distributed on the top and the bottom of the scaffold aggregating mainly on the top surface where the static deposition occurred. However, collagen fills the internal volume of scaffolds up to

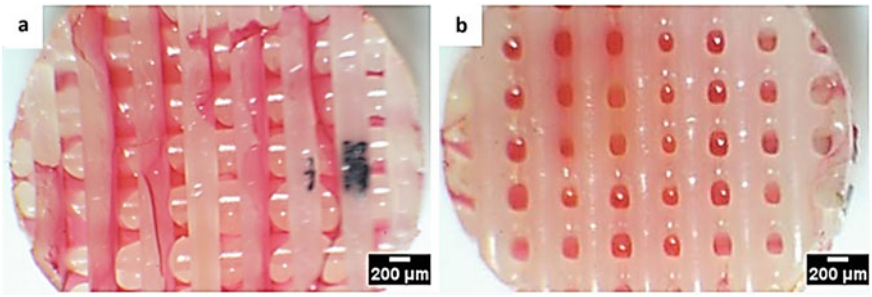

Fig. 3.8 (**a**) Top and (**b**) bottom view of collagen (red) stained with Sirius red

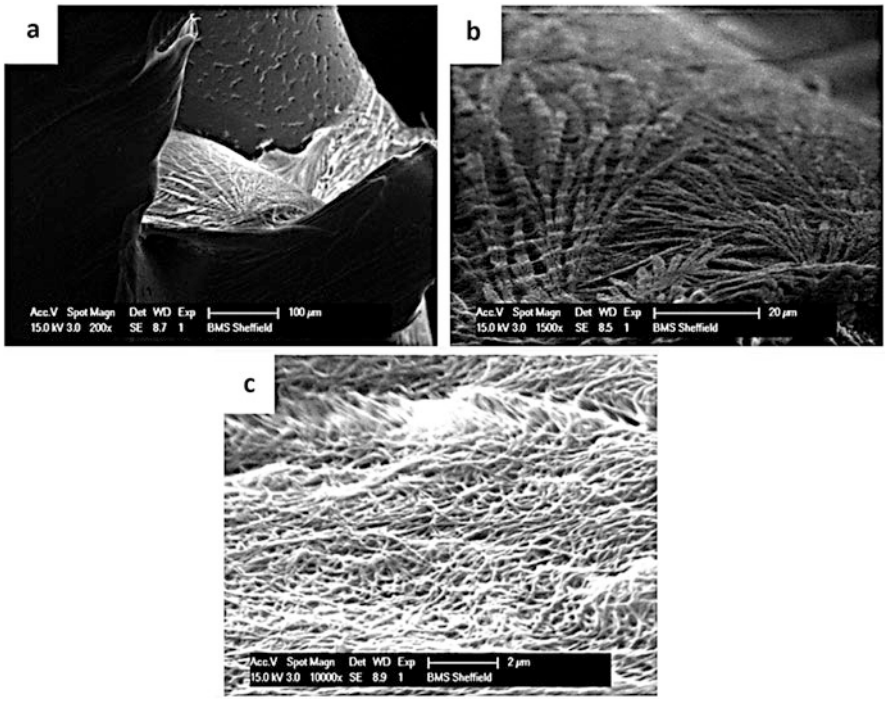

Fig. 3.9 SEM images of collagen organization at (**a**) macro-, (**b**) micro- and (**c**) nanoscale

the pores placed underneath the first layer of fibres (Fig. 3.8b). Further absorbance measurements helped quantify the total amount of collagen in samples amounting to 24 ± 5 µg.

The same architecture was observed by SEM images showing collagen layers bridging PCL fibres at macroscale (Fig. 3.9a). At lower scale (Fig. 3.9b), collagen organizes in a leaflike structure clearly showing aggregates of fibres following the same pattern of distribution. At nanoscale (Fig. 3.9c), fibres overlap randomly creating layers whose nano-porosity amounts to 500 nm according to segmentation

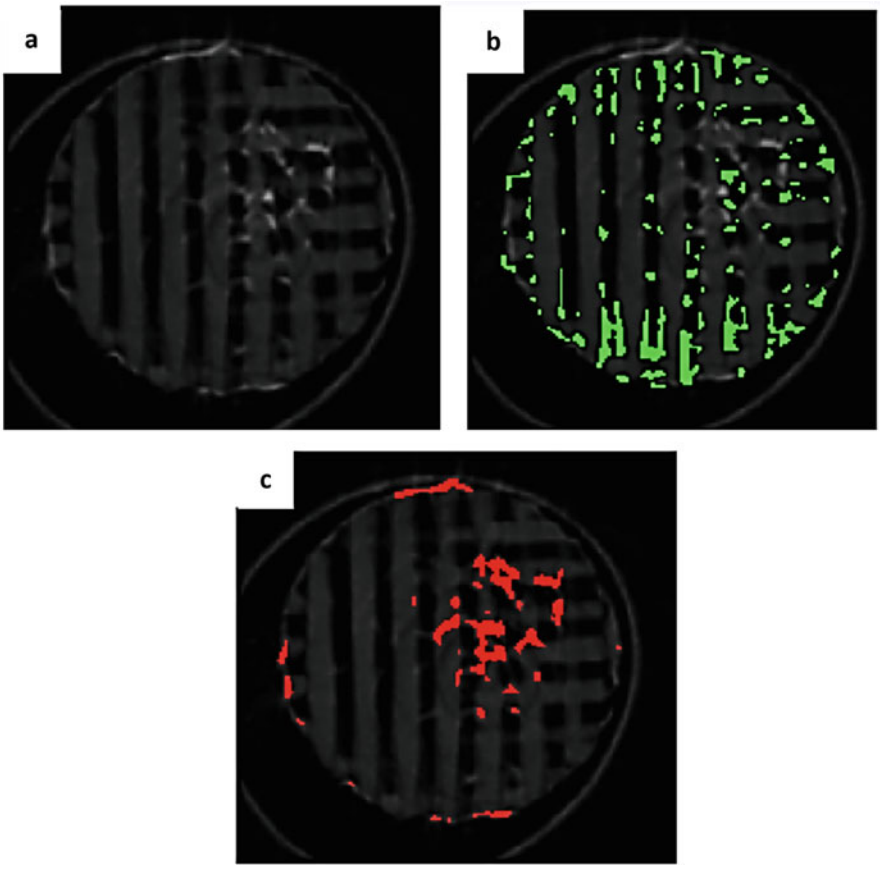

Fig. 3.10 2D slice of PCL (**a**) without masks or with masks highlighting (**b**) low-density and (**c**) high-density collagen

and reconstruction analysis performed by ImageJ software. Further microCT reconstruction of cPCL embedded with 2 mg/ml collagen was performed in order to define with more precision the density and distribution of collagen inside and outside the structure. Using Simpleware software, three cPCL samples were reconstructed after 24 h in medium and osmium staining. 2D slides were segmented in order to identify the scaffold structure and the collagen content.

The results showed a non-uniform density of collagen and content variation between the inner and the surface of the structure presenting signal relative to collagen at different ranges of grey values (Fig. 3.10a). According to the principle governing X-ray absorbance, high-density materials give signal closer to the white as consequence of lower X-ray transmission. Thus, lower signal between 4500 and 8000 was identified as low-density collagen (Fig. 3.10b), while values between 13,000 and 41,000 were addressed as high-density collagen (Fig. 3.10c). Merging the 2D slides with Simpleware, a qualitative distribution of collagen showed that

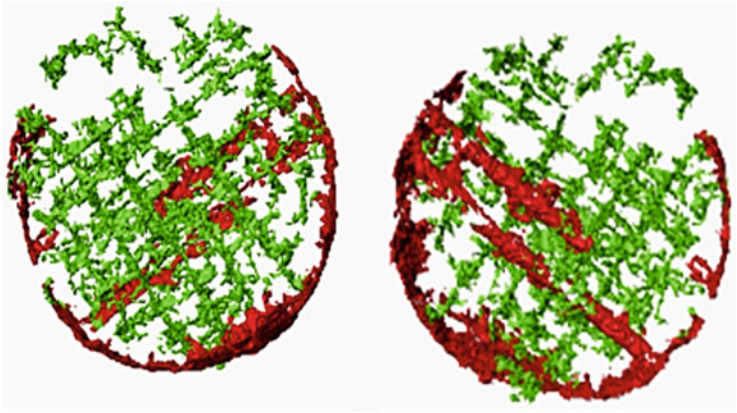

Fig. 3.11 Bottom (**a**) and top (**b**) view resulting from the volume rendering of 2D slices showing the distribution of collagen embedded into a PCL scaffold at low (green) and high (red) density

high-density collagen occupies mainly the top surface of the scaffolds, while low-density collagen was able to penetrate the scaffold and fill the inner pores (Fig. 3.11). Similar outcomes related to the distribution of cells seeded by static methods in 3D scaffolds were already found to lead to non-uniform distribution and accumulation of cells on the top volume of scaffolds (Declercq et al. 2013).

3.3.3 Seeding Efficiency and Proliferation

At first, 3D Insert PCL scaffolds were tested in order to define the role of plasma treatment on sample seeding efficiency and cellular distribution. Half samples ($N = 9$) undergo plasma treatment (PCLt), while the other half was directly seeded after sterilization. In order to promote cell survival over long periods of time, PCL and PCLt underwent sterilization by washing with 70% ethanol solution to prevent samples infection. After air drying, 20 µl of cellular suspension with or without collagen embedding 50,000 cells was placed on the top of scaffolds and let solidify at 37 °C and 5% CO_2. Fluorescence imaging of dead (red) and alive (green) cells showed that plasma treatment was necessary in order to avoid the spreading of collagen only to the areas of initial contact (Fig. 3.12a). Air plasma treatment guarantees uniform distribution of cells within the scaffold due to its ability to provide uniform distributed surface activity through the outer layer of fibres (Fig. 3.12b).

After 1.5 h, 180 µl of media was added to samples, and seeding efficiency was tested after 24 h from the seeding process by quantifying the DNA content in samples. Samples showed seeding efficiency up to 55 ± 5% regardless the

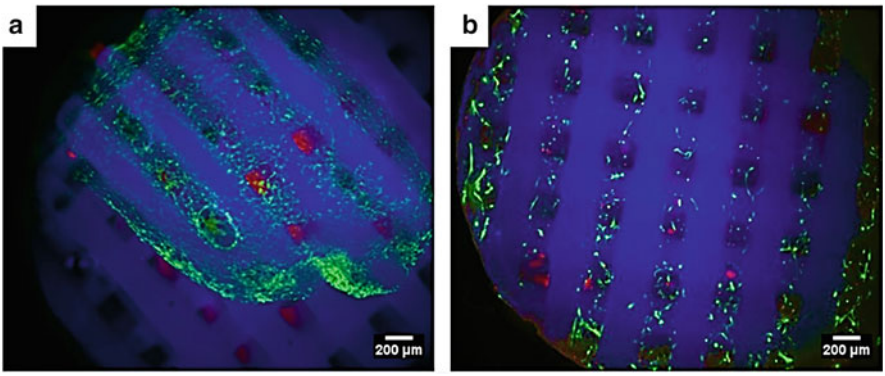

Fig. 3.12 Cells distribution on (**a**) not treated and (**b**) treated samples. Alive cells are shown in green by staining with calcein AM, while dead cells are red by ethidium bromide homodymer stain

application of plasma treatment or the concentration of collagen used. Absence of collagen led to lower attachment of cells leading to seeding efficiency values up to $40 \pm 5\%$ (Fig. 3.13a).

Cell metabolism was assessed by Presto Blue assay by varying collagen concentration (Fig. 3.13b) in order to find the best condition eliciting cells survival. Significant increase in cell metabolism was noticed already after 24 h from the attachment of cells on samples embedding 1.5 and 2 mg/ml collagen gel, suggesting a strong dependency between collagen concentration and cellular activities, and highlights the necessity for collagen content optimization. Indeed, cells presented a much lower metabolic activity when collagen was absent or in the presence of 2.5 mg/ml collagen concentration. The low proliferation potential of cells observed for high concentration of collagen is probably the consequence of the high degree of packing between fibres preventing the permeation of nutrients and gases through the collagenous matrix. Despite the positive effect of collagen on cell proliferation potential, significant increase in metabolic activity was observed after 3 days just on cells seeded without collagen matrix, while the presence of collagen prevented cell proliferation over 5 days regardless the concentration of collagen employed. These results are in accordance with other studies claiming the absence of proliferation of cells cultured in collagen gel over the same period of time (Parenteau-Bareil et al. 2010). Despite the low proliferation potential elicited from the presence of collagen over a rather short period of culture, samples embedding 1.5 and 2 mg/ml collagen were found to be the best enhancing cell survival at each time point, and the concentration of 2 mg/ml was selected as optimal for longer studies focusing on the effect of mechanical stimuli on cell response.

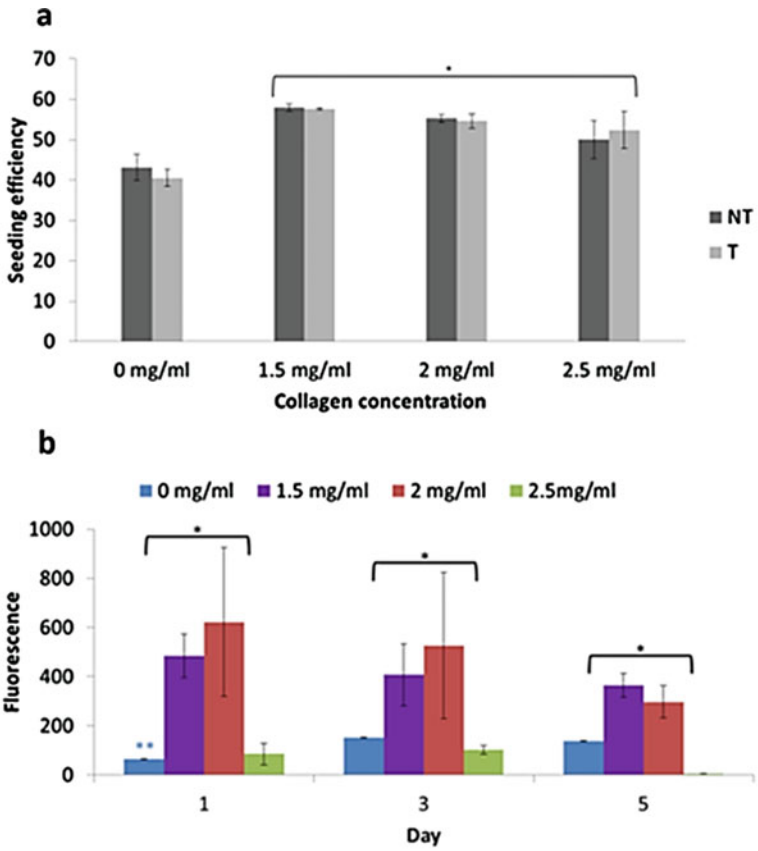

Fig. 3.13 Quantification of (**a**) the number of cells attached by DNA assay and (**b**) cells metabolic activity over 5 days by Presto Blue varying concentration of collagen in samples

3.3.4 Response of MSCs Seeded to Compression Stimuli

In order to investigate the role of compression stimuli on cell activities, the same compression protocol consisting in a superimposed ramp of 5% followed by sinewaves at 1 Hz and 1% strain peak to peak was applied to samples seeded with 2 mg/ml collagen embedding 50,000 cells for 15 min a day. Considering the seeding day as day 0, the first batch underwent compression from day 6 to day 10 ($L1$), while a second batch extracted from the first group of samples underwent further stimulation from day 16 to day 20 ($L2$) after resting for 5 days from the first burst of compression. Compressed samples are compared to unloaded conditions (U) at day 1, 3, 7, 14 and 21 in terms of DNA content and metabolic activity.

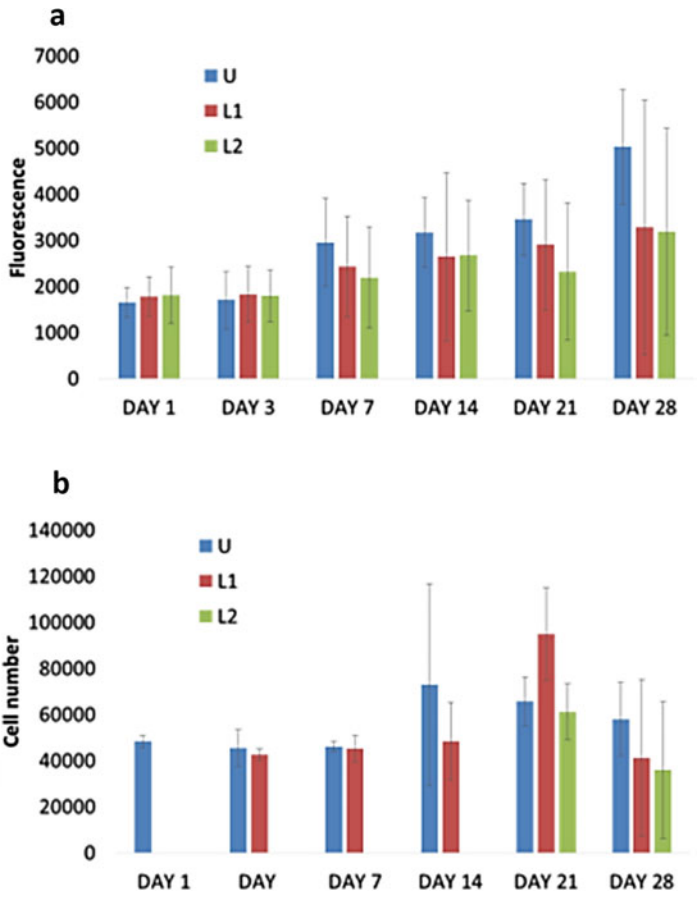

Fig. 3.14 Response of hMSCs seeded in 3D scaffolds undergoing compression in terms of (**a**) metabolic activity and (**b**) DNA content

The DNA quantification shows an increase in cell number on *U* samples after 14 days and on *L*1 samples at day 21 (Fig. 3.14a). On the contrary, cells which underwent twice the stimulation did not proliferate significantly over the 28 days showing constant cell number. Similar results can be noticed looking at the metabolic activity (Fig. 3.14b) where the increase in metabolic activity noticeable at day 7 for *U* is believed to be related to the increase in cell number registered at the next time point by DNA assay. The same fate was followed by *L*1, but the proliferation is delayed for 7 days as a result of the mechanical stimulation. Due to the increase in cell number observed at day 21 from *L*1, higher values of metabolic activity were expected to occur at day 14 following the same pattern observed by *U* samples. Despite this, *L*1 metabolic activity becomes statistically higher just at day

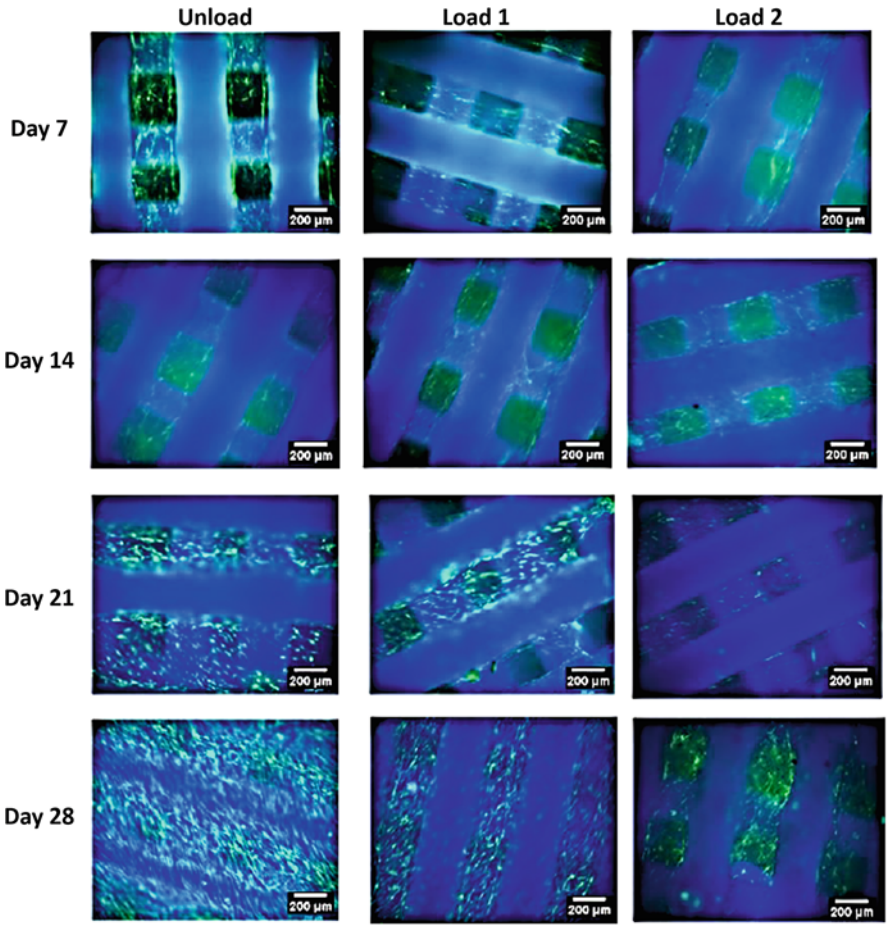

Fig. 3.15 Fluorescence pictures of PCL (blue) and alive cells (green) at different time points for unloaded (*U*) loaded once (*L*1) and twice loaded (*L*2) samples

21 probably due to the high standard deviation observed at day 14. However, the metabolic activity of *L*1 shows an average increase at day 14 which can be related to the increase in cell number observed at day 21. Eventually, fluorescence values from Presto Blue give insight of cell viability on the surface of the scaffold showing results in accordance with fluorescence images taken at each time point (Fig. 3.15) where the number of cells is clearly increasing on the surface of the scaffold over time for *U* as well as for *L*1 and *L*2 although in lower amount.

3.4 Discussion

In this study a 3D composite scaffold made of PCL and collagen gel was developed in order to observe the effect of mechanical stimuli on cellular activities. PCL is characterized by a stiff structure progressively decreasing its modulus with increasing temperature as expected from polymeric materials. Viscoelastic effects observed during dynamic stimulation are prevented by applying relaxation for 3 h. DMA analysis was in accordance with results obtained by Hutmacher et al. (2001) and Ghosh et al. (2008) where no significant differences were noticed testing five-angled scaffolds and by comparing elastic modulus in wet and dry conditions. Contradictory results were found in terms of viscoelastic response to frequency. Indeed, our results showed (1) a significant increase of elastic modulus for frequency above 5 Hz and (2) no significant differences in terms of loss modulus varying either frequency or state. These discrepancies can be explained by considering differences within the 3D Insert PCL scaffolds employed in our study and the starches used for comparison in terms of either porosity, lay-down pattern, raw material or differences in scaffolds handling, working humidity and application of relaxation protocols. Our results suggest that water does not elicit a plasticization effects on the structure as no differences were noticed applying the same conditions in dry or immersed state. Further dynamic mechanical analysis showed inconsistent mechanical behaviour comparing different PCL samples due to the small dimensions playing a role in the propagation of the compression stimuli through the structure and imperfections resulting from the fabrication process which lead to variable mechanical properties. A repositioning of the scaffold inside the testing machine showed high standard deviations with errors up to 30% in terms of stress transmitted to the structure as a consequence of the same strain.

In an attempt to clarify the distribution of stresses in the composite scaffold, a further complication arises from the use of collagen aiming to provide a soft matrix able to transmit the external stimuli to cells. As shown above, collagen does not create a compact matrix but organize itself in layers bridging between one fibre and the other varying its density and preferring lower collagen density in the inner of the scaffolds and higher aggregation of collagen on the outer surface of the scaffold. This behaviour is due to the porosity of the scaffold allowing just a small amount of collagen to reach the internal areas for capillarity effects, while the majority clusters on the surface. However, the average collagen distribution is uniform through the structure, and due to contact between PCL and collagen, the displacement of PCL fibres will be transmitted to collagen and sensed by cells.

The concentration of collagen in use was found to play a crucial role in cell survival and proliferation. A 2 mg/ml and 1.5 mg/ml collagen allow cells to increase their metabolic activity over time, promoting their proliferation in unloaded conditions at day 7 and 28. Over 28 days, compression showed its role on cell proliferation potential by delaying the peak of metabolic activity observed at 7 days on *U* samples to 21 days for *L*1. Applying the same stimulus a second time prevents any significant peak in cell number. Also the thick cellular layer developing in *U* conditions at day

21–28 is almost absent when samples undergo mechanical stimulation. This might be due to the contact between the machine and the sample and to friction effects caused by the motion of fluid and micro-movements of the scaffold, leading to disruption of the most exposed cells on the outer layer. Comparing DNA and metabolic activity results, an increase in metabolic activity can be associated to proliferation of cells during the 7 following days. Despite the constant increase in metabolic activity, DNA quantification shows a decrease in cell number after the proliferation peak. This is explained by considering proliferation to occur mainly on the surface layer. The growth of an external layer is believed to cause cellular death in the inner volume of the scaffold due to lack of nutrients, leading to no significant increase in DNA content in the interior of the scaffold and increased cell death. Further analysis of microCT scans at each time point is among the future plans in order to confirm this hypothesis.

3.5 Conclusion

The increased demand for mimicking the 3D environment in order to closely reproduce the same condition found in vivo led to the consideration of starch materials as the next approach to study how mechanical stimuli affect cell behaviour. Among the main advantages, 3D scaffolds are able to bear compression stimuli and optimization of parameters such as the porosity and offset between fibres which lead to satisfactory results in terms of cellular attachment and proliferation. Optimization of such parameters was found to be a key factor not only in promoting cells survival but also in defining the mechanical properties of the starch. On this purpose, 3D Insert PCL scaffolds demonstrate to bear compression stimuli employing a wide range of frequency, preventing plastic deformation for low applied strains and avoiding viscoelastic effects to occur following proper relaxation. This variability is among the main drawback carried by PCL scaffolds when employed in compression studies, but at the same time, this variation allows a good representation of the in vivo conditions. As a matter of fact, the human body performs different movements resulting in a global compressive stimuli acting at the injured areas. The compressive stimuli locally result in a combination of stretching and bending forces whose distribution depends on the shape of the fracture, the magnitude of the applied force and the stage of ossification (Lacroix and Prendergast 2002). The same distribution of stress is well mimicked in vitro inside a 3D fibrous specimen as fibres deform leading to local variation of the resulting stress in the structure. Embedding collagen led to the formation of protein layers bridging between fibres and able to transmit the stimuli resulting from the deformation of the structure to cells. These outcomes prove the suitability of PCL in bearing loading forces and the feasibility of transmitting the local stress to cells by embedding collagen in the structure. Computational analysis put alongside with experimental work can be used as a tool to define ranges of stresses acting on the structure as a consequence of the applied strain, further clarifying the real distribution of stress within the interior regions of

the structure and stimuli sensed by cells. In order to increase the trueness of stimulations, storage and loss modulus values obtained by DMA can be used as input for the simulation model.

Moreover, PCL was shown to be suitable in supporting cell activities over long periods of time. Collagen embedded scaffold presented enhanced seeding efficiency compared to scaffolds without collagen. 2 mg/ml concentrated collagen is found to enhance the metabolic activity of cells and two bursts of proliferation at day 7 and day 28 in unloading conditions. Compressive forces demonstrate to slow down cellular proliferation over 28 days leading to a delayed proliferation after a single application and to the absence of proliferation peaks when applied twice. Further investigation over protein expression will help clarifying the fate embraced by cultured cells and the effect of bursts of compression on differentiation.

References

Barbarisi M et al (2014) Use of polycaprolactone (PCL) as scaffolds for the regeneration of nerve tissue. Soc Biomater 103(5):1755–1760

Chen W, Zhang B, Forrestal MJ (1999) A split Hopkinson bar technique for low-impedance materials. Exp Mech 39(2):81–85

Chen G, Ushida T, Tateishi T (2002) Scaffold design for tissue engineering. Macromol Biosci 2 (2):67–77

Declercq HA, Desmet T, Berneel EEM, Dubruel P, Cornelissen MJ (2013) Synergistic effect of surface modification and scaffold design of bioplotted 3-D poly-E-caprolactone scaffolds in osteogenic tissue engineering. Acta Biomater 9(8):7699–7708

Engler AJ, Sen S, Lee Sweeney H, Discher DE (2006) Matrix elasticity directs stem cell lineage specification. Cell 126(4):677–689

Gama BA, Lopatnikov SL, Gillespie JW (2004) Hopkinson bar experimental technique: a critical review. Appl Mech Rev 57(4):223

Ghosh S et al (2008) Dynamic mechanical behavior of starch-based scaffolds in dry and physiologically simulated conditions: effect of porosity and pore size. Acta Biomater 4(4):950–959

Hutmacher DW (2000) Scaffolds in tissue engineering bone and cartilage. Biomaterials 21:2529–2543

Hutmacher DW et al (2001) Mechanical properties and cell cultural response of polycaprolactone scaffolds designed and fabricated via fused deposition modeling. J Biomed Mater Res 55 (2):203–216

Karageorgiou V, Kaplan D (2005) Porosity of 3D biomaterial scaffolds and osteogenesis. Biomaterials 26(27):5474–5491

Lacroix D, Prendergast PJ (2002) A mechano-regulation model for tissue differentiation during fracture healing: analysis of gap size and loading. J Biomech 35(9):1163–1171

Lohmann CH, Schwartz Z, Niederauer GG (2000) Pretreatment with platelet derived growth factor-BB modulates the ability of costochondral resting zone chondrocytes incorporated into PLA/PGA scaffolds to form new. Biomaterials 21:49

Marino G et al (2012) Growth and endothelial differentiation of adipose stem cells on polycaprolactone. J Biomed Mat Res A 100A(3):543–548

O'Keefe RJ, Mao J (2011) Bone tissue engineering and regeneration: from discovery to the clinic: an overview. Tissue Eng Part B Rev 17(6):389–392

Odusanya OS, Manan DMA, Ishiaku US, Azemi BMN (2003) Effect of starch predrying on the mechanical properties of starch/poly (E -Caprolactone) composites. J Appl Polym Sci 87:877–884

Parenteau-Bareil R, Gauvin R, Berthod F (2010) Collagen-based biomaterials for tissue engineering applications. Materials 3:1863–1887

Slivka, M. A., Leatherbury, N. C., Kieswetter, K., & Niederauer, G. G. (2000). In vitro compression testing of fiber-reinforced, bioabsorbable, porous implants. In *Synthetic bioabsorbable polymers for implants*. ASTM International

Sobral JM, Caridade SG, Sousa R a, Mano JF, Reis RL (2011) Three-dimensional plotted scaffolds with controlled pore size gradients: effect of scaffold geometry on mechanical performance and cell seeding efficiency. Acta Biomater 7(3):1009–1018

Yilgor P, Sousa RA, Reis RL, Hasirci N, Hasirci V (2008) 3D plotted PCL scaffolds for stem cell based bone tissue engineering. Macromol Symp 269(1):92–99

Chapter 4
Towards a New Approach to Analyse Quality Control and Morphometric Variability in a Scaffold

Rapid prototyping is a powerful manufacturing technique to fabricate tissue engineering scaffolds as it provides control over scaffold architecture while processing biomaterials. For the successful integration of tissue engineering scaffolds in clinical applications, the manufacturing process needs to the meet good manufacturing practice standards delivering quality and reproducibility. Unexpected variations in the scaffold microstructure due to limitations in the fabrication process could lead to undesired mechanical stimuli at the cell level. Thus, if cell activity is affected, tissue growth will be perturbed. In this chapter, an in silico protocol to analyse fabricated scaffolds is presented and used to evaluate a commercial regular porous scaffold from 3D Biotek. The actual μCT-based morphology of five fabricated samples was analysed and then integrated into computational fluid dynamics simulations to analyse the local fluid flow conditions. The fabricated samples present variations in the internal microstructured and in the local fluid dynamics compared to the CAD scaffold. In addition, the five samples show intersample variability as well as internal variability from pore to pore. It is demonstrated that geometrical imperfections can deviate scaffold performance from the intended purpose. In this chapter, it is shown that in silico methods can be part of standard inspection protocols for tissue engineering applications.

4.1 Introduction

4.1.1 Good Manufacturing Practice of Scaffolds

Scaffolds serve as 3D temporal templates for cells to form new tissue during bone healing. The purpose of scaffolds is to replicate the bone extracellular matrix to provide the adequate biomechanical support for cells. The mechanical properties of scaffolds depend on key structural factors such as porosity, pore size and pore

This chapter forms part the PhD thesis of Ana Campos available here: http://etheses.whiterose.ac.uk/12349/

© Springer Nature Singapore Pte Ltd. 2019

D. Lacroix et al., *Multiscale Mechanobiology in Tissue Engineering*,
Frontiers of Biomechanics 3, https://doi.org/10.1007/978-981-10-8075-3_4

interconnectivity. In addition to the mechanical properties, these factors are essential to allow homogeneous tissue ingrowth and the formation of new blood vessels that will ensure the right exchange of nutrients, O_2 and cell wastes. In the last years, rapid-prototyping (RP) techniques have shown the potential to fabricate scaffolds with controllable porous architectures**.** This group of techniques consist of building a pre-generated digital computer-aided design (CAD) geometry in a layer-by-layer fashion. For this, the CAD model is converted into the standard stereolithography (STL) format and sliced into layers prior to the physical fabrication (Hollister 2005). The manner in which the physical layers are deposed during the building process has served to categorize RP techniques in three main approaches: laser-based methods, 3D printing and melting extrusion (Yeong et al. 2004). Besides the ability of these techniques to build customized scaffold geometries, they are also able to process a wide range of scaffold biomaterials such as poly-(glycolic acid) (PGA) (Xu et al. 2010), poly-(lactic acid) (PLA) (Serra et al. 2013), polycaprolactone (PCL) (Gautam et al. 2013) and polyethylene glycol (PGE) (Hoque et al. 2005). Tissue engineering scaffolds must be biocompatible to avoid risk of rejection, and they must degrade at specific rates to let the newly formed tissue occupy the fracture gap and stimulate cell response.

Scaffold production must follow good manufacturing practice (GMP) standards in order to fabricate scaffolds within regulated tolerances that ensure the intended mechanical performance and therefore the right stimulation for bone growth. Many efforts have been made for the optimization of scaffold design such as controlling scaffold architecture over scales or delivering patient-specific geometries (Dias et al. 2014). Nevertheless, all these efforts are useless if the fabrication process is not accurate enough. Furthermore, a consistent fabrication process will minimize and control variability among samples in batch production, thereby providing always the same micromechanical environment for cells. Unfortunately, to date there are no regulatory protocols for the compliance of such standards. Despite the promising capability of RP techniques to build scaffolds with predefined architectures using biomaterials suitable for TE applications, scaffold fabrication still needs to follow regulatory pathways for the successful commercialization and translation of TE scaffolds into the clinics (Podshivalov et al. 2013).

4.1.2 Comparing Designed Structure with Real Scaffold

Some studies have made efforts to identify and eliminate technical limitations in the scaffold fabrication process. Van Bael et al. (2011) evaluated fabricated samples morphologically and mechanically in order to adjust the fabrication parameters until the expected scaffold properties were achieved. Domingos et al. (2012) studied the fabrication of PCL scaffolds by the fused deposition modelling (FDM) technique and showed that the speed of extrusion and temperature are critical factors that potentially determine the final scaffold shape. Garrett et al. (Ryan et al. 2009) analysed a regular 3D-printed titanium scaffold using micro-computed tomography

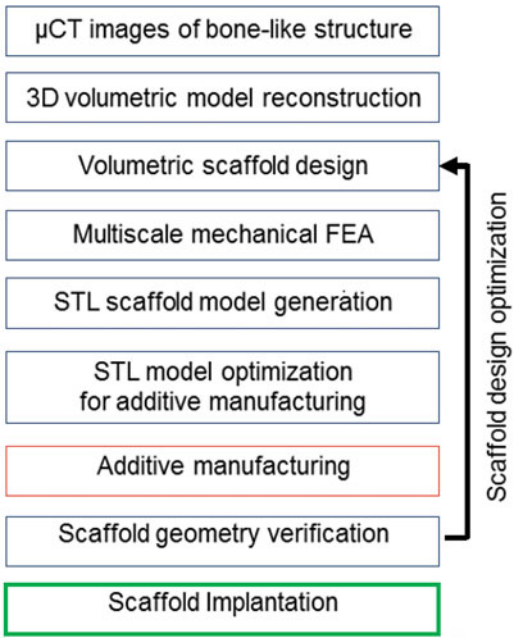

Fig. 4.1 Workflow proposed by Podshivalov et al. (2013) for scaffold-based treatments from the design of a patient-specific scaffold up to its implantation at the fracture site. It includes scaffold geometry verification to ensure that the fabrication process delivers the expected scaffold design. (Figure adapted from Podshivalov et al. 2013)

(μCT) scanning and compared it with its CAD model reporting significant variability in the scaffold microstructure and response during fatigue analysis. These studies show that RP methods need further optimization and the importance of inspecting fabricated scaffolds in a more systematic manner. Podshivalov et al. (2013) proposed an approach from patient-specific scaffold design up to its implantation at the fracture site with the inclusion of an inspection step to verify whether the final scaffold meets the design criteria. The integration of inspection protocols would help to optimise the scaffold design and manufacturing process as shown in Fig. 4.1. Furthermore, inspection methods will help to avoid undesired mechanical stimuli for cells due to variations in the final scaffold shape.

Current noninvasive imaging techniques such as μCT scanning are crucial to reverse-engineer fabricated scaffolds in order to assess the actual geometry, and, by the inclusion of digitalized scaffolds in finite element (FE) and computational fluid dynamics (CFD) simulations, it is possible to quantify the mechanical stimuli that cells will sense (Olivares and Lacroix 2013; Sandino and Lacroix 2011). In this chapter, different techniques to inspect fabricated scaffolds will be discussed, and a novel protocol will be proposed including the generation of the 3D digital representation of a RP fabricated scaffold, the analysis of scaffold microstructure and the mechanical performance under perfusion conditions. More specifically, a commercial regular scaffold from 3D BioTek (New Jersey, USA) made of polycaprolactone (PCL) will be investigated; the scaffold geometry variability due to the fabrication process is related to its fluid dynamic microenvironment. Five samples will be compared with their CAD design and also among them to report the quality and

reproducibility of the manufacturing process, respectively. Local values of wall shear stress (WSS) and fluid velocities will be calculated and compared from scaffold-to-scaffold at the same location within the pore level.

4.2 Scaffold Microstructure Image Acquisition

Some studies have characterized fabricated scaffolds by scanning electron microscopy (SEM) that provides 2D images with high resolution and contrast (Gautam et al. 2013). However, despite the great magnification of this method, scaffold samples need to be coated with gold by using a sputter coater before the image acquisition, and in order to obtain internal morphological information, the samples need to be cut. In addition, this invasive method does not permit the full characterization of 3D samples. μCT scanning is a non-destructive solution widely used by researchers for the entire scaffold characterization since it permits the generation of a 3D stack from a serial of sample cross-sectional images (Park et al. 2012). Magnetic resonance imaging (MRI) also allows the development of 3D models from a series of 2D images; however, this technique generally provides less resolution than μCT imaging, and it is more effective to differentiate soft tissues in clinical scenarios. Mather et al. (2008) compared the previous imaging techniques with terahertz pulsed imaging (TPI) showing the good contrast image data of this method although the terahertz radiation is not as penetrating in the scaffold material as the x-rays resulting in low lateral resolution.

Imaging segmentation softwares allow converting the generated μCT/MRI images into 3D data. The acquired images represent sample cross-sections compounded by grey-scale pixels. These images are stacked to recreate the scanned volume and the scaffolds region is segmented by selecting the pixels within a specific threshold of grey-scale values (Costa et al. 2014).

In this study, five fabricated samples were scanned with a μCT scanner (SkyScan 1172, Materialise, Belgium) at 59 kV voltage and 149 μA beam current. The samples were not treated prior to scanning. First, consecutive scans were performed reducing the voxel size until the μCT-based geometry was independent from the voxel size selected, and finally, $7 \times 7 \times 7$ μm^3 was the maximum voxel size that could accurately capture scaffold without compromising the size of the μCT data size.

The μCT images' data were reconstructed with Simpleware (Exeter, UK). The noise of the raw images was reduced using the median filter; this filter computes each output pixel as the statistical median of the neighbourhood of values around the corresponding input pixel. Once the raw images were filtered, the region of interest was segmented from the 3D stack and then smoothed using the recursive Gaussian filter in order to reduce outliers and simplify the surface meshing process (see Fig. 4.2). A final binarization filter was applied to the mask in order to cancel the

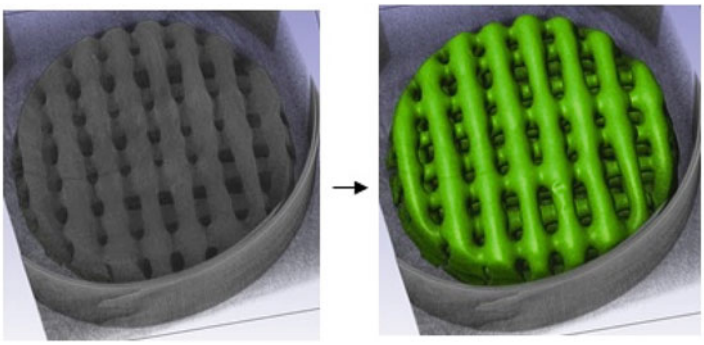

Fig. 4.2 The stack of μCT-images (left) was segmented to obtain the scaffold geometry (right) within the raw data

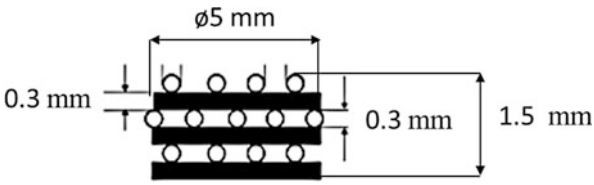

Fig. 4.3 PCL commercial scaffold design specifications

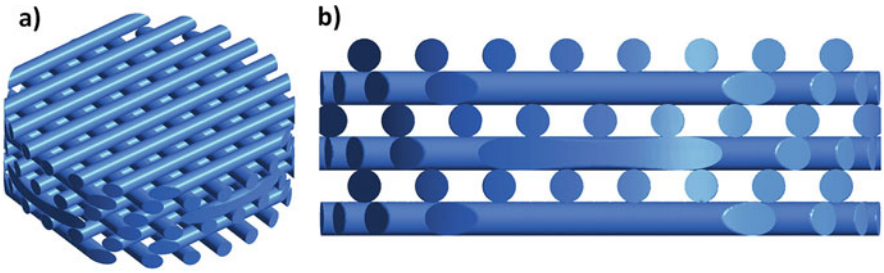

Fig. 4.4 (**a**) 3D CAD model of the scaffold. (**b**) Side view

connection between the background images and the segmented mask. Then, a triangular mesh was generated on the surface mask to represent the μCT-based scaffold geometry. The surface mesh was exported in STL format.

For the digital representation of the scaffold design, a CAD model was generated in ANSYS DesignModeler following manufacturer design specifications (see Figs. 4.3 and 4.4). The scaffold has a regular porous design compounded by layers of cylindrical fibres with 300 μm diameter and with a distance of 300 μm between fibres. It has six layers with an offset of 90° in the orientation of the fibres from layer to layer. In addition, there is a displacement of 300 μm among alternative layers. The scaffold has a cylindrical shape with 5 mm diameter and 1.5 mm height.

4.3 Microstructural Analysis of Scaffold

To fully characterize scaffold architecture, key parameters such as pore size, porosity, interconnectivity, volume and surface area need to be addressed. Despite the advantage of current imaging techniques to offer accurate 3D representations of actual scaffolds, sometimes the methods applied for the structural characterization of μCT-based models are not that accurate and need to be further developed. Many studies carry out manual measurements of structural variables such as pore size throughout the entire scaffold (Jamalpoor et al. 2015). This is a time-consuming approach that can become a significant source of error due to human handling. Other studies applied specific algorithms from the same imaging softwares used for μCT reconstructions to characterize scaffolds. For instance, Melchels et al. (2010) used the GE (General Electric) MicroView software to fit the largest sphere in each empty void which diameter corresponds with the pore size. This data was later used to quantity other structural factors such as porosity using numerical algorithms in MATLAB.

In this study, a combination of manual methods and software-specific algorithms from Simpleware was used to analyse the samples. The five μCT-reconstructed scaffolds were characterized using the Simpleware statistics and measuring package and for the CAD scaffold the ANSYS DesignModeler algorithms. Key structural factors such as pore size, porosity, surface area and volume were reported for all scaffolds. The five samples and the CAD scaffold have 100% pore interconnectivity. The CAD scaffold has 51% porosity, 193 mm^2 surface area and 14.6 mm^3 volume. The porosity of the five samples is $45.4 \pm 5.5\%$, the surface area is 206.4 ± 12.54 mm^2 and the volume is 16.1 ± 1.32 mm^3. The deviation of these mean values from the CAD scaffold in terms of porosity, surface area and volume is 0.6, 16.4 and 2.4, respectively.

The commercial scaffold selected for this study is fabricated with the fused deposition modelling (FDM) method. The PCL is preheated into a semi-molten temperature and extruded through a nozzle building layers of fibres on top of the other. Once the sheets of fibres are solidified, punching is applied to extract the cylindrical scaffolds. The five digitally reconstructed samples show a cone truncated shape instead of a cylindrical geometry. This is due to the punching process that also damages the side part of the samples as shown in Fig. 4.5. Therefore, they have a variable diameter from ~5 mm at the bottom layer to ~4.5 mm at the top of the scaffold. This undesired shape served in this study to select the top of the truncated cone scaffold as the first layer of fibres counting up to the sixth layer at the bottom of the scaffold. The five samples show a different internal distribution of fibres from the CAD scaffold. Alternative layers should present a fibre displacement of one fibre diameter distance; however, the displacement is only observed at the last two alternative layers at the bottom (see Fig. 4.6). This shows the lack of accuracy of the fabrication process to apply the expected fibre displacement when building the scaffold bottom-up layer by layer. Furthermore, one of the five samples presents a different internal pattern from the rest showing the fibre displacement at the top first

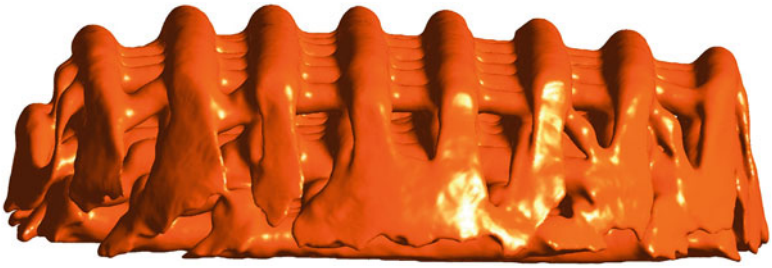

Fig. 4.5 Scaffold irregularities due to the punching process shown in a μCT-reconstructed scaffold

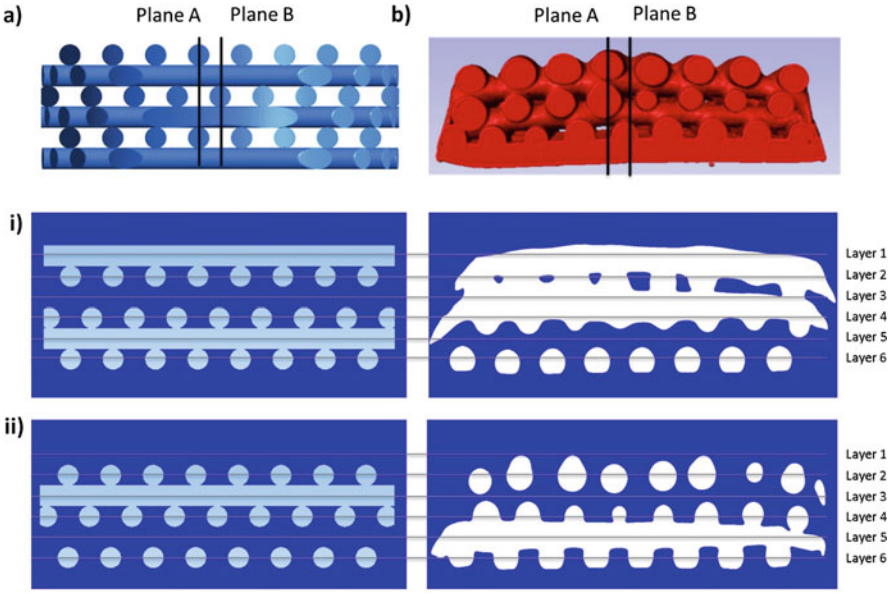

Fig. 4.6 Structural comparison between CAD (**a**) and a μCT-reconstructed scaffold (**b**). Cross-sections from planes A (i) and B (ii) show the internal spatial arrangement of fibres. The two scaffolds are compared at all layers so the structural limitations of the fabrication process can be identified

two alternative layers and not at last two (see Fig. 4.7). This could be due to the sheets of fibres being punched on the other side.

Other important structural aspects are the fibre diameter and fibre spacing that were measured in ImageJ. The fibre diameter and spacing of the five μCT-based samples are 220 ± 100 μm as also shown by Zermatten et al. (2014), whereas in the CAD scaffold, this value is constant and equal to 300 μm. This modification in the shape of fibres occurs while they solidify, and the gravity acts as well as the need of the fibres to overlap with the fibres from adjacent layers to maintain interlayer adhesion. Moreover, the depth of overlap between fibres is not constant; therefore,

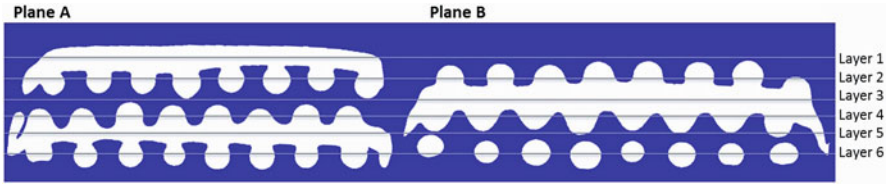

Fig. 4.7 Internal microstructure shown at the cross sections specified in Figs. 4.3, 4.4, 4.5, 4.6, 4.7, 4.8 and 4.9 of the sample with different fibre distribution from the other samples

the fibres that belong to the same layer are not well aligned. Consequently, scaffold height in fabricated samples is irregular and can vary from 1 mm up to 1.5 mm.

4.4 The Effect of Scaffold Geometrical Variations on Local Fluid Dynamics

4.4.1 Previous Studies on Local Fluid Dynamics of Scaffold

In early studies, perfusion of scaffolds was modelled assuming the scaffold microstructure as a continuous porous medium that obeys Darcy's law (Truscello et al. 2012)**.** This approach does not allow to calculate local shear stress values within the scaffold microstructure. The evolving μCT technology allows the creation of μCT-based CFD models that permit to quantify the scaffold local mechanical stimuli under fluid flow as well as its relationship with the actual scaffold microstructure. One of the main challenges in creating a μCT-CFD model is the generation of a mesh that represents the fluid domain around a complex μCT-based geometry. Some studies have used commercial softwares such as V. Acosta Santamaría et al. (2013) that imported the μCT scaffold in ICEM ANSYS (ANSYS, Pittsburgh, USA) to build the CAD-channel boundary conditions and generate a mesh between the scaffold and the channel wall boundaries. Cioffi et al. (2006) used the Amira (TGS, San Diego, CA) software to reconstruct the scaffold and to mesh the empty scaffold voids. Melchels et al. (2010) used Mimics to obtain the volumetric fluid mesh. Other researchers developed their own algorithms such as Zermatten et al. (2014) who generated an initial mesh with large elements followed by successively refinements on small features. These studies employed the finite volume method to solve the 3D Navier-Stokes equations in the generated computational meshes. The most common numerical tools for CFD simulations are Fluent and CFX from ANSYS (Cantini et al. 2009) and COMSOL Multiphysics (COMSOL Inc., Burlington, MA) (Podichetty et al. 2014). A different approach from conventional CFD methods was followed by Porter et al. (2005) who used the Lattice-Boltzmann (LB) model where the fluid volume is broken into a grid of nodes along where

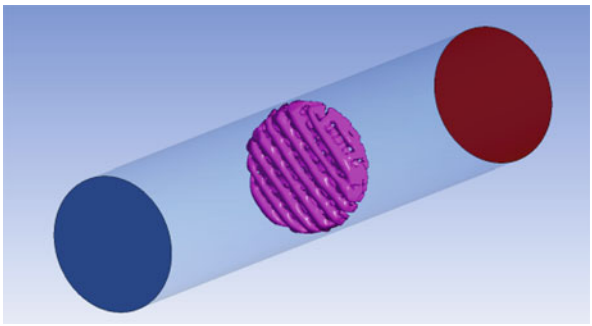

Fig. 4.8 Physical boundaries of the fluid volume mesh

particles that conform the fluid will propagate depending on the local mass distribution function and collide conserving mass and momentum. Despite the successful integration of μCT geometries in CFD simulations, further efforts need to be made to extract as much information as possible from the post-processing. Most of these studies report average values of the variables of interest; therefore, the effect of scaffold geometrical variations on the local fluid dynamics is missed.

4.4.2 Meshing Construction of Fluid Domain Around a μCT-Based Scaffold

The STL and the CAD scaffolds were imported into ICEM ANSYS. The scaffold was located in the middle of a cylinder generated with a radius of 2.72 mm and 28 mm length (see Fig. 4.8). These cylinder dimensions were selected to be able to enclose the five samples and the CAD scaffold ensuring no scaffold-cylinder intersection as that could complicate the meshing process. The fluid domain between the scaffold and cylinder wall boundaries was meshed with tetrahedral elements using the robust octree algorithm from ICEM ANSYS. This method ensures refinement near the scaffold while maintaining larger elements where possible. A grid independency study was carried out by calculating the impact of the maximum length of the edge of the triangular faces of the tetrahedral elements inside the scaffold and the maximum length for the rest of the elements outside the scaffold on velocity and wall shear stress values. As a result, around ten million tetrahedral elements represented the fluid domain with maximum element length of 20 μm inside the scaffold and maximum length of 1 mm outside. Despite the fact that elements outside the scaffold can be 50 times larger than the ones inside it, the meshing algorithm applied provides a smooth transition from the elements far from the scaffold to the elements close to it as shown in Fig. 4.9.

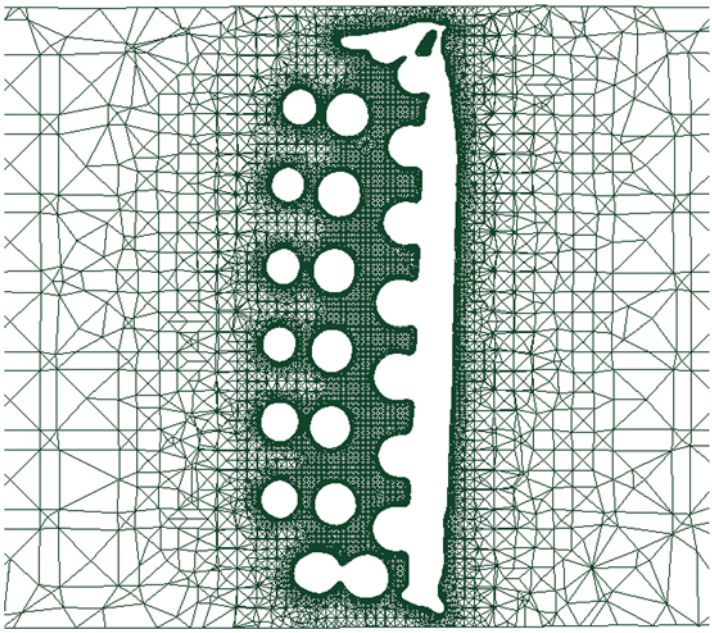

Fig. 4.9 Wire representation of the fluid mesh to observe the adaptation of the element size towards the scaffold

4.4.3 CFD Modelling and Prescribed Boundary Conditions

The fluid flow was described by the equation of continuity (Eq. 4.1) and Navier-Stokes (Eq. 4.2) for incompressible steady flows where v, p, ρ and μ are the velocity, pressure, density and viscosity of fluid, respectively. The equations were resolved using the commercial finite volume method of ANSYS Fluent 15.0 (ANSYS, Pittsburgh, USA). The fluid was modelled as an incompressible Newtonian fluid with a viscosity of 0.001 Pa·s and a density of 1000 kg/m^3. Steady state conditions were simulated for a laminar fluid flow.

$$\nabla \cdot \boldsymbol{\nu} = 0 \tag{4.1}$$

$$\boldsymbol{\nu} \nabla \boldsymbol{\nu} = -\frac{\nabla p}{\rho} + \mu \nabla^2 \boldsymbol{\nu} \tag{4.2}$$

An average velocity of 1 mm/s was applied at the inlet with a 3D parabolic profile to ensure that the fluid flow was fully developed at the scaffold entrance. The parabolic profile was described in a user-defined function (UDF) written in the programming language C++. The UDF was interpreted in Fluent and hooked at the inlet boundary. Zero pressure was applied at the outlet of the cylinder, and nonslip wall condition was modelled at the cylinder and scaffold surfaces.

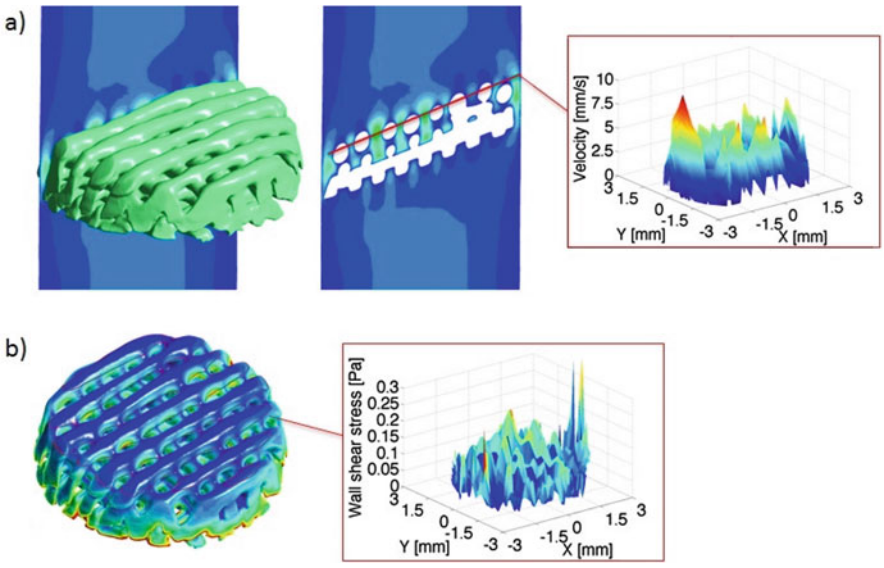

Fig. 4.10 The local velocity (**a**) and WSS (**b**) values extracted in CFD-Post and then arranged and plotted by layers with a MATLAB code

For the numerical calculations, the Fluent pressure-based coupled solver was selected where the continuity and momentum equations are solved simultaneously. The second order upwind scheme was applied for the interpolation of the momentum and pressure variables. For spatial discretization the gradient least square cell-based method was selected. Non-convergence criterion was imposed for the residuals so the numerical solution progressed until it reached a plateau.

A benchmark study of the computational model was carried out on a supercomputer (Iceberg, University of Sheffield). Serial and parallel calculations were performed to select the most cost-effective computational set-up to resolve the presented CFD model. Finally 8 partitions were selected in a node with 16 cores and 8 memory channels. The mesh was partitioned to assign one mesh part per machine core in order to speed up the numerical calculations. The data solution from the CFD simulations was first analysed in CFD-post ANSYS. Velocity and WSS data were extracted at the pore level in all the scaffolds and exported in Excel (Microsoft Office). The collected data were organized by scaffold layers using an in-house MATLAB (Natick, Massachusetts, The MathWorks Inc.) code. Once the data were organized according to scaffold locations, 3D contours of velocity and WSS values were plotted to characterize the fluid flow inside the scaffold at different layers (see Fig. 4.10). These 3D plots allow the comparison of the fluid flow conditions of all the scaffolds at the same location within the pore level (see Fig. 4.11). In addition, diagrams of frequency bars were plotted to see quantitatively the number of times a velocity or shear stress value is repeated in each scaffold at specific regions and compare these frequencies among scaffolds.

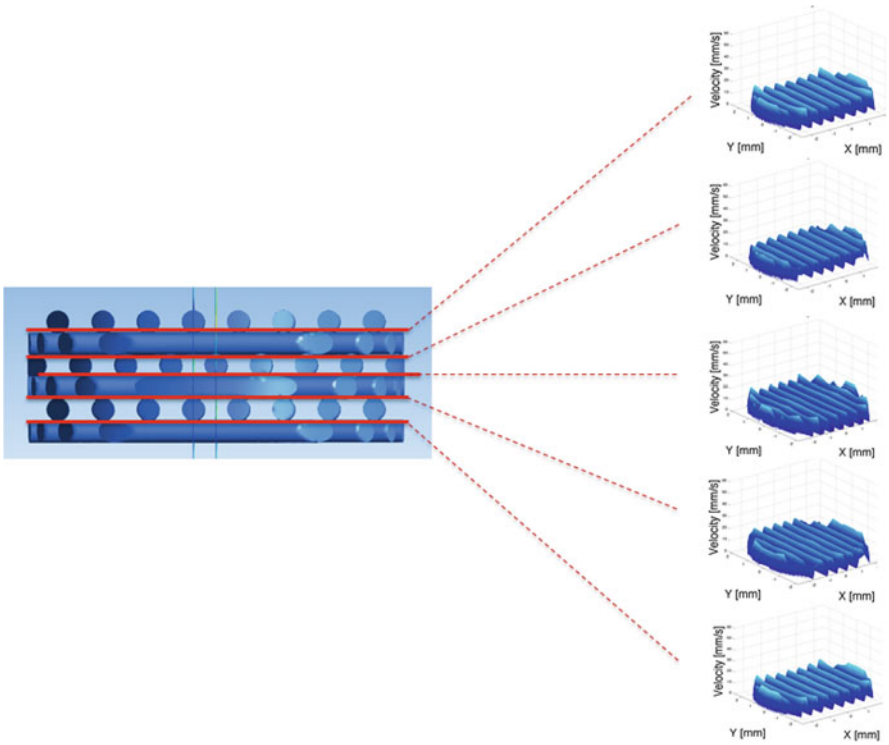

Fig. 4.11 Velocity profiles extracted from all scaffold levels

4.5 Repeatability Pre-analysis of Scaffold Inspection Model

Variability in the scaffold microstructure and the local fluid dynamics of the five samples due to the fabrication process is reported. However, the methodology developed to analyse the five samples may contribute to the variability calculated in this study. The analysis of the samples involved few steps from the μCT scanning up to the data collection in the CFD post-processing. Each step could be a source of error such as the filtering and segmentation of the μCT raw images or the extraction of velocity or WSS data from locations manually picked. Therefore, the same sample was analysed five times to assess the level of uncertainty that could be originated from the methodology proposed.

The same sample was reconstructed five times from scratch. It is noteworthy that the sample characterized five times is a different one from the five samples used in the intersample variability analysis. As a result, porosity, surface area and volume are $56 \pm 1.03\%$, 126.96 ± 0.34 mm^2 and 12.97 ± 0.3, respectively. There is less variability between the five analyses based on the same sample than in the structural analysis of the five reconstructed samples. The standard deviation of porosity, surface area and volume of the five analyses based on the same sample is much

Study	5 fabricated samples	5 analyses based on the same sample
Porosity [%]	45.4 ± 5.5	56 ± 1.03
Surface area [mm^2]	206.4 ± 12.54	126.96 ± 0.34
Volume [mm^3]	16.1 ± 1.32	12.97 ± 0.34

Fig. 4.12 Mean and standard deviation of the porosity [%], surface area [mm^2] and volume [mm^3] obtained from the intersample variability study and the sensitive analysis study performed in one sample

lower than for the five reconstructed samples (see Fig. 4.12). Therefore, the scaffold reconstruction process does not add noise to the scaffold variability analysis.

The velocity and WSS profiles calculated with CFD show a good agreement as seen in Figs. 4.13 and 4.14. However, statistical analyses only proved significant agreement between the five analyses in terms of fluid velocities, but no WSS. The sensitivity analysis shows that the main source of variability comes from the CFD-post-processing especially from the WSS measurements. These results identify the key aspects to be improved in the inspection protocol presented in order to design a consistent methodology able to report scaffold variability.

4.6 Local Shear Stress and Fluid Velocities Intersample Variability

The architecture of the five samples does not match with the CAD design as shown in the structural analysis. The local scaffold geometry is one of the factors that strongly determines the mechanical stimuli under fluid flow at the cell level. Therefore, in this study it was hypothesized that variations on the geometry of fabricated scaffolds due to the manufacturing process would alter the initial intended mechanical performance and thereby cell response. To investigate this, a computational methodology was developed to compare the fluid flow velocity and WSS values of the fabricated samples and the CAD design. An in vitro microfluidic scenario under laminar flow was represented in the CFD model since laminar conditions are the most suitable for bone tissue growth as demonstrated in literature (Mack et al. 2013; McCoy et al. 2012). The CFD solution supports this assumption as the local Reynolds number inside the scaffold pores is 10. The CFD study shows that the velocity and WSS profiles inside the CAD scaffold are regular and constant in all

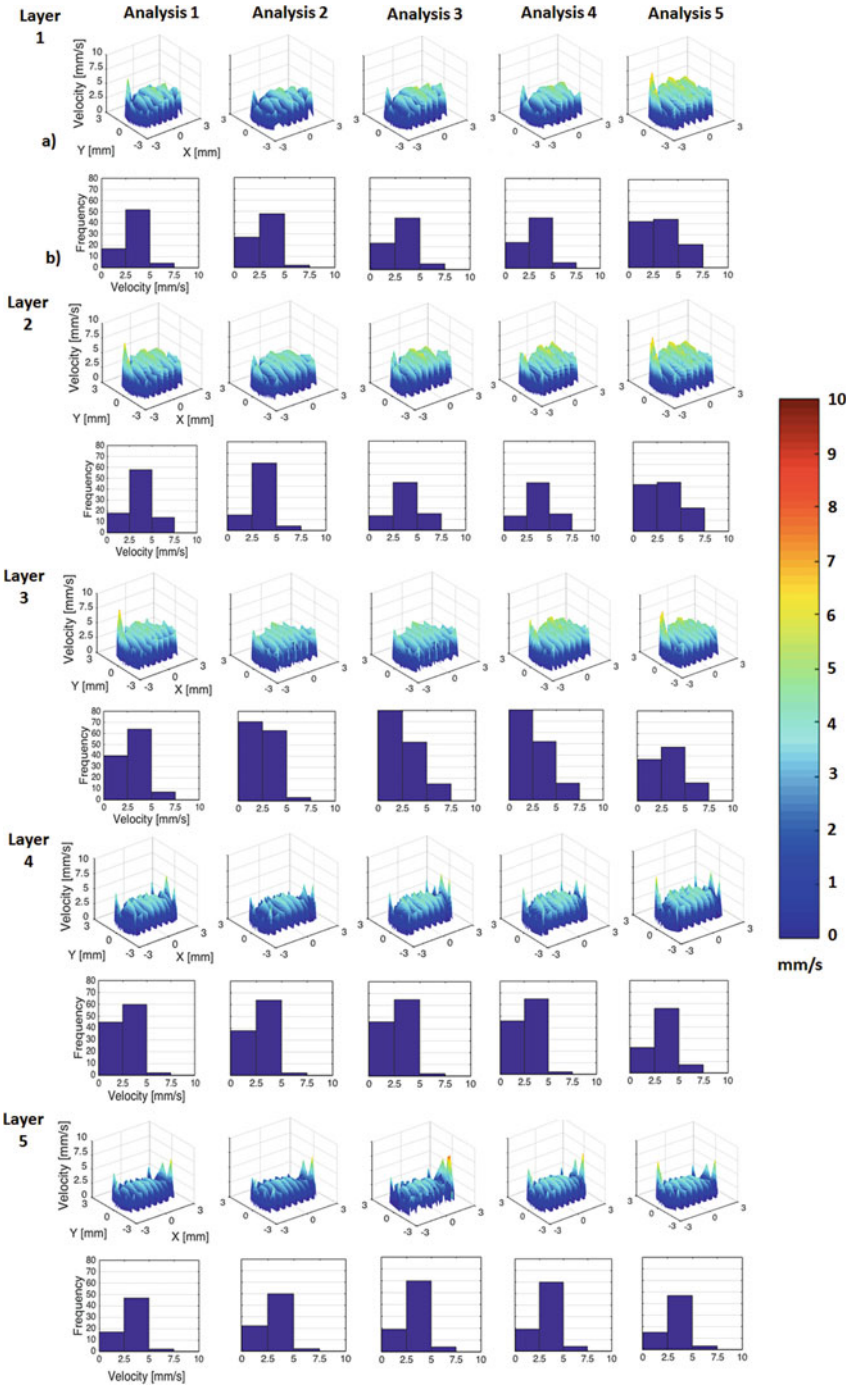

Fig. 4.13 (**a**) Velocity profiles and velocity frequency diagram bars (**b**) from the five analyses performed on the same reconstructed sample at all scaffold layers from layer 1 (top) to layer 5 (bottom)

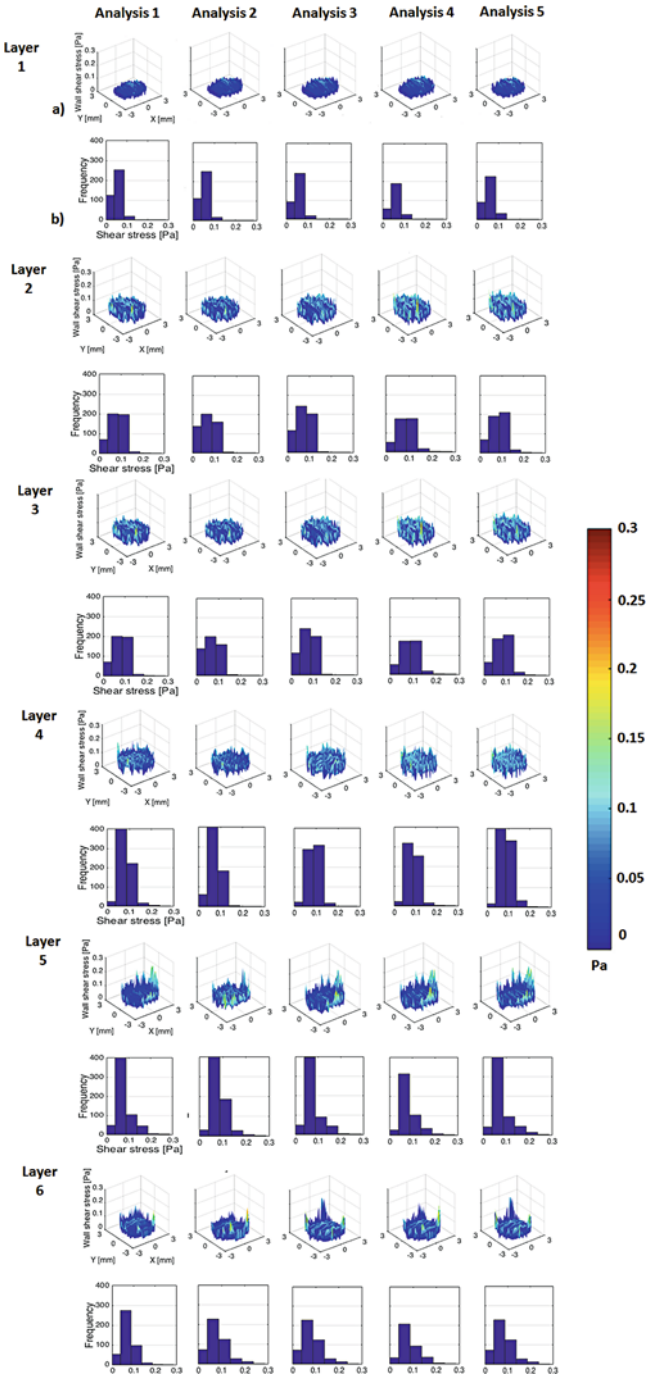

Fig. 4.14 (**a**) WSS profiles and velocity frequency diagram bars (**b**) from the five analyses performed on the same reconstructed sample at all scaffold layers from layer 1 (top) to layer 6 (bottom)

layers. As the pore size and pore distribution vary inside the five samples, they all present irregular velocity and WSS profiles which differ from the CAD profiles. Moreover, the calculated profiles of the five reconstructed scaffolds differ from layer-to-layer and also among samples. The fact that no similar patterns are found between samples highlights the lack of reproducibility in the fabrication process (see Figs. 4.15 and 4.16).

The consequence of side defects of the five samples due to the punching process can also be observed on the velocity and WSS profiles where higher values are found at the outer part in a random manner. The same cylinder dimensions were used to enclose all the μCT-reconstructed samples and the CAD scaffold. In the case of the CAD scaffold, the distance between the wall cylinder and the scaffold side was constant around the scaffold as it has a perfect circular profile. However, this does not occur to the five samples since the damage caused during punching at the scaffold periphery makes the cylinder-scaffold gap irregular, altering the velocity and WSS profiles. This variability at the scaffold-cylinder side is also found in in vitro experiments in the same manner. In cell culture studies, scaffold samples are fitted in commercial standard tubes with fixed diameter; however, they could present empty spaces between the wall of the tube and the scaffold due to irregularities in the scaffold geometry inducing the fluid flow passing by, instead of perfusing the scaffold pores.

μPIV data from an in vitro model would be necessary for the validation of the CFD simulations. However, the purpose of this study was to assess the variability in the local fluid dynamics due to scaffold geometry rather than predicting the physiological conditions. Thus, the exact same boundary conditions are applied regardless whether they are realistic or not to all scaffolds, ensuring that the only source of variability is the scaffold geometry which is the key aspect of this study. It is noteworthy to mention that the final geometry of μCT-based scaffolds could be affected by the partial-volume effect generated by the voxel size selected. Moreover, this effect becomes more significant for the adequate digital reconstruction of the scaffold substrate roughness that could potentially induce different cell response.

4.7 The Influence of Scaffold Microstructural Variability on the Mechanical Stimuli Sensed by Cells

It is unknown whether the variations found herein in terms of WSS would imply cell response variability. In the literature, there is no agreement yet on what range of shear stresses could alter cell behaviour. A multishear perfusion device was developed by Yu et al. (2014) to address this question permitting the analysis of cell constructs at different shear stress levels. It was found that the proliferation and differentiation as well as the expression of Runx2 of MCT3T3-E1 cells can be enhanced by applying low shear stresses ($1.5–52.6 \times 10^{-6}$ Pa). On the other hand, fluid-induced stresses over 4.12×10^{-4} Pa have contrary effects. Zhao et al. (2007)

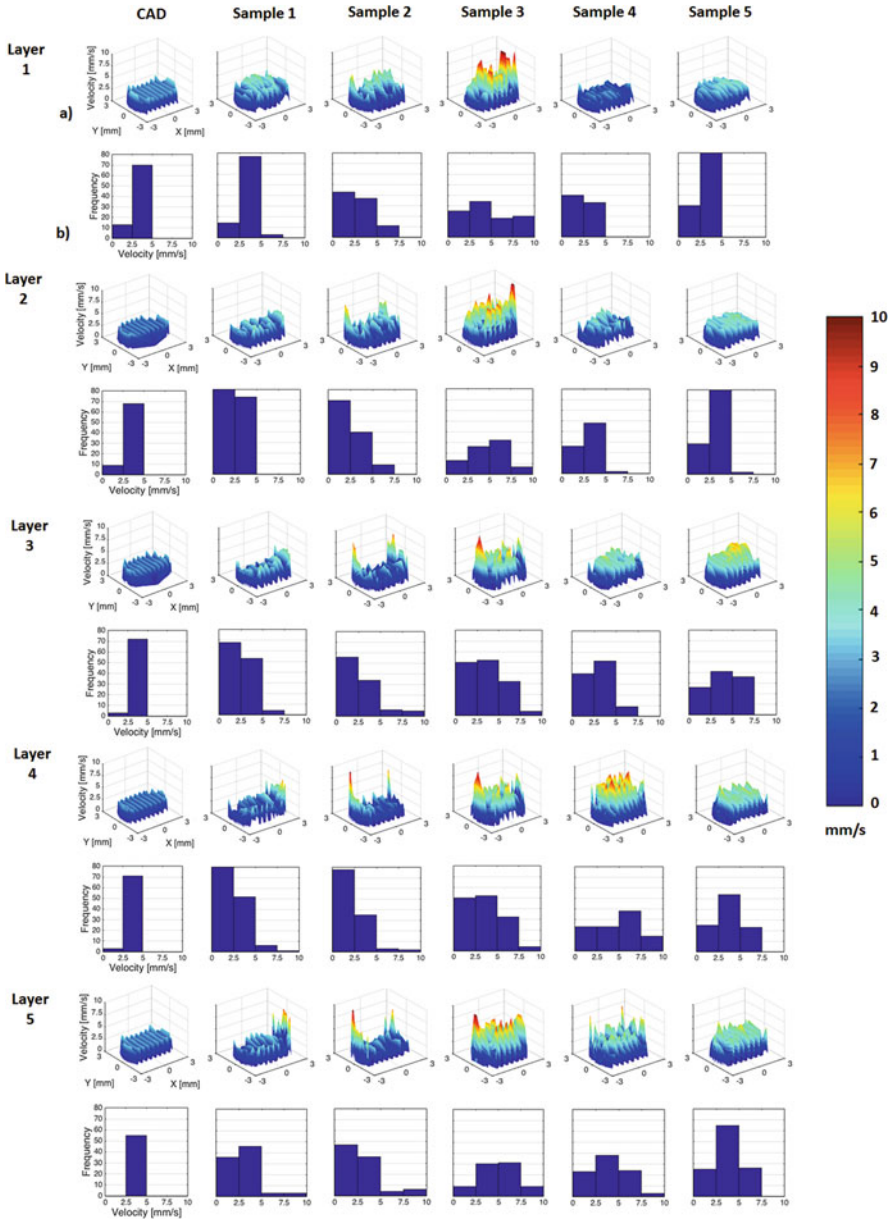

Fig. 4.15 (**a**) Velocity profiles and frequency diagram bars (**b**) of the CAD scaffold (left) and the five reconstructed samples (right) at all scaffold layers from layer 1 (top) to layer 5 (bottom)

investigated the effect of shear stresses ranging from 1×10^{-5}-1×10^{-4} Pa on 3D human mesenchymal stem cells (hMSCs) stating that lower shear values promote proliferation and higher values upregulate osteogenesis. Levels of shear stress within

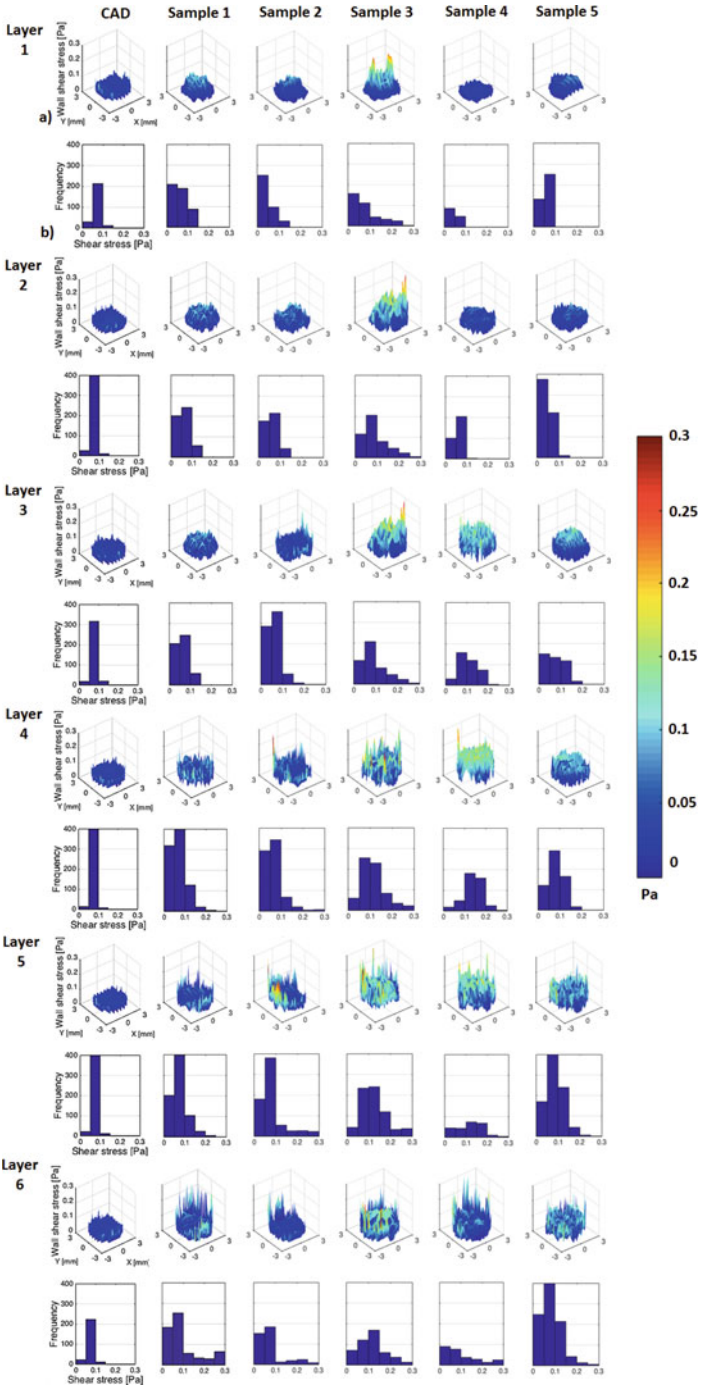

Fig. 4.16 (**a**) WSS profiles and frequency diagram bars (**b**) of the CAD scaffold (left) and the five reconstructed samples (right) at all scaffold layers from layer 1 (top) to layer 6 (bottom)

the same order of magnitude that the ones calculated in the CFD simulations of this study were imposed by Rotenberg et al. (2012) (static conditions up to 0.9 Pa) to human umbilical vein endothelial cells reporting shear-dependent expression levels of intercellular adhesion molecule-1 and the endothelial nitric oxide synthetase. Another study also investigated the effect of shear stress values within the same order of magnitude on the differentiation of MSCs into endothelial cells when subjected to 0.25 Pa, whereas under 1 Pa they showed high marker levels linked to smooth muscle cells (Kim et al. 2011). These studies suggest that the range of WSS variability reported in this chapter could induce changes in cell mechanoresponse. However, there is no clear understanding on how shear stress under fluid flow modifies the cell mechanoresponse. Moreover, the fact that cells hold intrinsic variability being able to respond differently under identical conditions makes more difficult to tackle this question.

The variability of local velocities can also influence cell outcome. Pore velocities affect the transport of nutrients and oxygen to the cells attached to the scaffold substrate. Therefore, in the case of irregular velocity profiles, not all the cells will be exposed to an adequate amount of solutes required to ensure their viability. In addition, cell seeding under heterogeneous velocity profiles can result in an irregular distribution of cells inside the scaffold, and those cells in direct contact with the fluid could induce variations in the local fluid flow.

Despite the potential of the methodology presented to evaluate the variability of the local mechanical stimuli due to imperfections in the scaffold geometry, this study lacks of experimental validation to determine the actual repercussion on cell activity. The use of the same five samples reconstructed with μCT images in in vitro experiments would be advantageous in order to relate the calculated shear stresses to cellular events throughout the entire scaffold structure. A first approach was followed by Jae et al. (2013) that measured the genetic markers of cells under the applied shear stress that was previously calculated with CFD being able to create a reference library of mechanical stimuli and cell phenotype.

4.8 Conclusions

Fabricated scaffolds could present variations from the intended-design purpose caused by limitations in the manufacturing process. In this chapter, current imaging techniques and in silico methods with great potential to inspect scaffolds are discussed. μCT scanning permits the digitalization of the actual shape of scaffolds for their structural characterization. Current available softwares are developing towards the automation of μCT-data reconstruction as well as the full shape characterization avoiding manual handling that could become a source of error. In addition, the inclusion of μCT-based scaffolds in CFD models allows the calculation of local fluid flow variables relating them to the actual scaffold geometry. In this study, a novel computational protocol to evaluate fabricated scaffolds in a systematic way was presented. A commercial RP scaffold was investigated by combining current

technology to analyse scaffold microstructure and its effect on the fluid dynamics. Five samples were analysed and significant variations from the initial design were quantified as well as variability from sample-to-sample. The inability of the fabrication process to replicate the scaffold design in a reproducible manner highlights the fact that fabricated scaffolds need to be analysed prior to any in vitro or clinical trial. The new proposed approach can be applied to any RP scaffold identifying any variation from the original design that could become a source of noise yielding to unexpected scaffold performance and tissue development. Furthermore, there is not a consensus yet in literature about the ranges of shear stress values that can induce different cell responses so any level of scaffold variability should not be underestimated as it could be detrimental for cell activity and tissue growth. Scaffold geometry can only be considered regular if there is not unexpected tissue development and tolerances of the fabrication process should be subjected to the final tissue properties. Moreover, inspection methods can serve as feedback for the fabrication method for further optimization.

References

Acosta Santamaría VA, Malvè M, Duizabo A, Mena Tobar A, Gallego Ferrer G, García Aznar JM, Doblaré M, Ochoa I (2013) Computational methodology to determine fluid related parameters of non regular three-dimensional scaffolds. Ann Biomed Eng 41:2367–2380

Cantini M, Fiore GB, Redaelli A, Soncini M (2009) Numerical fluid-dynamic optimization of microchannel-provided porous scaffolds for the co-culture of adherent and non-adherent cells. Tissue Eng Part A 15:615–623

Cioffi M, Boschetti F, Raimondi MT, Dubini G (2006) Modeling evaluation of the fluid-dynamic microenvironment in tissue-engineered constructs: a micro-CT based model. Biotechnol Bioeng 93:500–510

Costa PF, Martins A, Neves NM, Gomes M, Reis RL (2014) Automating the processing steps for obtaining bone tissue engineered substitutes: from imaging tools to bioreactors. Tissue Eng Part B Rev 20:567–577

Dias MR, Guedes JM, Flanagan CL, Hollister SJ, Fernandes PR (2014) Optimization of scaffold design for bone tissue engineering: a computational and experimental study. Med Eng Phys 36:448–457

Domingos M, Chiellini F, Gloria A, Ambrosio L, Bartolo P, Chiellini E (2012) Effect of process parameters on the morphological and mechanical properties of 3D bioextruded poly(-ε-caprolactone) scaffolds. Rapid Prototyp J 18:56–67

Gautam S, Dinda AK, Mishra NC (2013) Fabrication and characterization of PCL/gelatin composite nanofibrous scaffold for tissue engineering applications by electrospinning method. Mater Sci Eng C 33:1228–1235

Hollister SJ (2005) Porous scaffold design for tissue engineering. Nat Mater 4:518–524

Hoque ME, Hutmacher DW, Feng W, Li S, Huang MH, Vert M, Wong YS (2005) Fabrication using a rapid prototyping system and in vitro characterization of PEG-PCL-PLA scaffolds for tissue engineering. J Biomater Sci Polym Ed 16:1595–1610

Jae M, Dean D, Knothe ML (2013) Biomaterials mechanical modulation of nascent stem cell lineage commitment in tissue engineering scaffolds. Biomaterials 34:5766–5775

Jamalpoor Z, Mirzadeh H, Joghataei MT, Zeini D, Bagheri-Khoulenjani S, Nourani MR (2015) Fabrication of cancellous biomimetic chitosan-based nanocomposite scaffolds applying a combinational method for bone tissue engineering. J Biomed Mater Res Part A 103:1882–1892

Kim DH, Heo S-J, Kim S-H, Shin JW, Park SH, Shin J-W (2011) Shear stress magnitude is critical in regulating the differentiation of mesenchymal stem cells even with endothelial growth medium. Biotechnol Lett 33:2351–2359

Mack JJ, Youssef K, Noel ODV, Lake MP, Wu A, Iruela-Arispe ML, Bouchard L-S (2013) Real-time maps of fluid flow fields in porous biomaterials. Biomaterials 34:1980–1986

Mather ML, Morgan SP, White LJ, Tai H, Kockenberger W, Howdle SM, Shakesheff KM, Crowe J a (2008) Image-based characterization of foamed polymeric tissue scaffolds. Biomed Mater 3 (1):015011

McCoy RJ, Jungreuthmayer C, O'Brien FJ (2012) Influence of flow rate and scaffold pore size on cell behavior during mechanical stimulation in a flow perfusion bioreactor. Biotechnol Bioeng 109:1583–1594

Melchels FPW, Bertoldi K, Gabbrielli R, Velders AH, Feijen J, Grijpma DW (2010) Mathematically defined tissue engineering scaffold architectures prepared by stereolithography. Biomaterials 31:6909–6916

Olivares AL, Lacroix D (2013) In: Geris L (ed) Computational modeling in tissue engineering. Springer, Berlin, pp 107–126

Park SH, Park DS, Shin JW, Kang YG, Kim HK, Yoon TR, Shin J-W (2012) Scaffolds for bone tissue engineering fabricated from two different materials by the rapid prototyping technique: PCL versus PLGA. J Mater Sci Mater Med 23:2671–2678

Podichetty JT, Bhaskar PR, Khalf A, Madihally SV (2014) Modeling pressure drop using generalized scaffold characteristics in an axial-flow bioreactor for soft tissue regeneration. Ann Biomed Eng 42:1319–1330

Podshivalov L, Gomes CM, Zocca A, Guenster J, Bar-Yoseph P, Fischer A (2013) Design, analysis and additive manufacturing of porous structures for biocompatible micro-scale scaffolds. Procedia CIRP 5:247–252

Porter B, Zauel R, Stockman H, Guldberg R, Fyhrie D (2005) 3-D computational modeling of media flow through scaffolds in a perfusion bioreactor. J Biomech 38:543–549

Rotenberg MY, Ruvinov E, Armoza A, Cohen S (2012) A multi-shear perfusion bioreactor for investigating shear stress effects in endothelial cell constructs. Lab Chip 12:2696–2703

Ryan G, McGarry P, Pandit A, Apatsidis D (2009) Analysis of the mechanical behavior of a titanium scaffold with a repeating unit-cell substructure. J Biomed Mater Res B Appl Biomater 90:894–906

Sandino C, Lacroix D (2011) A dynamical study of the mechanical stimuli and tissue differentiation within a CaP scaffold based on micro-CT finite element models. Biomech Model Mechanobiol 10:565–576

Serra T, Planell JA, Navarro M (2013) High-resolution PLA-based composite scaffolds via 3-D printing technology. Acta Biomater 9:5521–5530

Truscello S, Kerckhofs G, Van Bael S, Pyka G, Schrooten J, Van Oosterwyck H (2012) Prediction of permeability of regular scaffolds for skeletal tissue engineering: a combined computational and experimental study. Acta Biomater 8:1648–1658

Van Bael S, Kerckhofs G, Moesen M, Pyka G, Schrooten J, Kruth JP (2011) Micro-CT-based improvement of geometrical and mechanical controllability of selective laser melted Ti6Al4V porous structures. Mater Sci Eng A 528:7423–7431

Xu H, Dong J, Chai G, Yu Z, Lang W (2010) Rapid prototyped PGA / PLA scaffolds in the reconstruction of mandibular condyle bone defects. The international journal of medical robotics and computer assisted surgery 6:66–72

Yeong W-Y, Chua C-K, Leong K-F, Chandrasekaran M (2004) Rapid prototyping in tissue engineering: challenges and potential. Trends Biotechnol 22:643–652

Yu W, Qu H, Hu G, Zhang Q, Song K, Guan H, Liu T, Qin J (2014) A microfluidic-based multi-shear device for investigating the effects of low fluid-induced stresses on osteoblasts. PLoS One 9:e89966

Zermatten E, Vetsch JR, Ruffoni D, Hofmann S, Müller R, Steinfeld A (2014) Micro-computed tomography based computational fluid dynamics for the determination of shear stresses in scaffolds within a perfusion bioreactor. Ann Biomed Eng 42:1085–1094

Zhao F, Chella R, Ma T (2007) Effects of shear stress on 3-D human mesenchymal stem cell construct development in a perfusion bioreactor system: experiments and hydrodynamic modeling. Biotechnol Bioeng 96:584–595

Chapter 5
Computational Simulation of Cell Seeding in a Tissue Engineering Scaffold

Perfusion systems can help to drive cells to scaffold substrate with regular distribution and high efficiency. However, it is difficult to predict experimentally which are the best bioreactor conditions for such outcomes. In this chapter, a CFD model is developed to predict the local fluid flow conditions inside the scaffold, and a discrete phase representing the cells is included to describe cell motion near the scaffold substrate. The computational model is developed in combination with particle tracking experiments performed inside a 3D scaffold in order to configure and validate the model with well-characterized experimental data. The study showed that the computational model can describe the velocity profiles inside the scaffold as well as cell path. It was found that cells mainly follow the fluid streamlines passing throughout all scaffold pores. High permeability in scaffolds is beneficial to distribute cells; however, it does not guarantee the deposition of cells on the scaffold substrate and cell adhesion. The presented CFD model can help to design and optimize perfusion systems to reach the desired cell distribution and density which will affect the final tissue properties.

5.1 Introduction

Tissue growth and functionality in 3D scaffolds are strongly related to the initial spatial distribution and density of cells (Braccini et al. 2005). Furthermore, maximum cell seeding efficiency is essential since donor cells are limited, and sufficient cell density in the scaffold unit is required to promote ECM formation and cell proliferation (Saini and Wick 2003).

Traditional static methods for cell seeding such as manual pipetting, where gravity-driven cell deposition occurs, generally result in irregular cell density with higher number of cells on the outer part. In addition, there is a lack of cell viability since nutrients and oxygen do not always reach the centre of the 3D structure (Xiao

This chapter forms part the PhD thesis of Ana Campos available here: http://etheses.whiterose.ac.uk/12349/

© Springer Nature Singapore Pte Ltd. 2019

D. Lacroix et al., *Multiscale Mechanobiology in Tissue Engineering*,
Frontiers of Biomechanics 3, https://doi.org/10.1007/978-981-10-8075-3_5

et al. 1999). As an alternative, different dynamic flow strategies have been presented such as spinner flasks (Vunjak-Novakovic et al. 1998), wavy-walled bioreactors (Bueno et al. 2005), rotating vessels (Nishi et al. 2013), compression force-induced suction techniques (Poly et al. 2006) and perfusion systems (Sonnaert et al. 2014). Among all these hydrodynamic-based strategies, perfusion seems the most promising solution for cell seeding since it enhances cell transfer inside the scaffold in comparison with the other approaches (Wendt et al. 2003; Xiao et al. 1999).

Many researchers have used computational fluid dynamics (CFD) techniques to optimize perfusion bioreactor's design in order to find the most suitable hydrodynamic conditions for the generation of engineered tissues while avoiding expensive and time-consuming trial and error experiments. For instance, Hidalgo-Bastida et al. (2012) presented a CFD model to study the effect of the chamber geometry on the flow profile inside the scaffold by comparing a circular and a rectangular bioreactor system. Also Papantoniou et al. (2014) used CFD simulations to show the impact of scaffold location inside the bioreactor and flow rate. However, CFD studies have mainly focused on cell culture conditions of idealized pre-seeded scaffolds, and little has been explored about the effect of the local fluid dynamics on deposition of cells on scaffold substrate and its impact on scaffold cell seeding. Melchels et al. (2011) showed the influence of scaffold pore size on the local shear rate and its effect on cell adhesion by stating that the gradient of fluid velocities will determine the velocity of the suspended cells passing near the scaffold substrate and therefore the number of cells passing by per unit of time.

However, the fact that cells penetrate in all scaffold regions during perfusion does not necessarily imply cell deposition on scaffold substrate. Cell deposition from suspension flow is a complex mechanism that is not well understood yet; it involves inertial impaction, interception, sedimentation and London-van der Waals forces (Li et al. 2001). Perfusion methods should be further optimized and developed to pursuit cell-scaffold substrate interception, so chemical signalling and cell adhesion may occur. Other studies have modelled the transport of cells in fluid flow by developing multiphase CFD models such as Adebiyi et al. (2011) who were able to quantify the relationship between initial vacuum pressure in their seeding system with the final cell seeding efficiency or the analysis of Olivares and Lacroix (2012) where the kinetics of cell seeding over time was determined as well as the final position of cells on the scaffold, so the initial conditions for tissue development could be established.

The aim of this study was to develop a multiphase-based CFD model able to predict how perfusion bioreactor conditions modulate the local fluid dynamics and cell deposition on scaffold substrate. Despite the potential of CFD, some studies have claimed the importance of complementing computational models with well-characterized experimental data such as micro-particle image velocimetry (μPIV) to optimize and make them more reliable (De Boodt et al. 2010). Thus, the CFD model was developed in combination with μPIV and particle tracking velocimetry (PTV) experiments using a commercial 3D regular scaffold. The goal of the experiments was to quantify the fluid flow and cell motion at the pore level inside the scaffold. The experimental data from the actual 3D scaffold was used to build the presented

CFD model that holds great potential to optimize cell seeding hydrodynamic-based systems in order to achieve maximum efficiency.

5.2 Investigation of Cell Seeding Under Perfusion Inside 3D Scaffolds Using μPIV and PTV Methods

5.2.1 Measurement of the Local Fluid Flow Properties Inside 3D Porous Scaffolds

The flow environment inside 3D porous scaffolds modulates key aspects of in vitro tissue growth such as the transport of cells to scaffold substrate during seeding or the fluid shear stress exerted on cells that affects cell response. Therefore, the acquisition of the spatial fluid flow conditions inside scaffolds is essential to understand the fluid-induced cell behaviour and control tissue development. μPIV has been widely used to quantify local fluid velocities and derived properties in microflows. Conventional μPIV consists of illuminating with a pulsed laser the fluid flow that contains tracer particles and capturing the reflected light with a high-speed camera in double-frame images under a specific time step. Then, flow vector maps are generated by PIV cross-correlation methods. μPIV is a method that needs optical access to the region of interest inside the scaffold; however, most of tissue engineering scaffolds are made of non-transparent materials. Despite this barrier, different approaches have been followed to extract representative fluid flow data from 3D scaffolds. For instance, Jae et al. (2013) used the μPIV to calculate the shear stress and its effect on cell differentiation on transverse and axial scaffold sections exemplifying the main architectural features of the 3D scaffold (see Fig. 5.1a). It is noteworthy to mention that classical μPIV only permits 2D measurement, and yet 3D flow environments are found inside scaffolds. Furthermore, it has been shown that the shear stress values to which cells respond can differ significantly from 2D to 3D environments (McCoy and O'Brien 2010). For this reason, De Boodt et al. (2010) claimed that μPIV experiments cannot be performed on 2D substrates, and they introduced the 2D+ concept by using a unit cell of a 3D RP scaffold as shown in Fig. 5.1b where in-plane velocities could be measured. A similar strategy was followed by Provin et al. (2008) investigating with μPIV a microstructure compounded by a pillar bundle in a parallel plate chamber to find the best scaffold geometrical design to achieve a trade-off between high supply of medium for cells and low shear stress values.

3D velocities can be derived from other optical techniques such as the stereoscopic PIV (Fouras et al. 2007) by using more than one capturing system in a stereoscopic arrangement. However, this leads to optical access constraints when investigating 3D scaffolds. Nevertheless, this method was successfully applied to calculate the fluid dynamics around a 3D scaffold in a stirring bioreactor where the effect of the bioreactor rotation rate was related to mixing properties (Fouras et al.

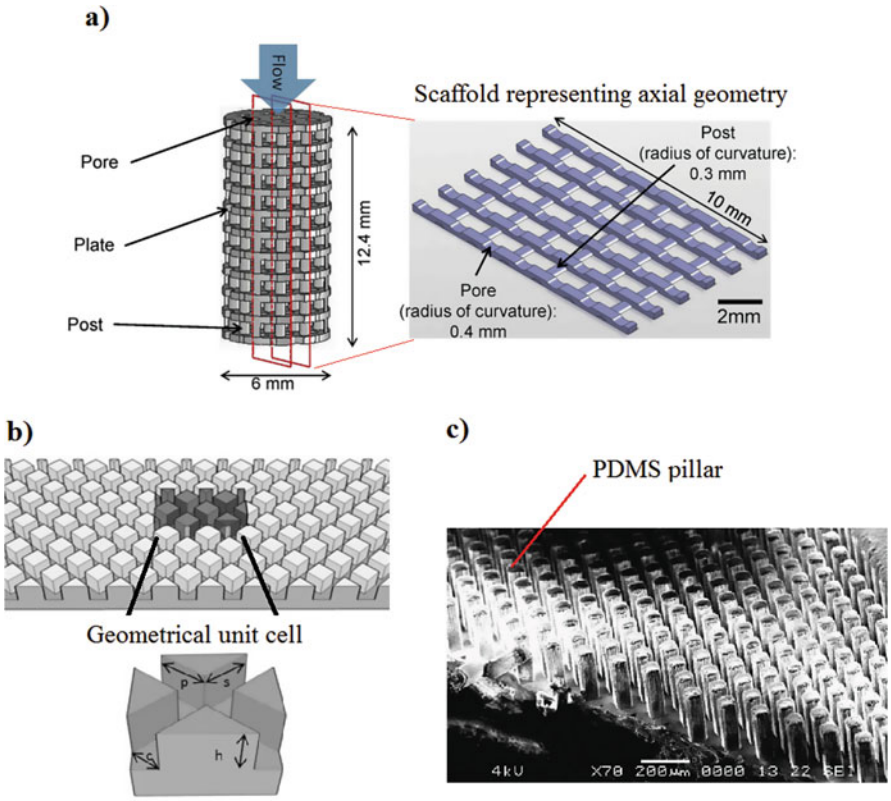

Fig. 5.1 (**a**) Transverse axial section representing the main architectural features of the 3D scaffold used by Jae et al. (2013) in μPIV experiments. (**b**) Unit cell of a 3D scaffold designed by De Boodt et al. (2010) to introduce the +2D μPIV concept. (**c**) Pillar bundle in a parallel plate chamber investigated by Provin et al. (2008) to find the optimal scaffold pore size for medium supply and local shear stress (Figure adapted from Jae et al. 2013; De Boodt et al. 2010; Provin et al. 2008) (Reprinted by permission of Elsevier and Mary Ann Liebert, Inc Publisher)

2009). Other promising methods such as the defocusing method can also detect 3D particles displacements although to the author's knowledge it has not been applied yet to investigate tissue engineering scaffolds. It consists of an aperture located on the objective lens that contains three pinholes forming an equilateral triangle. The light from the particle passes the aperture and then reaches three different positions at the image plane. Then, the particle position with respect to the focus plane is determined by measuring the distance between the projected triangle vertices (Lima et al. 2006). It is noteworthy to mention that nuclear magnetic resonance can measure 3D flows inside opaque materials as shown by Mack et al. (2013) who captured the local hydrodynamics inside a 3D porous scaffolds made of polycaprolactone (PCL). However, 1 mm^3 of spatial resolution was not enough to calculate the local mechanical stimuli at the pore level.

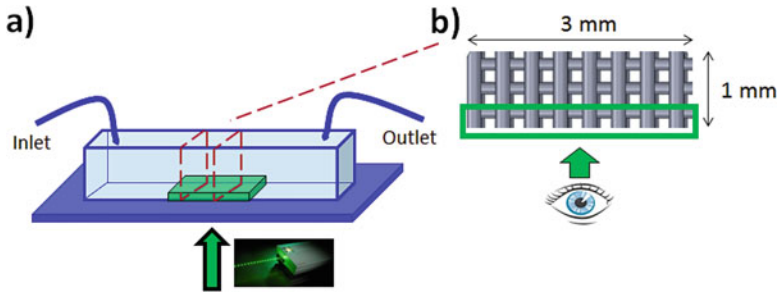

Fig. 5.2 (**a**) Microfluidic chamber made of PDMS mounted on the microscope stage. The trimmed scaffold (**b**) was placed inside the rectangular channel to allow optical access to the μPIV system

In this section, the aim is to quantify the fluid velocities inside a 3D porous scaffold made of PCL (described in Chap. 4) under perfusion to evaluate the initial mass transport properties for scaffold cell seeding.

5.2.1.1 Microfluidic Circuit

For the μPIV experiments, the cylindrical scaffold used in this study was trimmed and located inside a microchannel with rectangular profile to allow the access of the μPIV system inside the scaffold and therefore quantify the flow field in the vicinity of the scaffold fibres. The depth of field of the μPIV system permitted to focus the working plane within the first layer of pores that consisted of series of vertical and horizontal fibres arranged in 3D (see Fig. 5.2). The micro-chamber was made of PDMS with the following dimensions: $3 \times 1 \times 40$ mm^3. The chamber was mounted on a surface glass by plasma-activated bounding. A machined mould made of poly (methyl methacrylate) was utilized to build the chambers, thereby ensuring reproducibility among experimental trials. One micrometre diameter polystyrene fluorescent particles (orange, 540/560) were diluted in deionized water with a concentration of $2{\cdot}10^8$ beads/ml. A syringe pump was connected at the inlet of the chamber to infuse the working fluid with a constant flow rate of 18 μl/min corresponding with 0.1 mm/s at the scaffold entrance. The outlet of the chamber was connected to a tube that drove the fluid towards a reservoir.

5.2.1.2 μPIV Experimental Procedure

The microfluidic chamber was placed on top of an inverted Olympus IX71 microscope stage with 10× optics magnification. A synchronized laser (Nd:YAG 532) was used to excite the tracer particles at two time points with an interval of 10,000 μs. The emitted light from the particles was recorded by a camera (Power View 4 M, 2048×2048 pixels) in double-frame images. Then, the images were gridded in interrogation regions of 64×64 pixels. The field of view was

0.94×0.94 mm^2, and the regions investigated were in the vicinity of the fibres in order to understand the effect of the local fluid dynamics on cell-surface deposition. The noise background was subtracted from raw images, and the resulting images were processed with a Gaussian filter. Velocity vector maps were calculated by using 25% overlap with the recursive Gaussian algorithm of insight 3G (TSI Incorporated, Minneapolis, USA). The calculated velocity fields were analysed in Tecplot.

The presence of the out-of-plane particles in the captured images can bias the cross-correlation process to obtain fluid velocities. The depth of correlation (DOC) defines the thickness of the illuminated volume over which particles contribute to the correlation process. This parameter mainly depends on the optics system and the size of the particles. The depth of correlation (DOC) herein is –25 μm which was calculated using Eq. 5.1 proposed by Olsen and Adrian (2000):

$$\mathrm{DOC} = 2\left[\frac{1-\sqrt{\varepsilon}}{\sqrt{\varepsilon}}\left(f^{\#^2}d_p^2 + \frac{5.95(M+1)^2\lambda^2 f^{\#4}}{M^2}\right)\right]^{1/2} \tag{5.1}$$

where magnification, M, $= 10$; wavelength of the light emitted by the particles, λ, $= 0.532$ μm; diameter of the particles, d_p, $= 10$ μm; threshold value to determine the contribution of a particle to the measured velocity, ε, $= 0.01$; and focal number, $f^{\#}$, is calculated by Meinhart and Wereley (2003):

$$\mathbf{f^{\#}} = \frac{1}{2}\left[\left(\frac{\mathbf{n_o}}{\mathbf{NA}}\right)^2 - 1\right]^{1/2} \tag{5.2}$$

where $\mathbf{n_o}$, refractive index, $= 1$ and numerical aperture, $\mathbf{NA}$, $= 0.3$.

As the depth of the pore was around 300 μm, the effect of calculated DOC on the velocity measurements was considered negligible.

A preliminary study in a simple scenario was carried out to determine the accuracy of the system by comparing the μPIV measured velocities of a laminar flow inside the rectangular channel without scaffold with the analytical and CFD solutions.

The maximum velocity of a laminar flow inside a rectangular duct is not exactly double the average velocity as in circular pipes. For this reason, Martinelli and Viktorov (2009) presented the formula seen in Eq. 5.3, where h and w are the height and width, respectively, to calculate the ratio of maximum velocity to average velocity as a function of the channel aspect ratio (h/w) for incompressible flows:

$$\mathbf{v}^* = \frac{\mathbf{v}_{\max}}{\mathbf{v}_{\mathbf{average}}} = -0.56\left(\frac{\mathbf{h}}{\mathbf{w}}\right)^2 + 1.15\left(\frac{\mathbf{h}}{\mathbf{w}}\right) + 1.5 \tag{5.3}$$

The average inlet velocity is 1 mm/s for this test and the channel aspect ratio is 1/3; therefore, the expected maximum velocity at 1.5 mm distance from the lateral

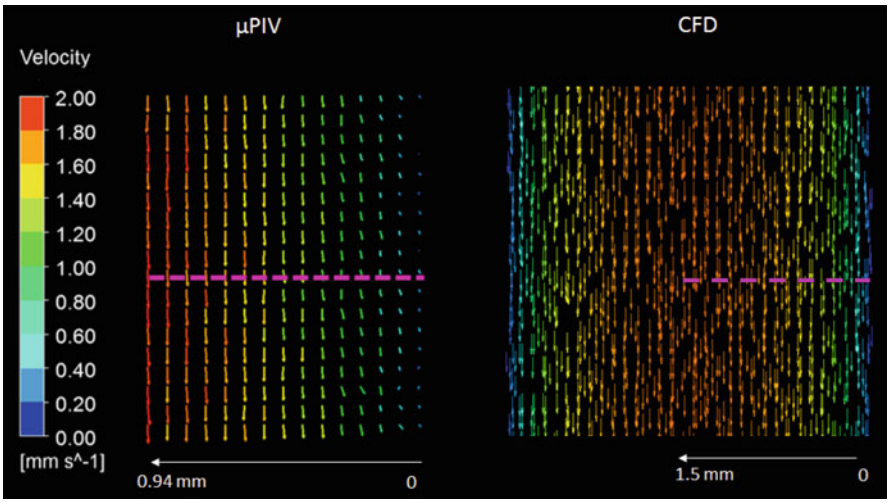

Fig. 5.3 Velocity vectors from a plane located in the middle of the rectangular channel calculated using µPIV (left) and CFD (right) methods. The pink dotted lines show from where the velocity values were extracted to compare both techniques numerically

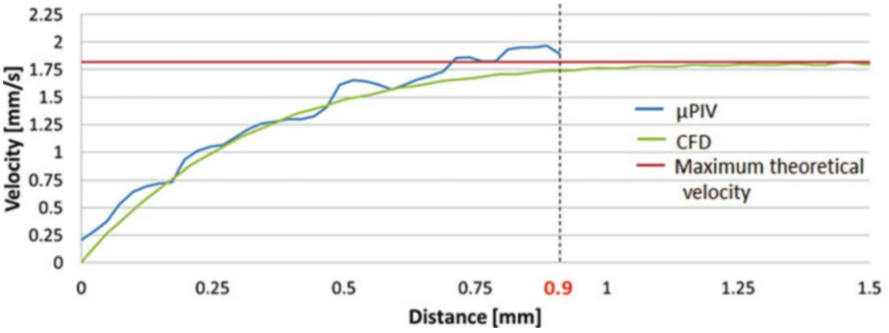

Fig. 5.4 The blue line and green lines represent the velocity values extracted from the profiles shown in Fig. 5.3 for the µPIV and CFD tools, respectively. The red line is the maximum fluid velocity calculated analytically that can be reached inside the rectangular channel

channel wall, corresponding to the centre of the channel, should be 1.82 mm/s. The CFD calculates a maximum velocity of 1.83 mm/s at the centre of the channel, so it agrees well with the analytical value calculated using the formula in Eq. 5.3. In the case of µPIV, the velocity extracted from the pink line in Fig. 5.3 reaches 1.89 mm/s at 0.9 mm distance from the channel wall, as seen in Fig. 5.4, whereas the CFD value at that location is 1.73 mm/s. Assuming that the CFD can predict with accuracy the fluid flow velocities, the expected error from the µPIV to calculate fluid velocities is –10% for the specific experimental scenario implemented in this study.

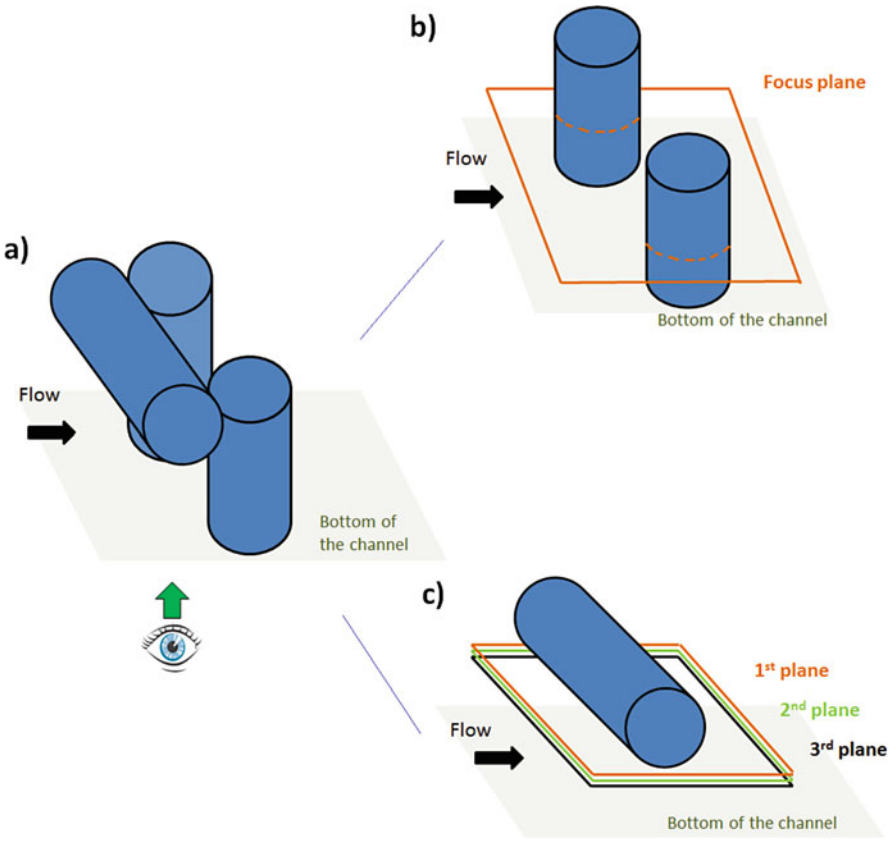

Fig. 5.5 (**a**) Representation of a scaffold pore where the flow field is analysed. (**b**) Region observed within the pore in order to assess the fluid flow passing between the two vertical fibres. (**c**) Three planes observed underneath the horizontal fibre within the scaffold pore

5.2.1.3 Scaffold Velocity Profiles Measured with μPIV

Two regions of interest were considered to characterize the fluid flow inside the scaffold pores. The fluid flow passing between the vertical fibres was observed as well as the fluid flow underneath the horizontal fibre as shown in Fig. 5.5.

Despite the 3D configuration of the observed pores and thereby the expected 3D tracer particles displacements, the velocity of the fluid flow mainly had in-plane component since the observed region was sufficiently close to the flat surface at the bottom of the channel which induces the local fluid flow to be parallel to this surface and to the working focus plane. Thus, the conventional μPIV system used in this study that only can measure 2D particles displacements could serve to analyse the fluid flow velocities inside the 3D pores of the selected scaffold.

The velocities of the fluid flow passing between the vertical fibres (Fig. 5.5b) show maximum values at the centre of the pore, and they decrease towards the wall

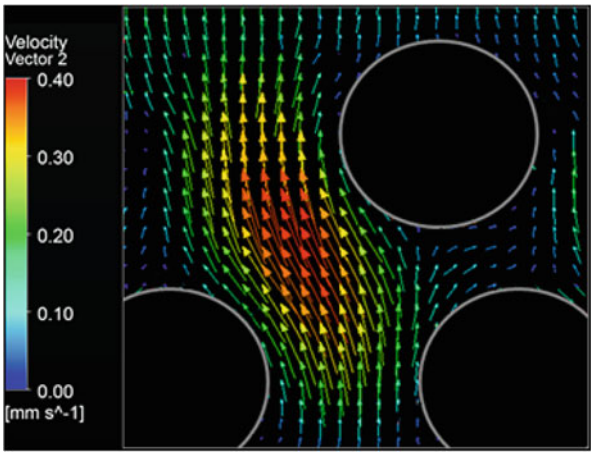

Fig. 5.6 Velocity map between vertical fibres calculated with μPIV

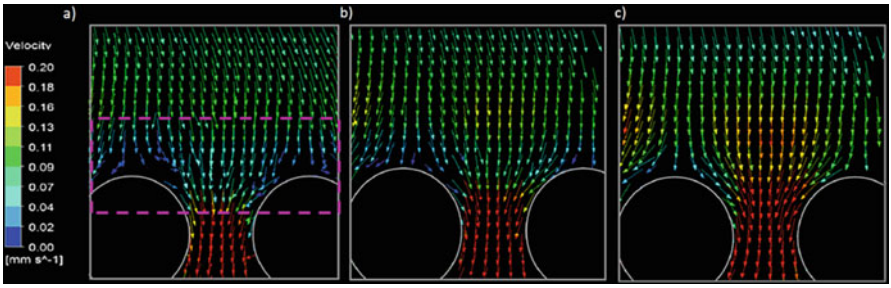

Fig. 5.7 Velocity vectors from the first (**a**), second (**b**) and third (**c**) planes underneath the horizontal fibres calculated with μPIV

of the fibres (see Fig. 5.6). On the other hand, three different working planes were set to investigate the velocity gradients when moving away from the horizontal fibre. The measured velocities increase as the distance of the focus plane to the fibre increases; the nonslip wall effect from the horizontal fibre is reduced, and the velocity maps are close to the expected continuity as the fluid velocity has to increase if it is forced to flow through a smaller area that, in this case, corresponds with the pore formed by the two vertical fibres (see Fig. 5.7).

5.2.2 Cell Tracking During Scaffold Seeding

PTV methods have been applied to study cell motion in physiological fluids such as blood flow. These methods follow a similar principle to the μPIV, but instead cells are tracked individually in a Lagrangian manner. Lima et al. (2009) used PTV in combination with confocal microscopy to analyse the dynamic flow behaviour of red

blood cells (RBCs) in different channel depths. They applied optical sectioning reporting the increase of lateral displacement of cells when moving away from the plane at the centre of the microtube. Sugii et al. (2005) investigated blood flow in a multiphase flow approach by using two sets of colour filters to obtain separate images of fluorescent-labelled RBCs and tracer particles that follow the plasma flow to explore blood rheology in microcirculation. Oshima and Oishi (2014) followed a similar approach although to obtain the motion of RBCs the cell membrane was marked by attaching electrically 0.2 μm fluorescent particles on the surface. In this way, the deformation and the movement of the cells could be captured as well as the velocity distribution of the corresponding surrounding flow.

To the author's knowledge, PTV methods have not been yet utilized to study cell motion in suspension during scaffold cell seeding under fluid flow. In this study, the aim is to extrapolate PTV techniques into in vitro cell seeding experiments in order to understand the complex mechanisms that can be involved in cell deposition from suspended flow on scaffold substrate.

MG63 cells were cultured in T-flasks under standard culturing conditions at 37 °C and 5% CO_2 in an atmosphere of 99% humidity. The culture medium was compounded by DMEM (Dulbecco's Modified Eagle Medium, Sigma D5671) supplemented with 1 mM sodium pyruvate, 10 mM HEPES buffer, 100 U/mL penicillin, 0.1 mg/mL streptomycin, 2 mM glutamine and 10% FBS (foetal bovine serum). The media was refreshed every 48 h, and when confluency was reached, cells were trypsinized prior to the experiment. Cells were labelled with orange CMTMR fluorescent dye (Life Technologies) using 10 μM concentration in serum-free medium. Cells were incubated for 45 min. Then cells were centrifuged to remove the cell tracker working solution. Labelled cells were resuspended in culture media before the experiments. The final cell concentration for each experimental trial was 1.10^6 cells/mL.

A time-dependent flow pattern using a programmable syringe pump (NE-500, New Era Pump Systems, Farmingdale, NY, US) was selected. At the beginning a 300 μl/min flow rate was selected to carry cells to the scaffold to avoid cell sedimentation in the channel. Then, the flow rate was changed from 90 to 50 μl/min every 0.125 s so that cells could be tracked by the camera while avoiding sedimentation. Single laser pulses were synchronized with the camera to capture the reflected light from the labelled cells in suspension in single-frame images with a frequency of 14.5 Hz. The same optical parameters from the μPIV experiments were applied for the PTV tests although the fact that cells are ten times bigger than the tracer particles increases the DOC to ~50 μm.

Recorded images were imported to ImageJ where manual tracking was carried out using the plugin MJTrack based on the bright centroid criteria. It is noteworthy to refer to other studies where automatic tracking methods were developed such as Pinho et al. (2013) that proposed a method able to compute multiple trajectories in a time effective manner while providing measurements with no significant difference with the manual tracking used herein. Nevertheless, the development of automatic tracking algorithms was out of the scope of this study, and MTrackJ was considered accurate enough to track labelled cells.

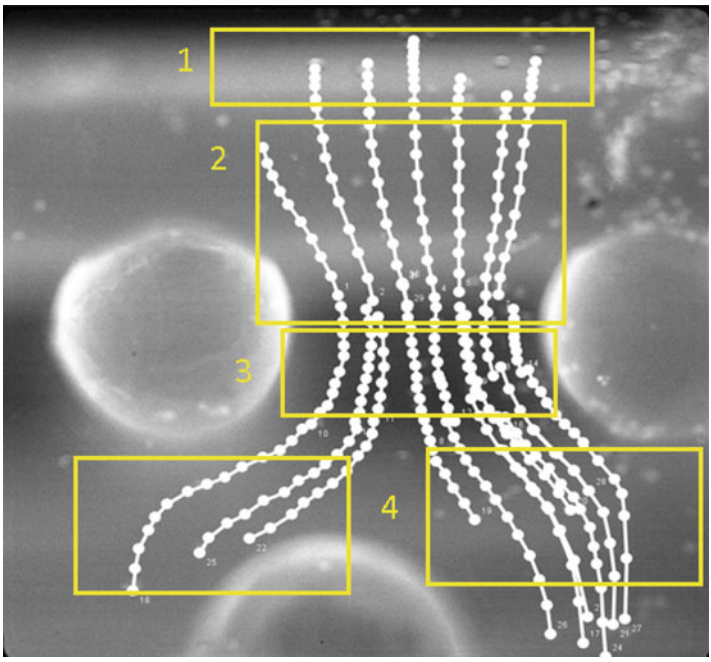

Fig. 5.8 (1) Cells approach to the horizontal fibre. (2) Cells travel towards the centre of the pore in the middle of the two vertical fibres. (3) Cells are in the centre of the pore and start deviating either towards the next left or right pore (4)

No cell adhesion on scaffold surface was observed in the experiments as shown in Fig. 5.8. Cells mainly followed the fluid streamlines showing that the main driving force on cell motion is the fluid drag force that overcomes other possible physical factors such as van der Waals forces, Brownian motion or electrostatics. It is noteworthy that experimental conditions were not the most suitable for cell attachment since the scaffold surface was not treated to promote cell adhesion, the experiments were not performed under controlled temperature and humidity conditions and no scaffold sterilization was performed. However, cells do not impact the fibres due to the strong effect of the fluid flow on the transport of cells, so even under the most adequate biochemical seeding conditions if there is no interception between cells and substrate, no chemical signalling for cell adhesion could occur. Nevertheless, a sensitivity analysis where the biochemical conditions are manipulated will provide a deeper insight in the actual effect of the fluid drag force over other forces.

In the presented experiments, fluid streamlines seem preferable channels for cells to travel inside the scaffold; during cell tracking up to ten cells can be observed passing by the same fluid streamline. In addition, higher frequency of cells travelling is found in the streamlines that pass by the centre of the pores where fluid velocities are higher as shown previously in Fig. 5.6. As a consequence, this fact reduces the possibility for cells to interact with scaffold substrate and therefore cell adhesion.

However, a better insight on the interaction between the fluid flow and cell motion could be obtained by combining tracer particles and labelled cells in the working fluid simultaneously, so the actual fluid flow conditions around the cells and the influence of the fluid flow on cell path could be better understood. Unfortunately, this strategy normally requires more than one filter to separate the fluorescence from labelled cells and tracer particles.

In Fig. 5.8, it can be seen that in region 1 the velocity of cells is slower, and they increase in region 2 where the cells travel towards the first pore. In region 3 where the first pore is found, the cells decrease their velocity, and then they move either to the left pore or the right one. More cells travel to the right pore as the pore is bigger although in principle the scaffold used for this study is a regular scaffold, and the same proportion of cells should travel to the left and the right pore providing a regular distribution of cells during seeding. This variability in the scaffold architecture can be due to the limitations in the fabrication process as discuss in Chap 4. Regarding the measured velocities of cells, it is noteworthy that the DOC is increased twice since the size of the cells is ten times bigger than the tracer particles used for the μ5. Thus, cells moving away with perpendicular component to the focus plane can be observed in the captured images as the projection of the trajectory of cells and this can lead to misleading cell velocity measurements. This limitation could be addressed by using calibration methods for PTV applications that the one presented by Winer et al. (2014) where the particle z-position is correlated to its apparent diameter.

Even though only 2D velocities could be measured, the velocities of cells showed significant difference from region to region inside the same scaffold with up to 50 times difference; in the region shown in Fig. 5.16a.1, values are within 50–100 μm/s, and in another region such as the one shown in Fig. 5.16b.1, the values are between 100 and 500 μm/s. That can be again consequence of the intrinsic scaffold variability yielding in undesired cell seeding outcomes.

5.3 Numerical Simulations to Explore Cell Seeding Under Perfusion Inside 3D Scaffolds

5.3.1 Predict Local Fluid Velocities at the Scaffold Pore Level

μPIV experimental data can help to understand the physics involved in microfluidic systems for tissue engineering applications. Even more, well-characterized μPIV data can be used to formulate and validate CFD models that in turn they will have the potential to substitute physical experiments becoming a virtual unlimited source of experimental trials. Song et al. (2010) extracted the flow fields at the cell scale in order to assess the ability of CFD to predict the local fluid-induced microenvironment around cells. De Boodt et al. (2010) used the μPIV measurements not only for CFD validation but also as feedback to improve the definition of the CFD model;

they found significant differences between μPIV and CFD results mainly due to the use of the idealized scaffold CAD geometry in the computational model instead of considering the actual scaffold geometry. The inclusion of the real scaffold geometry in CFD models can be performed through digital reconstruction using μCT data as discussed in Chap. 4. A μCT-based CFD model permits to analyse the same region as in the experiments. Furthermore, the use of a the scaffold μCT geometry can help to capture the variability in terms of pore velocities that can be expected due to alterations in scaffold micro-architecture during the fabrication process as discussed by Campos Marin and Lacroix (2015).

The scope of this study was to investigate the capability of the CFD model to predict the local fluid velocities calculated with μPIV and to obtain representative data of the effect of the pore geometry on the fluid flow. A μCT-based CFD model was developed to predict the real hydrodynamic conditions inside the scaffold during cell seeding. The trimmed scaffold was scanned using μCT with 7 μm^3 of voxel size and then reconstructed using Simpleware (see Fig. 5.9). The image-based reconstructed scaffold was then imported into Icem ANSYS where the microchannel boundary conditions were created. A tetrahedral mesh representing the fluid domain was generated with 10,322,962 elements with minimum element size of 20 μm. The fluid mesh was modelled in Fluent ANSYS 15.0 as an incompressible Newtonian fluid with viscosity of 1×10^{-3} Pa·s and density of 1000 kg/m^3 representing the deionized water from the experiments. The fluid flow was described by the 3D Navier-Stokes equation, and a steady-state laminar flow was simulated with a mass flow rate of 18 μl/min at the inlet, zero pressure at the outlet and nonslip wall condition.

The CFD results agree well with the velocity profiles calculated using the μPIV system as seen in Fig. 5.10. First, both approaches show that peak velocities are found at the centre of the pore defined by the vertical fibres (Fig. 5.5b), and they decrease as long as they approach to the wall fibres. The good agreement between the experimental and computational approach is not only qualitative but also in terms of velocity magnitude, and it is due to the almost zero fluid velocity component in the depth direction so fluid velocity vectors fall in the focus plane. There is only a maximum difference of 12% in velocity magnitude inside the pore; however, when reaching the fibre walls, the μPIV velocities are non-zero on the contrary as in the CFD where the nonslip condition was applied (Fig. 5.11). This could be due to the scaffold brightness that contributed to the velocity maps calculations in the vicinity of the fibres substrate.

The CFD and μPIV results show the same trend underneath the horizontal fibre; the fluid velocity is higher when approaching to the horizontal fibre; however, it decreases before entering in the pore formed by the vertical fibres (see Fig. 5.12). The region before entering the pore where velocity drops is the closest part of the focus plane to the horizontal fibre due to its cylindrical shape as previously shown in Fig. 5.7; thus, the nonslip wall effect reduces the fluid velocity. In theory, the fluid velocity should increase as travelling towards the pore since the area is reduced, and as an incompressible fluid, the velocity has to increase to obey continuity. In terms of velocity magnitude, the agreement becomes poorer as the fluid enters the pore with

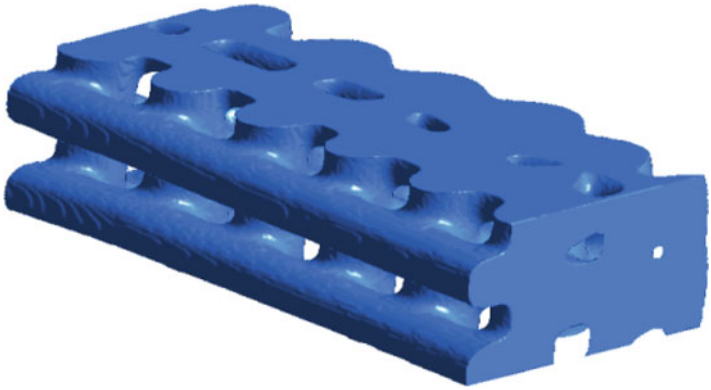

Fig. 5.9 3D digital reconstruction of the trimmed scaffold using μCT data

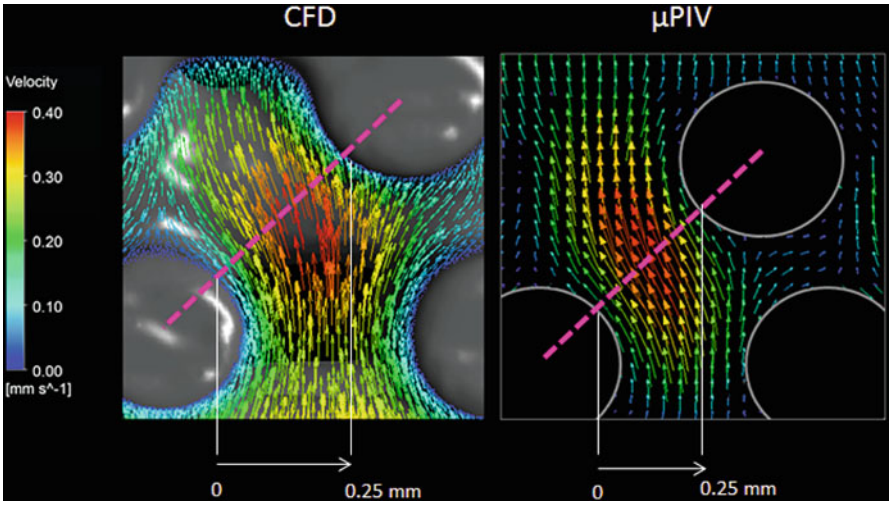

Fig. 5.10 Velocity vectors from a plane inside a pore between the vertical fibres calculated using μPIV (right) and CFD (left) methods. The pink dotted line shows where the velocity values were extracted to compare both techniques numerically

up to 70% difference even though the main velocity behaviour is captured by both techniques (see Fig. 5.13). In addition as seen in Fig. 5.14, the CFD and the μPIV agree well on the fact that the region where the velocity starts increasing due to the presence of the pore on the flow direction shows higher velocities at the centre part corresponding with the centre of the pore, and they decrease as moving to the sides. Both CFD and μPIV show this trend numerically reaching the same peak velocity at the centre; however, as moving away from the centre, they can differ up to 46% (see Fig. 5.15).

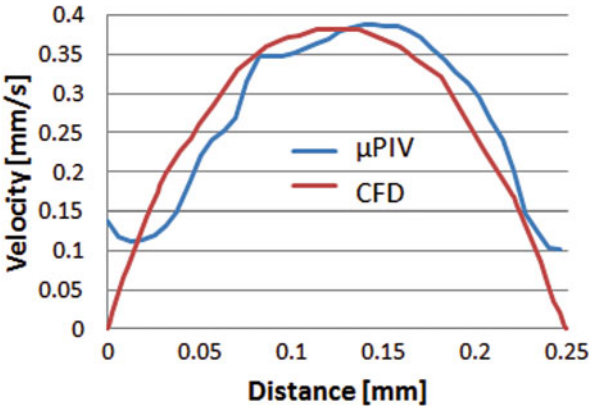

Fig. 5.11 The blue and red lines represent the velocity values extracted from the profiles shown in Fig. 5.10 for the μPIV and CFD, respectively

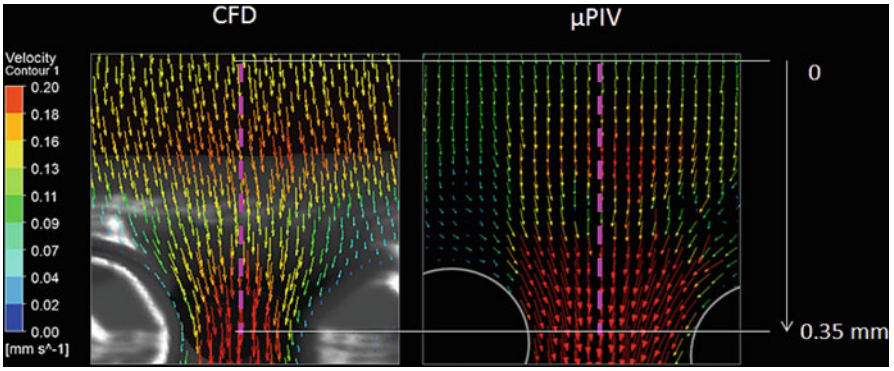

Fig. 5.12 Velocity vectors from a focus plane underneath the horizontal fibre calculated using μPIV (right) and CFD (left) methods. The pink dotted lines shows where the velocity values were extracted to compare both techniques numerically

Some of the disagreements found in terms of velocity values can be explained by different reasons such as the selection of the exact μPIV focus plane in the CFD when analysing the velocity maps close to the horizontal fibre that is critical for the adequate comparison of both methods. Furthermore, the realistic position of the trimmed scaffold inside the channel is unknown and cannot be incorporated in the CFD model; empty spaces between the scaffold and the channel wall or the scaffold orientation with respect to the channel and the flow direction could significantly alter the local fluid dynamics. Nevertheless, these velocity profiles are expected to be repeated throughout the scaffold although with possibly significant variance in terms of velocity magnitude in the presence of geometrical defects or microstructural variability. The analysis of more pores would be beneficial to obtain statistical significant data, but the working fluid stained the scaffold over time, thereby being unable to reuse the scaffold in more experiments.

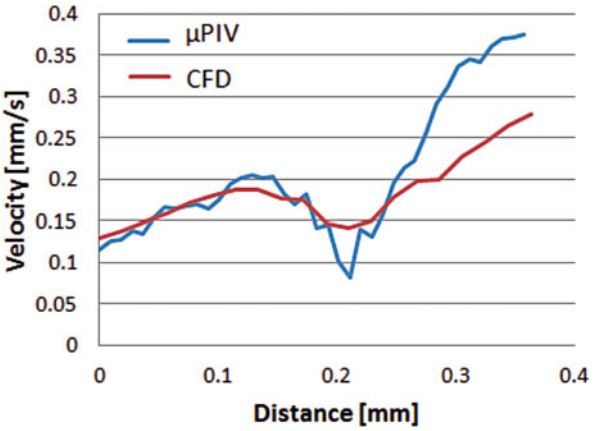

Fig. 5.13 The blue and red lines represent the velocity values extracted from the profiles shown in Fig. 5.12 for the μPIV and CFD, respectively

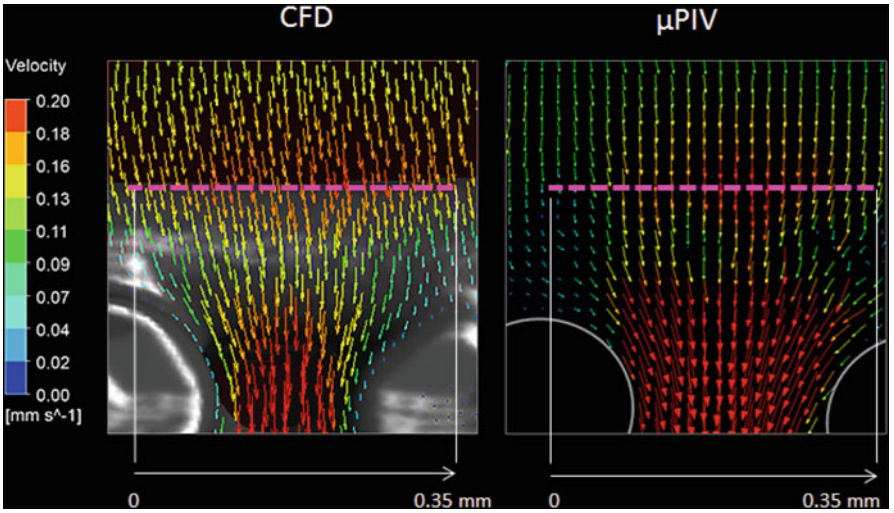

Fig. 5.14 Velocity vectors from a focus plane underneath the horizontal fibre calculated using μPIV (right) and CFD (left) methods. The pink dotted lines shows where the velocity values were extracted to compare both techniques numerically

5.3.2 Prediction of Cell Motion and Interactions with Scaffold Substrate with Numerical Simulations

Multiphase-based CFD models are a good solution to predict the local fluid dynamics for cell seeding and also cell transport in suspension flow. In the literature, only few studies have attempted to model scaffold cell seeding with the inclusion of cells as a single phase different from the fluid one. Spencer et al. (2013) developed a mathematical model to predict fluid flow inside a μCT-based scaffold as well as

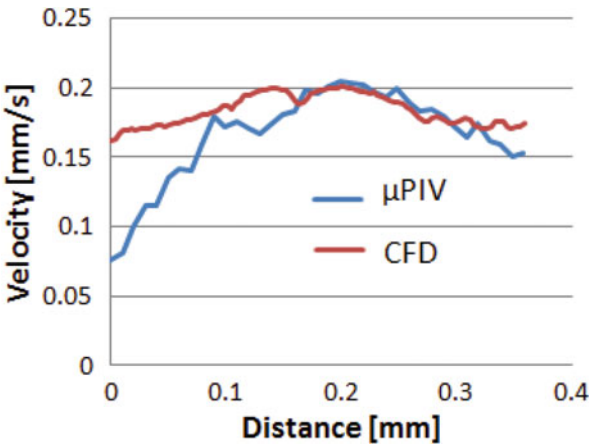

Fig. 5.15 The blue and red lines represent the velocity values extracted from the profiles shown in Fig. 5.14 for the μPIV and CFD, respectively

transport of species and cell adhesion, but no experimental validation was carried out, and cells were modelled as suspension concentrations being unable to predict individual cell path and cell deposition onto scaffold substrate. Adebiyi et al. (2011) used the Fluent ANSYS discrete phase model (DPM) where cells are modelled as individual sphere particles to simulate scaffold cell seeding on a vacuum-based bioreactor; however, the scaffold was simulated as a porous region that obeyed Darcy's law; therefore, real cell-substrate interaction was not investigated. Olivares and Lacroix (2012) also used the Fluent ANSYS DPM model but applied on the real scaffold structure by including the μCT-based geometry in the model. However, the velocity of the particles were not compared and validated with the velocity of the cells in the real experiment**.** PTV methods seem to be the key to enhance such multiphase models by using experimental data to define the computational model and also for validation.

In this study, cells were modelled as a discrete phase of inert microsphere particles with 10 μm diameter suspended within the continuous phase. DPM model of Fluent ANSYS 15.0 tracks the particles along the previously calculated continuous phase in a Lagrangian formulation. Only one-way coupling was considered between both phases, so the fluid phase could only affect the discrete phase. The discrete phase was sufficiently diluted that the effect of particle volume fraction on the continuum phase could be neglected. The same applies to particle-particle interactions as the particles were too dispersed to intercept each other. The trajectories of the particles were computed individually at specified time steps during the fluid phase calculation. The trajectory of the discrete phase was calculated by integrating the force balance acting on the particle as shown in Eq. 5.4 where the particle inertia is equal to the sum of the forces acting on the particle.

$$m_p \frac{\mathrm{d}v_p}{\mathrm{d}t} = \sum_{i=0}^{n} \overset{\rho}{F_i} \tag{5.4}$$

$$\frac{du_p}{dt} = \frac{18\eta}{\rho_p d_p^2}\frac{C_d \mathrm{Re}}{24}\left(u - u_p\right) + \frac{g\left(\rho_p - \rho\right)}{\rho_p} \tag{5.5}$$

The first term on the right of Eq. 5.5 is the drag force where η is the fluid dynamic viscosity, ρ is the fluid density, ρ_p is the density of the particle, d_p is the diameter of the particle and Re is the relative Reynolds number defined in Eq. 5.6. The drag force is based on Stokes' law, and it is due to the relative velocity of the particle and the fluid. The drag force was originally calculated for creeping flows where the inertia effects are negligible for Re < <1.

$$\mathrm{Re} \equiv \frac{\rho d_p \left| \vec{u}_p - \vec{u} \right|}{\eta} \tag{5.6}$$

However, the drag force can be accounted for over the entire range of Reynolds by expressing it in terms of an empirical drag coefficient factor for spherical particles C_d. This factor is described in Eq. 5.7 where the constants a_1, a_2 and a_3 define the range of Re as specified by Morsi and Alexander (1972). In the presented model, the fluid flow is laminar as the maximum fluid Re number is –10, and C_d approximates to 24/Re.

$$C_d = a_1 + \frac{a_2}{\mathrm{Re}} + \frac{a_3}{\mathrm{Re}} \tag{5.7}$$

The PTV experiments were essential to understand to configure the computational model. Cell sedimentation was observed in the experiments, so gravity force was accounted in the numerical simulations. The second term on the right of Eq. 5.5 considers the gravity effect and thereby the buoyancy force. This term contributes to the calculation of the trajectory of the particle as cell density is assumed to be different from the density of the fluid phase with a value of 1130 kg/m^3 (Bryan et al. 2014; Zhao et al. 2014).

Brownian forces were neglected due to the size of the particles that exceeds 0.03 μm of diameter. It is noteworthy that Saffman's lift force, which is the lift due to shear, could affect the deposition of the particles. However, this force could not be accounted for since Fluent only implements it for submicron particles.

The surface injection method was applied where one cell is injected per mesh element face at the inlet boundary. The inlet face presents 1000 surface elements, so four injections were required to inject a total of 4000 cells in the fluid domain. The cells were injected with zero initial velocity. To model the interaction of cells with scaffold surface, cells were trapped as soon as they were in contact with the scaffold or channel surfaces.

The CFD results show that the particles follow the fluid streamlines with higher velocities at the centre of the pores as observed in the experiments. In addition, a low percentage of particles contacting the scaffold substrate was found; particles were either lost in the channel due to sedimentation or travelled through the scaffold

without touching it passing mainly by the centre of the pores. It is noteworthy that the CFD model does not account for particle-particle interactions, so no cell-cell interactions could be modelled. This effect becomes significant when cell density increases, so there is more probability of cell collision deviating cells from their path and reducing their velocity leading to cell sedimentation or an increase of cells impacting the scaffold substrate.

Despite the fact that CFD results show the same tendency of cells to follow the fluid streamlines as in the PTV experiments, they don't agree in the velocity values. Velocity values found in the CFD simulations can be from two to ten times higher than the values found in the PTV experiments. However, the CFD results from the same two scaffold regions that were investigated in the PTV tests also show a significant increment in the velocities of cells from region to region as shown in Fig. 5.16b.1, b.2. The disagreement between the PTV and CFD in terms of cells velocity magnitude can be a consequence of different factors such as the limitation of the μPIV system used in this study to measure 3D displacements and the large DOC in the PTV experiments. Also, it can be due to the difficulty of recreating the exact geometrical boundary conditions; the real location of the scaffold with regard to the channel walls is unknown, so there is a possibility of finding gaps that can potentially

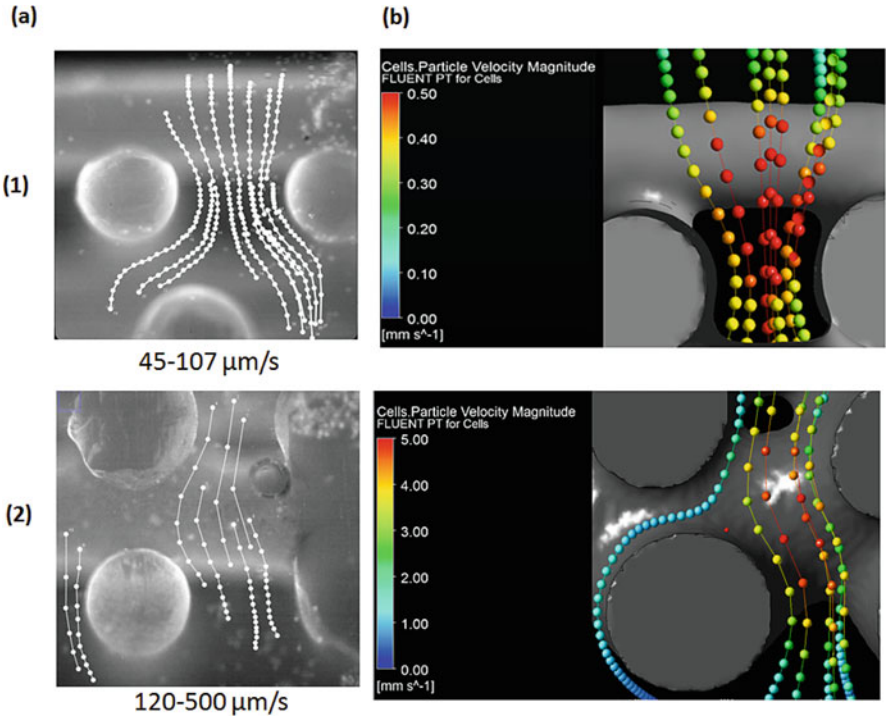

Fig. 5.16 Cell motion and velocity in two scaffold regions (1) and (2) using PTV (**a**) and CFD (**b**) methods

affect the local fluid dynamics and therefore the motion of suspended cells. Furthermore, the μCT-based scaffold used in the CFD model was not the same scaffold from the experiments as it could not be reused due to the increase of its brightness after the first μPIV experiment. The new scaffold was trimmed manually resulting in a different shape from the one used in the CFD, so the exact same scenario could not be replicated. Thus, the geometrical boundary conditions of the scaffold used in the CFD can vary from the one of the experiments. Also, repeated PTV experiments on the same scaffold could help to gain statistical significance, but the working fluid with labelled cells stained the scaffold as occurred in the μPIV experiments. It is important as well to consider the real-time response of cells to changes in the fluid flow that can be different from the time response of the sphere particles simulated in the CFD model. This parameter depends on the cell density that herein has been estimated based on literature and on the fluid viscosity that has not been experimentally measured. Nevertheless, this presented computational model shows the potential to predict cell path, but it also corroborates the key role of fluid dynamics in cell transport during scaffold cell seeding.

5.3.3 Computational Methods for the Optimization of Perfusion Bioreactors

Bioreactors need to be designed to promote cell-scaffold collision in order to enhance cell seeding efficiency. In the scenario of this study where more cells travel in the middle of the pores far from the fibres, the combination of perfusion with the rotation of the bioreactor could help cells to collide with the scaffold (Haykal et al. 2014). This idea has been implemented in the study of Melchels et al. (2010) to analyse the seeding performance in a scaffold with regular pore network similar to the one used in the present study. A homogeneous cell distribution was found showing the benefit of this type of configuration for seeding. However, the static seeding showed the negative effect of the permeability in the open scaffold where most of the cells travel throughout the scaffold driven by the gravity in the fluid flow without cell attachment. Nonetheless, scaffold permeability is essential to distribute nutrients and oxygen to cells to ensure cell viability. A good solution to maintain scaffold permeability as well as enhance cell entrapment has been presented by Papadimitropoulos et al. (2013) that increased the surface area in a regular open scaffold using collagen network as filling material. The computational model presented in this study can help researchers to stop seeing perfusion bioreactors as black boxes and providing potential hints for the optimization and design of hydrodynamic cell seeding bioreactors.

5.4 Conclusions

The combination of regular permeable scaffolds with perfusion systems enhances mass transfer inside the scaffold during cell seeding. However, this does not necessarily imply cell deposition on scaffold substrate. The aim of this study was to investigate the local fluid flow conditions and the transport of cells inside a 3D scaffold during perfusion cell seeding. To the author's knowledge, this is the first time that fluid flow and cell seeding are observed and quantified inside a 3D porous scaffold by performing μPIV and PTV experiments. Furthermore, these data served to formulate and validate a CFD model able to predict the fluid flow inside the scaffold pores and cell path. The PIV results show that the CFD model can describe the velocity maps at the scaffold pore level. Moreover, the PTV experiments and the CFD model agree that cells follow the fluid streamlines, and more cells pass by the centre of the pores where local fluid velocities are higher. Thus, cells travel far from the scaffold substrate reducing the possibility of cell-scaffold interception and cell adhesion. Despite the advantage of regular porous scaffolds to transport cells to all scaffold regions, it doesn't guarantee that cells intercept with scaffold substrate. This study reveals that fluid drag force and sedimentation are the main mechanisms on cell transport under perfusion, and these findings can serve researchers to design new strategies to promote cell deposition on scaffold substrate. In addition, the presented computational model could be used to exploit different cell seeding conditions in order to find the optimal configuration to maximize cell seeding efficiency. Nonetheless, the computational model requires further validation as significant differences were found in terms of cell velocity magnitude between the CFD model and the PTV experiments. Further experiments using devices able to track 3D displacements could provide valuable data to gain better insight into the cell transport phenomena and validate the CFD model. On the other hand, more efforts should be made to obtain better geometrical representations of the experimental setup in the CFD model since small variations could significantly alter the results of the local fluid flow.

References

Adebiyi AA, Taslim ME, Crawford KD (2011) The use of computational fluid dynamic models for the optimization of cell seeding processes. Biomaterials 32:8753–8770. https://doi.org/10.1016/j.biomaterials.2011.08.028

Braccini A, Wendt D, Jaquiery C, Jakob M, Heberer M, Kenins L, Wodnar-Filipowicz A, Quarto R, Martin I (2005) Three-dimensional perfusion culture of human bone marrow cells and generation of osteoinductive grafts. Stem Cells 23:1066–1072. https://doi.org/10.1634/stemcells.2005-0002

Bryan AK, Hecht VC, Shen W, Payer K, Grover WH, Manalis SR (2014) Measuring single cell mass, volume, and density with dual suspended microchannel resonators. Lab Chip 14:569–576. https://doi.org/10.1039/c3lc51022k

Bueno EM, Bilgen B, Barabino GA (2005) Wavy-walled bioreactor supports increased cell proliferation and matrix deposition in engineered cartilage constructs. Tissue Eng 11:1699–1709. https://doi.org/10.1089/ten.2005.11.1699

Campos Marin A, Lacroix D (2015) The inter-sample structural variability of regular tissue-engineered scaffolds significantly affects the micromechanical local cell environment. Interf Focus 5:20140097–20140097. https://doi.org/10.1098/rsfs.2014.0097

De Boodt S, Truscello S, Ozcan SE, Leroy T, Van Oosterwyck H, Berckmans D, Schrooten J (2010) Bi-modular flow characterization in tissue engineering scaffolds using computational fluid dynamics and particle imaging velocimetry. Tissue Eng Part C Methods 16:1553–1564. https://doi.org/10.1089/ten.tec.2010.0107

Fouras A, Dusting J, Hourigan K (2007) A simple calibration technique for stereoscopic particle image velocimetry. Exp Fluids 42:799–810. https://doi.org/10.1007/s00348-007-0293-3

Fouras A, Dusting J, Sheridan J, Kawahashi M, Hirahara H, Hourigan K (2009) Engineering imaging: using particle image velocimetry to see physiology in a new light. Clin Exp Pharmacol Physiol 36:238–247. https://doi.org/10.1111/j.1440-1681.2008.05102.x

Haykal S, Salna M, Zhou Y, Marcus P, Fatehi M, Frost G, Machuca T, Hofer SOP, Waddell TK (2014) Double-chamber rotating bioreactor for dynamic perfusion cell seeding of large-segment tracheal allografts: comparison to conventional static methods. Tissue Eng Part C Methods 20:1–12. https://doi.org/10.1089/ten.TEC.2013.0627

Hidalgo-Bastida LA, Thirunavukkarasu S, Griffiths S, Cartmell SH, Naire S (2012) Modeling and design of optimal flow perfusion bioreactors for tissue engineering applications. Biotechnol Bioeng 109:1095–1099. https://doi.org/10.1002/bit.24368

Jae M, Dean D, Knothe ML (2013) Biomaterials mechanical modulation of nascent stem cell lineage commitment in tissue engineering scaffolds. Biomaterials 34:5766–5775. https://doi.org/10.1016/j.biomaterials.2013.04.023

Li Y, Ma T, Kniss DA, Lasky LC, Yang ST (2001) Effects of filtration seeding on cell density, spatial distribution, and proliferation in nonwoven fibrous matrices. Biotechnol Prog 17:935–944. https://doi.org/10.1021/bp0100878

Lima R, Wada S, Tsubota K, Yamaguchi T (2006) Confocal micro-PIV measurements of three-dimensional profiles of cell suspension flow in a square microchannel. Meas Sci Technol 17:797–808. https://doi.org/10.1088/0957-0233/17/4/026

Lima R, Ishikawa T, Imai Y, Takeda M, Wada S, Yamaguchi T (2009) Measurement of individual red blood cell motions under high hematocrit conditions using a confocal micro-PTV system. Ann Biomed Eng 37:1546–1559. https://doi.org/10.1007/s10439-009-9732-z

Mack JJ, Youssef K, Noel ODV, Lake MP, Wu A, Iruela-Arispe ML, Bouchard LS (2013) Real-time maps of fluid flow fields in porous biomaterials. Biomaterials 34:1980–1986. https://doi.org/10.1016/j.biomaterials.2012.11.030

Martinelli M, Viktorov V (2009) Modelling of laminar flow in the inlet section of rectangular microchannels. J Micromech Microeng 19:025013. https://doi.org/10.1088/0960-1317/19/2/025013

McCoy RJ, O'Brien FJ (2010) Influence of shear stress in perfusion bioreactor cultures for the development of three-dimensional bone tissue constructs: a review. Tissue Eng Part B Rev 16:587–601. https://doi.org/10.1089/ten.teb.2010.0370

Meinhart CD, Wereley ST (2003) The theory of diffraction-limited resolution in microparticle image velocimetry. Meas Sci Technol 14:1047–1053. https://doi.org/10.1088/0957-0233/14/7/320

Melchels FPW, Barradas AMC, van Blitterswijk CA, de Boer J, Feijen J, Grijpma DW (2010) Effects of the architecture of tissue engineering scaffolds on cell seeding and culturing. Acta Biomater 6:4208–4217. https://doi.org/10.1016/j.actbio.2010.06.012

Melchels FPW, Tonnarelli B, Olivares AL, Martin I, Lacroix D, Feijen J, Wendt DJ, Grijpma DW (2011) The influence of the scaffold design on the distribution of adhering cells after perfusion cell seeding. Biomaterials 32:2878–2884. https://doi.org/10.1016/j.biomaterials.2011.01.023

Morsi S, Alexander A (1972) An investigation of particle trajectories in two-phase flow systems. J Fluid Mech 55:193–208. https://doi.org/10.1017/S0022112072001806

Nishi M, Matsumoto R, Dong J, Uemura T (2013) Engineered bone tissue associated with vascularization utilizing a rotating wall vessel bioreactor. J Biomed Mater Res Part A 101A:421–427. https://doi.org/10.1002/jbm.a.34340

Olivares AL, Lacroix D (2012) Simulation of cell seeding within a three-dimensional porous scaffold: a fluid-particle analysis. Tissue Eng Part C Methods 18:624–631. https://doi.org/10.1089/ten.tec.2011.0660

Olsen MG, Adrian RJ (2000) Out-of-focus effects on particle image visibility and correlation in microscopic particle image velocimetry. Exp Fluids 29:S166–S174. https://doi.org/10.1007/s003480070018

Oshima M, Oishi M (2014) Continuous and simultaneous measurement of micro multiphase flow using confocal micro-particle image velocimetry (micro-PIV) 3. Measurement for Droplet Formation, 4th Micro and Nano Flows Conference (MNF2014), London, (2014). pp 7–10

Papadimitropoulos A, Riboldi SA, Tonnarelli B, Piccinini E, Woodruff MA (2013) A collagen network phase improves cell seeding of open-pore structure scaffolds under perfusion. J Tissue Eng Regen Med 7:183–191. https://doi.org/10.1002/term

Papantoniou I, Guyot Y, Sonnaert M, Kerckhofs G, Luyten FP, Geris L, Schrooten J (2014) Spatial optimization in perfusion bioreactors improves bone tissue-engineered construct quality attributes. Biotechnol Bioeng 111:2560–2570. https://doi.org/10.1002/bit.25303

Pinho D, Lima R, Pereira AI, Gayubo F (2013) Automatic tracking of labeled red blood cells in microchannels. Int J Numer Meth Biomed Engng 29:977–987. https://doi.org/10.1002/cnm.2526

Poly L, Kim YHA, Matsuda T (2006) New technique of seeding chondrocytes into microporous. Tissue Eng 12:1811–1820. https://doi.org/10.1089/ten.2006.12.1811

Provin C, Takano K, Sakai Y, Fujii T, Shirakashi R (2008) A method for the design of 3D scaffolds for high-density cell attachment and determination of optimum perfusion culture conditions. J Biomech 41:1436–1449. https://doi.org/10.1016/j.jbiomech.2008.02.025

Saini S, Wick TM (2003) Concentric cylinder bioreactor for production of tissue engineered cartilage: effect of seeding density and hydrodynamic loading on construct development. Biotechnol Prog 19:510–521. https://doi.org/10.1021/bp0256519

Song MJ, Dean D, Knothe Tate ML (2010) In situ spatiotemporal mapping of flow fields around seeded stem cells at the subcellular length scale. PLoS One 5:1–7. https://doi.org/10.1371/journal.pone.0012796

Sonnaert M, Papantoniou I, Bloemen V, Kerckhofs G, Luyten FP, Schrooten J (2014) Human periosteal-derived cell expansion in a perfusion bioreactor system: proliferation, differentiation and extracellular matrix formation. J Tissue Eng Regen Med. https://doi.org/10.1002/term.1951

Spencer TJ, Hidalgo-Bastida LA, Cartmell SH, Halliday I, Care CM (2013) In silico multi-scale model of transport and dynamic seeding in a bone tissue engineering perfusion bioreactor. Biotechnol Bioeng 110:1221–1230. https://doi.org/10.1002/bit.24777

Sugii Y, Okuda R, Okamoto K, Madarame H (2005) Velocity measurement of both red blood cells and plasma of in vitro blood flow using high-speed micro PIV technique. Meas Sci Technol 16:1126–1130. https://doi.org/10.1088/0957-0233/16/5/011

Vunjak-Novakovic G, Obradovic B, Martin I, Bursac PM, Langer R, Freed LE (1998) Dynamic cell seeding of polymer scaffolds for cartilage tissue engineering. Biotechnol Prog 14:193–202. https://doi.org/10.1021/bp970120j

Wendt D, Marsano A, Jakob M, Heberer M, Martin I (2003) Oscillating perfusion of cell suspensions through three-dimensional scaffolds enhances cell seeding efficiency and uniformity. Biotechnol Bioeng 84:205–214. https://doi.org/10.1002/bit.10759

Winer MH, Ahmadi A, Cheung KC (2014) Application of a three-dimensional (3D) particle tracking method to microfluidic particle focusing. Lab Chip 14:1443–1451. https://doi.org/10.1039/c3lc51352a

Xiao YL, Riesle J, Van Blitterswijk CA (1999) Static and dynamic fibroblast seeding and cultivation in porous PEO/PBT scaffolds. J Mater Sci Mater Med 10:773–777

Zhao Y, Lai HSS, Zhang G, Lee G-B, Li WJ (2014) Rapid determination of cell mass and density using digitally-controlled electric field in a microfluidic chip. Lab Chip 14:4426–4434. https://doi.org/10.1039/C4LC00795F

Chapter 6
Collagen Gel Cell Encapsulation to Study Mechanotransduction

Mechanical forces and 3D topological environment can be used to control differentiation of mesenchymal stem cells (MSCs). However, the effects of physical and mechanical cues of the microenvironment on MSC fate determination have not yet been fully understood. This study investigates and compares the effect of mechanical stimulations on soft cellular microspheres when subjected to dynamic fluid compression. Microspheres were produced by gelation of bovine collagen type I with concentrations of 2 mg/ml and 1000–2000 hES-MP cells per 5 µl droplet. A loading condition of 10% dynamic loading was applied by a BOSE BioDynamic bioreactor for 15 and 40 min/day for 5 and 10 days on the cell-seeded collagen microspheres. Cell viability and proliferation, alkaline phosphatase activity and mineralization were compared with controls. Monitoring alkaline phosphatase level reported a significant increase in the enzyme activity by day 14 in loaded samples of 40 min/day loading protocol compared with other experimental conditions. Mineralization was assessed by measuring calcium, phosphorous concentrations and intensity of H&E and alizarin red S staining and showed the highest mineral accumulation in the loaded samples on day 28 post encapsulation. This study indicated that loading of very low cell number seeded on soft natural scaffold can encourage osteogenesis of cells by enhancing both early stage bone marker and mineralization. Self-assembled cell/collagen microspheres present exceptional cell delivery model in bone healing/repair process and field of regenerative medicine.

6.1 Introduction

Stiffness and/or topography of cellular microenvironment along with physical factors such as tension can dictate stem cell fate determination. Although physical cues control mesenchymal stem cell (MSC) lineage specification by tuning cytoskeleton, the full mechanism of how physical signals are sensed by cells and transformed into biochemical and biological signals remains unclear. Numerous studies have focused intensively on the effects of chemical signals in differentiation of stem cells; the effects of physical/mechanical signals of the microenvironment on MSCs have long been neglected. However, few studies provided evidence that both direct and indirect

© Springer Nature Singapore Pte Ltd. 2019

D. Lacroix et al., *Multiscale Mechanobiology in Tissue Engineering*,
Frontiers of Biomechanics 3, https://doi.org/10.1007/978-981-10-8075-3_6

mechanical signals are important regulating a stem cell commitment. While most studies showed that compression forces can induce chondrogenic differentiation rather than osteogenesis, few studies have demonstrated the osteogenic effect of compressive loading on stem cells (Delaine-Smith and Reilly 2011). Therefore our objectives were (1) to produce a soft 3D environment that consisted of self-assembled bovine collagen I fibres to support long-term viability and proliferation of human embryonic mesenchymal progenitors (hES-MP) and (2) to investigate how dynamic mechanical loading and fluid shear stress would stimulate the osteogenesis of 3D human embryonic mesenchymal stem (hES-MP) cell cultures.

6.2 Natural Polymer Scaffolds Can Support Long-Term Cell Viability and Proliferation

6.2.1 Cell Encapsulation

The encapsulation of living cells within a soft hydrogel matrix has numerous applications in many biomedical, clinical and biotechnological technologies, such as allogenic or xenogenic cell transplantation, cell-based biosensors and bio printing of three-dimensional scaffolds for tissue engineering and regenerative medicine.

The aim of cell encapsulation is to entrap functional cells within a semi-permeable matrix. A suitable matrix must be biocompatible, support cell survival and also be permeable to oxygen, other nutrients and toxic metabolites.

Suitable materials for cell encapsulation should mimic the cells' extracellular matrix. Many of these materials are based on hydrogels, which are highly hydrated and composed of hydrophilic polymers that are cross-linked to form three-dimensional networks. Hydrogels derived from natural materials such as collagen have comparable structures to the extracellular matrix of many human tissues.

Agarose, polyethylene glycol and sodium alginate are the most commonly used materials in this process. Yet limitations of these materials in supporting cell attachment and growth in addition to being impenetrable to the cells has made collagen a strong alternative supplement for enhancement in viability of the encapsulated cells. Collagen gels are more readily used in regenerative medicine and tissue engineering, which involves close host-implant interaction at the cellular level and uniform microsphere dimensions and morphology (Chan et al. 2007; Uludag et al. 2000).

Natural extracellular polymers such as collagen are encapsulation materials of choice since they are the most abundant scaffold protein in tissues (DiLullo et al. 2002), their specific cell-binding sites are involved in normal cell function and they have excellent biocompatibility and negligible immunogenicity. Collagen has been used as carriers of antibiotics genes and proteins, as well as scaffolds (Ruszczak et al. 2003). However, because collagen has poor mechanical and shape stability and because no microencapsulation system has been fully developed, they are

incompatible with current microencapsulation techniques, which involve vigorous mechanical disturbances including pressurized nozzle, emulsification or stirring during droplet generation (DiLullo et al. 2002).

Collagen microsphere generation involves forming microdroplets of cells in collagen via direct aliquoting or via emulsification and consequently gelation of the collagen which forms microspheres. In emulsification, microdroplets are made by dispersing the aqueous collagen solution within a continuous oil phase solution and separating the microsphere from oil phase by centrifugation. In aliquoting, on the other hand, small volumes (a few microliters) of aqueous collagen solution is dispersed onto a surface (Brouzes et al. 2009). Major drawback of these techniques is being tedious and it requires that each step of droplet generation, gelation and extraction be performed separately. Another downside would be the challenge to maintain uniform microsphere dimensions and shapes at a high production rate.

Few studies have used bioprinting platform technique in producing cell-encapsulated collagen droplets involving long-term cell viability, multilayered 3D cell-laden hydrogel structures and high-throughput droplet generation, yet unable to produce spherical collagen droplets due to gravity effect. More recently, an integrated high-throughput microfluidic platform was designed to generate more uniform collagen microspheres size and shape with high cell viability. Since both the collagen microdroplet generation and the gelation processes occurred on a chip, the time lag between these two steps was adequately short to eliminate microdroplets coalescence. Also by employing microfluidic extraction approach, cell viability was considerably improved (Hong et al. 2012).

In 2007 Chen et al. introduced a novel cell microencapsulation technique by entrapping human MSCs (hMSCs) in a dense meshwork of reconstructed rat tail collagen I fibres that generated self-assembled collagen-hMSC microspheres. Their approach illustrated the feasibility of utilizing these microspheres for MSC delivery by investigating the microsphere injectability, the cellular growth kinetics and the migration capability in addition to their self-renewal capacity and multipotent differentiating potential (Chan et al. 2007).

6.2.2 Mechanical Conditioning of Cells

Many cell types including osteoblasts, chondrocytes, fibroblasts and endothelial cells are load sensitive and subjected to daily mechanical loading. Dense connective tissues like tendon and ligament are stretched frequently through muscle contraction caused by movement while bone is under dynamic loading to resist and adapt to the experienced forces by maintaining homoeostasis through tissue remodelling. Most of the forces applied in vivo are dynamic and cyclic that means often the tissue is under loading and resting cycles. For example, leg bones undergo cyclic compression and tensile forces as human walks; therefore, it is possible that cells respond more to cyclic loading as opposed to constant load that could increase the risk of cells being overloaded and become unresponsive to the applied load.

A key area of research in tissue engineering is concerned with finding the answers to how mechanical loading transfers to the cells, how cells sense mechanical forces and how and when cells response to the applied external stimuli. Both 2D and 3D cultures have been used to apply mechanical loading onto cells. Nevertheless, 2D experiments are carried out on flat surfaces and do not mimic in vivo 3D architecture. Therefore, 3D in vitro models may provide more physiologically relevant environments for mechanotransduction studies (Barron et al. 2010). Studies have shown that cell response in 2D culture to dynamic stimulation is mainly due to the deformation of the substrate with additional minor fluid flow effects as there is little movement of fluid flow which provide minimal effect on the cells (Juhasova et al. 2011). In contrast, cell response to the load in 3D constructs is related to both the mechanical stimulation that was initiated within the system and nutrient transport mechanism generated by fluid movement through the scaffold (Tian et al. 2008). Various techniques have been used to study the response of cells to mechanical stimulation. Yet, their main focus was on simple 2D surfaces such as coated gelatin, plastic and glasses that do not fully reflect the nature of the in vitro 3D environment. Therefore, these surfaces do not fulfil the necessary requirement in regeneration of functional tissue approach. Culturing cells on 3D environment will provide a more realistic and physiological model for studying load-driven biochemical responses in cells and mimic in vivo conditions.

Many studies investigated the role of mechanical stimulation in the control of cell fate and mechanical conditioning of mesenchymal stem cells (MSCs) in directing MSC behaviour for tissue engineering applications.

Delaine Smith reported that tensile loading favours osteogenesis through initiation of more fibrous matrix, while compression loading encourages generation of a more GAG-rich matrix and chondrogenesis (Delaine-Smith and Reilly 2011). Other studies demonstrated the effect of longitudinal forces in upregulation of early ALP activity level and mineralisation markers both in the presence and absence of osteogenic media (Jacobsen et al. 2008; Kearney et al. 2010).

So far there are limited studies on the effect of compression loading on the osteogenesis of stem cells. Therefore, the aim of this chapter was to investigate the effects of cyclic mechanical-induced osteogenic differentiation and long-term proliferation of progenitor cells and assess cellular mechanisms involved in mechanotransduction and osteogenesis of hES-MPs. The main purpose was to apply short bouts of mechanical loading, mainly tensile and compression, on the hES-MP-seeded collagen microspheres through shortening a channel in a microfluidic chamber. Another goal of this study was to investigate the effect of this mechanical stimulation on osteogenic differentiation of cells through quantification of ALP activity and deposited mineral levels in the hES-MP-seeded collagen microspheres. In addition, cellular matrix production and remodelling along with alignment of collagen fibre were evaluated to confirm load-driven differentiation of cells. Applied loading regime was established by literature (Delaine-Smith and Reilly 2011; Mouw et al. 2007) and cells were subjected to indirect dynamic compression and tensile forces through a PDMS loading chamber.

6.3 Material and Methods

Cell culture: hES-MP cells were grown in T75 gelatin-coated flasks in basal media culture which contained Dulbecco's alpha minimum essential medium (α MEM) from Sigma-Aldrich supplemented with 10% foetal bovine serum (FBS), 1% L-glutamine (G), and 1% streptomycin penicillin (P/S) (v/v). Passages 4–8 of hES-MPs were detached by 0.05% trypsin/25 mmol EDTA to be used in microcapsulation.

Cell-seeded/collagen gelation: bovine collagen type I (5 mg/ml) solution in 0.02 N acetic acid was neutralized by 1 N NaOH and 10× phosphate balance solution (PBS) and diluted into final concentrations of 0.5, 1, 2 or 3 mg/ml. Then, hES-MPs were suspended in the neutralized collagen solution to make up cell-matrix mixtures with final cell densities of 5×10^5, 1×10^6 or 5×10^6 cells/ml. Collagen microspheres of 2.5 and 5 ml were dispensed onto 90 mm diameter Petri dish covered with UV-irradiated Parafilm and were incubated for 45 min at 37 °C and with 5% CO_2 for 45 min to induce gelation of collagen.

Gelated collagen-hES-MP microspheres were then gently flushed with full medium (αDMEM, 10% FBS and 1% penicillin, streptomycin and L-glutamine) from the Parafilm into the Petri dish and maintained free floating during 28-day experiment. Medium was replaced with fresh complete media every 48 h.

Cell viability: cell-seeded microspheres with different collagen concentration and cell density were then stained with 200 μl of 2 mM calcein AM in DMSO (= 495 nm/λem = 515 nm) and 4mM ethidium homodimer-1 in DMSO (λex = 515 nm/λem = 595 nm) at 8 h, 3, 5, 7, 28 and 35 days pc (post encapsulation).

Collagen gel contraction: for each condition mean area and diameter of collagen microspheres were measured to compare collagen gel contractility over 7-day experiment by ImageJ software.

Evaluation of cell-seeded/collagen microstructure: collagen microstructure was compared with the cell-seeded collagen I samples using Oregon Green® 488 carboxylic acid, succinimidyl ester and 5-isomer collagen tracker. Both samples were visualized under second harmonic generation (SHG) obtained by Zeiss Axioskop 2FS MOT upright laser scanning confocal microscope equipped with tunable Chameleon Ti:sapphire multi-photon laser, laser confocal microscope (LSM 510 Zeiss) and fluorescent microscope (Nikon Ti-E) equipped with FITC/Cy2 and ET Texas red filters. Haematoxylin and eosin (H&E) staining of 10 μm cross sections and scanning electron microscopy (SEM) of collagen samples were also performed to identify the role of MSCs in reorganizing and remodelling the collagen fibre microstructure over different time points.

Characterizing of soft collagen gel mechanical properties: mechanical properties of bovine collagen gel (2 mg/ml) were also characterized by using rheometer at 37C° and 1 Hz to calculate elastic modulus, viscous modulus and shear modulus as shown in detail in Chap. 7.

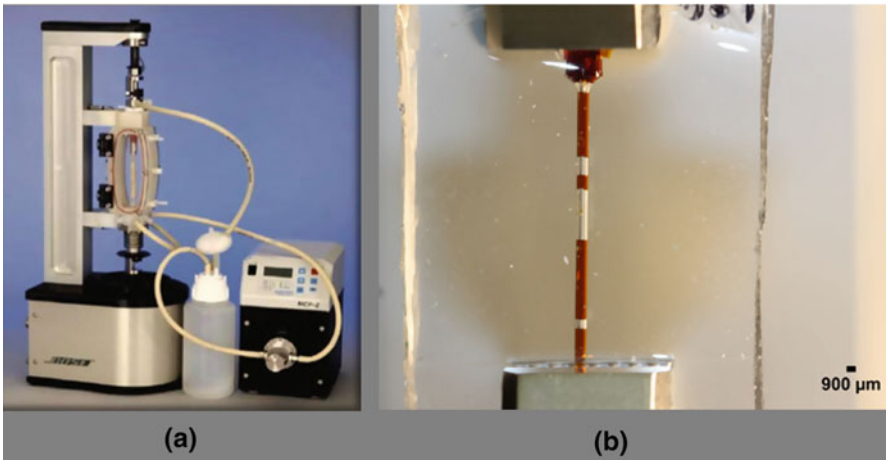

Fig. 6.1 BOSE bioreactor machine (**a**) and compression grips and loading chamber (**b**) were used to apply mechanical loading on the cell-seeded collagen microsphere and encourage osteogenesis of progenitor cells

Characterization of polydimethylsiloxane (PDMS) mechanical properties: Young's modulus, Poisson's ratio and plastic elongation were calculated using high-resolution imaging technique (DIC) and Kelkins software.

Dynamic compression regime: compression chamber was made of PDMS, and the central channel diameter was optimized based on the measurement of average collagen microsphere diameter ($n = 20$) on day 6 post encapsulation (Fig. 6.1). This measurement would confirm that on average the difference between the diameter of each collagen bead and PDMS central chamber is not bigger than 50–80 μm and collagen microsphere would not move to the bottom of the PDMS chamber while being compressed. hES-MP-seeded collagen microspheres were then subjected to dynamic compression of 10% strain with frequency of 1 Hz for 5 and 10 days starting on day 6 pc.

Determination of mineralization and osteogenesis: DNA PicoGreen assay was performed to confirm cell viability and proliferation under compression. Alkaline phosphatase (ALP) activity of samples and controls was measured to validate early stage mineralization and extracellular matrix calcium and phosphorous quantification done by Inductively coupled plasma emission spectrometry (ICP-ES). Mineralization was also visualized by ALP and alizarin red staining of compressed and control cross-sectional samples on 24 h, day 6, day 21 and day 28 pc.

Reorientation of collagen fibre: reorientation and reorganization of compressed collagen fibres were investigated by SHG confocal microscopy on day 21 post encapsulation. Similarly, cell attachment, elongation and new ECM collagen lay-down were examined by SEM on days 6, 16 and 28 pc.

6.4 Results and Discussions

6.4.1 Collagen Gel Microstructure

Viscoelastic properties and shear modulus of very soft collagen gel (0.2% of collagen/hydrogel) were measured by rheometer at 37 °C and 1.3–0.012 Hz. The elastic modulus varied from 0.0146 kPa at 1.3 Hz to 0.0077 kPa at 0.012 Hz, while the viscous modulus varied between 0.0037 and 0.0017 kPa. Average standard deviations were 0.0019–0.0005 kPa, respectively. The average shear moduli were calculated as 0.0103 kPa with standard deviation of 0.0019, average elastic moduli were measured as 0.0101 kPa with standard deviation of 0.0019, and average viscous moduli were calculated as 0.0023 kPa with standard deviation of 0.0005 kPa.

SEM microscopy showed highly porous surface structure of collagen gel and entrapment of hMSCs within collagen matrix with little or no visible aligned fibres (Fig. 6.2a, b). Also amorphous fluffy structures of collagen gel with random orientation and meshwork of collagen fibres were confirmed by ColI-specific fluorescent staining and SHG microscopy (Fig. 6.2d, e).

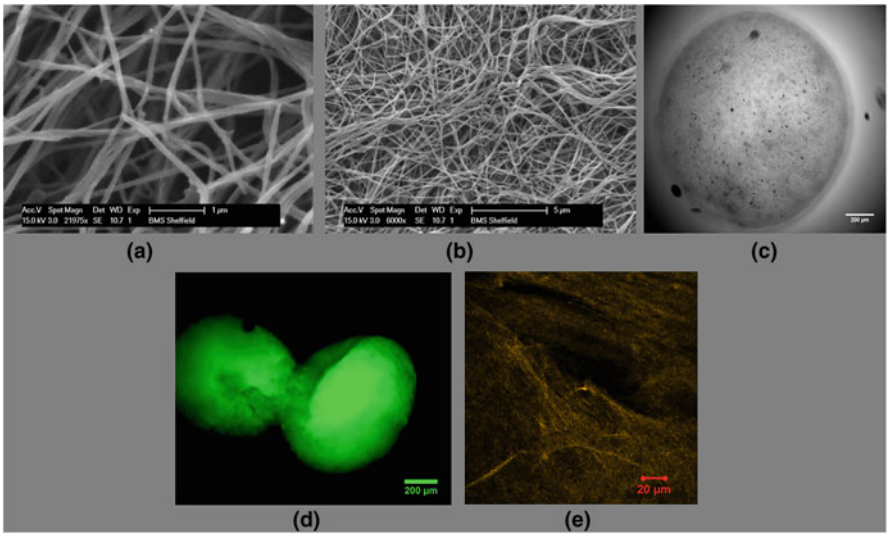

Fig. 6.2 Visualization of bovine collagen I microspheres, microstructure and meshwork of collagen fibres by (**a** and **b**) SEM, (**c**) bright field, (**d**) SHG microscope and (**e**) fluorescent staining of collagen fibres 24 h post encapsulation (SHG image was taken by Dr. Green at Kroto Research Institute, Department of Material Sciences, University of Sheffield). Scale bar for (**d**) 20 µm; scale bars for SEM images are (**a** and **b**) 5 and 1 µm and (**e**) 200 µm

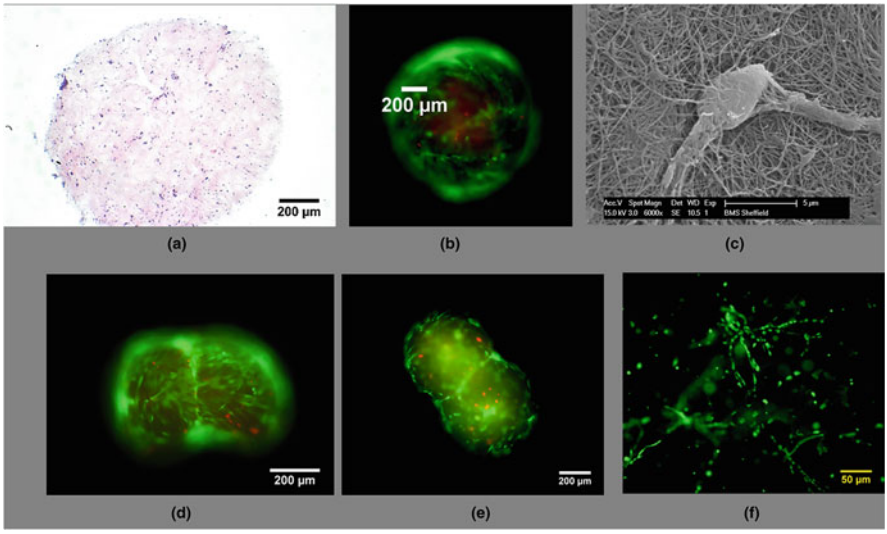

Fig. 6.3 Short and long hES-MP cell viability and cell-cell interaction and network were visualized by (**a**) H&E staining of collagen microspheres, (**b** and **c**) live and dead fluorescent staining of cells and SEM image of an elongated cell on the surface of collagen microsphere at day 6 pc. Long-term hES-MP viability was checked by live and dead fluorescent staining of cells on days 21 (**d** and **e**) and 35 (**f**) post encapsulation. Scale bars for (**a**–**e**) are 200 µm, (**c**) 5 µm and (**e**) 50 µm

6.4.2 Cell Viability of hES-MPs

hES-MPs with cell seeding density of 100–2000 cells/droplet which were embedded in 1.5 and 2 mg/ml collagen I emitted strong green signal with calcein AM and low red signal with ethidium bromide homodimer on day 6 pc suggesting high viability and low mortality of cells (Fig. 6.3b), while collagen microspheres with higher cell displayed very weak cell viability and most cells died within the next 24 h of pc.

Regardless of cell seeding density, very weak or no fluorescent signal was detected following encapsulation of hES-MP cells in 0.5, 1 and 3 mg/ml collagen, and cells presented mostly round morphology on day 6 pc. Cell viability and elongation also confirmed by SEM, H&E and fluorescent staining of samples in different time points (Fig. 6.3a–f).

Those cells that stayed alive migrated to the surface of collagen beads and proliferated steadily till day 35 pc which confirmed that soft microenvironment provided by low concentration of collagen can indeed support hES-MP long-term viability and proliferation.

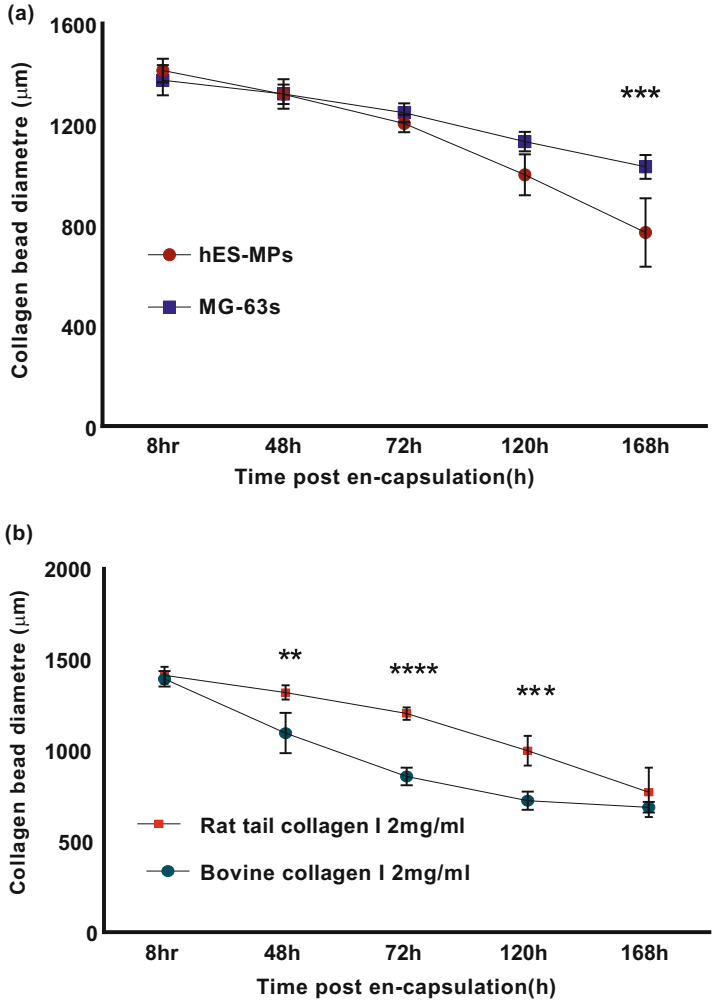

Fig. 6.4 Effect of two cell lines and collagen I sources on the contraction of collagen I gel with concentration of 2 mg/mL was investigated, (**a**) collagen contractibility of hES-MPs/bovine collagen I was compared with rat tail collagen I by measuring the diameter of 12 samples at each time point, (**b**) ability of hES-MPs versus MG-63 cell line in contracting collagen gel was assessed, * indicates statistical significance (**$p < 0.01$, ***$p < 0.001$, ****$p < 0.0001$). Data is mean ± SD $n = 9$

6.4.3 Microsphere Contraction

Results of hES-MPs/collagen beads monitoring demonstrated that collagen microspheres were significantly contracted by an average of 43% in diameter within 7 days pc, while other cell seeding density and collagen concentration showed no or small contraction over the same period of time (Fig. 6.4a). Average diameter reduction of

20% was reported between day 3 and day 5, while least contraction with only 14% change in diameter was observed between days 0 and 3 pc. Microsphere diameter was observed as 1410 μm on average at 8 h pc; then this figure was reduced to 1210 μm on day 3 and to 910 μm on day 5 before shrinking to the diameter of 815 μm on day 7 pc. The biggest drop in microsphere diameter and most substantial contraction were reported between days 3 and 7 pc. In contrast, seeded MG-63 cells in collagen microspheres contracted up to 15% over 7 days of experiment (Fig. 6.4a). At 8 h pc, collagen microsphere diameter was reported on average as 1385 μm, beads then marginally contracted by 10% and their diameter reduced to 1230 μm on day 3 pc. Collagen microsphere diameter was measured as 1192 μm and 1125 μm on days 5 and 7 pc, respectively. Most significant contraction was 12% between 48 and 168 h of the experiment and while least change (8%) was observed between hours 8 and 48 pc.

Nonetheless, hES-MPs contracted collagen gel considerably more than MG-63 cells, and their average diameter on day 7 pc was significantly smaller than MG-63s (28%, $p \leq 0.001$).

The results of bovine and rat tail collagen gel contraction revealed that bovine collagen played greater role in supporting hES-MP collagen contraction (Fig. 6.4b). Bovine collagen microspheres contracted more considerably within the first 72 h pc (39%), while rat tail collagen gel showed more stable contraction of 15% in same period of time. On average rat tail collagen gel contracted 2% ($p \leq 0.0001$) less than bovine within 72 h of gelation, but, in the second half of experiment, the average diameter of rat tail collagen microsphere dropped significantly by 35% compared to 20% decrease in bovine sample to reach around 700 μm on day 7 pc. Overall rat tail collagen gel contraction began much later than bovine and showed to be more subtle over the 7-day experiment.

6.4.4 Dynamic Compression

PDMS is classed as a viscoelastic material as shown in stress/strain graph in Fig. 6.5. The DIC software Kelkins calculated the displacement/strain on the surface of the PDMS and on average for the imposed 10% global strain, 7.5% strain along the vertical direction of solicitation and 3.75% strain along the horizontal transverse direction was measured as demonstrated in Fig. 6.6. Poisson's ratio was then calculated as 0.5 which is consistent with the polymer behaviour. The difference between global and vertical direction strain can be related to strain localization or sample slipping out of the grips during the experiment. Young's modulus of the polymer was calculated as 1000 kPa after relaxation, and plastic deformation was calculated as 0.7 mm after applying 10% strain and using cycle blocks in BOSE BioDynamic machine (Fig. 6.5a, b).

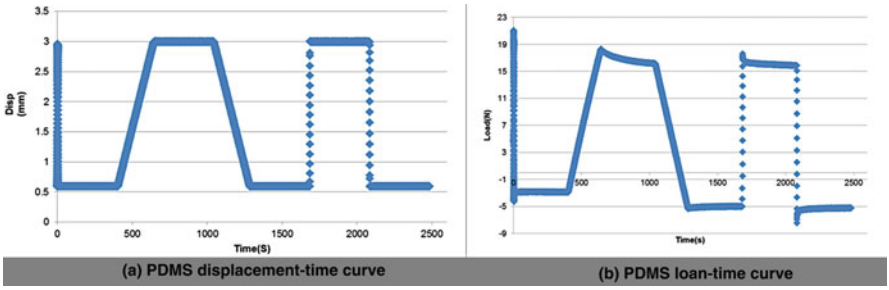

Fig. 6.5 Mechanical properties of PDMS polymer were characterised using ten step blocks of sinusoidal waves and ramps. Sinusoidal wave of (**a**) displacement to load was applied to each sample. Samples then were held at a displacement level for a specific time. PDMS sample was subjected to (**b**) relative tensile loading of 2.35 mm that applied from 0 mm to 2.35 mm, the sample was then held at 2.35 mm for 400 s

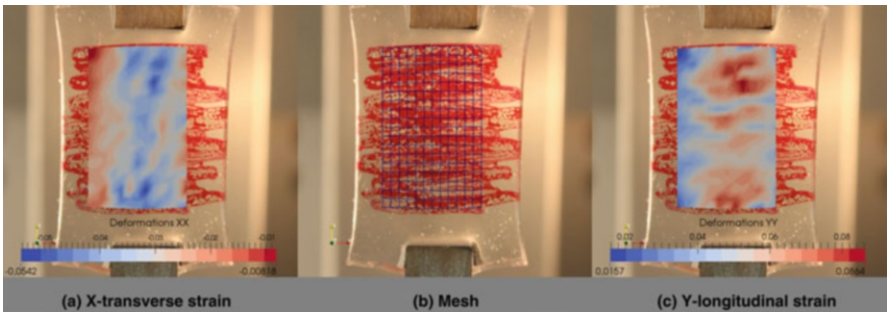

Fig. 6.6 Measurement of (**a**) transversal and (**b**) longitudinal strains on the (**c**) PDMS meshed surface when subjected to 10% global strain using Kelkins software

6.4.5 Mechanical Stimulation Increase Early Osteogenetic Marker

DNA PicoGreen assay results showed that cell remained viable and proliferated steadily well over 28 days post encapsulation (Fig. 6.7a). Although free-floating controls seemed to have higher DNA content, no significant change in proliferation was detected between different conditions and time points. The only exception was day 14 post encapsulation in which proliferation in free-floating controls (DNA content = 60 ng) reported twice as high as 5 days 15- and 40-min compression/day samples (30 ng).

The osteogenic differentiation of hES-MPs was investigated by measurement of ALP as an early stage mineralization marker and was further confirmed by H&E and ALP staining.

Alkaline phosphatase activity level increased substantially from day 6 to day 14 pc when the activity level reached a peak, followed by a drop to nearly half the level on day 21 and remained stable up to day 28 pc (Fig. 6.7b). All conditions

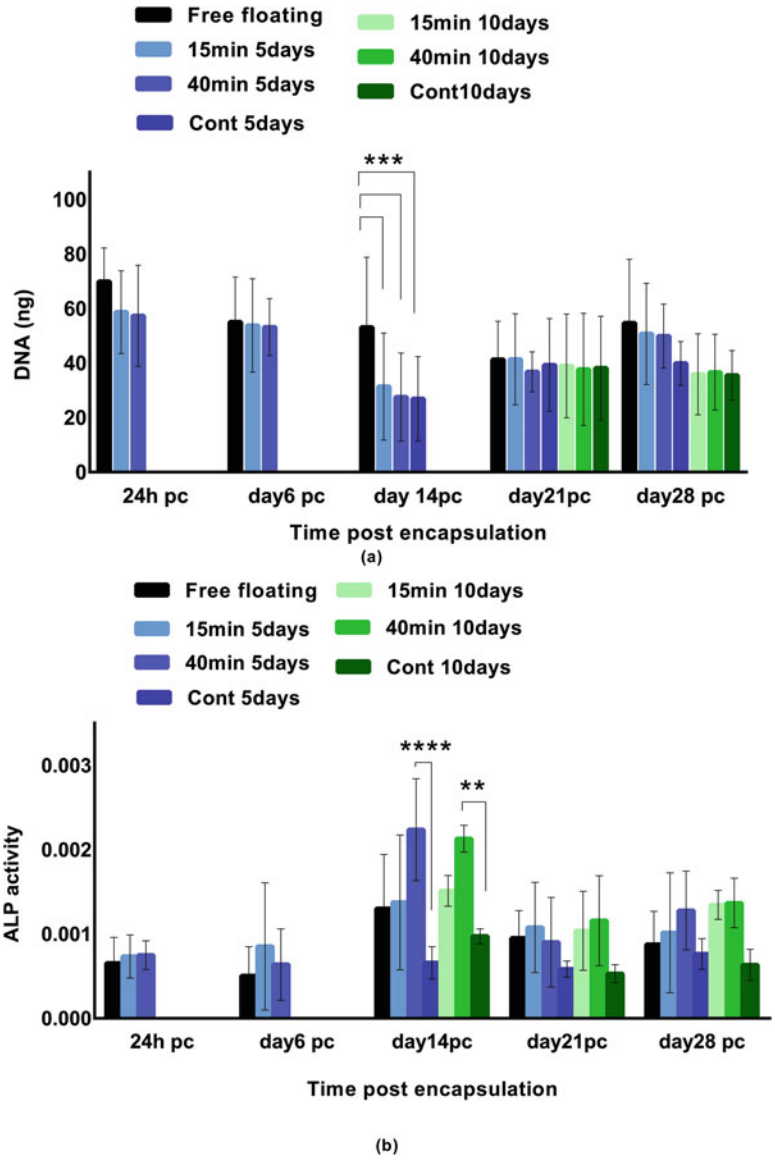

Fig. 6.7 Evaluation of cell viability and ALP activity of cells in loaded samples versus control over 28 day pc. (**a**) Total DNA content and ALP level of loaded samples in 15 min/day and 40 min/day for 5- and 10-day protocols were compared with controls. Total DNA concentration presented steady cell viability in all conditions during 28-day experiment with no significant changes between different time points. (**b**) ALP activity reported significantly higher in loaded samples of 40 min in both 5- and 10-day loading regimes on day 14 pc in comparison with other conditions. Enzyme activity of all experimental conditions dropped to the lower level from day 21 pc onwards. * indicates statistical significance (****$p \leq 0.0001$, ***$p \leq 0.001$, **$p \leq 0.01$). Data is mean SD, $n = 9$

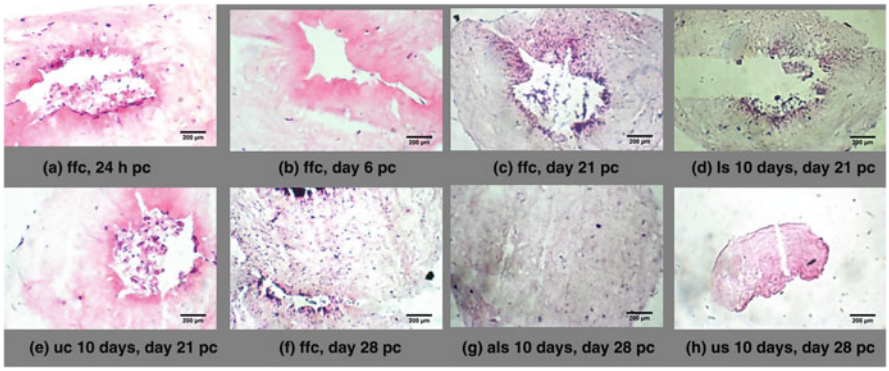

Fig. 6.8 (**a**) 24 h post encapsulation, (**b**) day 6 post encapsulation, (**c**), (**d**) and (**e**) at day 21 post encapsulation, (**f**), (**g**) and (**h**) at day 28 post encapsulation

followed the same trend for ALP activity level which was normalized to the total DNA content of each sample. The ALP level in 5- and 10-day loading regimes, 40 min/day loaded samples, surged significantly up to 40% ($p \leq 0.0001$) of controls and 15 min/day sample activity level on day 14 pc. The enzyme level dropped to around 0.001 in free floating while 40 min/day loaded samples of 10 day regime presented marginally highest enzyme activity. In addition, all 10-day loading cycle samples showed slightly higher ALP activity levels compared to other conditions on day 28 pc, but no statistical significance was found between these experimental groups on day 28 pc. Interestingly, both 5- and 10-day unloaded controls that remained in the PDMS chamber presented marginally greater ALP level than free-floating controls from day 14 pc onwards.

In contrary, ALP staining of sample cross sections revealed slightly different results as free-floating controls exhibited more intense purple colour on days 21 and 28 pc compared to other conditions as indicated in Fig. 6.9. Also, ALP colour intensity was considerably higher in loaded samples of adjusted strain of 40 min/day in 10-day loading regime in comparison with constant loading protocol and unloaded controls on day 28 pc. In addition, H&E staining of microsphere cross sections presented darker sections in the loaded samples that were subjected to the adjusted loading regime compared with constant protocol and unloaded controls as shown in Fig. 6.8. Microscopic images of free-floating control cross sections also showed higher intensity of stains from day 21 pc (Fig. 6.9).

Also, all 10-day loaded samples showed slightly higher ALP activity levels compared to other conditions on day 28 pc, but no statistical significance was observed. Also osteogenesis and mineralization of extracellular matrix supported by manifesting significantly greater calcium and phosphorous concentration and higher intensity of alizarin red and ALP staining on day 28 pc in compressed sample compared to controls. Interestingly, 5-day controls that remained in the PDMS chamber without being compressed presented marginally greater ALP level than free-floating controls from day 14 post encapsulation onwards.

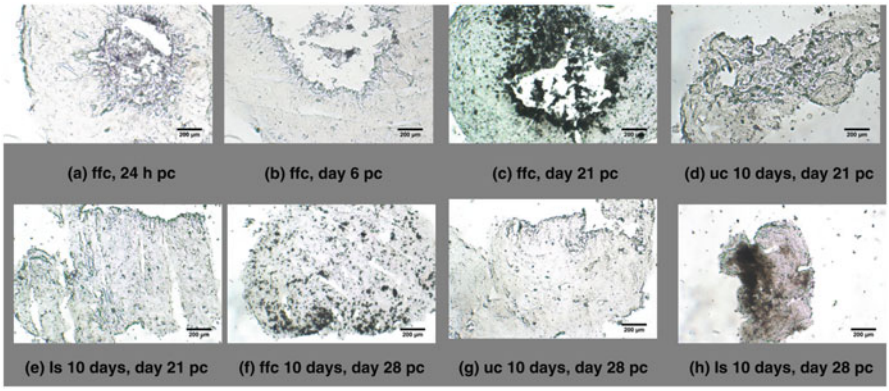

Fig. 6.9 (**a**) 24 h post encapsulation, (**b**) day 6 post encapsulation, (**c**), (**d**) and (**e**) at day 21 post encapsulation, (**f**), (**g**) and (**h**) at day 28 post encapsulation

6.4.6 Mechanical Stimulation Increases Bone Mineralized Extracellular Matrix Deposition

Hydroxyapatite $Ca_{10}(PO_4)_6(OH)_2$ crystals are one of the main components of human skeleton and are an important substance of extracellular matrix. To assess osteogenetic differentiation of hES-MPs under dynamic loading, extracellular matrix calcium and phosphorous (as key parts of hydroxyapatite molecular structure) were quantified.

Mineralization was detected from day 21 and showed significant increase on day 28 pc (Fig. 6.10a, b). Loaded samples presented the highest calcium level compared to the controls on day 28 which was nearly twice as much as detected calcium in free-floating and 10-day controls (25,000 μg/L, $p < 0.0001$). In addition, the calcium level of 10-day unloaded controls on day 28 pc was reported to be around 25% more than free-floating controls. It seemed that optimizing the loading protocol by subtracting the calculated PDMS plastic elongation from 10% global imposed strain can elevate the manifestation of mineralization by more than 70% within a week of applying 40 min/day 10-day loading regime.

The calcium quantification results were further backed up by alizarin red staining of treated and untreated sample cross sections. Both compressed sample and free-floating controls presented more intense red colour in comparison with 10-day controls on days 21 and 28 pc (Fig. 6.11a). Extracellular matrix phosphorous concentration followed same trend as calcium in which its level was first detected by day 21 and peaked on day 28 pc (Fig. 6.11b). Interestingly free-floating controls presented higher phosphorous amount than that of other conditions on day 21 (nearly 500 μg/L), but loaded sample manifested the highest phosphorous level after an 80% increase on day 28 pc. The finding was in parallel with calcium concentration on day

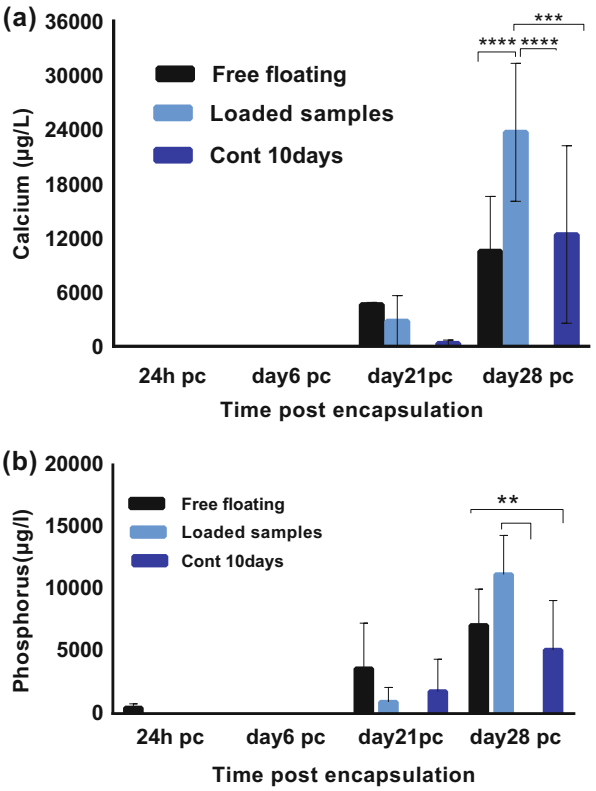

Fig. 6.10 Evaluation of deposited extracellular matrix calcium and phosphorous in loaded samples of 40 min/day in 10-day loading regime versus controls over 28 days pc, (**a**) measurement of deposited calcium in the loaded samples compared with controls, (**b**) comparison of phosphorous level in the loaded samples versus controls, * indicates statistical significance (****$p < 0.0001$, ***$p < 0.001$, **$p < 0.01$). Data is mean ± SD, $n = 9$

28. However, free-floating controls exhibited higher phosphorous level than 10-day controls (33% $p < 0.001$) which was in contract with calcium quantification results.

6.4.7 Dynamic Loading Promotes Extracellular Collagen Fibre Reorientation and Alignment

The reorientation and more aligned organization of collagen fibres in compressed samples were substantially more evident on day 21 pc, while control free-floating samples and control samples that were kept in PDMS chamber presented more visible dense collagen fibres with random orientation and reorganization (Fig. 6.12). It was more evident that cells and newly laid down collagen fibres were mostly located at 10–20 µm from the microspheres surface. All conditions noticeably showed different collagen fibre organization in later time point in comparison with free-floating controls on day 6 pc. Nevertheless, it was impossible to identify the axis of imposed strain due to random rotation of collagen microsphere in PDMS chamber during and after dynamic loading regime.

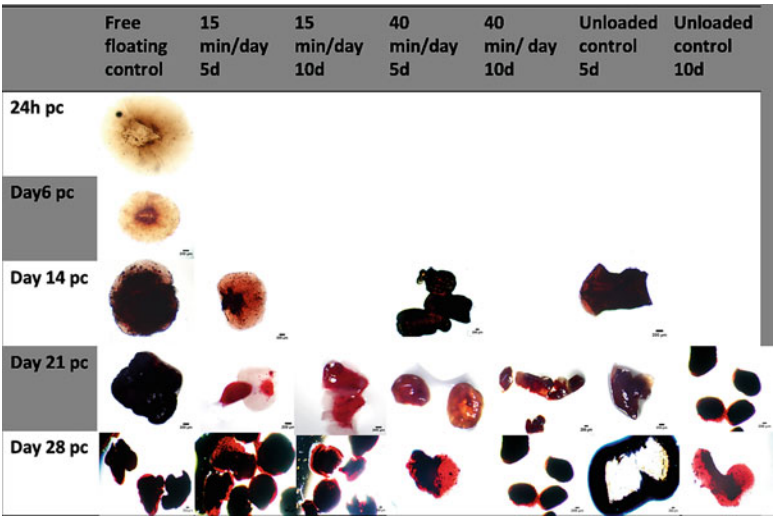

Fig. 6.11 Alizarin red staining of hES-MP-seeded collagen microspheres loaded under constant loading protocol versus controls over 28 days pc. Both 15–40 min/day loaded samples of 5- and 10-day experiment presented higher accumulation of deposited alizarin red stain compared to unloaded controls from day 21 pc onwards. (All images were taken by light microscope, 20×)

Surface structure of collagen microsphere, cellular elongation and extracellular matrix reorganization of collagen fibres were further assessed by SEM microscopy (Fig. 6.13). Collagen fibres of microspheres were visibly thinner compared to extracellular matrix fibres on day 28 pc and showed more distinct organization of fibres as compared to day 6 pc.

Many studies reported the effect of longitudinal stretching on the osteogenesis of stem cells (Yang et al. 2010; Ngiam et al. 2010a), while others revealed how compression could induce chondrogenic differentiation (Mauck et al. 2007). Still, to the author's knowledge, no studies reported the effect of compression on osteogenic differentiation of stem cells in soft scaffold. Therefore, analysing the combined effects of tensile and compression loading on the cell-seeded microspheres was a main focus of this study.

A loading regime consisting of 10% global strains for 15 min/day and 40 min/day for 5 and 10 days at 1 Hz was applied to cell-seeded microspheres as suggested by literature (Delaine-Smith and Reilly 2011) (Mouw et al. 2007). The reason behind the selection of 15 and 40 min/day loading cycles was to evaluate how duration of loading can influence the osteogenic differentiation. Also, to examine how long and how frequent, progenitor cells needed to be mechanically loaded to sense and respond to the stimuli and how repetition of load can encourage the mineralization of hES-MPs. 40 min/day loading was chosen over 1 h as 40 min was the longest time hES-MPs survived without CO2 and added buffer agents.

Mechanical properties and plastic elongation of PDMS chamber were characterized by DIC Kelkins software and repeated cycles of ramp and sinusoidal waves.

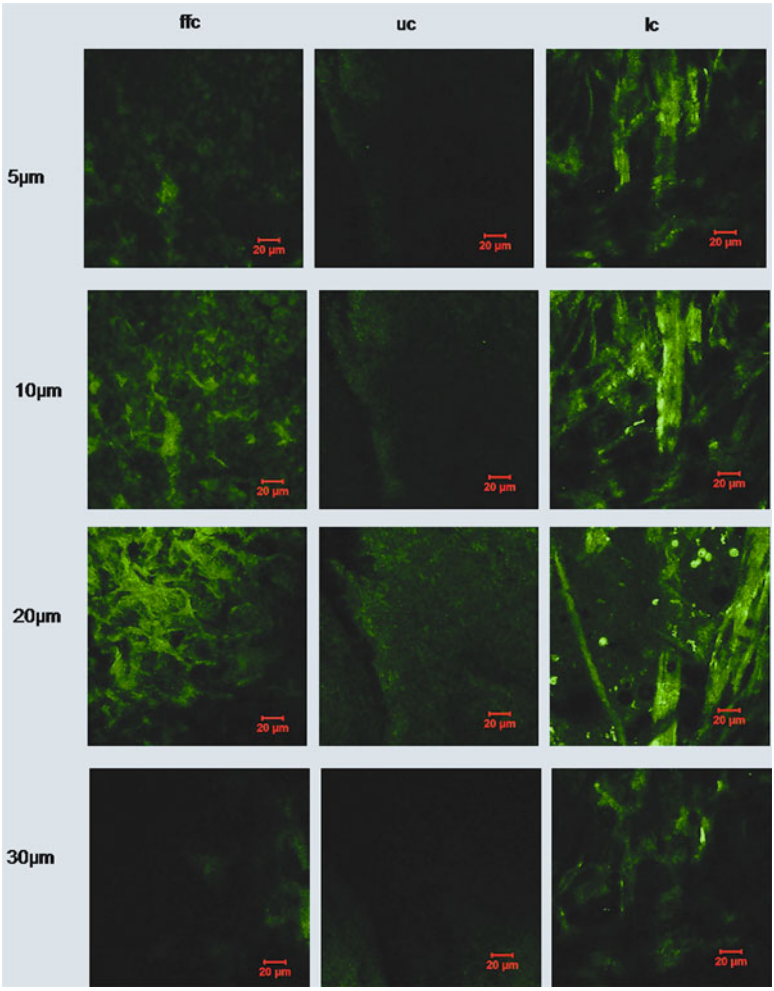

Fig. 6.12 SHG microscopic images of reorientation and alignment of collagen fibres on day 21 pc in 10-day cyclic loading experiment. SHG signal intensity was higher in loaded samples compared to the controls. *ffc* free-floating control, *uc* unloaded control, *lc* adjusted loading sample. Collagen fibres of loaded sample in adjusted protocol visibly reorganized and aligned in comparison with more random organization of collagen fibre in other conditions. Settings for images taken at 50–75 μm on all samples were optimized to visualize collagen SHG. (All images were taken by confocal microscope, EC 40×/1.3 plan-Neofluar oil DIC)

These findings then were employed to optimize the loading protocol as deducting the calculated plastic elongation of polymer guaranteed the transmission of more homogeneous global load to the microspheres. In addition, subtracting the PDMS plastic elongation eliminated the persistent appearance of longitudinal strains with the negative load of up to −5 N showing in the load displacement graph. It also reduced

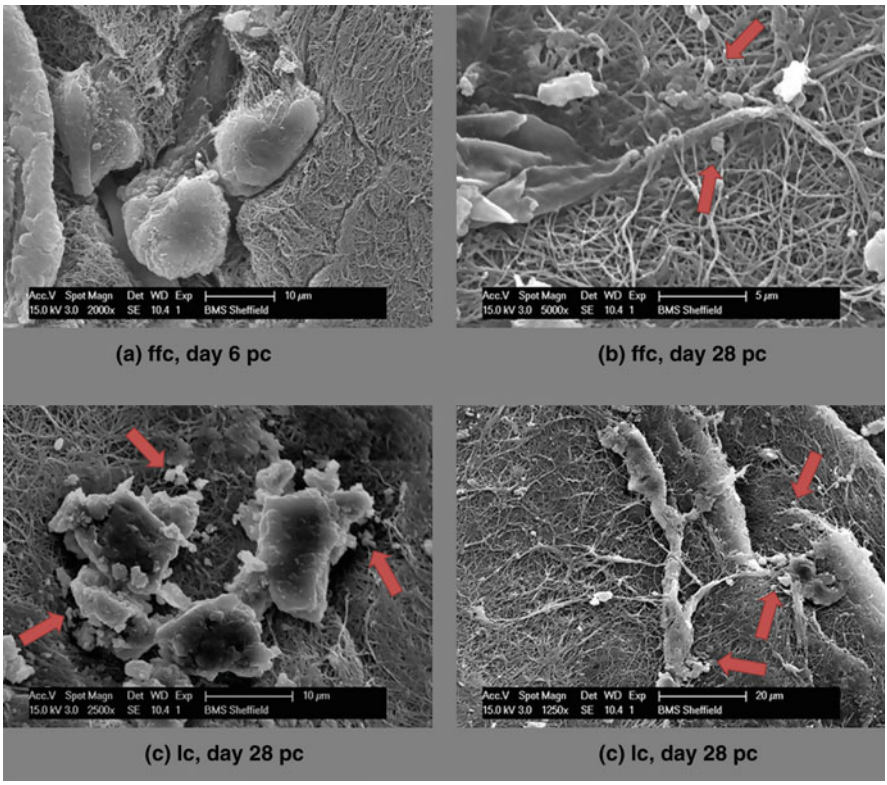

Fig. 6.13 (**a**) At day 6 post encapsulation, (**b**), (**c**) and (**d**) at day 28 post encapsulation

the inter-variabilities between repeats of experiment and 15 min/day and 40 min/day loading cycles as our results indicated a larger plastic deformation in 40 min/day loading chamber.

Alkaline phosphatase activity level is an early stage mineralization marker in osteogenic differentiation (Golub and Boesze-Battaglia 1992) that works through its enzymatic hydrolysis activity (Sugawara et al. 2002). Several studies demonstrated a growth in the cellular ALP activity in the presence of osteogenic supplements, while it has been shown that shear stress had no effect on the cellular ALP levels in non-osteogenic conditions (Yourek et al. 2010). Grellier et al. revealed that hMSCs that were subjected to short bouts of FSS (30 min) in osteogenic conditions can upregulate ALP mRNA, but 90-min exposure had an opposite effect (Grellier et al. 2009).

Furthermore, Sittichokechaiwut et al. suggested that compression loading at 5% global strain of seeded hMSCs on a porous scaffold increased ALP activity in non-osteogenic medium compared with the unloaded controls in static and osteogenic conditions (Sittichokechaiwut et al. 2010), while others showed tensile loading

of MSCs in polyurethane scaffold upregulated the ALP activity in non-osteogenic conditions (Friedl et al. 2007). The results of these studies clearly suggested that the effect of mechanical stimulation on ALP activity level and the downstream signalling events of ALP are complex.

Interestingly free-floating control enzyme level was much higher than the unloaded controls in both constant and adjusted strain protocols. One explanation would be that collagen microspheres and cells in free-floating controls experience the combined effects of shear stress and hydrostatic pressure as opposed to the confined space of loading chamber that might encourage a considerable change in the ALP activity level at different time points (Hess et al. 2010).

Mineralization was assessed based on the concentration of deposited calcium, phosphorous and zinc levels in the extracellular matrix. Calcium concentration was highest in all conditions on day 28 pc and cells that were subjected to adjusted cyclic loading showed greatest calcium accumulation in comparison with other experimental conditions. These findings were in agreement with the alizarin staining of sample cross sections, while the results of alizarin staining of microspheres were not conclusive due to the same colour intensity of the deposited stains that was reported in controls and loaded samples and between earlier and later time points of encapsulation. Stimulation of cells under adjusted loading protocol was significantly superior owing to the highest upregulation of phosphorous accumulation in loaded samples of the adjusted loading protocols on days 21 and 28 pc and was in agreement with the results of calcium deposition.

6.5 Conclusions

Applying mechanical stimulation can effect cell commitment, but at the same time, it shows that mechanical loading on its own fails to provide all necessary signals important for cell commitment and osteogenic differentiation of hES-MPs as compared to chemical stimulation. Combining mechanical and chemical stimulations can increase the osteogenesis as suggested in previous chapters and other studies. It was shown that loading of very low cell number seeded on soft natural scaffold can encourage osteogenesis of undifferentiated cells by enhancing both early stage bone marker and extracellular mineral deposition of calcium, phosphorous and zinc. Monitoring alkaline phosphatase level reported significant increase in the enzyme activity by day 14 pc in loaded samples compared to free-floating controls. Staining of cross section further confirmed the enhancement of mineral deposition in the loaded samples in comparison with other experimental conditions at the later time points. In addition, SHG microscopic images revealed more defined, aligned and reorganized lay-down of new ECM in the loaded samples on day 21 pc compared with other conditions. Nevertheless, better handling of collagen beads is required as hydrogel soft geometry could easily be affected by transferring microspheres to the loading chamber. Due to very small size and lightweight of microspheres, collagen microspheres may rotate through loading chamber and may cause non-homogeneous

transfer of forces to the cells as shown in histological staining of microspheres. Therefore, cells in different areas of a microsphere may experience more random mechanical forces and respond differently to the applied load.

Although this study revealed strong links between the deposited extracellular minerals and osteogenic differentiation, more osteogenic-specific protein quantification is required to define a complete signalling pathway(s) consisting of genes, proteins and deposited minerals in mechanotransduction and osteogenesis process. Therefore, gene expression studies (qPCR) of bone and early stage mineralization markers including ALP, osteocalcin, osteonectin, Runx, BMPs and ColI and ColII along with phenotyping of differentiated cells are recommended in the future. Furthermore, studying the combined and individual effects of applying direct cyclic loading with fluid flow and shear stress on cells is required to draw the map of load transfer between different layers of collagen microspheres and cells.

Also, more sample imaging for different time points and several areas/focal planes within each sample is needed to comment more accurately on the effect of sample variability in cell triggered remodelling of collagen fibres. Application of cyclic loading on 3D culture of hES-MP cells could be used as a model to study the effect of mechano-stimulation on osteogenesis both in vitro and in silico.

References

Barron MJ, Tsai C-J, Donahue SW (2010) Mechanical stimulation mediates gene expression in MC3T3 osteoblastic cells differently in 2D and 3D environments. J Biomech Eng 132 (4):041005

Brouzes E, Medkova M, Savenelli N, Marran D, Twardowski M, Hutchison JB, Rothberg JM, Link DR, Perrimon N, Samuels ML (2009) Droplet microfluidic technology for single-cell high-throughput screening. Proc Natl Acad Sci U S A 106(34):14195–14200

Chan BP, Hui TY, Yeung CW, Li J, Mo I, Chan GCF (2007) Self-assembled collagen-human mesenchymal stem cell microspheres for regenerative medicine. Biomaterials 28 (31):4652–4666

Delaine-Smith RM, Reilly GC (2011) The effects of mechanical loading on mesenchymal stem cell differentiation and matrix production. Vitam Horm 87:417–480, 1st edn

Uludag H, De Vos P, Tresco PA (2000) Technology of mammalian cell encapsulation. Adv Drug Deliv Rev 42:29–64

Friedl G, Schmidt H, Rehak I, Kostner G, Schauenstein K, Windhager R (2007) Undifferentiated human mesenchymal stem cells (hMSCs) are highly sensitive to mechanical strain: transcriptionally controlled early osteochondrogenic response in vitro. Osteoarthr Cartil 15 (11):1293–1300

Golub EE, Boesze-Battaglia K (1992) The role of alkaline phosphatase in cartilage mineralization. Bone Miner 17(2):273–278

Grellier M, Bareille R, Bourget C (2009) Responsiveness of human bone marrow stromal cells to shear stress. J Tissue Eng Regen Med 3:302–309

Hess R, Douglas T, Myers KA, Rentsch B, Rentsch C, Worch H, Shrive NG, Hart DA, Scharnweber D (2010) Hydrostatic pressure stimulation of human mesenchymal stem cells seeded on collagen-based artificial extracellular matrices. J Biomech Eng 132(2):021001

Hong S, Hsu H-J, Kaunas R, Kameoka J (Sep. 2012) Collagen microsphere production on a chip. Lab Chip 12(18):3277–3280

Juhásová J, Juhás S, Klíma J, Strnádel J, Holubová M, Motlík J (2011) Osteogenic differentiation of miniature pig mesenchymal stem cells in 2D and 3D environment. Physiol Res 60(3):559–571

Kearney EM, Farrell E, Prendergast PJ, Campbell VA (2010) Tensile strain as a regulator of mesenchymal stem cell osteogenesis. Ann Biomed Eng 38(5):1767–1779

Mauck RL, Byers BA, Yuan X, Tuan RS (2007) Regulation of cartilaginous ECM gene transcription by chondrocytes and MSCs in 3D culture in response to dynamic loading. Biomech Model Mechanobiol 6:113–125

Mouw JK, Connelly JT, Wilson CG, Michael KE, Levenston ME (2007) Dynamic compression regulates the expression and synthesis of chondrocyte-specific matrix molecules in bone marrow stromal cells. Stem Cells 25:655–663

Ngiam M, Liao S, Ong Jun Jie T, Sui X, Dong Y, Ramakrishna S, Chan CK (2010) Effects of mechanical stimulation in osteogenic differentiation of bone marrow-derived mesenchymal stem cells on aligned nanofibrous scaffolds. J Bioact Compat Polym 26:56–70

Ruszczak Z (2003) Collagen as a carrier for on-site delivery of antibacterial drugs. Adv Drug Deliv Rev 55(12):1679–1698

Sittichokechaiwut A, Edwards JH, Scutt a M, Reilly GC (2010) Short bouts of mechanical loading are as effective as dexamethasone at inducing matrix production by human bone marrow mesenchymal stem cell. Eur Cell Mater 20:45–57

Sugawara Y, Suzuki K, Koshikawa M, Ando M, Iida J (2002) Necessity of enzymatic activity of alkaline phosphatase for mineralization of osteoblastic cells. Jpn J Pharmacol 88(3):262–269

Di Lullo GA, Sweeney SM, Korkko J, Ala-Kokko L, San Antonio JD (2002) Mapping the ligand-binding sites and disease-associated mutations on the most abundant protein in the human, type I collagen. J Biol Chem 277(6):4223–4231

Jacobsen KA, Al-Aql ZS, Wan C et al (2008) Bone formation during distraction osteogenesis is dependent on both VEGFR1 and VEGFR2 signaling. J Bone Mineral Res 23(5):596–609. https://doi.org/10.1359/JBMR.080103

Tian X-F, Heng B-C, Ge Z, Lu K, Rufaihah AJ, Fan VT-W, Yeo J-F, Cao T (2008) Comparison of osteogenesis of human embryonic stem cells within 2D and 3D culture systems. Scand J Clin Lab Invest 68(1):58–67

Yang X, Gong P, Lin Y, Zhang L, Li X, Yuan Q, Tan Z, Wang Y, Man Y, Tang H (2010) Cyclic tensile stretch modulates osteogenic differentiation of adipose-derived stem cells via the BMP-2 pathway. Arch Med Sci 6:152–159

Yourek G, McCormick SM, Mao JJ, Reilly GC (2010) Shear stress induces osteogenic differentiation of human mesenchymal stem cells. Regen Med 5(5):713–724

Chapter 7
Collagen Gel Cell Encapsulation to Study the Effect of Fluid Flow on Mechanotransduction

Mesenchymal stem cells (MSCs) are widely implicated for their potential use as a cell source for tissue engineering of skeletal tissue in regenerative medicine and tissue engineering. Mechanical forces from the microenvironment have a significant influence on differentiation of MSCs, and the resulting mechanotransduction would provide crucial adjuncts to standard biochemical signalling pathways. Combining microfluidic systems with mechanical stimulation for osteogenesis represents both a scientific and technological innovation that would greatly impact the field of regenerative medicine. We demonstrate a microfluidic chamber design for mechanical stimulation of flexible cellular microspheres and possibly a high-throughput microfluidic system for parallel processing of stem cell aggregation. We also showed that collagen microspheres serve an efficient cell delivery device supporting cell viability and migration post encapsulation.

A microfluidic chamber was made of PDMS with a central compression channel (0.6–0.9 mm). Bovine collagen type I with concentrations of 2 mg/ml and 2450 human embryonic mesenchymal stem progenitors (hES-MPs)/2.5 μl droplet was produced through gelation.

The microspheres were passed through the constriction at a flow rate of 320 μl/min for three cycles/day for 3 days starting at day 3 post encapsulation. Also effect of fluid sheer stress on the osteogenic differentiation of hES-MPs collagen microspheres was investigated using shaker and rocker systems. Cell viability, proliferation and bone markers alteration were monitored before and after compression.

7.1 Microfluidic System

7.1.1 Introduction

Current approaches for generation of mechanical stimulation imply dynamic bioreactor culture systems, for in vitro culture and differentiation of tissue engineering constructs. Compared with static bioreactor system, dynamic bioreactors can enhance the mass transport of nutrients to the cells. In addition, cells that are subjected to the mechanical stimulation of dynamic media flow showed augmented

© Springer Nature Singapore Pte Ltd. 2019

D. Lacroix et al., *Multiscale Mechanobiology in Tissue Engineering*,
Frontiers of Biomechanics 3, https://doi.org/10.1007/978-981-10-8075-3_7

osteogenesis and mineralization (Gomes et al. 2003). Because of bioreactors bulkiness and their limitation in processing large number of samples at the same time, microfluidic devices are ideal to overcome these restrictions and improve the overall efficiency of dynamic bioreactor systems. Many studies have reported the numerous applications for microfluidic systems in biochemical analysis, chemical reactions and cell-based assays (Vincent and Engler 2013; Huebsch et al. 2010). The advantage of using this system over conventional benchtop systems includes reduced size of operating systems, its flexibility in design modification, lower reagent consumption, lower waste production and power requirements to operate, disposability, increased speed of analyses and system portability. One key factor in designing a functional microfluidic device is the type of material used for the fabrication of the device. This material should be economical and compatible with microfabrication techniques, while being perfectly matched with micrometre-scale structure and allowing the integration of functional components. In addition, chamber will enable chemical and mechanical stimulation of cells in a controlled environment, while reducing the overall volume of the systems enabling both reduction in cost and possibility of high-throughput testing.

Popular polymers that have been used to fabricate microfluidic systems include polydimethylsiloxane (PDMS), polyurethane, polyvinyl chloride, polymethyl methacrylate (PMMA), polyethylene terephthalate glycol (PETG), polycarbonate, polyethylene and polystyrene (Augello and Bari 2010).

Soft-polymeric systems, particularly systems made in polydimethylsiloxane (PDMS), present many desirable properties for use in microfluidic devices. Soft lithography is a commonly used technique in fabrication of PDMS which involves elastomeric polymer moulding by rapid prototyping of microfluidic devices. PDMS-made devices are easily integrated with outside components due to compatibility of this polymer with most materials. Because of its temperature stability in biological ranges (40–95 °C), PDMS have vast applications in processes requiring temperature gradient. PDMS optical transparency has made it compatible with conventional imaging techniques and optical detection methods in the visible and UV region. PDMS channels are perfectly suited for protein, cell-based and biological assays due to their permeability to gases and their nontoxic nature. Some of PDMS properties may be unfavourable in some applications including its elastomeric nature that may cause shrinkage or sagging of device features (Odom et al. 2002). In addition PDMS incompatibility with many organic solvents may affect the nonspecific adsorption in biological samples which could be rectified by improving its surface chemistry (Uludag et al. 2000).

Soft lithography technique is currently moving towards commercialization with using PDMS microfluidic chips to develop DNA, protein and cell-based assays accompanied by fabricating the microfluidic analytical systems which is indeed an indication of great growing area of interest in polymeric microfluidic systems. Our aim was to design a highly compatible microfluidic system for parallel processing of MSCs aggregation. Such a system would allow optimizing mechanical stimulation and fluid flow regime critical in mediating hES-MPs osteogenic differentiation.

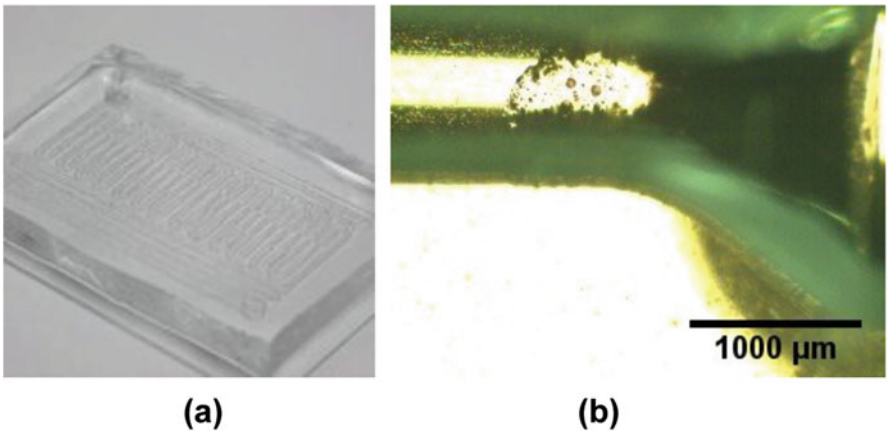

Fig. 7.1 (**a**) PDMS-made microfluidic device, (**b**) higher magnification

7.1.2 Material and Methods

7.1.2.1 Microfluidic Chamber Design

Different approaches were applied to build a microfluidic channel consisting of one main channel with 1 mm diameter and constraining channel of 0.5 mm (Fig. 7.1). Glass capillary and shrinking tubes, dough-covered tubes and 3D printing methods in PDMS were examined to obtain the most accurate design. The microfluidic chamber design was further optimized by using brass rod as templates to make a PDMS-made compression chamber with diameter ranging from 0.6 to 0.9 mm. This diameter range enabled to build more specific channel for each experiment, according to the collagen microsphere contraction and their average diameter on day 6 post encapsulation, which minimized the inter-variability of average microsphere diameter in or between each experiment and repeats. Consequently, more unified compression forces would be delivered to cell-seeded microspheres.

To prepare PDMS a ratio of 10:1 of base to initiator was mixed together. The silanizing agent tridecafluoro-1h,1h,2h,2h-tetrahydrooctyl trichlorosilane was added to the surface of laser printed mould by vacuum deposition for 20 min. The PDMS was then poured on the mould containing slide in a container. The PDMS was cured 60 °C for 3 h and then peeled and removed from the slide.

A 2 mm biopsy punch was used to create the input/output channels. The polymer channel was then bound irreversibly to a glass slide using an air plasma machine 50 W for 2 min. Flexible silicone tubes 2 mm external diameter and 0.5 mm internal diameter were inserted into the channels to pump the calculated flow to the chamber using 5 ml syringes and syringe pumps. 70% ethanol was passed through the chamber several times and rinsed with PBS before overnight treatment with 1.5 mg/ml bovine serum albumin (BSA). Based on the computational modelling, the chamber diameter was calculated and made in such a way that it was

approximately 50–80 μm smaller than the diameter of cell-seeded collagen beads on day 6 post encapsulation. This would ensure that collagen microspheres would not get damaged and torn apart by being squeezed too hard through PDMS chamber. The diameter of chamber, therefore, varied broadly from 550 to 850 μm to fit the experiment more accurately.Flow rate was initially set to 8.49 mm/s, to pump the collagen microspheres in to the microfluidic chamber which was later reduced by 20% to 6.79 mm/s and further 20% decrease to 5.43 mm/s using the equation below:

$$\dot{m} = \cdot\rho \cdot \times \cdot v \cdot \times \cdot A$$

when $\dot{m}$ is the mass flow rate kg/s, ρ is the density kg/m^3, v is the flow velocity mm/s and A is the cross-sectional vector area/surface m^2.

7.1.2.2 Cellular Assays

Cell culture: hES-MP cells were grown in T75 gelatin-coated flasks in basal media culture which contained Dulbecco's alpha minimum essential medium (α MEM) from Sigma-Aldrich supplemented with 10% foetal bovine serum (FBS), 1% L-glutamine (G) and 1% streptomycin penicillin (P/S) (v/v). Passages 4–8 of hES-MPs were detached by 0.05% Trypsin/25 mmol EDTA to be used in microcapsulation.

Cell seeding density: hES-MP cells were used between passages 3 and 7. Cell lines seeding density were 5×10^5 cells/ml that were embedded on collagen microspheres with bovine collagen I concentration of 2 mg/ml.

Cell viability and proliferation: total DNA per sample was assessed by DNA PicoGreen assay at 8 h, days 6, 14, 21 and 28 post encapsulation.

Dynamic compression: hES-MP-seeded collagen microspheres were forced through PDMS-made chamber with a flow rate 100 μl/min for three cycles/day for 5 days from day 6 post encapsulation using syringe pumps.

7.1.2.3 Statistics

All experiments were performed three times in triplicates ($n = 9$). PDMS chamber visualization was performed by bright-field filter on two or three samples of each condition during experimental repeat. Cell viability at different time points, ALP and mineralization comparison as well as statistical differences between free-floating and compressed samples were completed using one-way ANOVA followed by Sidak's multiple comparisons test.

Determination of mineralization and osteogenesis: alkaline phosphatase (ALP) activity of samples and controls was measured to validate early stage mineralization and extracellular matrix calcium and phosphorous quantification done by inductively coupled plasma emission spectrometry (ICP-ES) on 24 h, day 6, day 21 and day 28 post encapsulation.

7.1.3 Results and Discussions

7.1.3.1 Microfluidic System Can Induce Osteogenesis of Human Embryonic Mesenchymal Stem Progenitors by Increasing Early Stage Bone Marker

The aim of this study was to design a microfluidic chamber as an alternative to bulkier bioreactors to apply mechanical loading to cell-seeded collagen constructs and stimulate hES-MPS osteogenic differentiation. Many studies showed the importance of integrating mechanical force and fluid flow to the cell's microenvironment to influence stem cell fate and induce the osteogenic differentiation.

Recently, microfluidic systems have been used to study the effect of these forces and fluid flow, in particular, in stem cell commitment. Nonetheless, most of these researches employed either 3D stem cell culture and microfluidic devices to mimic flow condition or microfluidic system to produce 3D microdroplets for tissue engineering applications (Ma et al. 2014). Different approaches were implemented in building a microfluidic chamber from soft lithographic technique to rapid prototyping and replica moulding to achieve appropriate geometry, height and surface structure. Our results indicated that the best outcome was attained when metal rod was used as a replica, while other approaches failed to provide required height and surface smoothness for the chamber. Despite the reports from Wong et al. and Windvoel et al. on surface modification via physical adsorption for prevention of protein nonspecific binding, washing the chamber with BSA proved ineffective in preventing collagen microsphere entrapment in the channel (Wong and Ho 2009; Windvoel et al. 2010). Furthermore, Cecchet et al. and Choi et al. studies revealed that treating the chamber with graft polymer coating of PEG or self-assembled monolayer of PEG-silane could amplify the hydrophilicity and protein resistance through formation of self-assembly of poly(ethylene glycol methyl ether) (MPEG) film that leads to bonds between the substrate and the PDMS layer (Cecchet et al. 2006; Choi et al. 2003). Yet, PEG treatment did not show any positive effect on alteration of surface chemistry, hence prevention of collagen attachment to the chamber. Surface roughness can also be modified at the nanoscale through acetone vapour polishing that involved immersion of PDMS mould or 3D print template into an acetone bath and enhancing the hydrophilicity. However, our results showed that acetone vapour technique was unsuccessful in improving surface smoothness. The height of chamber was calculated according to the measurement of collagen microspheres average diameter on day 6 pc to ensure a uniform compression load was sensed by all samples and to reduce the variability between repeat experiments. Still, changing the height of channel without adjusting the flow rate meant that the cells would be subjected to different shear stress conditions. Therefore, the outcome of this experiment could be inconsistent due to application of non-identical mechanical stimulation regime on hES-MPs.

The collagen microspheres that passed through the microfluidic chamber showed good cell viability over 28 days post encapsulation (Fig. 7.2a). Early increase in cell

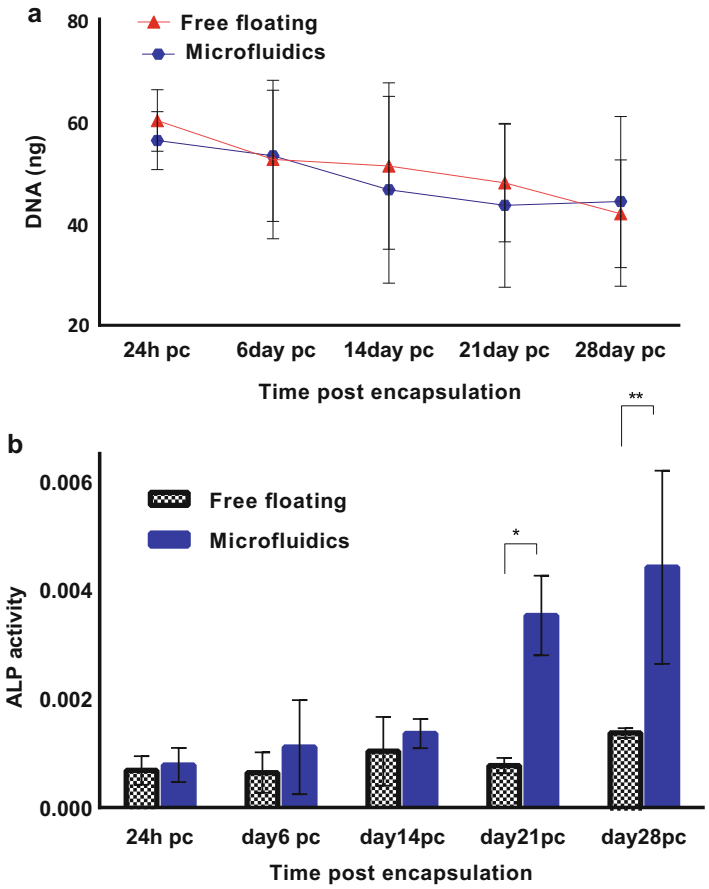

Fig. 7.2 (**a**) Cell proliferation comparison between free-floating controls and microfluidic samples; (**b**) alkaline phosphatase activity of free-floating controls and compressed sample was assessed by fluorometric assay. * indicates statistical significance (*$p < 0.01$, **$p < 0.001$). Data is mean ± SD for nine samples

proliferation was reported after day 6 and peaked by the total DNA content of 50 ng on day 14 pc. Cell growth then reached a plateau with a marginal fluctuation between day 21 and day 28 post encapsulation, while cell proliferation of free-floating controls presented a steady drop over the same period of time. DNA content was reduced from over 60 ng on 24 h post seeding to just below 40 ng on day 28 which indicated the positive effect of microfluidic system on viability and proliferation of hES-MP cell line.

Assessing alkaline phosphatase activity of compressed and control sample revealed that this early stage mineralization marker level enhanced considerably over 28 days post encapsulation (Fig. 7.2b). ALP activity of compressed sample showed an increase up to fivefold by day 28, while in free-floating controls, ALP

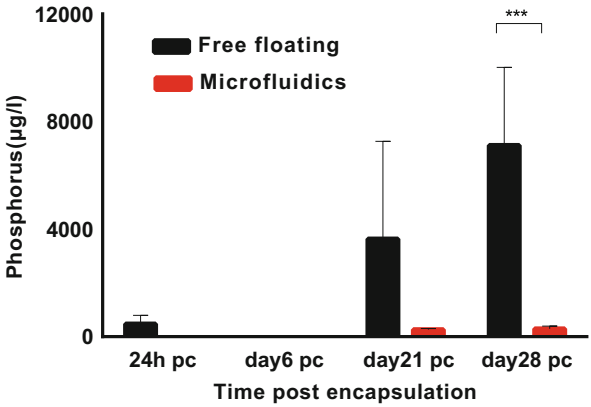

Fig. 7.3 Evaluation of deposited extracellular matrix phosphorous level between microfluidic compressed samples and free-floating controls over 28 days pc. * indicates statistical significance (***$p < 0.0001$). Data is mean ± SD for nine samples

peaked on day 14, dropped to half of its value on day 21 (0.0005) and reached the same level as day 14 on day 28 (0.001). Although both sample and control groups manifested similar ALP activity on day 14 (just above 0.001), compressed sample presented up to four times increase in alkaline phosphatase level on day 21 (0.004, 0.0005 p value <0.01) compared to controls, and this figure also remained significantly higher on day 28 post encapsulation (0.005 and 0.001, respectively, p value <0.001). Our finding indicated that the mineralization was still an ongoing event in compressed group, long after the completion of compression stimulation on day 11 post encapsulation, whereas free floating exhibited much earlier peak and on average very low ALP activity level per cell. Despite the high ALP activity level, the extracellular calcium level revealed to be undetectable as the concentration of calcium was well below the threshold on all samples. Nevertheless, ICP-MS detected phosphorous on days 21 and 28 post encapsulation but the level much lower than control group at the same time points (Fig. 7.3). Phosphorous values were up to four times higher in free-floating controls than compressed sample on day 21 (4000 µg/l and 1000 go/l, respectively, p value <0.01), and its level increased to nearly 8000 µg/l on day 28 in control group against 500 µg/l in compressed sample (p value <0.0001). Overall, phosphorous level was considerably lower compared to free-floating controls which was in disagreement with ALP results.

7.2 Effect of Fluid Flow

7.2.1 Introduction

When a fluid passes over the surface of an object, it generates fluid flow-induced shear stress (FSS). This force is believed to be one of the main mechanical stimuli in vivo and for bone in particular, as interstitial fluid movement in the lacunar-canalicular system can create high shear forces on osteocytes and trigger a

biochemical response to initiate remodelling (Klein-Nulend et al. 2005). In 2D systems, the most common system to apply shear stresses on monolayers of cells include an oscillating orbital shaker system, the cone and plate system, the parallel-plate flow chamber system, the rotating disc or radial flow devices and the rocking "see-saw" systems (Wang et al. 2010). In order to allow seeded cells on scaffold materials to experience the flow-induced shear forces, 3D culture bioreactors including rotating wall vessels, spinner flasks and perfusion systems have been designed (El Haj and Cartmell 2010) (see Chap. 1 for a review). In bioreactors the nutrients transfer to cells has been improved by forcing the media through the scaffold, and cells in the centre will receive a greater supply of nutrients. In perfusion system of both 2D and 3D culture, separating the effects of enhanced nutrient transfer from a direct mechanical effect of shear stress at the cell membrane still remains challenging. Bakker et al. investigated this in 2D bone cells by altering media viscosity so that for a given flow rate the shear stress is changed and showed that cell response mainly depended on shear stress and nutrient transport more than flow rate (Bakker et al. 2001). Applying similar technique in 3D, calcium phosphate porous scaffolds indicated that mineralized matrix deposition was dependent on both shear stress and flow rate (mass transport) and too high flow rate played an inhibitory role in extracellular matrix (ECM) deposition. For that reason, biochemical/nutrient movement alone cannot explain the effects of flow within perfusion systems on MSCs ECM production.

McCoy and O'Brien (2010) findings illustrated that MSCs seeded on 2D substrates are usually subjected to levels of shear stress around 0.1–2 Pa, while in 3D constructs these levels are often much lower (0.1 mPa–0.03 Pa). 3D perfusion systems apply fluid flow over the seeded constructs for the entire length of the culture period (Vangordon et al. 2011), whereas in 2D systems cells are subjected to shear forces more erratically and for relatively shorter amounts of time, for example, from 30 min to 24 h (Grellier et al. 2009). But recently Jaasma and O'Brien revealed that short bouts of flow applied to 3D scaffolds induced osteogenic differentiation in both MSCs and osteoblast (Jaasma and O'Brien 2008). This response may also vary with the type of flow, for example, both oscillatory flow and unidirectional steady flow tend to upregulate various mechanotransduction pathways in mature bone cells and also were shown to have a similar osteogenic effect on a pre-osteoblast cell line (Jacobs et al. 1998).

Grellier et al. work indicated the dual role of fluid shear forces in induction as well as enhancement of osteogenesis in MSCs (Grellier et al. 2009). By subjecting 1.2 Pa shear forces to human bone marrow mesenchymal stem cells (BMSCs) seeded in a parallel-plate flow chamber, precultured in osteogenic media, for 30 or 90 min, the measured ALP activity level was shown to increase. Thirty minutes of stimulation showed the highest levels, while Runt-related transcription factor 2 (RUNX2) expression level remained unchanged, and collagen I (COLI) gene expression was reported lower after applying the flow. Some studies, however, have pointed to inhibition of ALP activity by flow. Steady perfusion of 3D cell-seeded constructs

seems to induce ALP activity, with the highest response occurring at the earlier time points of 4–8 days before levelling off (Sikavitsas et al. 2003 and Vangordon et al. 2011). In 3D perfusion systems, ALP activity level is not affected by increasing the rate of shear forces; however, higher calcium production emphasizes that increasing the fluid shear force rather regulates later stages of differentiation and is essential for ECM formation more than for stimulation of differentiation (Gong et al. 2001). Also Augst et al. revealed an increase in COLI and calcium production in osteogenic differentiation of seeded human BMSCs on 3D silk scaffold subjected to 16 rpm of steady rotation for 6 weeks (Yadav et al. 2008).

Porosity, scaffold architecture and the mechanical properties of the scaffold can influence the forces experienced by seeded cells. Perfusion fluid forces (1 ml/min) applied to rat BMSCs that were seeded on titanium mesh scaffolds with 20 and 40 mm pore sizes revealed the highest levels of calcium produced at day 8 in the 40 mm mesh while the 20 mm mesh showing the highest levels at day 16. Van Gordon study also reported similar results with seeded rat BMSCs on PLA foam or fibrous scaffolds with different pore sizes that subjected to daily perfusion flow of 0.5 ml/min (Vangordon et al. 2011).

In brief, within a tissue-engineered scaffold, matrix distribution and/or production is enhanced when subjected to flow (Sikavitsas et al. 2003). However, it still not clear whether fluid flow alone is able to stimulate the necessary mechanical signals for differentiation of MSCs and matrix production or additional strain stimuli are required. Bearing in mind the significance of rest periods in mechanical loading to induce tissue formation, it can be emphasized that rest periods are vital in obtaining ideal stimulation regimens for MSCs; but the best rest periods to use within any specific MSC-stimulating flow regimen is yet to be identified (Srinivasan et al. 2002).

The aim of this study was to investigate the effect of shear stress on osteogenic differentiation of hES-MPs seeded soft collagen microspheres and to compare the effect of mechanical stimulation versus chemical stimulation in determining stem cell fate.

To further investigate the effect of chemical stimulation versus shear stress in osteogenic differentiation of hES-MPs, three conditions which consisted of fibroblast growth factor (FGF-β)-containing media, osteogenic media and stem cell media with no added FGF-β were compared together.

7.2.2 Methods

Orbital shaker experiment: each cell-seeded collagen microsphere fixed with a mesh sheet and metal ring and placed at the centre of each well in 12 well plates. The

shaker rotation regime involved 50 rpm for 40 min 10 days starting from day 6 post encapsulation and shear stress calculated using the following equation (Eq. 7.1):

$$\tau_{\max} = a\left(\eta\rho(2\pi f)^3\right)^{1/2} \tag{7.1}$$

where a is the orbital radius of rotation of shaker (5 mm), ρ is the density of culture medium (0.1 g/ml), η is the viscosity of the medium (10^{-3} Pa s) and f is the frequency of rotation (50 rpm equal to 1.2 rotation/s).Shear stress was calculated at the centre of well as 0.0597 Pa.

Rocker experiment: rocker regime consisted of 45 cycles/min for 40 min during 10 days and was started on day 6 post encapsulation. The following equation was applied to calculate characteristic shear stress, defined as the shear stress at the centre of dish bottom when the dish is horizontal, ($\theta = 0$, $x = 0.5$ L) (Eq. 7.2):

$$\tau_w = (3\pi\mu\theta_{\max})/\left(4\delta^2 T\right) \tag{7.2}$$

where μ is the fluid viscosity (10^{-3} Pa.s), $\theta_{\max}$ is the maximal flip angle (the rocking platform had a maximum tilt angle of 6°), δ is the ratio of the fluid depth to the wall length (3 ml and 7 ml respectively) and T is the time for one cycle. This model assumed that fluid movement was mainly caused by gravity and the fluid-free surface remains horizontal. Also, the effect of centrifugal forces on the fluid was ignored due to the low angular acceleration and velocity. Shear stress was calculated as 0.0578 Pa.

Determination of mineralization and osteogenesis: alkaline phosphatase (ALP) activity of samples and controls was measured to validate early stage mineralization and extracellular matrix calcium and phosphorous quantification done by inductively coupled plasma emission spectrometry (ICP-ES). Mineralization was also visualized by 1% alizarin red staining of sample and control groups on 24 h, day 6, day 21 and day 28 post encapsulation.

7.2.3 *Results and Discussions*

7.2.3.1 Shear Stress Induces Osteogenesis of Human Embryonic Mesenchymal Stem Progenitors

The results of cell viability indicated that in all conditions cells proliferated well during 28 days experiment (Fig. 7.4a). The early cell viability surged after day 5 post encapsulation and continued to improve till day 14 and then dropped and increased on days 21 and 28 post encapsulation, respectively. All sample and control groups followed the same trend, and there were no significant differences between groups over 21 days. On day 28, however, samples treated with osteogenic media showed significantly higher DNA than those treated with FGF which kept the cell in undifferentiated status (110 ng compared to 75 ng p value <0.0001). Furthermore,

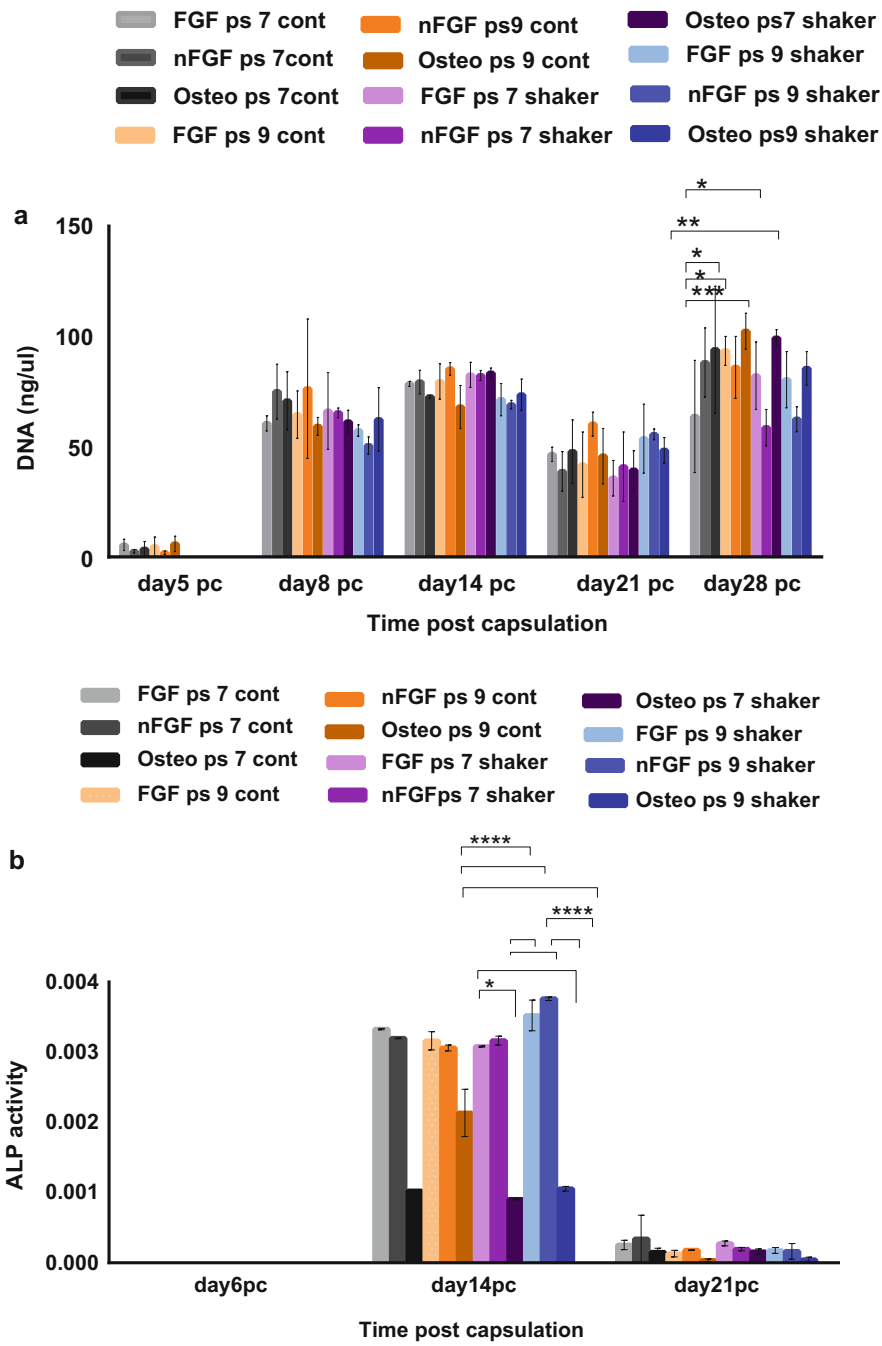

Fig. 7.4 Cell viability and ALP activity of shear stress-induced samples were assessed against static free-floating controls over 28 days pc. (**a**) Total DNA measurement was performed for cell proliferation; (**b**) ALP activity was evaluated to study the osteogenic effect of fluid flow-induced shear stress on cells. * indicates statistical significance (****$p < 0.0001$, ***$p < 0.001$, **$p < 0.01$ and *$p < 0.1$). Data is mean ± SD for $n = 9$ samples

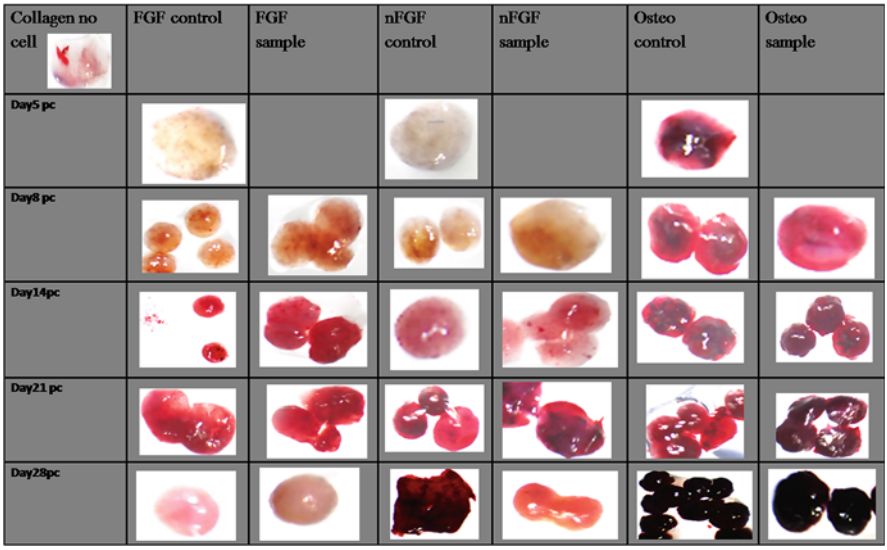

Fig. 7.5 Assessment of mineralization by alizarin red staining in chemically treated samples vs controls over 28 days post encapsulation, x4. Comparison of ARS red S staining intensity between shaker samples and static free-floating controls that were treated with osteogenic, basal media with added FGF-β and basal media. Deposited ARS stain was considerably higher in shaker samples that were treated with osteogenic media compared with other experimental conditions from day 14 pc onwards

FGF-treated samples subjected to shear stress also presented greater DNA compared to controls (102 ng and 75 ng, respectively, p value <0.001). Nevertheless, non-chemically treated samples showed lower DNA content than controls (p value <0.01) on day 28. Stem cells with different passage numbers were compared to rule out possible inter-variability between older cells.

ALP activity level of different conditions was compared to investigate the early sign of mineralization (Fig. 7.4b). ALP level showed a peak on day 14 in all groups; in both passages chemically stimulated samples and controls presented significantly lower level of ALP. Shaker samples manifested higher ALP level compared to osteogenic controls. Interestingly, samples treated with osteogenic media presented much lower ALP activity level compared to both FGF- and nFGF-treated samples which may suggest early differentiation and mineralization of cells due to combined effect of osteogenic media shear stress (Gong et al. 2001; Zhou et al. 2010). Following the increase on day 14, ALP activity level reduced dramatically to below 0.0005 on day 21 post encapsulation.

Applying shear stress in combination with chemical stimulation presented highest effect in initiation of mineralization that was supported by alizarin red staining of all three conditions in shaker experiment (Fig. 7.5). Osteogenic samples and controls showed more calcium than other conditions at all time points. Both treated samples in FGF-β and nFGF-β media presented relatively higher calcium deposition from

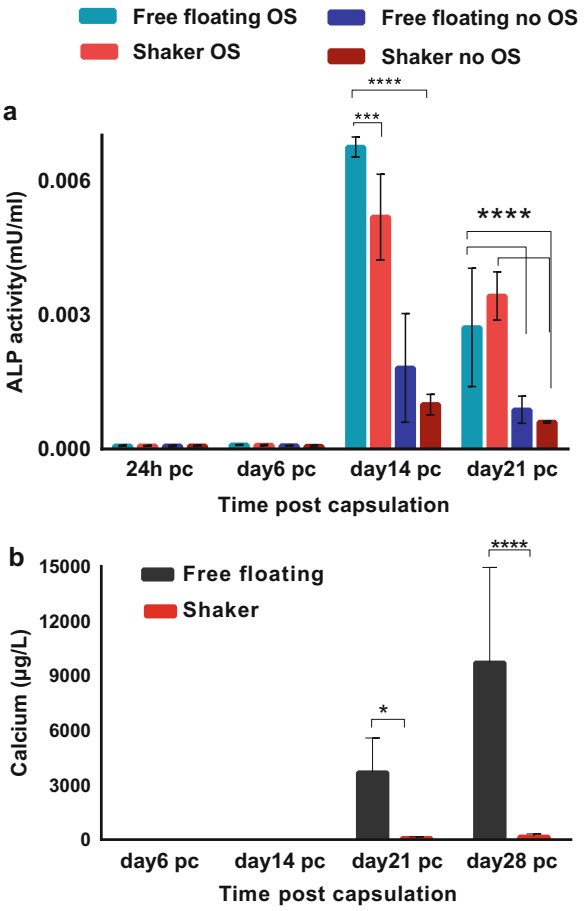

Fig. 7.6 Measurement of alkaline phosphatase activity and deposited calcium in shaker experiment compared with static controls over 28 days pc. (**a**) Samples that were treated with osteogenic media (OS) presented significantly higher ALP level from day 14 pc onwards, (**b**) deposited calcium upregulated considerably from day 21 pc onwards in static controls compared with the shaker samples, and * indicates statistical significance (****$p < 0.0001$, ***$p < 0.001$ and **$p < 0.001$). Data is mean ± SD for $n = 9$ samples

day 14 onwards. Yet, the effect of shear stress in mineralization of chemically and non-chemically treated samples was inconclusive.

The effect of chemical stimulation was further tested by comparing the subjected samples to shear stress with and without osteogenic media (Fig. 7.6a). ALP activity level of different conditions was compared to investigate the early sign of ECM mineralization. Samples subjected to shear stress showed the lowest ALP level in all time points. Although the level peaked on day 14, it remained around 0.01 mU/ ml on day 21 post seeding and reported four times lower than chemically treated samples (0.01,0.04, p value <0.0001). Moreover, free-floating controls treated with osteogenic media reported highest ALP activity level (0.06 mU/ml) at all the time points which peaked on day 14 and remained stable till day 21 post encapsulation (0.04 mU/ml). These findings were in agreement with calcium deposition results which indicated significantly higher calcium level in free-floating controls than shear stress-subjected samples on days 21 and 28 post encapsulation (Fig. 7.6b). Our results suggested that chemical stimulation had the greatest effect in initiation of

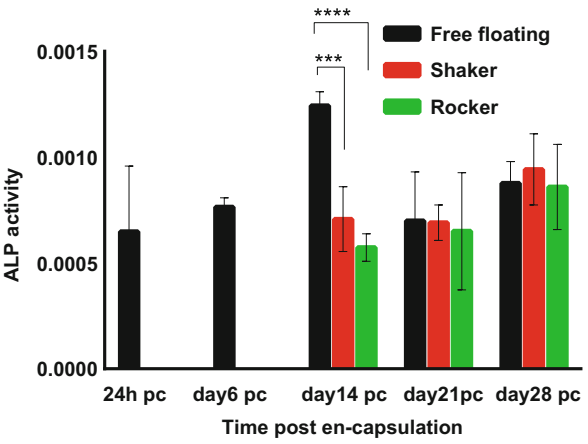

Fig. 7.7 Comparison of ALP activity level between shaker, platform rocker samples and free-floating controls over 28 days pc. Alkaline phosphatase level was reported significantly higher in free-floating controls compared to fluid flow-induced samples of rocker and orbital shaker conditions. * indicates statistical significance (***$p < 0.001$ and **** $p < 0.0001$). Data is mean $\pm$ SD for $n = 9$ samples

mineralization and mechanical forces and shear stress on their own may not be sufficient to encourage osteogenic differentiation.

In a separate study the osteogenic differentiation of subjected hES-MPs to shear stress was examined and compared using orbital shaker and rocker (Fig. 7.7). Applied shear stress by orbital shaker was shown to favour mineralization as higher ALP activity was reported on both days 21 and 28 post encapsulation. Yet again extracellular calcium level showed little or no increase to indicate mineralization in shaker experiment (Fig. 7.6b).

7.3 Conclusions

The microfluidic chamber enables chemical and mechanical stimulation of cells in a controlled environment, while reducing the overall volume of the systems. Such a system provides both reduction in cost and possibility of high-throughput testing. Applied compressive force on the cell-seeded microspheres supported long-term cell viability and encouraged the osteogenesis of hES-MPs and could be used as a model to further study the effect of mechanostimulation on osteogenesis. Our findings indicate that microfluidic system can increase the ALP activity of compressed cells which imply mineralization, but more tests such as study of bone marker genes are needed to definitely show the osteogenic differentiation of hES-MP cell line.

The role of shear stress in initiation of osteogenesis is still not well defined. Our results showed that combination of chemical stimulation and shear stress can promote osteogenesis, but mechanical forces alone may not provide all the necessary signals for osteogenic differentiation. Therefore, more studies are needed to fully unveil the role of shear stress and mechanical stimulation in mechanotransduction and determination of stem cell fate.

References

Augello A, Bari CD (2010) Review the regulation of differentiation in mesenchymal stem cells. Hum Gene Ther 21(10):1226–1238

Bakker AD, Soejima K, Klein-nulend J, Burger EH (2001) The production of nitric oxide and prostaglandin E 2 by primary bone cells is shear stress dependent. J Biomech 34:671–677

Cecchet F, De Meersman B, Demoustier-Champagne S, Nysten B, Jonas AM (2006) One step growth of protein antifouling surfaces: monolayers of poly(ethylene oxide) (PEO) derivatives on oxidized and hydrogen-passivated silicon surfaces. Langmuir 22(3):1173–1181

Choi H, Boccazzi P, Laibinis PE, Sinskey AJ, Jensen KF (2003) Poly (ethylene glycol) (peg) – modified poly (dimethyl-siloxane) (PDMS) for protein- and cell-resistant surfaces in microbioreactor. In: 7th international conference on miniaturized chemical and biochemical analysts systems, 1 1105–1108

El Haj AJ, Cartmell SH (2010) Bioreactors for bone tissue engineering. Proc Inst Mech Eng H J Eng Med 224(12):1523–1532

Gomes ME, Sikavitsas VI, Behravesh E, Reis RL, Mikos AG (2003) Effect of flow perfusion on the osteogenic differentiation of bone marrow stromal cells cultured on starch based three-dimensional scaffolds. J Biomed Mater Res A 1(67):87–95

Gong Y, Slee RB, Fukai N, Rawadi G, Roman-roman S, Reginato AM, Wang H, Cundy T, Glorieux FH, Lev D, Zacharin M, Oexle K, Marcelino J, Suwairi W, Heeger S, Sabatakos G, Apte S, Adkins WN, Allgrove J, Arslan-kirchner M, Batch JA, Beighton P, Black GCM, Boles RG, Boon LM, Borrone C, Brunner HG, Carle GF, Dallapiccola B, De Paepe A, Floege B, Halfhide ML, Hall B, Hennekam RC, Hirose T, Jans A, Kim CA, Keppler-noreuil K, Kohlschuetter A, Lacombe D, Lambert M, Lemyre E, Letteboer T, Peltonen L, Ramesar RS, Romanengo M, Somer H, Steichen-gersdorf E, Steinmann B, Sullivan B, Superti-furga A, Swoboda W, Den Boogaard V, Van Hul W, Vikkula M, Votruba M, Zabel B, Garcia T, Baron R, Olsen BR, Warman ML (2001) LDL receptor-related protein 5 (LRP5) affects bone accrual and eye development. Cell 107:513–523

Grellier M, Bareille R, Bourget C (2009) Responsiveness of human bone marrow stromal cells to shear stress. J Tissue Eng Regen Med 2:302–309

Huebsch N, Arany PR, Mao AS, Shvartsman D, Ali O a, Bencherif S a, Rivera-Feliciano J, Mooney DJ (2010) Harnessing traction-mediated manipulation of the cell/matrix interface to control stem-cell fate. Nat Mater 9:518–526

Jaasma MJ, O'Brien FJ (2008) Mechanical stimulation of osteoblasts using steady and dynamic fluid flow. Tissue Eng A 14(7):1213–1223

Jacobs CR, Yellowley CE, Davis BR, Zhou Z, Cimbala JM, Donahue HJ (1998) Differential effect of steady versus oscillating flow on bone cells. J Biomech 31:969–976

Klein-Nulend J, Bacabac RG, Mullender MG (Dec. 2005) Mechanobiology of bone tissue. Pathol Biol 53(10):576–580

Ma Y, Neubauer MP, Thiele J, Fery A, Huck WTS (2014) Artificial microniches for probing mesenchymal stem cell fate in 3D. Biomater Sci 2:1661–1671

Mccoy RJ, Brien FJO (2010) Influence of shear stress in perfusion bioreactor cultures for the development of three-dimensional bone tissue constructs: a review. Tissue Eng Part B Rev 16 (6):587–601

Odom TW, Love JC, Wolfe DB, Paul KE, Whitesides GM (2002) Improved pattern transfer in soft lithography using composite stamps. Langmuir 18(9):5314–5320

Sikavitsas VI, Bancroft GN, Holtorf HL, Jansen JA, Mikos AG (2003) Mineralized matrix deposition by marrow stromal osteoblasts in 3D perfusion culture increases with increasing fluid shear forces 33:2–7

Srinivasan S, Weimer DA, Agans SC, Bain SD, Gross TEDS (2002) Low-magnitude mechanical loading becomes osteogenic when rest is inserted between each load cycle. J Bone Miner Res 17 (9):1613–1620

Uludag H, De Vos P, Tresco PA (2000) Technology of mammalian cell encapsulation. Adv Drug Deliv Rev 42:29–64

Vangordon SB, Voronov RS, Blue TB, Shambaugh RL, Papavassiliou DV, Sikavitsas VI (2011) Effects of scaffold architecture on preosteoblastic cultures under continuous fluid shear 620–629

Vincent LG, Engler AJ (2013) Stem cell differentiation: post-degradation forces kick in. Nat Mater 12:384–386

Wang XZ, Liu D, You L, Liyun (2010) Quantifying fluid shear stress in a rocking culture dish. J Biomech 43(8):1598–1602

Windvoel T, Mbanjwa M, Mokone N, Mogale A, Land K (2010) Surface analysis of polydimethylsiloxane fouled with bovine serum albumin. Waset 61:3

Wong I, Ho CM (2009) Surface molecular property modifications for poly(dimethylsiloxane) (PDMS) based microfluidic devices. Microfluid Nanofluid 7(3):291–306

Yadav VK, Ryu J-H, Suda N, Tanaka KF, Gingrich JA, Schütz G, Glorieux FH, Chiang CY, Zajac JD, Insogna KL, Mann JJ, Hen R, Ducy P, Karsenty G (2008) Lrp5 controls bone formation by inhibiting serotonin synthesis in the duodenum. Cell 135(5):825–837

Zhou X, Liu D, You L, Wang L (May 2010) Quantifying fluid shear stress in a rocking culture dish. J Biomech 43(8):1598–1602

Chapter 8
Computational Modelling of Collagen Hydrogel

Collagen is one of the most used biomaterials in tissue engineering applications. It is abundant in biological tissues, namely, constituting approximately 30% of all musculoskeletal tissues, through the presence in the extracellular matrix. Along the years, several works tried to characterize this biomaterial, as isolated fibres or as part of hydrogels, but the fragility of this material has been deferring its full characterization. This chapter presents an experimental and numerical characterization of a highly hydrated collagen hydrogel, with 0.20% of collagen concentration. The experimental data obtained through rheology experiments with three hydrogel samples was complemented with numerical simulation through finite element techniques. This framework was complemented with literature data, resulting on a set of biomechanical parameters that can describe the hydrogel behaviour, namely, a shear modulus of 0.023 kPa and a bulk modulus of 0.769 kPa, corresponding to a Poisson's ratio of 0.485. The ultimate aim for this work is to contribute for the determination of the load transfer mechanisms through a collagen medium, i.e. to understand the contribution of collagen on the mechanical stimuli that affect cell behaviour on scaffold cell seeding.

8.1 The Importance of Collagen in Tissue Engineering

This chapter presents an experimental and numerical characterization of a highly hydrated collagen hydrogel, with 0.20% of collagen concentration, given the importance of collagen in tissue engineering (TE). This work is part of an integrated framework that aims at studying the load transfer mechanisms from the scaffold to the cells, i.e. to understand the contribution of collagen on the mechanical stimuli that affect cell behaviour (Lacroix et al. 2006).

8.1.1 Collagen in Biological Tissues

Collagen is one of the major components of extracellular matrix, constituting approximately 25% of all the proteins in the human body and around 30% of all

© Springer Nature Singapore Pte Ltd. 2019

D. Lacroix et al., *Multiscale Mechanobiology in Tissue Engineering*,
Frontiers of Biomechanics 3, https://doi.org/10.1007/978-981-10-8075-3_8

musculoskeletal tissues. Along with such abundance, its intrinsic biocompatibility and low immunogenicity unsurprisingly made collagen one the first biomaterials with natural origin (Abou Neel et al. 2006; Arevalo et al. 2010).

As so, collagen-based hydrogels have been used successfully in diverse TE applications, namely, on the production of scaffolds or scaffold's coatings. In fact, challenges in current TE research point towards tissue differentiation, molecular structures and optimization of scaffold design and performance (Campos Marin and Lacroix 2015; Yan et al. 2015).

Collagen is mostly used as a cell substrate, since it is naturally remodelled by those cells in a three-dimensional lattice shape that forms a cage for cell entrapment, providing an advantageous environment for tissue growth and organ regeneration. It can be easily altered by adding other molecules and substances, but the high hydration level of the hydrogels makes them difficult to manipulate, as they are inherently weak. The water concentration may also increase the risk of drying in contact with air (Abou Neel et al. 2006; Arevalo et al. 2010).

There are at least 28 different collagen types, but collagen type I is the most common and is primarily found in the skin and bone (Ricard-Blum 2011). Type II collagen is the main component of cartilage, while type III is commonly found alongside type I in blood vessel walls (Haycock 2011).

There is a need for the biomechanical characterization of collagen, because most of its biological functions are related to tissue mechanics and stimuli. As collagen is present at different levels, it is also necessary to consider a multiscale approach, from the cellular interaction to the organ level. Collagen fibres are a good example of intricate biomechanical behaviour, having their intrinsic anisotropy and inhomogeneity, which derive from their microstructure and influence the overall tissue behaviour. These fibres contribute greatly to the compressive stiffness of cartilaginous tissues, such as the annulus fibrosus of the intervertebral disc, due to their spatial arrangement. At high strain magnitudes, fibrillar arrangement is most likely more determinant to the compressive behaviour of these soft tissues than osmotic swelling behaviour (Römgens et al. 2013; Wenger et al. 2007).

8.1.2 Applications

Collagen hydrogels have a wide range of applications, given to its previously described importance and abundance in organic systems. There are a large number of papers published on this subject in the current decade, due to the advances in TE technologies. This section is devoted to a brief overview on some of the most recent publications on collagen applications for TE.

Tanaka et al. (2011) started with monomeric collagen solutions to produce collagen-based scaffolds for ocular applications, namely, protective membranes and corneal stromal implants. The anisotropic properties of the collagen network allowed for the ocular flow, along with the transmission of the visible light. Biocompatibility with human corneal epithelial cells was ensured by this construct as

well. This approach also has the potential to be extended to other applications with strong dependency on tissue orientation.

Sirivisoot et al. (2014) developed conductive collagen hydrogels to be used as biomimetic scaffolds for regeneration of nerve and skeletal muscle. Cell viability and proliferation promoted by their constructs were comparable to natural substrates. Electrical stimulation might also result in higher cell density and differentiation, namely, in what concerns to the chemically synthetized conductive PANI and PEDOT nanofibers.

Sharabi et al. (2014) developed a biocomposite based on an alginate matrix reinforced with long collagen fibres, in order to obtain a wide range of engineered soft tissues. The hyperelastic response of this new material, grounded on the collagen fibres' individual and collective arrangement, ensures a similar mechanical behaviour to biological tissues, such as the bladder or annulus fibrosus.

Finally, Deponti et al. (2014) developed a scaffold based on collagen and fibrin glue. The collagen provided the correct histological and immunohistochemical environment for cellular growth and differentiation, while the fibrin glue improved cellular distribution and survival rate. Such construct was thus able to support chondrocyte survival in vitro, which leads to applications in cartilage replacement and other chondral-like tissues.

For more details on the relationship between collagen and diverse TE applications, the interested reader is referred to the papers of Campos Marin and Lacroix (2015), Khoshgoftar et al. (2013), Lacroix et al. (2006), Malandrino et al. (2013), Olivares and Lacroix (2013), and Yan et al. (2015).

8.2 Rheology Experiments

This section is devoted to rheometer experiments of hydrogels with 0.20% of collagen concentration, at different temperatures. The goal is to obtain *in-house* stiffness data on these hydrogels, in order to feed numerical simulations and compare with literature data.

8.2.1 Previous Rheology Studies

Rheology is one of the most used techniques for the evaluation of biomechanical properties of soft tissues and hydrogels. The short duration of the experiments and the absence of specific testing jigs are some of the encouraging features of this method.

Several groups have tested different types of collagen hydrogels through this method, in order to obtain information on the shear and viscous behaviour of such

materials. For example, Velegol and Lanni (2001) aimed at determining the local shear modulus of type I collagen. Their samples were hydrogels with 0.05–0.23% concentration of bovine dermal collagen. Frequency sweeps between 0.06 and 60 rad/s were performed at 22 °C and 37 °C, in a parallel plate rheometer. The shear modulus of these hydrogels was found to be between 3 and 80 Pa.

Wu et al. (2005) focused on finding the age-related differences in rat-tail collagen over a frequency sweep from 0.1 to 25 rad/s. The experiments were run at 25 °C, using a cone plate support with 2° angle and 60 mm diameter. They found that stiffness increases with age.

Xu et al. (2011) tested the properties of collagen scaffolds crosslinked with genipin, using a parallel plate rheometer, at 37 °C. The amount of genipin, added to the collagen through a controlled assembly process, increased the overall stiffness of the material. The alignment of the fibres and the crosslinking proved to be essential to the outcomes. On a different angle, the same group performed biaxial tensile stress relaxation experiments, in order to evaluate the relaxation behaviour at the different levels of the collagen structure (fibre, inter-fibril and fibril), which is directly connected with its viscoelastic properties. These experiments proved to be a valuable source of parameters for numerical approaches, namely, for generalized viscoelastic Maxwell models (Xu et al. 2013).

Stein et al. (2011) used type I bovine collagen to prepare hydrogels with different concentration levels (0.05, 0.1 and 0.15%). They aimed at characterizing the hydrogels as a function of the concentration, using confocal microscopy and rheology. The rheometer experiments were ran at 37 °C, using a cone plate support with 4° angle and 40 mm diameter. They found that crosslinking plays a major role in the overall hydrogel biomechanics, and thus it shall be understood before parting for collagen application.

Knapp et al. (1997) stated that rheology is not able to collect any information on the interphase drag, while confined compression allows for the fluid exudation, i.e. relative motion between solid and fluid components of the hydrogel. Therefore, this group combined both rheometer and confined compression experiments, using hydrogels with 0.1% concentration of bovine dermal collagen. This integrated approach allowed them to conclude that the microstructural organization of the fibrils plays an essential role on collagen behaviour, by influencing both tension and compression responses, at the solid-fluid interaction level.

There are only a few more studies in the literature which have done confined compression of collagen hydrogels, as, for example, Chandran and Barocas (2004) and Busby et al. (2013). Such experiments are one of the most reliable approaches for the determination of the biphasic behaviour of this type of hydrogels, but the authors faced several difficulties in obtaining a stable creep deformation. While Busby et al. (2013) focused on ramp compression experiments, Chandran and Barocas (2004) performed both instantaneous and extended compression rates. As indicated by Knapp et al. (1997), the creep data is hardly linear. The step compression tests are even more challenging, due to the fast fluid exudation.

8.2.2 Materials and Methods

A Bohlin Gemini 200 HR Nano rheometer (Malvern Instruments, Malvern, United Kingdom) was used to test four samples of a hydrogel with 0.2% of collagen concentration. Type I bovine collagen was neutralized with 10x PBS and 1 N NaOH, followed by distilled water. The droplets were made by pipetting around 20 µl of gel mixture (drawing a few 20 mm diameter circles on paradigm) on the marked areas of paraffin. The hydrogel was then incubated at 37 °C for 40–45 min, and, finally, the droplets were suspended in PBS/distilled water.

The experimental protocol was based on a frequency sweep from 16 to 0.016 Hz (descending order), on a total of 22 frequency steps. A parallel plate with 20 mm of diameter was used and sample height was 1 mm. The first sweep was performed at 25 °C, followed by a similar frequency sweep at 37 °C. A comparable sample configuration and a dual temperature scheme (22° and 37 °C) were used by Velegol and Lanni (2001), while Wu et al. (2005) performed their tests at 25 °C. The average duration for a full frequency sweep at a given temperature was 10 min. To conclude the experiments, a third sweep at 25 °C was performed, from 1.6 to 0.1 Hz, in 13 steps (Chaudhury et al. 2011; Velegol and Lanni 2001). However, this third sweep was only successful in three of the samples, so a sample number $n = 3$ will be considered along this section.

The elastic (or storage, G') and viscous (or loss, G'') moduli were measured for each frequency. The shear (or complex, G) modulus was calculated as:

$$G = \sqrt{(G')^2 + (G'')^2} \tag{8.1}$$

Due to equipment limitations on testing such a soft material, reliable measurements were only obtained under 1.3 Hz, which corresponded to 11 steps. Consequently, measurements at higher frequencies were excluded.

8.2.3 Results

Figure 8.1 shows the average values of elastic and viscous moduli at 25 °C, with the corresponding standard deviation. It must be highlighted that only the first sweep was considered in this case, in order to allow for the comparison with the following frequency sweep (at 37 °C). Shear modulus varied from 0.0353 kPa at 1.3 Hz to 0.0207 kPa at 0.016 Hz, while viscous modulus stood between 0.0058 and 0.0046 kPa. Average standard deviations were 0.0024 kPa and 0.0006 kPa, respectively.

Figure 8.2 shows the average values of elastic and viscous moduli at 37 °C, with the corresponding standard deviation. Shear modulus varied from 0.0287 kPa at

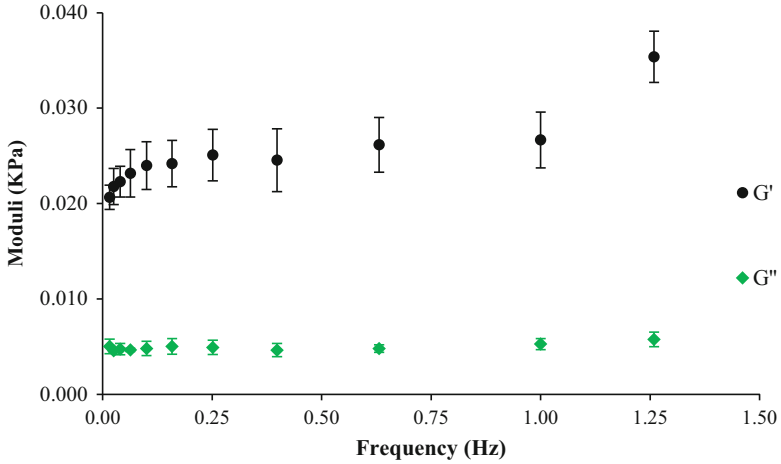

Fig. 8.1 Elastic and viscous moduli as a function of the frequency, at 25 °C. Average of the samples and standard deviations ($n = 3$) are shown

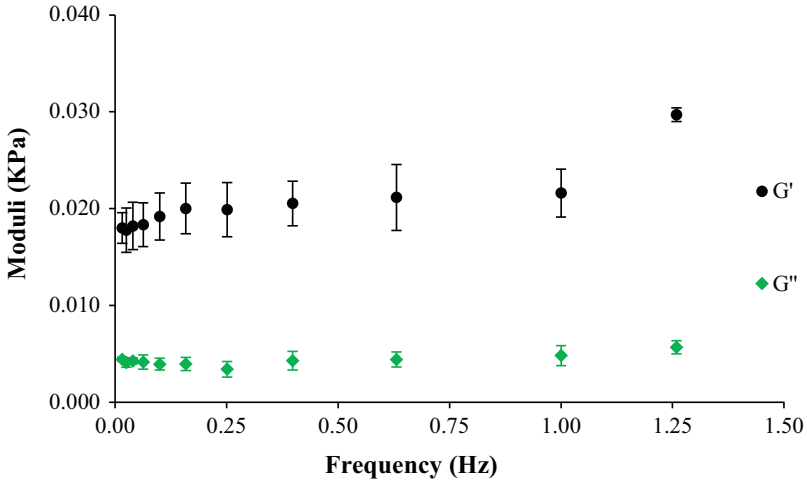

Fig. 8.2 Elastic and viscous moduli as a function of the frequency, at 37 °C. Average of the samples and standard deviations ($n = 3$) are shown

1.3 Hz to 0.0171KkPa at 0.016 Hz, with average standard deviation of 0.0023 kPa. Viscous modulus stood between 0.0058 and 0.0041 kPa, with average standard deviation of 0.0007 kPa.

The configurations of both moduli vs frequency curves are very similar for both temperatures, i.e. the shear modulus decreased approximately 40% along the frequency sweep, while the viscous modulus decreased approximately 20%. The

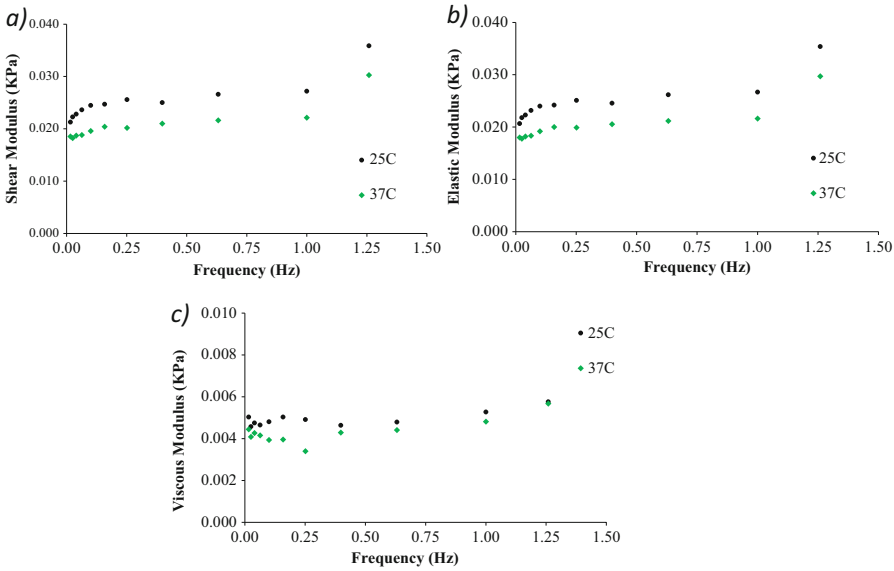

Fig. 8.3 Comparison between the behaviour of the hydrogel at 25° and 37 °C. (**a**) Shear modulus; (**b**) elastic modulus; (**c**) viscous modulus

viscous modulus is approximately only 20% of the elastic modulus (in average). The average standard deviations were also very close for both temperatures.

Figure 8.3 shows the comparison between the behaviour of the hydrogel at the different temperatures, in terms of shear, elastic and viscous moduli. The comparison between the first and the third frequency sweeps at 25 °C is presented in Fig. 8.4.

The three evaluated moduli decreased by about 16% when tested at 37 °C, in comparison with the first test, at 25 °C. Then, the shear and elastic moduli decreased by about 20% from the first to the third frequency sweep at 25 °C. Differences are not so significant for the case of the viscous modulus (less than 10%), but the global tendency is still to lower values on the third sweep. It must be highlighted that only frequency values between 0.1 and 1.3 Hz were considered for this comparison. If one compares the first and second sweeps at that frequency range, the shear and elastic moduli decreased by about 18%, while the viscous modulus decreased by about 13%. Therefore, the results on Figs. 8.3 and 8.4 show that there is a tendency for collagen to lose stiffness with the temperature changes.

8.2.4 Discussion

The rheology results are aligned with the global behaviour of several literature studies, as both elastic and viscous moduli decreased slowly as the frequency was

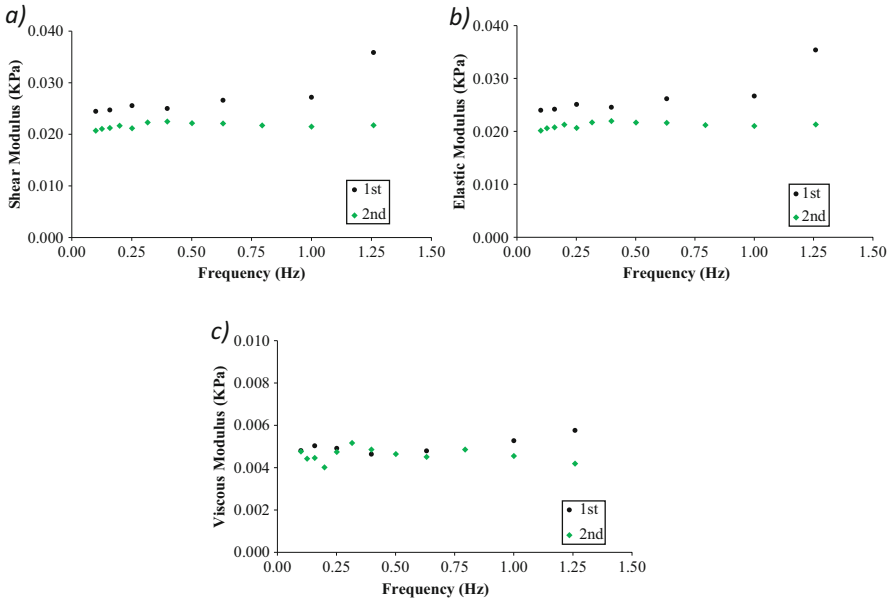

Fig. 8.4 Comparison between the first and second frequency sweeps at 25 °C. (**a**) Shear modulus; (**b**) elastic modulus; (**c**) viscous modulus

also decreasing. In addition, the viscous modulus is approximately 20% of the elastic modulus (on average). A quantitative comparison cannot be held, because these studies did not use the same type of collagen hydrogel (Knapp et al. 1997; Mori et al. 2012; Velegol and Lanni 2001; Wu et al. 2005; Xu et al. 2013). The minor standard deviation found in the experiments warranted the quality of the results.

The evolution of the temperature (25°–37°–25 °C) was probably majorly responsible for the stiffness decrease along the experiments, i.e. the temperature scheme seems to be affecting the hydrogel's stiffness. Further tests may only consider 37 °C, as this is the average temperature of the human body. Alternatively, a descending temperature scheme (37–25 °C) may also be tested, in order to better evaluate the collagen hydrogel behaviour in relation to temperature changes.

8.3 Finite Element Simulations

This section is devoted to FE analysis of the collagen hydrogel, combining *in-house* experimental data and literature data for the input parameters. The goal is to obtain consistent information on the mechanical behaviour of these hydrogels and, thus, to establish a working set of parameters for forthcoming studies.

8.3.1 Numerical Characterization of Collagen Hydrogel

Having strong nonlinear poro-viscoelastic properties, collagen hydrogels are difficult to characterize, both experimentally and numerically (McGann et al. 2014). The properties of collagen depend on its origin, which is usually rat tail or bovine, in the available experimental studies. In addition, concentration, crosslinking and even sample preparation may influence the experimental outcomes (McGann et al. 2014). Stiffness properties (shear, viscous or even Young's moduli) or permeability of collagen hydrogels were experimentally measured by several groups (Busby et al. 2013; Knapp et al. 1997; Velegol and Lanni 2001), but numerical modelling is an important complement (Stylianopoulos and Barocas 2007; Xu et al. 2013).

Most studies on the constitutive modelling of collagen fibres are related to cartilaginous and intervertebral disc tissues (Marini and Ferguson 2014; Noailly et al. 2011). Collagen fibres play a major role on the stress/strain behaviour of soft tissues, and the stiffness properties of the collagen hydrogels are also mostly due to these structures (Römgens et al. 2013; Vader et al. 2009).

The major challenge for numerical modelling of collagen hydrogels, namely, through finite element (FE) simulations, is directly related to the experimental difficulties. FE simulations require reliable input data, which is not always available. However, through inverse engineering and retro-feedback with experimental work, it is possible to establish a complete approach for the analysis of the behaviour of these biomaterials (Liu and Ovaert 2011).

Hydrogel characterization requires a numerical multiphasic approach, rather than the customary monophasic FE simulations. Bi-, tri- or quadriphasic approaches can be followed (Liu and Ovaert 2011; Snijders et al. 1995; Van Loon et al. 2003), but the biphasic approach is the most used, due to the abovementioned input data issue (Roos et al. 2015; Seifzadeh et al. 2012).

8.3.2 Materials and Methods

As previously mentioned, confined compression studies of collagen hydrogels present several issues, mostly due to inhomogeneous deformation (Knapp et al. 1997). However, such issues are not significant under the computational point of view. Therefore, FE simulations are here employed to characterize the poro-viscoelastic behaviour of collagen hydrogels.

Busby et al. (2013) experimentally performed confined compression studies, using cylindrical samples of radius 8 mm and height 5 mm, considering hydrogels with 0.20, 0.30 and 0.40% of collagen concentration. The protocol was divided in compression and relaxation stages: (1) 5% compression at 0.005 s^{-1} and (2) compression hold for 300 s (stress relaxation period).

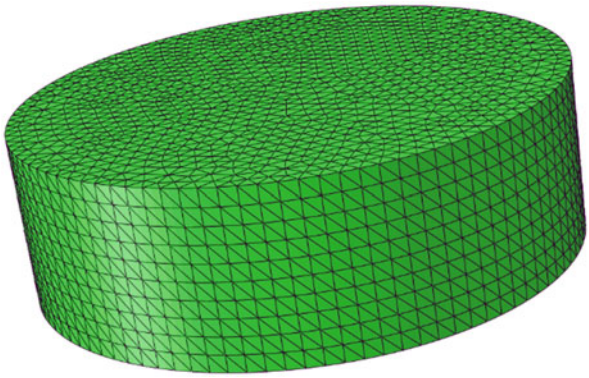

Fig. 8.5 FE mesh of the collagen hydrogel sample

A similar protocol was simulated using the biphasic module of FE solver V-Biomech® (Castro et al. 2014), for the case of the hydrogel with 0.20% of collagen concentration, in order to match the rheometer experiments. A geometrical model with the same dimensions of the testing sample from Busby and co-workers was meshed with 9120 quadratic 10-node tetrahedral elements (Fig. 8.5). The boundary conditions considered bottom and lateral confinement (X- and Y-axis), with the compression applied at the top (Z-axis). Fluid was allowed to exudate through the top as well.

A compressible Neo-Hookean model (Bonet and Wood 1997) was used to characterize the isotropic hyperelasticity of the collagen hydrogel, in terms of shear (G) and bulk moduli (K):

$$\bar{W}_{\mathrm{NH}}(\mathbf{C}) = \frac{G}{2}(I_1 - 3) - G(\ln J) - \frac{G}{3}(\ln J)^2 + \frac{K}{2}(\ln J)^2 \tag{8.2}$$

In addition, van der Voet model was applied to describe the strain-dependent permeability, K^* (Noailly et al. 2008; Van der Voet 1997):

$$K^*(J) = K_0^* \left(\frac{1 - n_{f,0}}{1 - n_f}\right)^M = K_0^* J^M \tag{8.3}$$

Regarding Eqs. 8.2 and 8.3, J is the determinant of the transformation gradient, K_0^* is the zero-strain hydraulic permeability and M is the dimensionless nonlinear permeability parameter.

The constitutive modelling partially relied on the parameters provided by Busby and co-workers for a hydrogel with 0.2% of collagen concentration, namely, the aggregate modulus (Ha), the zero-strain hydraulic permeability and the nonlinear permeability parameter (Table 8.1).

Table 8.1 Constitutive parameters for a hydrogel with 0.2% of collagen

Ha (kPa)	0.8
K_0^* (m^4/Ns)	1.5×10^{-10}
M	1.8

Adapted from Busby et al. (2013)

Table 8.2 Young, shear and bulk moduli calculated as function of the Poisson's ratio

v	E (kPa)	G (kPa)	K (kPa)
0.050	0.796	0.265	0.295
0.100	0.782	0.261	0.326
0.200	0.720	0.240	0.400
0.250	0.667	0.222	0.444
0.300	0.594	0.198	0.495
0.400	0.373	0.124	0.622
0.450	0.211	0.070	0.703
0.480	0.091	0.030	0.759
0.485	0.069	0.023	0.769
0.490	0.047	0.016	0.779

Then, a range of Young (E), shear and bulk moduli values was calculated as a function of the (unknown) Poisson's ratio (v), as shown in Table 8.2, keeping the aggregate modulus constant (Krenk 2009; Oomens et al. 2009):

$$\mathrm{Ha} = E\frac{(1-\nu)}{(1+\nu)(1-2\nu)} \tag{8.4}$$

$$G = \frac{E}{2(1+\nu)} \tag{8.5}$$

$$K = \frac{E}{3(1-2\nu)} \tag{8.6}$$

Three sets of parameters were simulated, by altering the shear and bulk moduli in accordance with Poisson's ratio, namely, for 0.20, 0.30 and 0.485 (Table 8.2), fulfilling the requirements of the compressible Neo-Hookean model (Eq. 8.2). The van der Voet model (Eq. 8.3) requires the zero-strain hydraulic permeability and the nonlinear permeability parameter (Table 8.1). These permeability-related parameters and the boundary conditions remained unaltered for the three different simulations. No viscoelasticity was considered for these particular trials, due to the long-term compression rate, i.e. only a poroelastic approach was followed (Noailly et al. 2008).

Knapp et al. (1997) pointed out that this type of hydrogel should be compressible and have a Poisson's ratio between 0.20 and 0.30.

However, if one assumes that the Poisson's ratio of this collagen hydrogel is approximately 0.485 (almost incompressible material), the parameters provided by Busby and co-workers (aggregate modulus, zero-strain hydraulic permeability and nonlinear permeability coefficient) match with the stiffness properties extracted from

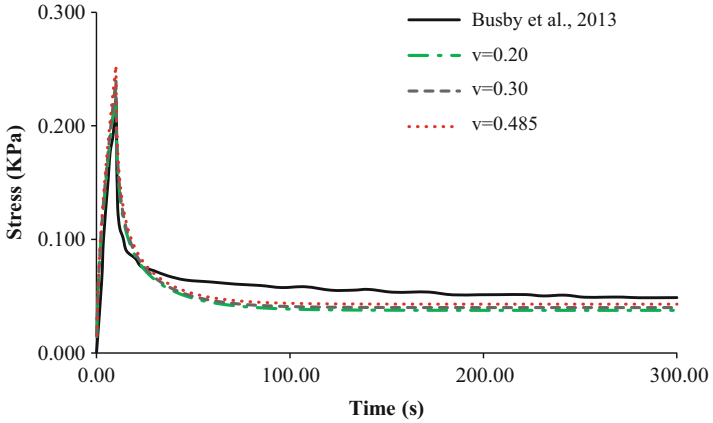

Fig. 8.6 Comparison between the experimental work of Busby et al. (2013) and the three numerical approaches, considering stress vs time

Table 8.3 Comparison between the experimental work of Busby et al. (2013) and the three numerical approaches, considering peak and relaxation stress values

	Peak stress at 10 s (kPa)	Relaxation stress at 300 s (kPa)
Busby et al. (2013)	0.223	0.049
$\nu = 0.20$	0.232	0.038
$\nu = 0.30$	0.240	0.040
$\nu = 0.485$	0.253	0.043

the rheometer experiments (average shear modulus of 0.025 KPa at 25 °C and 0.021 KPa at 37 °C). Therefore, the goal for these numerical simulations is to evaluate the behaviour of the collagen hydrogel model with the different Poisson's ratio values and to compare the outcomes with the experimental data from Busby and co-workers.

8.3.3 Results

Figure 8.6 and Table 8.3 show the comparison between the experimental stress curve of Busby and co-workers and the three numerical approaches (Poisson's ratio of 0.20, 0.30 and 0.485). For this purpose, the Z-axis component of stress was selected from the numerical outcomes.

The differences between the behaviour of the three numerical approaches are residual, but a Poisson's ratio of 0.485 allows a better approximation to the experimental results, mostly due to its behaviour during the stress relaxation period. Overall, the resultant Z-axis component of stress increased with the increase of the Poisson's ratio, as expected.

8.3.4 Discussion

It is possible to compare the rheometer experiments with confined compression tests, if one associates the stiffness properties resultant from each experiment. As stated by Knapp et al. (1997), rheology is not able to collect any information on the interphase drag, but it is a valid method for the analysis of shear and compressive mechanical properties. In this work, the rheology experiments were complemented with numerical confined compression tests and associated literature data. The differences are minor, but the model with $\nu = 0.485$ is the closest one to the experimental results presented by Busby et al. (2013), which is a good indication of the bridging between the different data sources.

Nevertheless, it is necessary to evaluate the behaviour of the material under the light of the different assumptions. The work presented by Busby et al. (2013) on the determination of aggregate modulus, zero-strain hydraulic permeability and nonlinear permeability coefficient is essential for the current findings, because no permeability-related experiments were performed. This group has used rat-tail collagen, which could have conditioned the comparison with the bovine collagen used for this study, but that origin difference turned out as not significant. Cross-linking and sample preparation approaches were also negligible for this purpose, but they could have played a role if this study was extended to the biological level (McGann et al. 2014).

Discussion on the Poisson's ratio of biocomposites pointed out that most soft tissues are almost incompressible, being particularly sensitive to the properties of the soft matrix (Liu et al. 2006), even if the overall approach to biological hydrogels tends to adopt a Poisson's ratio between 0.20 and 0.30 (Knapp et al. 1997). Having in mind that direct determination of soft tissues' Poisson's ratio is a highly demanding task, the inverse engineering approach implemented in this work showed to be a viable strategy to overcome such experimental difficulties (Liu and Ovaert 2011). The calculations here presented proved that assuming this 0.20% collagen hydrogel as an almost incompressible domain is adequate, based on the stiffness-related bridging between rheology and confined compression.

8.4 Conclusion

Rheology is known to be a good method to determine mechanical properties of soft tissues, despite having some intrinsic limitations, as it does not allow for any interphase drag. The behaviour of the hydrogel solid part was successfully characterized in this work, being the average shear modulus 0.025 kPa at 25 °C and 0.021 kPa at 37 °C.

In silico FE studies are also highly applied, due to their versatility and increasing speed. Having the results from the rheometer experiments and significant literature data, it was possible to develop a model which mimicked the biphasic behaviour of

the collagen hydrogel. Nonlinear poroelastic modelling proved to be a valid approach to understand the behaviour of these types of hydrogels, as the comparison between numerical and experimental curves revealed a close agreement, both in peak and relaxation stress stages over time. The model with mechanical properties associated with $\nu = 0.485$ proved to be the closest one to the benchmark of Busby et al. (2013).

The data obtained with this experimental-numerical approach leads to the extrapolation that a similar (or approximated) Poisson's ratio (i.e. in the almost-incompressibility zone) may be considered for the 0.30% and 0.40% hydrogels that were also tested by Busby et al. (2013). Therefore, the next task may be to try the current approach with different hydrogels, in terms of collagen concentration or sample preparation. The experimental work on the confined compression of similar collagen hydrogels performed by Chandran and Barocas (2004) may also be reproduced, as a second validation step, with a different protocol.

To sum up, the current study can be considered as a good starting point for the characterization of collagen hydrogels, due to its integrated experimental-numerical approach. Given the importance of collagen for tissue engineering applications and its connection with cellular stimuli, a biomechanical characterization of this material is of upmost importance, and this work established the grounds towards that goal.

Acknowledgements The authors would like to acknowledge the funding from the European Research Council (no. 258321). In addition, the cooperation of Chris Holland and Peter Laity (Natural Materials Group, Dept. Materials Science and Engineering, The University of Sheffield) with the rheology experiments is also gratefully acknowledged.

References

Abou Neel EA, Cheema U, Knowles JC, Brown RA, Nazhat SN (2006) Use of multiple unconfined compression for control of collagen gel scaffold density and mechanical properties. Soft Matter 2:986

Arevalo RC, Urbach JS, Blair DL (2010) Size-dependent rheology of type-I collagen networks. Biophys J 99:L65–L67

Bonet J, Wood RD (1997) Nonlinear continuum mechanics for finite element analysis. Cambridge University Press, Cambridge, UK

Busby GA, Grant MH, Mackay SP, Riches PE (2013) Confined compression of collagen hydrogels. J Biomech 46:837–840

Campos Marin A, Lacroix D (2015) The inter-sample structural variability of regular tissue-engineered scaffolds significantly affects the micromechanical local cell environment. Interface Focus 5:20140097–20140097

Castro APG, Wilson W, Huyghe JM, Ito K, Alves JL (2014) Intervertebral disc creep behavior assessment through an open source finite element solver. J Biomech 47:297–301

Chandran PL, Barocas VH (2004) Microstructural mechanics of collagen gels in confined compression: poroelasticity, viscoelasticity, and collapse. J Biomech Eng 126:152

Chaudhury S, Holland C, Vollrath F, Carr AJ (2011) Comparing normal and torn rotator cuff tendons using dynamic shear analysis. J Bone Joint Surg Br 93:942–948

Deponti D, Di Giancamillo A, Gervaso F, Domenicucci M, Domeneghini C, Sannino A, Peretti GM (2014) Collagen scaffold for cartilage tissue engineering: the benefit of fibrin glue and the proper culture time in an infant cartilage model. Tissue Eng A 20:1113–1126

Haycock JW (2011) 3D cell culture: a review of current approaches and techniques. Methods Mol Biol 695:1–15

Khoshgoftar M, Wilson W, Ito K, van Donkelaar CC (2013) Influence of tissue- and cell-scale extracellular matrix distribution on the mechanical properties of tissue-engineered cartilage. Biomech Model Mechanobiol 12:901–913

Knapp DM, Barocas VH, Moon A, Yoo K, Petzold L, Tranquillo R (1997) Rheology of reconstituted type I collagen gel in confined compression. J Rheol (N Y N Y) 41:971–993

Krenk S (2009) Non-linear modeling and analysis of solids and structures. Cambridge University Press, Cambridge

Lacroix D, Chateau A, Ginebra M-P, Planell J a (2006) Micro-finite element models of bone tissue-engineering scaffolds. Biomaterials 27:5326–5334

Liu K, Ovaert TC (2011) Poro-viscoelastic constitutive modeling of unconfined creep of hydrogels using finite element analysis with integrated optimization method. J Mech Behav Biomed Mater 4:440–450

Liu B, Zhang L, Gao H (2006) Poisson ratio can play a crucial role in mechanical properties of biocomposites. Mech Mater 38:1128–1142

Malandrino A, Noailly J, Lacroix D (2013) Regional annulus fibre orientations used as a tool for the calibration of lumbar intervertebral disc finite element models. Comput Methods Biomech Biomed Engin 16:923–928

Marini G, Ferguson SJ (2014) Modelling the influence of heterogeneous annulus material property distribution on intervertebral disk mechanics. Ann Biomed Eng 42:1760–1772

McGann ME, Bonitsky CM, Ovaert TC, Wagner DR (2014) The effect of collagen crosslinking on the biphasic poroviscoelastic cartilage properties determined from a semi-automated microindentation protocol for stress relaxation. J Mech Behav Biomed Mater 34:264–272

Mori H, Shimizu K, Hara M (2012) Dynamic viscoelastic properties of collagen gels in the presence and absence of collagen fibrils. Mater Sci Eng C 32:2007–2016

Noailly J, Van Oosterwyck H, Wilson W, Quinn TM, Ito K (2008) A poroviscoelastic description of fibrin gels. J Biomech 41:3265–3269

Noailly J, Planell JA, Lacroix D (2011) On the collagen criss-cross angles in the annuli fibrosi of lumbar spine finite element models. Biomech Model Mechanobiol 10:203–219

Olivares AL, Lacroix D (2013) Computational methods in the modeling of scaffolds for tissue engineering. Stud Mechanobiol Tissue Eng Biomater 10:107–126

Oomens C, Brekelmans M, Baaijens F (2009) Biomechanics: concepts and computation

Ricard-Blum S (2011) The collagen family. Cold Spring Harb Perspect Biol 3:1–19

Römgens AM, van Donkelaar CC, Ito K (2013) Contribution of collagen fibers to the compressive stiffness of cartilaginous tissues. Biomech Model Mechanobiol 12:1221–1231

Roos RW, Pel L, Huinink HP, Huyghe JM (2015) 1D measurement of sodium ion flow in hydrogel after a bath concentration jump. Ann Biomed Eng 2–7

Seifzadeh A, Oguamanam DCD, Trutiak N, Hurtig M, Papini M (2012) Determination of nonlinear fibre-reinforced biphasic poroviscoelastic constitutive parameters of articular cartilage using stress relaxation indentation testing and an optimizing finite element analysis. Comput Methods Programs Biomed 107:315–326

Sharabi M, Mandelberg Y, Benayahu D, Benayahu Y, Azem A, Haj-Ali R (2014) A new class of bio-composite materials of unique collagen fibers. J Mech Behav Biomed Mater 36:71–81

Sirivisoot S, Pareta R, Harrison BS (2014) Protocol and cell responses in three-dimensional conductive collagen gel scaffolds with conductive polymer nanofibres for tissue regeneration. Interface Focus 4:20130050

Snijders H, Huyghe JM, Janssen JD (1995) Triphasic finite element model for swelling porous media. Int J Numer Methods Fluids 20:1039–1046

Stein AM, Vader DA, Weitz DA, Sander LM (2011) The micromechanics of three-dimensional collagen-I gels. Complexity 16:22–28

Stylianopoulos T, Barocas VH (2007) Volume-averaging theory for the study of the mechanics of collagen networks. Comput Methods Appl Mech Eng 196:2981–2990

Tanaka Y, Kubota A, Matsusaki M, Duncan T, Hatakeyama Y, Fukuyama K, Quantock AJ, Yamato M, Akashi M, Nishida K (2011) Anisotropic mechanical properties of collagen hydrogels induced by uniaxial-flow for ocular applications. J Biomater Sci Polym Ed 22:1427–1442

Vader D, Kabla A, Weitz D, Mahadevan L (2009) Strain-induced alignment in collagen gels. PLoS One 4:e5902

Van der Voet A (1997) A comparison of finite element codes for the solution of biphasic poroelastic problems. Proc Inst Mech Eng H 211:209–211

Van Loon R, Huyghe JM, Wijlaars MW, Baaijens FPT (2003) 3D FE implementation of an incompressible quadriphasic mixture model. Int J Numer Methods Eng 57:1243–1258

Velegol D, Lanni F (2001) Cell traction forces on soft biomaterials. I. Microrheology of type I collagen gels. Biophys J 81:1786–1792

Wenger MPE, Bozec L, Horton MA, Mesquida P (2007) Mechanical properties of collagen fibrils. Biophys J 93:1255–1263

Wu C-C, Ding S-J, Wang Y-H, Tang M-J, Chang H-C (2005) Mechanical properties of collagen gels derived from rats of different ages. J Biomater Sci Polym Ed 16:1261–1275

Xu B, Chow M-J, Zhang Y (2011) Experimental and modeling study of collagen scaffolds with the effects of crosslinking and fiber alignment. Int J Biomater 2011:172389

Xu B, Li H, Zhang Y (2013) An experimental and modeling study of the viscoelastic behavior of collagen gel. J Biomech Eng 135:54501

Yan L, Oliveira JM, Oliveira AL, Reis RL (2015) Current concepts and challenges in osteochondral tissue engineering and regenerative medicine. ACS Biomater Sci Eng 150220124046001

Chapter 9
Mechanical Load Transfer at the Cellular Level

Cells interact with their extracellular environment, from which they gather information that influences their behaviour. The cytoskeleton provides a bridge to transmit information between the extracellular and the intracellular environments. It has been suggested that the CSK components may have distinct mechanical roles in the cell and that they might form the structure that defines cell rigidity. One approach to studying the mechanosensing processes is to understand the mechanical properties of cells' constitutive components individually. In this chapter we describe the development of a multi-structural 3D finite element model of a single-adherent cell to investigate the biophysical differences of the mechanical role of each cytoskeleton component. The model includes prestressed actin bundles and microtubule within the cytoplasm and nucleus, which are surrounded by the actin cortex.

With the multi-structural model, we predicted that actin cortex and microtubules were targeted to respond to compressive loads, while actin bundles and microtubules were major components in maintaining cell forces during stretching. Additionally, corroboration of the multi-structural model regarding its ability to identify the role of the CSK components was obtained by comparing the numerical predictions with AFM force measurements on U2OS-osteosarcoma cells exposed to different cytoskeleton-disrupting drugs. Overall, the multi-structural model not only illustrates that a combination of cytoskeletal structures with their own properties is necessary for a complete description of cellular mechanics but also clarifies the effects of cytoskeletal heterogeneity on the interpretation of force-deformation measurements.

9.1 Cell Mechanoresponse for Tissue Engineering

The emerging field of tissue engineering aims to repair and regenerate functional tissue in patients that suffer from tissue degeneration or loss of function. Tissue engineering involves the integration of three key factors: an appropriate scaffold to

This chapter forms part the PhD thesis of Sara Barreto available here: http://etheses.whiterose.ac.uk/4928/

© Springer Nature Singapore Pte Ltd. 2019

D. Lacroix et al., *Multiscale Mechanobiology in Tissue Engineering*,
Frontiers of Biomechanics 3, https://doi.org/10.1007/978-981-10-8075-3_9

mimic the role of the extracellular matrix and cells and a controlled and reproducible culture environment, such as growth factors and bioreactor culture systems, in which the cells seeded into the scaffolds can be directed to initiate the required tissue formation.

One of the key challenges of tissue engineering is the ability to grow large amount and 3D tissue structures of relevant clinical size. In order to establish the optimal conditions for tissue formation, most of the in vivo experiments in tissue engineering are initiated in 2D cultures. However, the response of cells when cultured in 2D conditions can be very different from a 3D environment (Pampaloni et al. 2007; Khetan et al. 2013) demonstrating the importance of an established 3D local microenvironment for a functional cellular behaviour and differentiation of mesenchymal stromal cells. Cells are dynamic units that possess structural and physical properties that enable them to perform specialized functions and to withstand the physiological environment and balance of mechanical forces and mechanical stimuli occurring in the body.

The study of the coupling between mechanical forces and cellular biological processes is referred to as mechanobiology. These forces are generated from intrinsic molecular components along with actively generated forces from the extracellular environment and are transmitted to the nucleus (Wang and Ingber 1994) through the cytoskeleton. Cells respond to a variety of stimuli, including mechanical forces that appear in the form of changes in the rigidity of the extracellular matrix, cellular contraction due to cell-cell interactions and deformation due to interstitial fluids. This balance of the mechanical forces leads to CSK remodelling and allows the cells to adapt to and withstand new environments, while maintaining their physiology. Loss of force transmission between the extracellular matrix, the cytoskeleton and the interior of the nucleus is implicated in loss of tissue homeostasis and is a hallmark of many mechanobiological diseases, including muscular dystrophies, degenerative diseases, cancer and progression and metastases (Wang et al. 2009; Tapley and Starr 2013; Pelissier et al. 2014).

The mechanism by which cells transform mechanical signals into biological responses is known as mechanotransduction, and the response of cells to applied forces from the surrounding environment is divided into two parts: the first is a mechanical response consisting of the deformation of the cell's load-bearing structures (Gardel et al. 2006; Janmey and Weitz 2004; Kasza et al. 2007); and the second is the biochemical signalling response, which potentially leads to most force-induced changes in cell behaviour (Geiger and Bershadsky 2002). Therefore, understanding the changes occurring in the internal structure of cells to respond to different mechanical cues from a 3D extracellular environment is fundamental to establish tissue formation using bioreactors systems.

The cytoskeleton (CSK) is the structural component of cells and a key element for cell mechanoresponses. The CSK is involved in the mechanotransductive process in the cellular interior, transducing the mechanical forces from the external environment to the nucleus and vice versa. The CSK is composed of hundreds of associated proteins organized into three major classes of filamentous proteins known as actin filaments, microtubules and intermediate filaments. These proteins form a highly

complex network that provides a structural and dynamic natural organization to the cell. The CSK is also involved in the maintenance of cell shape and integrity, and in generating movements of the whole cell, and of the intercellular components.

Recent studies evaluating the physical principles of cell mechanics and the relationship between tissue elasticity and cell function have shown that specific cell properties, including the critical role of internal cell forces due to cell-matrix interactions, are an important factor for differentiation of stem cells into specific tissues (Engler et al. 2006). Application of mechanical forces on cells has shown to induce chemomechanical responses that can change gene expression, control stem cell differentiation (McCoy et al. 2012; Mullen et al. 2015) and induce changes in pathways involved in tissue development, growth and homeostasis (Hao et al. 2015; Wozniak and Chen 2009). Further understanding and development of in vitro mechanical cues for stem cell differentiation into different types of tissue cells is an important step in the tissue engineering, cell therapy and regenerative medicine fields.

In vitro cell culture is used to study the effect of mechanical loading in cell deformations, cell-matrix interactions, motility, adhesion, reorganization of the cytoskeleton, force transmission and gene expressions. Computational models are another way of experimentation that can be used to analyse mechanical responses that have been implicated at the cellular and molecular level in terms of complex biological processes on tissue and organ levels. The importance of mechano-computational studies can be appreciated for predicting mechanical parameters of cells such as apparent stiffness, Young's modulus and rigidity. These predictive models are advantageous tools to understand cellular processes that involve internal cellular changes as well as the impact of mechanical alterations of the extracellular environment. To appreciate the mechanical operation of a whole cell, one must understand how its components behave both in isolation and as a composite structure. It is important to understand individual behaviour of cellular components as it is equally important to assemble the components and observe how the cell functions as a whole. Understanding the relationship between forces, intracellular structures and cell function may require meaningful quantification of these coupled variables. This can be done by using a multi-structural cell model, including all the relevant load-bearing structures in the cell and their interconnections, to predict the static and dynamic cellular responses to mechanical perturbations.

9.2 Computational Models to Study Load Transfer at Cellular Level

9.2.1 The Benefits of Computational Models

Computational modelling offers a higher degree of complexity that includes molecular, cellular, tissue and organ levels for a better understanding of force transmission

processes by which mechanical conditions influence an integrated biological system. Integrating experimental and computational approaches can make the engineering of cells with enhanced functional properties possible. Finite element (FE) simulations in cell mechanics are also useful in predicting the response of living cells at physiologically relevant temporal and spatial scales. This is done by solving together the continuum and discrete scale constitutive equations arising in multiscale biomechanics problems.

The shape, function and mechanical properties of tissues and, therefore, adherent cells depend mainly on the mechanical properties of the CSK (Ingber 1993; Janmey 1998; Heidemann and Wirtz 2004). Evidences of this include the non-uniformity of the distribution of strain throughout the cell (Bausch et al. 1998) and the propagation of forces over long distances across the cytoskeleton (Maniotis et al. 1997). For adherent cells, it is therefore more reasonable to model the cytoskeleton as the key structure to define their mechanical properties.

Several theories have been proposed to develop FE computational models to understand cell mechanical properties and mechanotransduction. Other FE models are based on experimental techniques for the application of force on cells by simulating the forces as inputs to the cell model to explain the experimental observations of cell interaction with the surrounding environment. The experimental techniques to apply external forces to the cells include atomic force microscopy (Nawaz et al. 2012), magnetic tweezers or micropipette aspiration (Ohayon and Tracqui 2005; Karcher et al. 2003; Reynolds et al. 2014) traction force microscopy (Lemmon et al. 2009; Legant et al. 2010), substrate stretching (Legant et al. 2013), etc.

9.2.2 Tensegrity Models

The tensegrity theory has been extensively used to investigate cellular deformability as a mean to represent the various structural elements of the cytoskeleton and cell adhesion to the ECM. Tensegrity is a building technique in which the mechanical integrity of a structure is maintained by some members that are under tension (cables) and others that are under compression (struts) in which the structural stability is maintained by a pre-existing stress (prestress) created in the mechanical elements. In the absence of prestress, the structure would lose its stability and collapse. At the level of adherent cells, it was proposed that the actin and intermediate filaments play the role of the tension elements, while microtubules are the compressive elements (Ingber 2003). Some FE computational models have been developed based on the tensegrity theory – (McGarry and Prendergast 2004) developed a finite element cell model based on tensegrity to describe the microtubules and the actin filaments of the prestressed CSK. This model also incorporates, in an idealized geometry, the other cellular components considered structurally significant: the cytoplasm, nucleus and membrane components. The results obtained by applying external forces suggest a key role for the cytoskeleton in determining

cellular stiffness. The model is proposed as one that is sufficiently complex to capture the nonlinear structural behaviours, such as stiffening and prestress effects, and variable compliance along the cell surface. Parametrical studies reveal that material properties of the cytoplasm (elasticity and compressibility) also have a large influence on cellular stiffness (McGarry and Prendergast 2004). This model was further developed to make qualitative and quantitative predictions of the differences in cellular deformation caused by fluid shear stress and substrate strain at magnitudes commonly applied in vitro (McGarry et al. 2005a, b) and for cell-substrate contact during cyclic substrate deformation (McGarry et al. 2005b).

A more recent FE tensegrity-based model was developed to study the mechanosensory process of osteocytes due to the direct connection of the cytoskeleton to the nucleus (Kardas et al. 2012). This has an impact on the remodelling and mineralization of bone tissue. The computational cell model includes the major components with respect to mechanical aspects: the integrins that connect the cell with the extracellular bone matrix; prestressed tensegrity elements representing microtubules and intermediate filaments; the membrane-cytoskeleton; the nucleus and the centrosome. This is a more complete model where the cell is simulated on its physiological environment, representing in vivo conditions. The results showed that the deformation of the membrane-CSK, with actin properties, is directly mapped to the nucleus, with this latter being more affected if the elements that carry the forces are randomly distributed.

9.2.3 Computational Modelling of Stress Fibres

Other computational models for stress fibre formation and contractility are based on cellular signalling and tension-dependent dissociation via a muscle-like constitutive law (Deshpande et al. 2006). McGarry et al. (2009) used the theory presented in Deshpande et al. (2006) to predict the relation between cell tractions and contractility of cells adhered to arrays of microposts, as well as to predict the effects of the stiffness and geometry of the microposts on the response of smooth muscle cells, mesenchymal stem cells and fibroblasts using FE analysis. This model predicted that the forces exerted by the cells would increase with both increasing post-stiffness and area of cell spreading and was demonstrated to be consistent with in vitro measurements.

Kaunas and Hsu (2009) used a kinetic model based on constrained mixture theory to model stress fibre dynamics with a formulation assuming that stress fibres dissociation occurs when a fibre has been stretched past a critical length. In response to a step change in matrix stretch, this model predicted that stress fibres are initially stretched in registry with the matrix but that these overly stretched fibres are gradually replaced by new fibres assembled with the homeostatic level of stretch in the new configuration of the matrix. The model was able to describe experimentally measured time courses of stress fibre reorientation perpendicular to the direction of cyclic uniaxial stretch, as well as the lack of alignment in response to

equibiaxial stretch, in accordance with the in vitro experiments with endothelial cells (Kaunas et al. 2006). Furthermore, the model of Kaunas and Hsu (2009) predicted that the rate of stretch-induced stress fibre disassembly determines the rate of alignment and that stress fibres tend to orient towards the direction of minimum matrix stretch where the rate of stress fibre turnover is a minimum.

Ronan et al. (2012) expanded the formulation presented in the study of McGarry et al. (2009) into a fully 3D framework to account for the simulation of realistic cell geometries, including round and spread cell configurations, with the inclusion of a separately modelled nucleus. This study was used to investigate differences in stress fibre evolution in a range of cell types with varying contractility. The authors predicted that highly contractile cells form more dominant circumferential stress fibres to provide greater resistance to compression, whereas fewer stress fibres were predicted for round cells with lower resistance to compression. Furthermore, Weafer et al. (2013) simulated irregular geometries while including a complex active constitutive law for stress fibre formation and distribution. The passive mechanical properties of the cytoplasm and nucleus are simulated with a passive hyperelastic material model, combined with active actin contractility parameters, to simulate the experimental data of AFM compression for osteoblasts. The study showed that cells treated with cyto-D had about a 50% decrease in the mean cell compression force compared to untreated control cells, demonstrating that the actin cytoskeleton plays a significant role in the resistance of osteoblasts to compression. The model also simulated the experimental observations of increased resistance to cell compression due to the presence of actin cytoskeleton contractility.

9.2.4 Dynamic Cell Modelling

More recently, Reynolds et al. (2014) developed a computational-experimental approach using micropipette aspiration – until now, a technique extensively used to probe suspended cells – combined with an active computational FE framework to understand the rearrangements of the actin stress fibres of contractile cells adhered to an extracellular matrix. The authors simulated the active stress fibres remodelling and the contribution of stress fibres to the mechanical response of the cell during micropipette aspiration of spread cells and conclude that a passive viscoelastic model is not sufficient to capture the response of spread adhered cells over a range of applied pressures.

Although recent models of active remodelling of the stress fibres and cell contractility have been developed and incorporated with formulations to explain the passive response of cells, they lack on explaining the contributions of other cytoskeletal components and in differentiating the mechanical role of different actin networks focusing mainly on the behaviour of stress fibres. New models should aim at describing a larger consensus picture of cell mechanical structure-function to make proper predictions about the absolute value of cell stiffness, the nonlinear

effects of cell mechanics, the role of forces and dynamic heterogeneity. But all of these predictions are only possible after an accurate description of the passive responses of cells.

9.2.5 Objectives

Our aim was to develop a single-cell multi-structural FE model to predict, reproduce consistently and compare cell mechanical properties between various probing techniques, across different cell types, but that is, at the same time, detailed enough to be mechanistically useful at describing relevant cell substructures and their passive response (Barreto 2013). These mechanical properties of individual cells are the basis for understanding the complex universal aspects of cell mechanics, such as the role that forces play in regulating the structure and function of cells and how it has been implicated at the tissues and organ levels. The new multi-structural single-cell model that we propose aims to investigate the passive response of the internal cellular components during compression and stretching, by modelling contractility of actin bundles through the incorporation of a prestrain at the beginning of the FE analysis (Barreto 2013).

9.3 Force Transduction in the CSK Components Using a New FE Single-Cell Model Including Prestress

9.3.1 Model Definition

A computational 3D FE multi-structural model of a single cell was developed (Barreto et al. 2013) including the intracellular components likely to be mechanically significant for cell behaviour: the cytoplasm, the nucleus and some cytoskeleton networks, namely, actin and microtubules (see Fig. 9.1).

In the model, continuum and discrete elements were used to represent the continuum media and the fibres of the cytoskeleton, respectively. In situ microscope images of cell shape adhered to a substrate and images of the distribution of stained actin and microtubules were used to create the 3D model of the cell and the architectural structure of the intracellular components. The geometry of the cell was developed and meshed using the finite element software Abaqus/Standard (Dassault Systemes, France). The shape of the cell was defined based on a semi-ellipsoidal profile with 19 μm diameter on the long axis (y-direction), 8 μm on the smaller axis (x-direction) and about 4 μm height (z-direction) on the highest part of the cell that corresponds to the centre of the y axis. However, the centre of the cell is located 3.5 μm from the centre of the y axis. The nucleus was modelled with an ellipsoidal shape, which is consistent with measures reported by Caille et al. (2002),

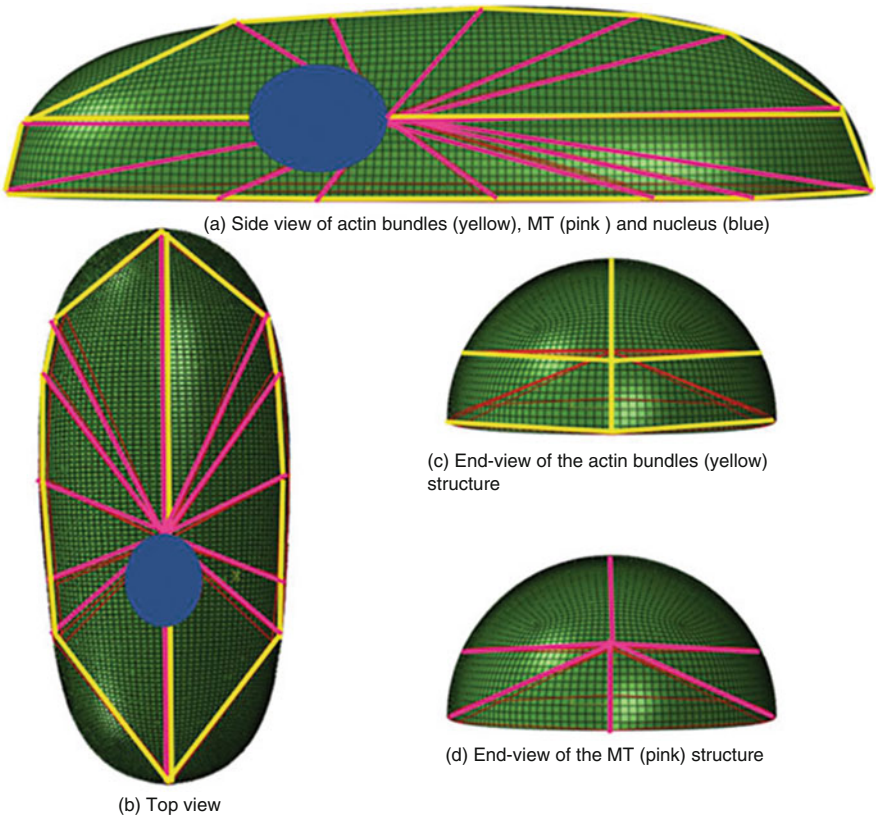

Fig. 9.1 Projections of actin bundles and microtubules distribution in the cell model with respect to the nucleus. (**a**) Side view of actin bundles (yellow) and MT (pink) with respect to the nucleus; (**b**) top view of actin bundles (yellow) and MT (pink), with a similar distribution of the discrete CSK components as it is found in the bottom view (not shown); (**c**) end-view distribution of actin bundles; and (**d**) end-view distribution of MT

and it is positioned at the centre of the y axis (that corresponds to the highest portion in the cell) and 2.5 μm from the bottom of the cell. The remaining space is filled with cytoplasm. Both cytoplasm and nucleus were modelled with 8-node continuum hexahedral solid elements (Table 9.1).

The cytoplasm was covered with a surface representing the actin cortex. The cortex is a thin layer of cytoskeleton actin gel, which exists in all types of animal cells, and is represented in the current cell model with shell elements (Table 9.1), originated from the outer surface of the quadrilateral elements of the cytoplasm, with a thickness of 0.2 μm (Unnikrishnan et al. 2007). Discrete elements were included within the cytoplasm to represent other CSK components, microtubules and actin bundles. Beam elements were used to model the microtubules structure (Table 9.1), originated from one common node near the nucleus, representing the centrosome. The beams were defined with a pipe section with external radius of 12.5 nm and wall

Table 9.1 Cell mesh properties used in the FE analysis

Cell component	Element type	N° of elements
Cytoplasm	Solid continuum	95,151
Nucleus	Solid continuum	5484
Microtubules	Beam	277
Actin cortex	Shell	11,748
Actin bundles	Truss	33

thickness of 5 nm. Microtubules are long and arranged in a star shape that grow from the centrosome to the cortex; see Fig. 9.1.

In many cells, actin is present in large groups of actin fibres, parallel to each other, joined by actin-binding proteins, known as actin bundles, normally localized around the cell periphery, that are referred to as dense peripheral band (Deguchi et al. 2006). In this model, they are arranged in the whole cell above the cortex and both ends are anchored to it (Fig. 9.1). The actin bundles were modelled as discrete truss elements (Table 9.1) with a radius of 12.5 nm (Deguchi et al. 2006). Truss elements are one-dimensional line elements that have two nodes and can be oriented anywhere in 3D space. Truss elements are long, slender structural members that have only axial stiffness and are three degrees-of-freedom elements, which allow translation only and not rotation. Therefore, truss elements do not transmit moments. For this reason, they were selected to better represent the mechanical behaviour of actin bundles that behave in a similar way as ropes. Beam elements are a one-dimensional line element in 3D space or in the XY plane that has stiffness associated with deformation of the line (the beam's axis). Two nodes define element geometry, and the third node defines the cross-sectional orientation. Beam elements are six degrees-of-freedom elements allowing both translation and rotation at each end node. Beam elements offer additional flexibility associated with transverse shear deformation between the beam's axis and its cross-sectional directions. That is the primary difference between beam and truss elements.

The different element types for actin bundles and microtubules were chosen to better represent their idealized structural role. Although microtubules were thought to have compression-only behaviour, there is now evidence that they can buckle and appear highly curved in living cell, when compression reaches critical values (Stamenović and Coughlin 1999; Stamenović et al. 2002; Schaap et al. 2006). Thus, microtubules were simulated to resist both compressive and tensional forces. Stiffness of actin bundles varies depending on both the number of fibres aligned together and on the mechanics of the type of actin-binding proteins that holds them together. Actin bundles are reported as rope-like behaviour and were modelled to resist only to tensional forces. These fibres have an inherent tensile stress and are internally prestressed even without application of an external load. Thus, these are the components in the model responsible for generating contractile forces. Previous experimental studies reported pre-existing strain values of 0.24 ± 0.18 and pre-existing force level of 4.08 nN (Deguchi et al. 2005) in actin filaments. The force-strain relationship measured by the previous authors was used to calculate the mechanical properties for the actin bundles of the current model: Young's modulus

and prestress. The value of 82 kPa, calculated from experimental measurements of stress fibre length and force (Deguchi et al. 2005; Kumar et al. 2006), was introduced in the model using UMAT subroutine of Abaqus (Dassault Systemes, France). This subroutine was modified to define the stress-strain relationship for actin bundles taking into account the initial state of stress caused by the 24% of initial strain of the bundles. The actin cortex, the other actin network in the model, was modelled as merely linear elastic and does not have a prestrain.

UMAT is the Abaqus subroutine used to define the mechanical constitutive behaviour of a material, which is called at all material calculation points of elements at the end of each increment for which the material definition includes a user-defined material behaviour. In this case the material Jacobian matrix is calculated for the actin bundles, where the UMAT subroutine is customized for the application of a prestrain of 24% (Barreto et al. 2013). Briefly, at the beginning of the simulation, for zero deformation of the actin bundles, a prestress of 82 kPa is defined. During the following increments, if the deformation of the bundles is higher than 24%, then the stress-strain relationship is linear; and if the deformation of the actin bundles is smaller than 24%, then the resultant stress in these elements is zero, as it can be seen in Fig. 9.2. For optimization of the running time of the analysis, all the actin bundles in the model are initially prestrained to the same level.

Interaction between all the components of the CSK is ensured at the cortex, where the elements of microtubules and actin bundles are connected by sharing the same end nodes (Fig. 9.1). Homogeneous, isotropic and elastic material properties were assumed for all the components and were taken from the literature (summarized in Table 9.2).

A 4.5 mm diametrical bead was modelled on the top of the cell to exert different external mechanical stimuli and measure the reaction force and deformation of the cell. The bead was moved towards the cell in the axial direction to establish the contact and further compression. This axial applied displacement was 0.5 mm, the same indentation depth applied during AFM experiments (Barreto et al. 2013). The bead was then moved horizontally with a sinusoidal

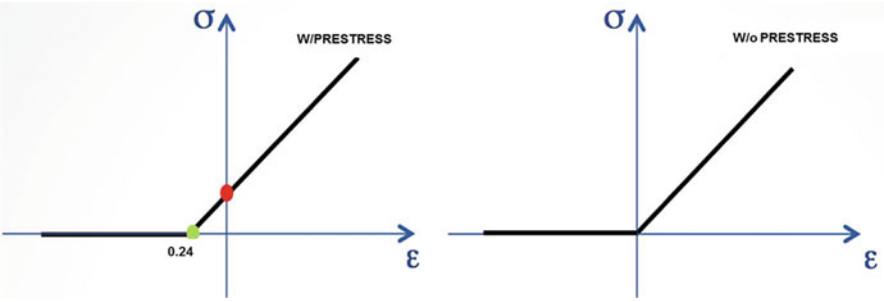

Fig. 9.2 Stress-strain relationship defining the mechanical behaviour of actin bundles with and without prestrained conditions. The green dot defines the amount of prestrain defined for the actin bundles in the subroutine UMAT, whereas the red dot defines the resultant prestress (i.e. the stress for zero deformation), which is imposed at the beginning of the FE simulation

Table 9.2 Material properties of the components of the cell model

Cell component	Young's modulus	Poisson ratio
Cytoplasm	0.25 kPa	0.49
Nucleus	1 kPa	0.3
Microtubules	2 GPa	0.3
Actin cortex	2 kPa	0.3
Actin bundles	341 kPa	0.3

movement with amplitude of 0.25 μm to stretch the cell and simulate the movement of the bead in MTC experiments (Mijailovich et al. 2002). From the stretching, longitudinal forces are computed. Zero displacement was applied to the bottom of the cell as a boundary condition, simulating full cell attachment to a rigid substrate.

The FE method was used to evaluate force and deformation of the cell when external forces were applied and how those forces were transmitted inside the cell. Cell forces and deformation to resist compression and stretching were evaluated by looking at the importance of incorporating different components of the cell (such as the cortical and deep CSK components) but also other factors (such as prestress and different external stimuli including compression and stretching).

The multi-structural model was used to compute cell forces and deformation due to various in vitro mechanical stimuli, such as compression and stretching, as sensed by cells due to cell-cell interactions and under fluid flow conditions. We analysed the effect of two single-cell stimulation methods, AFM and MTC, by application of the appropriate loading conditions in order to understand the biomechanical origins of differences in observed cell response. Other mechanical loading conditions could be applied in this model to study different mechanical environments or to compare different single-cell stimulation techniques, such as optical tweezers or microplate manipulation.

When creating this model, while it is understood that the CSK has a spectrum of elastic and viscous properties, in addition to a capacity to contract and remodel, it has been hypothesized that in the static regimen, there is a dominant elastic component to the mechanical properties and as such, these elastic properties dictate the response of the cell to a greater extent than the viscous properties.

9.3.2 Force and Deformation of the CSK Components Due to Mechanical Stimulation

With this model, we first analysed whether cell deformation is associated with specific components of the CSK, by looking at the strains in the individual elements of the model (Fig. 9.3). Strains observed in the cortex, nucleus and cytoplasm reached a maximum of about 40% when the cell was compressed (Barreto et al. 2013). During stretching, maximum strain was about 74% (Barreto et al. 2014). These high strains are due to localized deformation of the nodes caused by the

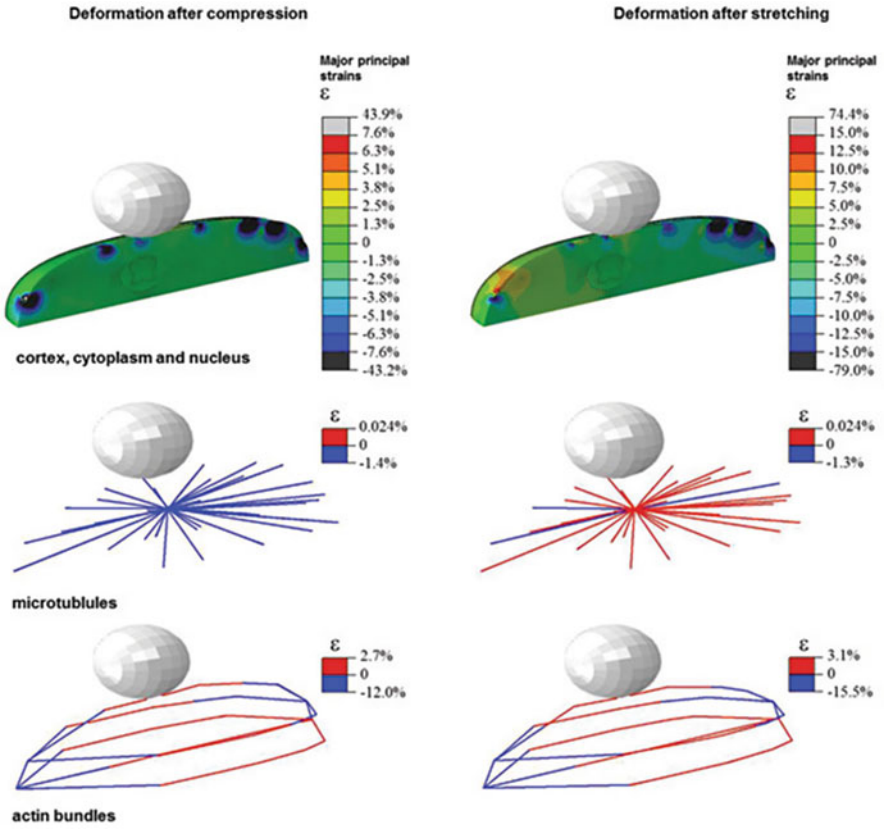

Fig. 9.3 Deformation of the different cellular components. Top represents strain distribution in the cortex, cytoplasm and nucleus after compression and stretching; middle shows deformation of microtubules after compression and stretching; and bottom shows deformation of actin bundles upon compression and stretching

attached discrete elements of the cytoskeleton. Low strains in microtubules are predicted by the model, which can be explained by microtubules' high rigidity. Depending on the stimulus (compression or stretching), microtubules would be more under compression (blue) or under stretching (red) depending on the external applied force.

Heterogeneous distribution of force on the bottom of the cell was obtained when the discrete elements of the CSK were introduced in a homogeneous elastic continuum model. The bottom part of the cell was fully constrained, simulating the contact with a rigid substrate. Higher localized forces were obtained on the end nodes of interconnection between actin bundles and microtubules, forming punctuated concentrations of force at the periphery of the cell. The maximum value of force obtained was 11 nN for both stimuli of compression and stretching. This high

concentration of forces is very likely associated with the formation of focal adhesions, which connects integrins from the substrate with the CSK to the interior of the cell. The preferential location for the formation of the focal adhesion complexes can be predicted by the numerical results, including the edge of the cell and the nodes of the CSK for force transmission to the substrate. The computed distribution of the force that the cell develops to resist the external stimulus in the presence of the CSK directs the formation of focal points, corresponding to the end nodes of the CSK and the edge of the cell.

Considering the cell shape in the model, forces developed in the bottom of the cell in response to stretching tend to be more concentrated at the periphery, with higher concentration in the two cell extremities defining an axis of orientation in the direction of the applied stretching. This distribution of forces indicating a potential preferential cell orientation is supported by the cell polarization theory (Rehfeldt and Discher 2007; Zemel and Safran 2007). This theory defines that cell orientation is governed by a contractile force dipole along the axis of orientation defined with respect to the applied force. The dipoles, defining cell polarization, are generated either by forces applied externally or generated internally due to prestress (Zemel and Safran 2007). Experiments in favour of this theory showed that for static or quasi-static strain, cells generally align parallel to the direction of principal strain (Collinsworth et al. 2000), while cyclic strain drives a near perpendicular orientation of cells (Wang et al. 2001; Kurpinski et al. 2006). The local tensile forces that were originated in the extremities of the discrete CSK elements can be seen when the CSK was modelled and these forces were higher when prestress was modelled in response to shearing, as discussed before. Even though the actin bundles in the model cell were not all aligned in the same direction, it is still possible to see a preferential direction of higher local forces in the cell model that relates prestress, CSK and focal adhesions obtained in this FE analysis.

9.3.3 Mechanical Role of Actin Fibres and Microtubules: Highlighting the Role of the Actin Cortex

CSK components are part of an integrated intracellular complex that maintains the force balance between CSK networks, focal adhesions, ECM and other cellular components (Huang et al. 2004). Due to this integrated system in cells, isolating individual components of the cell and identifying their role for force transmission is challenging. CSK-disrupting drugs have been used in combination with different cell stimulation techniques to study the mechanical role of each CSK component by selectively disrupting actin, intermediate filaments and/or microtubules. Though many studies have been performed in vitro to investigate the adaptation of the individual CSK components to mechanical stimuli (Wang 1998; Pelham and Wang 1999; Charras and Horton 2002; Collinsworth et al. 2000; Kasas et al. 2005),

results from different stimulation techniques cannot be pulled together for the analysis of the contribution of the individual fibres for the cellular response.

A deeper understanding of the effect of cytoskeletal disruption for force transmission during force application can now be achieved with our multi-structural single-cell model. The structure stability of the multi-structural model allows the individual CSK components to change form and organization without collapsing the cell shape when they are removed and, therefore, can investigate how the particular CSK components contribute to the mechanics of adherent cells.

We performed a computational-experimental analysis of the contribution of the individual CSK components for force transmission within the cell. The results indicate that during deformation, individual CSK components have different mechanical responses to specific external perturbation (Fig. 9.4). Although the model is a quasi-static analysis and does not include CSK remodelling essential for physiological cell functions, it suggests how the individual components of the CSK interact with each other depending on the type of forces the cells sense. The results showed that the actin cortex and microtubules are the main components to resist compression, while when sensing shear forces, cells activate the actin bundles and microtubules to resist stretching (Fig. 9.4).

The computational analysis also showed that when compressed, about 48% of the cell force is inhibited when all three components of the CSK were removed (Barreto et al. 2014). The numerical results during compression were experimentally validated with the use of AFM for the same amount of indentation. The apparent Young's modulus, when CSK was disrupted with nocodazole (chemical disruption of microtubules) and cytochalasin D (chemical disruption of actin) during the AFM experiments, decreased $58 \pm 6\%$ for U2OS cells. U2OS cells are a cell line originally cultivated from human bone with osteosarcoma that exhibit epithelial adherent morphology. In these cells actin fibres are uniformly distributed all over the cell, and the shape is consistent with the one of the computational multi-structural model. Fluorescence images of U2OS cells with GFP-actin showed disruption of the entire assembly of actin networks when exposed to 0.5 μM of cytochalasin D (Fig. 9.5). In these conditions, a decrease in apparent Young's modulus of $49 \pm 17\%$ was obtained during AFM indentation, which matched the 51% decrease in force obtained with the FE model when actin cortex and actin bundles were removed from the cell.

Attempts to quantify the contribution of the different actin networks to the mechanical properties of cells have been done experimentally (Lang et al. 2000; Van Citters et al. 2006) but with difficulties in isolating the role of actin cortex at the cell periphery from deep actin cytoskeleton networks. To overcome this issue, this multi-structural FE model is the first study that can accurately isolate and quantify the actin cortex role from other actin networks within cells when subjected to different static loads. Removal of actin bundles from the multi-structural cell model did not change the resulting force of the cell to resist compression. However, when removing the actin cortex, there was a 51% decrease in cell force (Fig. 9.4a). This result demonstrates that almost half of the cell force during compression is sustained by the actin cortex, whereas the other part is sustained by the microtubules.

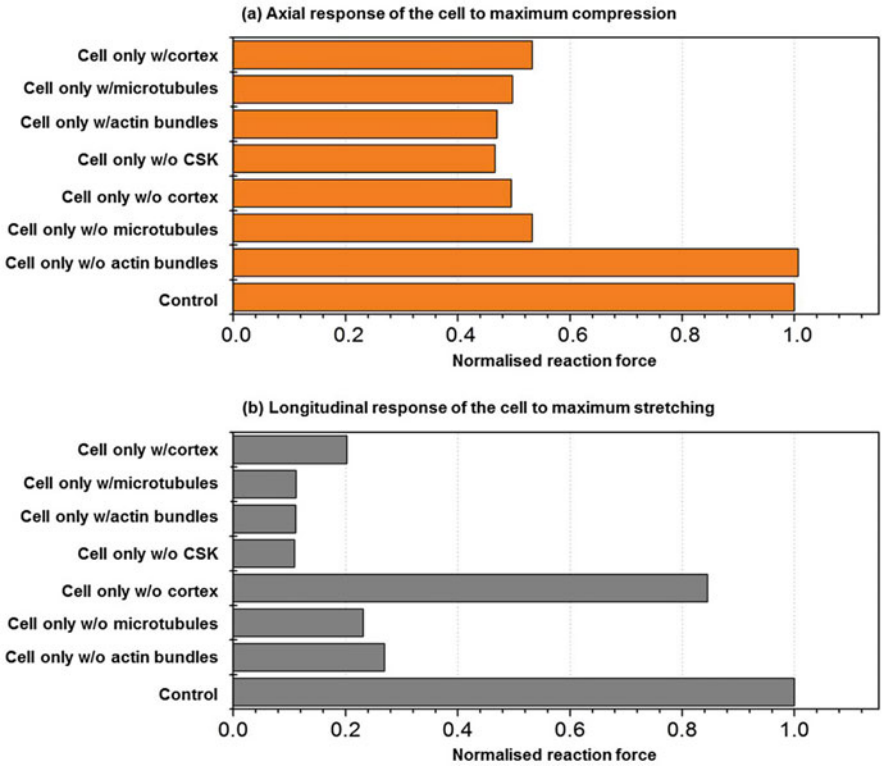

Fig. 9.4 Contribution of each component of the cytoskeleton for the different stimuli and effect of interaction between the elements of the cytoskeleton. (**a**) Axial force for maximum compression and (**b**) longitudinal force for maximum stretching. Reaction force of the cell for the different models is normalized to the control model

When cells are subjected to shear forces, the contribution of the individual CSK components is different (Fig. 9.4b). The 89% computationally predicted decrease in reaction force during stretching is in good agreement with the 75–80% decrease in stiffness observed when drugs were combined to disrupt both actin and microtubules and actin, microtubules and intermediate filaments (Wang 1998). The current model showed the low ability of the cortex to resist stretching, which is also suggested experimentally by Wang et al. (2002). Another study by Van Citters et al. (2006) compared the mechanical properties of the cortical region of the lamellipodial region with the F-actin in the interior of epithelial cells during stretching with MTC. The authors did not observe changes in cell stiffness of the cortical region upon actin disruption with latrunculin A after stretching, though that cell behaviour became closer to a pure elastic response when F-actin in the cell interior was disrupted. A purely elastic response is frequency-independent. Therefore, this experimental study corroborates the low ability of the cortex to resist shear forces for quasi-static conditions.

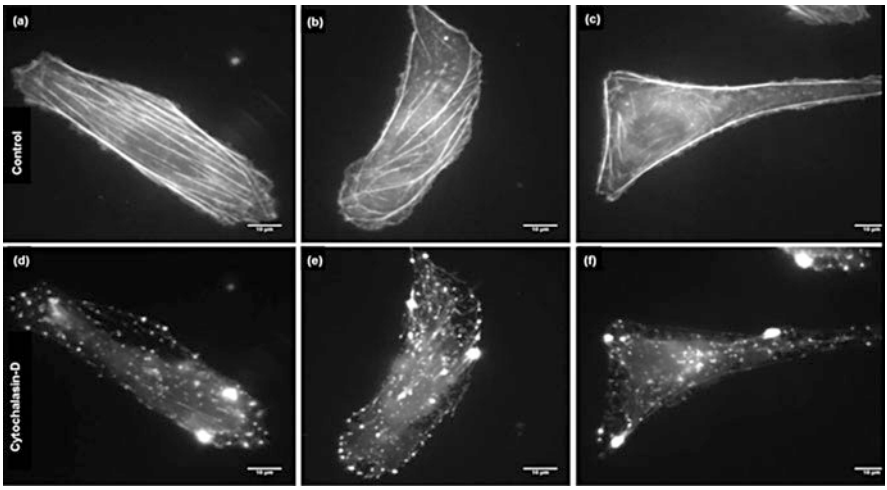

Fig. 9.5 Microscopic images of the actin structure of U2OS GFP-actin cells before and after exposure to cytochalasin D, during AFM experiments

9.3.4 Analysing Different Cell Probing Techniques

As an attempt to investigate cellular responses when probed by different experimental techniques for cell indentation as well as the accuracy of these techniques, specifically AFM and MTC, different indentation positions and amplitudes of stimuli were considered to probe cells. Variation of the compressive stimulus in the present study (Fig. 9.6) showed that the results in terms of reaction force were dependent of the degree of bead embedding in the cell, which is in agreement with results reported by other authors using single-cell FE simulations (Mijailovich et al. 2002; Karcher et al. 2003). Nonetheless, the degree of embedding did not affect the response of the cell in stretching (Fig. 9.6). A nonlinear increase of the reaction force of the cell when the compressive stimulus is increased was verified. The deformation of the cytoplasm, nucleus and cortex in response to 0.05 μm compression was two-times higher than when the cell was compressed at 0.5 μm (a ten-times increase in the applied stimulus). By observing separately the deformation of each component of the CSK, changes in the compressive strains of the elements for different values of compression were not noticed. The explanation for this nonlinearity of the results in the model is due to high concentration of tensile strains in the cortex below the bead due to changes in the contact surface as the bead approaches the cell, originated from the nonlinear problem of contact between the two surfaces. Nonetheless, compressive strains in the cortex do not depend on the applied force. Therefore, the

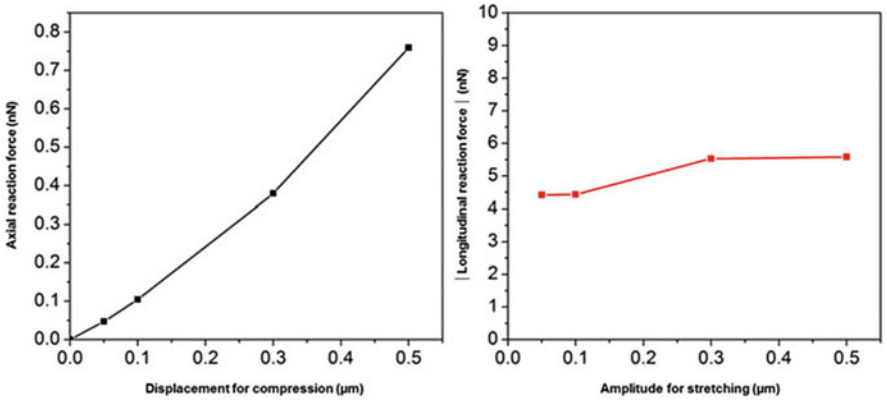

Fig. 9.6 Effect of variation of indentation depth on (**a**) axial forces after compression and (**b**) longitudinal forces after the cycle of stretching

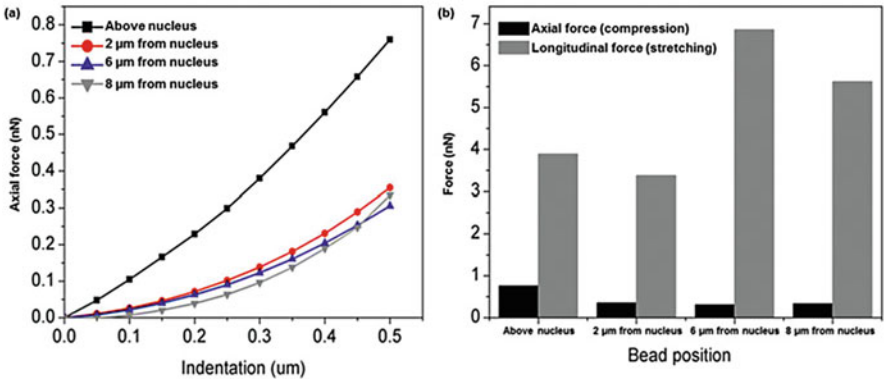

Fig. 9.7 Cell force considering different indentation positions. (**a**) Force-indentation relationship for different bead positions. (**b**) Maximum axial and longitudinal forces for different bead positions, for indentation of 0.5 μm and shear amplitude of 0.25 μm, respectively

nonlinearity caused by tensile strains does not affect the deformation in compression. Single-cell techniques apply localized forces, and the response of cells to those local stimuli is dependent on the distribution of the cellular components inside the cell and the application of the external stimuli (Fig. 9.7), which corroborates the measurements of cell elasticity obtained with AFM and optical trapping by Nawaz et al. (2012) and Xu et al. (2012). This new methodology explains the different published results obtained with different experimental stimulation techniques, which are important for understanding the biomechanical origin of differences in the observed cell responses.

9.4 Conclusions

This multi-structural model of an adherent cell specifies the elementary mechanical nature of the CSK components to resist external stimuli including compression and stretching. This new methodology predicts the capacity of the cytoskeleton to establish an elastic network to sense and transmit mechanical stimuli and provides a tool to explain variations in the results obtained with different experimental techniques. Furthermore, this new concept explains cell mechano-physics by establishing a relationship between cell rigidity and prestress during compressive loading and stretching. The concept implemented to define the CSK structure in this FE model defines prestress as an essential parameter to generate initial force and maintain cell shape, although not essential to define the interplay between discrete components.

The developed model is a fusion of the contrasting theories to describe cells, the continuum and discrete approaches, by including the nucleus and a continuum cytoplasm with actin cortex with discrete components representing the actin bundles and microtubules. While the structural stability defined for the actin bundles and microtubules in this model takes into account the interconnectivity between these elements, it also allows for an independent organization of the individual components without collapsing the cell. For example, we can specifically isolate the actin cortex from the remaining CSK components and quantify the contribution of the cortex for cellular forces, which is not possible to assess in vitro. This unique feature of the model opens new perspectives in studying the correlation of cellular mechanical properties and stress distribution within particular CSK components and on the mechanisms of force propagation by cells.

References

Barreto S (2013) Biomechanical study of the mechanical and structural properties of adherent cells. University of Sheffield

Barreto S, Casper HC, Perrault CM, Fletcher DA, Lacroix D (2013) A multi-structural single cell model of force-induced interactions of cytoskeletal components. Biomaterials 34 (26):6119–6126. https://doi.org/10.1016/j.biomaterials.2013.04.022

Barreto S, Perrault CM, Lacroix D (2014) Structural finite element analysis to explain cell mechanics variability. J Mech Behav Biomed Mater 38:219–231. https://doi.org/10.1016/j.jmbbm.2013.11.022

Bausch AR, Ziemann F, Boulbitch AA, Jacobson K, Sackmann E (1998) Local measurements of viscoelastic parameters of adherent cell surfaces by magnetic bead microrheometry. Biophys J 75(4):2038–2049. https://doi.org/10.1016/S0006-3495(98)77646-5

Caille N, Thoumine O, Tardy Y, Meister J-J (2002) Contribution of the nucleus to the mechanical properties of endothelial cells. J Biomech 35(2):177–187

Charras GT, Horton MA (2002) Determination of cellular strains by combined atomic force microscopy and finite element modeling. Biophys J 83(2):858–879. https://doi.org/10.1016/S0006-3495(02)75214-4

Collinsworth AM, Torgan CE, Nagda SN, Rajalingam RJ, Kraus WE, Truskey GA (2000) Orientation and length of mammalian skeletal myocytes in response to a unidirectional stretch. Cell Tissue Res 302(2):243–251. https://doi.org/10.1007/s004410000224

Deguchi S, Ohashi T, Sato M (2005) Evaluation of tension in actin bundle of endothelial cells based on preexisting strain and tensile properties measurements. Mol Cell Biomech: MCB 2 (3):125–133

Deguchi S, Ohashi T, Sato M (2006) Tensile properties of single stress fibers isolated from cultured vascular smooth muscle cells. J Biomech 39(14.) (January):2603–2610. https://doi.org/10.1016/j.jbiomech.2005.08.026

Deshpande VS, McMeeking RM, Evans AG (2006) A bio-chemo-mechanical model for cell contractility. Proc Natl Acad Sci U S A 103(38):14015–14020. https://doi.org/10.1073/pnas.0605837103

Engler AJ, Sen S, Sweeney HL, Discher DE (2006) Matrix elasticity directs stem cell lineage specification. Cell 126(4):677–689. https://doi.org/10.1016/j.cell.2006.06.044

Gardel ML, Nakamura F, Hartwig JH, Crocker JC, Stossel TP, Weitz DA (2006) Prestressed F-actin networks cross-linked by Hinged Filamins replicate mechanical properties of cells. Proc Natl Acad Sci U S A 103(6):1762–1767. https://doi.org/10.1073/pnas.0504777103

Geiger B, Bershadsky A (2002) Exploring the neighborhood: adhesion-coupled cell mechanosensors. Cell 110(2):139–142

Hao J, Zhang Y, Jing D, Shen Y, Tang G, Huang S, Zhao Z (2015) Mechanobiology of mesenchymal stem cells: perspective into mechanical induction of MSC fate. Acta Biomater 20:1–9. https://doi.org/10.1016/j.actbio.2015.04.008

Heidemann SR, Wirtz D (2004) Towards a regional approach to cell mechanics. Trends Cell Biol 14 (4):160–166. https://doi.org/10.1016/j.tcb.2004.02.003

Huang H, Kamm RD, Lee Ri T (2004) Cell mechanics and mechanotransduction: pathways, probes, and physiology. Am J Phys Cell Phys 287(1):C1–C11. https://doi.org/10.1152/ajpcell.00559.2003.

Ingber DE (1993) Cellular tensegrity: defining new rules of biological design that govern the cytoskeleton. J Cell Sci 104(Pt 3):613–627

Ingber DE (2003) Tensegrity I. Cell structure and hierarchical systems biology. J Cell Sci 116 (7):1157–1173. https://doi.org/10.1242/jcs.00359

Janmey PA (1998) The cytoskeleton and cell signaling: component localization and mechanical coupling. Physiol Rev 78(3):763–781

Janmey PA, Weitz DA (2004) Dealing with mechanics: mechanisms of force transduction in cells. Trends Biochem Sci 29(7):364–370. https://doi.org/10.1016/j.tibs.2004.05.003

Karcher H, Lammerding J, Huang H, Lee RT, Kamm RD, Kaazempur-Mofrad MR (2003) A three-dimensional viscoelastic model for cell deformation with experimental verification. Biophys J 85(5):3336–3349. https://doi.org/10.1016/S0006-3495(03)74753-5

Kardas D, Nackenhorst U, Balzani D (2012) Computational model for the cell-mechanical response of the osteocyte cytoskeleton based on self-stabilizing tensegrity structures. Biomech Model Mechanobiol. https://doi.org/10.1007/s10237-012-0390-y

Kasas S, Wang X, Hirling H, Marsault R, Huni B, Yersin A, Regazzi R et al (2005) Superficial and deep changes of cellular mechanical properties following cytoskeleton disassembly. Cell Motil Cytoskeleton 62(2):124–132. https://doi.org/10.1002/cm.20086

Kasza KE, Rowat AC, Liu J, Angelini TE, Brangwynne CP, Koenderink GH, Weitz DA (2007) The cell as a material. Curr Opin Cell Biol 19(1):101–107. https://doi.org/10.1016/j.ceb.2006.12.002

Kaunas R, Hsu H-J (2009) A kinematic model of stretch-induced stress fiber turnover and reorideshentation. J Theor Biol 257:320–330

Kaunas R, Usami S, Chien S (2006) Regulation of stretch-induced JNK activation by stress fiber orientation. Cell Signal 18:1924–1931

Khetan S, Guvendiren M, Legant WR, Cohen DM, Chen CS, Burdick JA (2013) Degradation-mediated cellular traction directs stem cell fate in covalently crosslinked three-dimensional hydrogels. Nat Mater 12(5):458–465. https://doi.org/10.1038/nmat3586

Kumar S, Maxwell IZ, Heisterkamp A, Polte TR, Lele TP, Salanga M, Mazur E, Ingber DE (2006) Viscoelastic retraction of single living stress fibers and its impact on cell shape, cytoskeletal organization, and extracellular matrix mechanics. Biophys J 90(10):3762–3773. https://doi.org/10.1529/biophysj.105.071506

Kurpinski K, Chu J, Hashi C, Li S (2006) Anisotropic mechanosensing by mesenchymal stem cells. Proc Natl Acad Sci U S A 103(44):16095–16100. https://doi.org/10.1073/pnas.0604182103

Lang T, Wacker I, Wunderlich I, Rohrbach A, Giese G, Soldati T, Almers W (2000) Role of actin cortex in the subplasmalemmal transport of secretory granules in PC-12 cells. Biophys J 78 (6):2863–2877. https://doi.org/10.1016/S0006-3495(00)76828-7

Legant WR, Miller JS, Blakely BL, Cohen DM, Genin GM, Chen CS (2010) Measurement of mechanical tractions exerted by cells in three-dimensional matrices. Nat Methods 7(12). https://doi.org/10.1038/nmeth.1531

Legant WR, Choi CK, Miller JS, Shao L, Gao L, Betzig E, Chen CS (2013) Multidimensional traction force microscopy reveals out-of-plane rotational moments about focal adhesions. Proc Natl Acad Sci 110(3):881–886. https://doi.org/10.1073/pnas.1207997110

Lemmon CA, Chen CS, Romer LH (2009) Cell traction forces direct fibronectin matrix assembly. Biophys J 96(2):729–738. https://doi.org/10.1016/j.bpj.2008.10.009

Maniotis AJ, Chen CS, Ingber DE (1997) Demonstration of mechanical connections between integrins, cytoskeletal filaments, and nucleoplasm that stabilize nuclear structure. Proc Natl Acad Sci U S A 94(3):849–854

McCoy RJ, Jungreuthmayer C, O'Brien FJ (2012) Influence of flow rate and scaffold pore size on cell behavior during mechanical stimulation in a flow perfusion bioreactor. Biotechnol Bioeng 109(6):1583–1594. https://doi.org/10.1002/bit.24424

McGarry JG, Prendergast PJ (2004) A three-dimensional finite element model of an adherent eukaryotic cell. Eur Cell Mater 7:27–33; discussion 33–4

McGarry JP, Klein-Nulend J, Mullender MG, Prendergast PJ (2005a) A comparison of strain and fluid shear stress in stimulating bone cell responses – a computational and experimental study. FASEB J: Off Publ Fed Am Soc Exp Biol 19(3):482–484. https://doi.org/10.1096/fj.04-2210fje

Mcgarry JG, Murphy B, Mchugh P (2005b) Computational mechanics modelling of cell–substrate contact during cyclic substrate deformation. J Mech Phys Solids 53(12):2597–2637. https://doi.org/10.1016/j.jmps.2005.07.006

McGarry JP, Fu J, Yang MT, Chen CS, McMeeking RM, Evans AG, Deshpande VS (2009) Simulation of the contractile response of cells on an array of micro-posts. Philos Transact A Math Phys Eng Sci 367(1902):3477–3497. https://doi.org/10.1098/rsta.2009.0097

Mijailovich SM, Kojic M, Zivkovic M, Fabry B, Fredberg JJ (2002) A finite element model of cell deformation during magnetic bead twisting. J Appl Physiol 93:1429–1436. https://doi.org/10.1152/japplphysiol.00255.2002

Mullen CA, Vaughan TJ, Billiar KL, McNarama LM (2015) The effect of substrate stiffness, thickness, and cross-linking density on osteogenic cell behavior. Biophys J 108(7):1604–1612

Nawaz S, Sánchez P, Bodensiek K, Li S, Simons M, Schaap IAT (2012) Cell visco-elasticity measured with AFM and optical trapping at sub-micrometer deformations. Aegerter CM (ed). PLoS One 7(9): e45297. https://doi.org/10.1371/journal.pone.0045297.

Ohayon J, Tracqui P (2005) Computation of adherent cell elasticity for critical cell-bead geometry in magnetic twisting experiments. Ann Biomed Eng 33(2):131–141. https://doi.org/10.1007/s10439-0058972-9.

Pampaloni F, Reynaud EG, Stelzer EHK (2007) The third dimension bridges the gap between cell culture and live tissue. Nat Rev Mol Cell Biol 8:839–845

Pelham RJ, Wang YL (1999) High resolution detection of mechanical forces exerted by locomoting fibroblasts on the substrate. Mol Biol Cell 10(4):935–945

Pelissier FA, Garbe JC, Ananthanarayanan B, Miyano M, Lin CH, Jokela T, Kumar S, Stampfer MR, Lorens JB, LaBarge MA (2014) Age-related dysfunction in mechanotransduction impairs differentiation of human mammary epithelial progenitors. Cell Rep 7(6):1926–1939. https://doi.org/10.1016/j.celrep.2014.05.021

Rehfeldt F, Discher DE (2007) Cell dipoles feel their way quantum to classical and back. Nat Phys 3:592–593

Reynolds NH, Ronan W, Dowling EP, Owens P, McMeeking RM, McGarry JP (2014) On the role of the actin cytoskeleton and nucleus in the biomechanical response of spread cells. Biomaterials 35(13):4015–4025

Ronan W, Deshpande VS, McMeeking RM, McGarry JP (2012) Numerical investigation of the active role of the actin cytoskeleton in the compression resistance of cells. J Mech Behav Biomed Mater 14:143–157. https://doi.org/10.1016/j.jmbbm.2012.05.016

Schaap IAT, Carrasco C, de Pablo PJ, MacKintosh FC, Schmidt CF (2006) Elastic response, buckling, and instability of microtubules under radial indentation. Biophys J 91 (4):1521–1531. https://doi.org/10.1529/biophysj.105.077826

Stamenović D, Coughlin MF (1999) The role of prestress and architecture of the cytoskeleton and deformability of cytoskeletal filaments in mechanics of adherent cells: a quantitative analysis. J Theor Biol 201(1):63–74. https://doi.org/10.1006/jtbi.1999.1014

Stamenović D, Mijailovich SM, Tolić-Nørrelykke IM, Chen J, Wang N (2002) Cell prestress. II. Contribution of microtubules. Am J Phys Cell Phys 282(3):C617–C624. https://doi.org/10.1152/ajpcell.00271.2001

Tapley EC, Starr DA (2013) Connecting the nucleus to the cytoskeleton by SUN-KASH bridges across the nuclear envelope. Curr Opin Cell Biol 25(1):57–62. https://doi.org/10.1016/j.ceb.2012.10.014

Unnikrishnan GU, Unnikrishnan VU, Reddy JN (2007) Constitutive material modeling of cell: a micromechanics approach. J Biomech Eng 129(3):315–323. https://doi.org/10.1115/1.2720908.

Van Citters KM, Hoffman BD, Massiera G, Crocker JC (2006) The role of F-actin and myosin in epithelial cell rheology. Biophys J 91(10):3946–3956. https://doi.org/10.1529/biophysj.106.091264

Wang N (1998) Mechanical interactions among cytoskeletal filaments. Hypertension 32 (1):162–165

Wang N, Ingber D (1994) Control of cytoskeletal mechanics by extracellular matrix, cell shape, and mechanical tension. Biophys J 66(6):2181–2189. https://doi.org/10.1016/S0006-3495(94)81014-8

Wang JH, Goldschmidt-Clermont P, Wille J, Yin FC (2001) Specificity of endothelial cell reorientation in response to cyclic mechanical stretching. J Biomech 34(12):1563–1572

Wang N, Tolić-Nørrelykke IM, Chen J, Mijailovich SM, Butler JP, Fredberg JJ, Stamenović D (2002) Cell prestress. I. Stiffness and prestress are closely associated in adherent contractile cells. Am J Phys Cell Phys 282(3):C606–C616. https://doi.org/10.1152/ajpcell.00269.2001

Wang N, Tytell JD, Ingber DE (2009) Mechanotransduction at a distance: mechanically coupling the extracellular matrix with the nucleus. Nat Rev Mol Cell Biol 10(1):75–82. https://doi.org/10.1038/nrm2594

Weafer PP, Ronan W, Jarvi SP s, McGarry JP (2013) Experimental and computational investigation of the role of stress fiber contractility in the resistance of osteoblasts to compression. Bull Math Biol 75(8):1284–1303. https://doi.org/10.1007/s11538-013-9812-y.

Wozniak MA, Chen CS (2009) Mechanotransduction in development: a growing role for contractility. Nat Rev Mol Cell Biol 10(1):34–43. https://doi.org/10.1038/nrm2592

Xu W, Mezencev R, Kim B, Wang L, McDonald J, Sulchek T (2012) Cell stiffness is a biomarker of the metastatic potential of ovarian cancer cells. PLoS One 7(10):e46609. https://doi.org/10.1371/journal.pone.0046609

Zemel A, Safran S (2007) Active self-polarization of contractile cells in asymmetrically shaped domains. Phys Rev E Stat Nonlinear Soft Matter Phys 76(2 Pt 1):021905. https://doi.org/10.1103/PhysRevE.76.021905

Chapter 10
Quantification of CSK Mechanics and Deformation in Relation to Cellular Functioning

The ability to predict the mechanical responses of different adherent cell types presents many opportunities to mechanobiology research to further identify changes from cell physiological conditions to disease. Using the multi-structural cell model presented in Chap 9, we aim to show how variation of the material properties of the intracellular components affects cell response after compression and shearing. A parametric study was performed to understand the key mechanical features from different cell types, focussing on variation of the mechanical properties of specific cytoskeleton components and prestress. Using the previously defined elastic formulation, we predicted that cell force is mainly affected by changes in cortex thickness, cortex Young's modulus and rigidity of the cytoplasm. Changes in rigidity of actin bundles and number of microtubules influence cell response to shear loads, while a higher number of actin bundles aligned in the direction of applied compression increase cell response to compression.

Furthermore, we also performed a parametric study to evaluate the contribution of the viscoelastic properties of the cortex and cytoplasm under compressive loading, in which the mechanical behaviour of these components was represented by a power-law model. The time-dependent responses observed were remarkably similar to those reported for a variety of measurements with atomic force microscopy, suggesting this model is a consensus description of the fundamental principles defining cell mechanics. Additionally, we reported that viscoelastic properties of the cortex are essential to define the time-dependent response of the cell to compressive loads.

10.1 Mechanical Properties of the CSK Components

10.1.1 Actin Component Arrangement

At the cellular level, tissue generation is mediated by signalling mechanisms that are dependent on the stimuli from the surrounding environment. When cells sense

This chapter forms part the PhD thesis of Sara Barreto available here: http://etheses.whiterose.ac.uk/4928/

© Springer Nature Singapore Pte Ltd. 2019

D. Lacroix et al., *Multiscale Mechanobiology in Tissue Engineering*,
Frontiers of Biomechanics 3, https://doi.org/10.1007/978-981-10-8075-3_10

mechanical changes in the environment, including sensing compression by other cells (Shih and Yamada 2012; Mui et al. 2015), changes in the stiffness of the extracellular matrix (Crow et al. 2012; Engler et al. 2006) or shear stress caused by fluid flow (Mccoy and O'Brien 2010), cells mechanically adapt their structure accordingly to maintain cell function (proliferation, migration, differentiation, etc.) and tissue homeostasis. Furthermore, the tissues in the body present different elasticity that range from 1 kPa in the brain microenvironment to 10 kPa in the muscle and 100 kPa for collagenous bone (Engler et al. 2006), and this again modulates the cytoskeletal rearrangements of the cells of a specific tissue that will affect the way adhesion forces are generated in between cells and the extracellular matrix. Therefore, we investigated the mechanical properties and rearrangements of the CSK in order to understand which configuration of the CSK better correlates with the forces that the cell is generating when sensing different external forces and ultimately, link the CSK mechanics with the range of the stiffness of the different tissues in the body.

This brings again into play the different rearrangements of the actin components, which can be organized within the cell into a variety of linear bundles, two-dimensional networks and three-dimensional gels, according to cell function and external environment (Fletcher and Mullins 2010). The actin bundles of migrating cells, cross-linked by actin-binding proteins (ABPs), form filopodia; while adherent cells develop strong stress fibres in between focal adhesion complex for contact with the extracellular matrix. Nervous cells have single actin filaments without stress fibres, whereas myocytes and osteoblasts have actin bundles organized into differently thick stress fibres (Gardel et al. 2004). Cellular processes also influence cell mechanical properties, including differentiation of stem cells, which have been found to undergo massive structural changes that involve nuclear changes needed for gene transcription for differentiation (Pajerowski et al. 2007).

This variability in cell mechanical properties adds a degree of complexity to biomechanical experimental and theoretical studies. Therefore, accurate in vitro phenotypic classification might be only possible in combination with numerical models.

10.1.2 The Effect of Cell Component Mechanical Properties on Apparent Stiffness

We took into consideration these different properties and arrangements of the CSK in our multi-structural model by performing a sensitivity analysis in terms of the number, rigidity and orientation of actin bundles and actin cortex as well as the interplay between the CSK components, in order to better understand the source of heterogeneity in cell mechanics. All these parameters affect the way in which cells respond to external forces. In order to make reliable statements based on FE analysis, it is important that input parameters introduced in the model are in relation with the

biological variation found in literature for changes in cell mechanics depending on its structure and function. The ultimate goal is to understand which important parameters are needed to be measured experimentally for an accurate classification of the cellular mechanical behaviour of a cell line and to identify which biological parameters in cells influence tissue mechanics the most (Barreto et al. 2014).

The parametric study showed that axial force was highly sensitive to changes of the mechanical properties of the cell components, including cortex thickness, cortex Young's modulus and rigidity of the cytoplasm, and to the increased number of actin bundles in the interior of the cell (Barreto et al. 2014); see Fig. 10.1. However, axial force was relatively insensitive to changes in the Young's modulus of microtubules, nucleus rigidity and cytoplasm compressibility. Overall, the parameters that influence the most the changes in cell force to resist compression are cortex thickness and rigidity. This is in accordance with our previous findings showing that the cortex is the major component to resist compression.

Longitudinal force was sensitive to changes in the rigidity of actin bundles and increase in the number of microtubules in the cell but relatively insensitive to

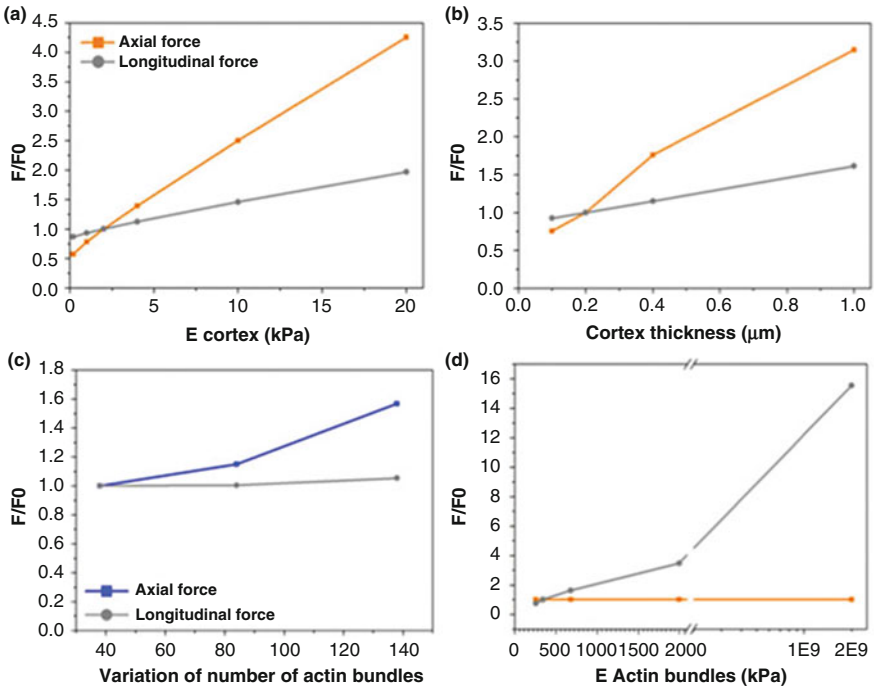

Fig. 10.1 Parametrical study of the mechanical properties of the CSK components and the effect in the overall reaction force of the cell: (**a**) variation of cortex rigidity and (**b**) thickness; (**c**) effect of the density on cellular force was analysed for compression and stretching by varying the number of actin bundles; (**d**) sensitive analysis of the discrete structure of the actin bundles for force transmission

changes in the mechanical properties of the remaining cell components (Barreto et al. 2014) (Fig. 10.1). Changing the interconnection of the discrete elements affected the cell response when the cell was stretched but not in compression. The decrease in the force during stretching, when the discrete components were not connected to each other or to the cortex, is because the cell loses the main structure responsible to resist this type of forces. This shows the importance of having connections between the discrete elements of the CSK for force balance. This only happens in response to shearing because the load applied in the model for compression is not sufficient to activate the response of actin bundles, using this configuration/distribution of the bundles in the interior of the cell model.

10.1.3 The Importance of Actin Orientation to Define Cell Force

Increasing the number of actin bundles in the cell model, resulted in higher compressive forces originated in the cell. In this new configuration, we generated actin bundles randomly distributed inside the cell (Barreto et al. 2014). After analysis of the new configuration, more fibres were oriented in the direction of the force applied on top of the cell due to bead displacement. This suggests that actin bundle orientation defines the compressive forces of the cell: more actin fibres oriented in the direction of indentation induce higher compressive forces. This increase capability of the cell to respond to compressive forces depending on the orientation of the actin bundles may be related with contractility functions of some cell types, while less contractile cells might not have as many stress fibres oriented in the direction of the force.

Research studies suggest the existence of a link between cell contractility and resistance to compression (Caille et al. 2002; Peeters et al. 2004; Ofek et al. 2009; Weafer et al. 2013), for example, long stress fibres were found to extend during compression, leading to a high compression force in myoblasts, which are highly contractile cells (Peeters et al. 2004); peak forces of 2500 nN were reported for highly contractile myoblasts (Peeters et al. 2005); less contractile chondrocytes exhibit a much lower compression force (Ofek Gi and Athanasiou 2009); and endothelial cells, which are somewhere in between contractile myoblasts and chondrocytes, were found to exhibit forces of about 500 nN (Caille et al. 2002). Therefore, here we propose a link between contractility, resistance to compression and orientation of the stress fibres. In the same way, increasing either cortex elasticity or thickness in the FE model provided information about forces generated during compression by stiffer cells. When we model cells with either thicker or more rigid cortex, higher forces to resist the compressive loads are generated. This shows that mechanical properties of CSK networks characterize cells with different rigidities.

10.2 Rheological Properties of Cells

Previously, we analysed the elastic response of CSK components in the initial instants of force application. However, if we are to analyse cell deformation over time, we need to consider not only the elastic response but also the intrinsic flow of the matter. Rather than only deforming elastically in response to an applied force, both solid deformation and liquid flow states of cells must be considered, under conditions in which cells respond with plastic deformation. In the study of the flow and deformation of the CSK, we used a mechanical behaviour called power law to define the intrinsic features of the cell structure when responding to mechanical stimuli analysed over time. Power law is a promising framework for the microscopic description and interpretation of the viscoelastic behaviour of live cells that describes the cell as a soft glassy material with rheological properties that are scale-free in time and frequency (Hecht et al. 2015).

The attention that power-law behaviour of cells has received is, in part, due to experiments examining the behaviour of cells under cyclic loading conditions (Bursac et al. 2005), AFM (Dahl et al. 2005), or micropipette aspiration (Zhou et al. 2010) and FE models incorporating material properties associated with power-law rheology have been developed in the frequency domain (Vaziri et al. 2007; Dailey and Ghadiali 2010) or time domain (Zhou et al. 2012). A more recent experimental study used force clamp force mapping, an AFM technique for measuring the viscoelastic creep behaviour of live cells with sub-micrometre spatial resolution that allowed for the first time the measurement of two-dimensional maps of power-law exponent and modulus scaling parameter (Hecht et al. 2015). Despite the great variation of mean power-law exponents and the mean modulus scaling parameters among individual cells, the authors showed that both parameters are highly correlated: stiffer cells consistently show a smaller power-law exponent.

However, the contribution of specific CSK mechanical material properties to cell heterogeneity remain difficult to map and to quantify due to active cytoskeletal forces, irregular geometry and a complex viscoelasticity (Lim et al. 2006; Zhou et al. 2012). With this multi-structural FE single-cell model, we investigated whether the generation of forces is associated with altered viscoelastic properties of specific CSK elements using power law to define the mechanical behaviour of those CSK elements.

The force-relaxation response of cells is investigated under compressive loading conditions in the time domain. This biomechanical multi-structural model is used to explore the role of material constants associated with power-law rheology affecting the whole-cell viscoelastic response. The goal is to explore whether the simulations with this cell model provide data that is in line with the experimental force-relaxation tests performed with AFM and, therefore, presenting a novel, AFM-based stress relaxation FE model, to determine the contribution of the CSK to the viscoelastic properties of living cells.

10.2.1 Power-Law Implementation in the Multi-structural Cell Model

In this study, we firstly implemented of viscoelastic properties for the cytoplasm described with power-law behaviour, while the remaining components of the cell were defined with elastic properties. Zhou et al. (2012) used a force-relaxation curve to calculate the Prony-series coefficients and calculate the power-law parameters, the shear modulus $G(t)$, which is a measure of the sample's rigidity, and the power-law exponent β ($0 < \beta < 1$), which is a measure of the sample's fluidity and dissipative energy. In this study we used $\beta = 0.2$ and $G_0 = 250$ Pa.

The bead was modelled to apply a displacement of 0.5 μm in compression and was held constant for 15 s, after which the bead was retracted to its original position on the top of the cell and relaxation was registered for 15 s more (Rosenbluth et al. 2008). The loading rate is the same as the unloading rate applied and unloading does not entail a new displacement boundary condition.

10.2.2 Mapping Viscoelasticity Distribution in the Cell

Mapping strain distribution in the whole cell in different time points was possible using this FE multi-structural model combined with power-law behaviour to simulate AFM force-relaxation during indentation. Upon indentation, high values of minimum principal strains were located under the bead and at the end nodes of the CSK due to actin contractility, as reported in Fig. 10.2. The maximum and minimum principal strain values obtained in the cell were slightly higher than the values obtained considering elastic material properties. These changes were expected since different properties were considered with the inclusion of viscoelastic material properties. The nucleus was mainly affected during indentation, where minimum principal strain values were concentrated under the bead and the nucleus, and during bead retraction, where maximum principal strain values were observed. The distribution of strain in the cell changes over time, mainly under the indentation zone, around the nucleus and in the end nodes of CSK (Fig. 10.2).

10.2.3 Viscoelastic Contribution of the Actin Cortex

Altered viscoelastic properties of the cortex have been associated with evolution of certain diseases and cell injury. Also, due to the large spatial variation across cell surface found by Hecht et al. (2015), we investigated how changes in power-law

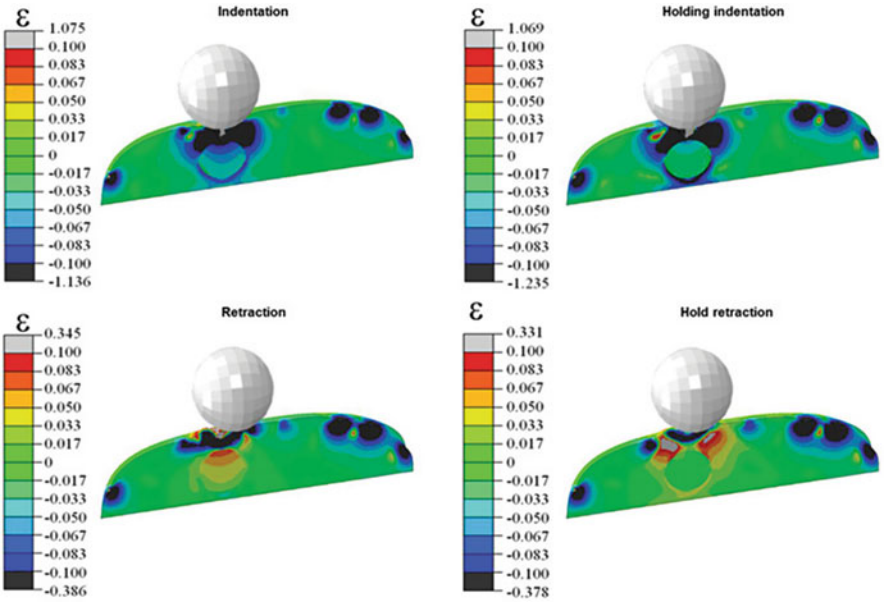

Fig. 10.2 Cross-sectional view of strain distribution in the cell over time when viscoelastic properties are considered in the cytoplasm of the cell

parameters in the cortex affect whole-cell viscoelastic response to compression. Therefore, we implemented viscoelastic properties for the cytoplasm and for the cortex, both described with power-law behaviour.

In Fig. 10.3, the viscoelastic responses of the cell considering the different material properties were observed in detail for the bead positions represented as bead 0 (on top of the nucleus) and bead 6 (6 μm away from the nucleus). Here, for the same initial elastic response, the equilibration time during the viscous response of the cell (after 15 s) increased when both cortex and cytoplasm were modelled as viscoelastic. This difference was much higher for the position represented as bead 0 than when the bead was further away from the nucleus.

When comparing viscoelastic properties in different components of the cell, the increase in the equilibration time was higher for *bead 0* position than for the *bead 6* position. This means that the viscous contribution of the cortex becomes more important in regions where the thickness of the cytoplasm is smaller, as it happens in *bead 0* position. These changes in cell viscosity when testing zones with different thickness shows a bimodal response from the cytoplasm to the cortex layer, which were also observed in the experimental study of Moreno-Flores et al. (2010) using AFM.

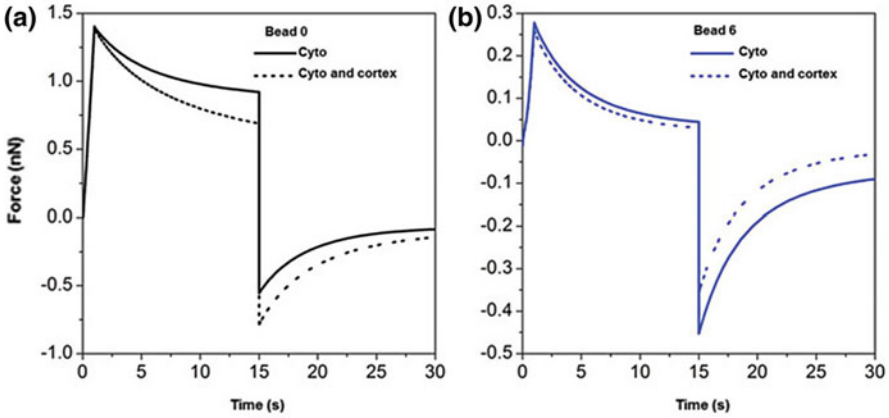

Fig. 10.3 Comparing force-relaxation curves for two bead positions: (**a**) *bead 0*, the original position for indentation on top of the nucleus, and (**b**) *bead 6*, which represents indentation with the bead 6 μm away from original position. Different material properties of the cell component are considered with straight lines representing viscoelastic material properties defined for the cytoplasm and dashed lines indicating the response of the cell obtained with a model considering viscoelastic properties for both cytoplasm and cortex

10.2.4 Distance-Dependence Force Propagation

Whole-cell force and equilibration times depend on the position of the indenter on the top of the cell (Fig. 10.4). Therefore, both elastic and viscoelastic response of the cell during compression were affected by the exact location of indentation.

When comparing the force-relaxation for different bead positions, the elastic response is always higher for the *bead 0* position due to the elastic contribution of the nucleus (in *bead 0* position, the bead is on the top of the nucleus). Further away from the nucleus, the elastic contribution observed in the force-relaxation curves did not vary considerably. This happened because there is no strong influence of the other elastic components of the cell, except for the *bead 2* position, in which the end node of one microtubule is below the bead (Fig. 10.4). Therefore, that microtubule contributes to the peak of elastic force observed in the force-relaxation curves for *bead 2* position. Taken together, the physical mechanism for the different elastic response of the cell indented in different positions is related to the spatial heterogeneity of the CSK and is dependent on the distance of the indenter to the nucleus. No trend was observed upon bead retraction, at $t = 30$ s. Retractions that happened more rapidly might be explained by the rapid release of discrete elastic elements representing the CSK back to their initial configuration.

The inclusion of viscoelastic material properties in the actin cortex made the variation in the force-relaxation curves for different bead positions much smoother than when compared to the results obtained when viscoelastic material properties were defined in the cytoplasm alone. To evaluate if this observation is dependent on singularities of the FE formulation, we analysed the possible presence of extreme

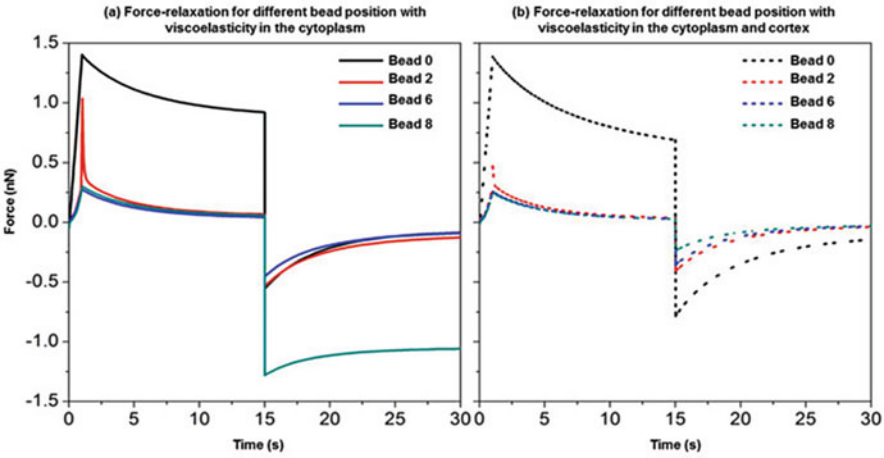

Fig. 10.4 Force-relaxation curves for different bead positions: (**a**) considering viscoelasticity defined in the cytoplasm and elastic material properties defined for the remaining components of the cell and (**b**) considering viscoelastic material properties for both the cytoplasm and cortex

forces, stresses or strains in one of the discrete components of the CSK, in both models of cytoplasm alone and cytoplasm together with cortex modelled as viscoelastic materials. If singularities are not observed, then it is valid to consider the importance of the cortex for the viscoelastic response of the cell. And this is undoubtedly important for the understanding of the role of the cellular components for the viscoelastic response of the cell at different times. When varying bead positions, no peaks of stress, reaction force or deformation were observed in the microtubules and actin bundle structures, for the model with cytoplasm as viscoelastic. Moreover, these values were not considerably different from the model with cortex and cytoplasm modelled as viscoelastic materials. Taken together, there are no singularities in the distribution of forces when the bead position is varied considering the two models and the peaks of force and the differences between the models are attributed to the spatial location of the discrete fibres of the CSK in the model cell. The investigation of the viscoelastic response of the cortex is key to the relationship between cell injury and the changes in the power-law parameters over time, especially for modelling the failure phenomena at the cortex/membrane areas of cells. This has been done for cell injury during airway reopening (Dailey and Ghadiali 2010) and can now be applied for different cell types and biological processes.

The results suggest that the origin of different relaxation times is related with the spatial arrangement of the CSK structure in the cell and on the location of the load applied to the cell. This multi-structural cell model is a robust tool for investigating the specific contribution of actin cortex for cell rheology. The results reported here add to a growing body of literature pertaining to power-law behaviour of cells

mainly from dynamic mechanical analyses and creep measurement (Fabry et al. 2003; Desprat et al. 2005; Hemmer et al. 2009) and now AFM stress relaxation. This FE cell model may represent a significant contribution to the field of computational cell mechanics with insights on the dynamics of cytoskeletal viscoelasticity under mechanical perturbation.

10.3 Advances in Computational Cell Mechanics

With this multi-structural model, we were able to isolate the contribution of each individual cytoskeletal component when responding to specific external stimulation. Additionally, we were able to relate the structure of the internal CSK components with a potential cell function by looking at the way each CSK resists specific loading conditions: while actin cortex is the main component to resist compressive loads, we also predicted that cells that are under high compressive loads would also present a higher number of actin bundles aligned in the direction of applied compression. Moreover, cell types that are predominantly subjected to stretching conditions would have greater tension in the actin bundles and microtubules. From the results of this multi-structural model, the actin cortex does not have a mechanical role in resisting shearing loads. However, both elastic and viscoelastic properties of the cortex are essential to maintain cell integrity when responding to compressive loads. With this multi-structural model, we demonstrated that mechanical forces can provide instructive signals that direct structural changes in the interior of the cell and, ultimately, direct cell behaviour.

However, this multi-structural model only explains the passive mechanical behaviour of cells. Because cells are living systems capable of active responses, they are able to remodel in response to changes in the extracellular environment. Although a dynamic analysis of cell response to mechanical forces over time was investigated, the actin and microtubules remodelling was not simulated. Other assumptions taken for the implementation of this model need to be addressed: (1) cell-specific shapes were not considered – however, the hypothesis that CSK components were the main contributors to cell stability was verified, which means that the presence of these components defines the shape of the cell and not the other way around; (2) material properties for the cellular components of the FE model are taken from both experimental data and FE model predictions, from literature – this issue was addressed by performing the sensitivity study of the material properties of all the cellular components present in the model; and (3) a rigid bonding of the cell to the substrate is assumed, where all the nodes of the basal part of the cell are fully constrained – cells attach to the extracellular matrix through focal adhesions, which could have been modelled as local points of contact between the cell and the substrate by defining that only the end nodes of the CSK at the basal part of the cell would be constrained. This would have been of particular importance to understand how the forces are transmitted from the exterior on the top of the cell through the CSK to the underlying substrate.

Therefore, FE computational analysis are now focusing on the inclusion of other mechanosensor components of the cell, such as the inclusion of integrins and focal complexes as well as the inclusion of a primary cilia (PC). The PC sense the fluid flow and contribute to cell mechanics and to define cell forces by interacting with the CSK (Mazzag and Barakat 2011; Vaughan et al. 2014; Khayyeri et al. 2015). Khayyeri et al. (2015) used the multi-structural cell model presented here and incorporated a PC within a finite element representation of a flow chamber. This model of the cell in a perfusion flow bioreactor environment was developed to investigate how the PC mechanical characteristics are involved in the mechanotransduction and how PC deflection under fluid flow induces strains on the internal cell components that regulate the cell's mechanosensitive response.

Since the primary cilium undergoes large deformations, the structure was modelled as compressible neo-Hookean material and as extension of the basal body that sits just beneath the cell surface. The microtubule configuration from the original cell model (Barreto et al. 2013) was modified such that the microtubule origin at the centrosome was located at the base of the primary cilium docked on the cell surface and therefore, further way from the nucleus. Simulations of cells with different PC mechanical characteristics showed that, under perfusion flow, the length and the stiffness of PC are responsible for the transmission of mechanical stimuli to the CSK. Fluid flow deflects the PC, with the highest strains found at the base of the PC in the cytoplasm and further away in the cell nucleus. Our results indicate that PC deflection under fluid flow stimulation transmits mechanical strain primarily to other essential organelles in the cytoplasm, such as the Golgi complex, that regulate cells' mechanoresponse. The simulations further suggest that cell mechanosensitivity can be altered by targeting PC length and rigidity (Khayyeri et al. 2015).

This valuable framework integrates prestress and discrete cytoskeletal elements into an overall multi-structural single-cell model that can be applied to explain the mechanics of many cell types. Moreover, a PC was further incorporated not only to explain internal changes but also fluid flow mechanosensation (Khayyeri et al. 2015). With this regard, future cell mechanics models are likely to more and more incorporate together the greater complexity of the cellular structures involved in mechanotransduction. As recently reviewed in Lim et al. (2015), this includes, among others, the ciliary compartment revealed by electron microscopy (Hoey et al. 2012), sub-ciliary compartment that acts at different length scales remodelling microtubule attachment at the primary cilium base (Espinha et al. 2014), intermediate filaments, Golgi complex and cell-cell junctions.

References

Barreto S, Clausen CH, Perrault CM, Fletcher DA, Lacroix D (2013) A multi-structural single cell model of force-induced interactions of cytoskeletal components. Biomaterials 34 (26):6119–6126. https://doi.org/10.1016/j.biomaterials.2013.04.022

Barreto S, Perrault CM, Lacroix D (2014) Structural finite element analysis to explain cell mechanics variability. J Mech Behav Biomed Mater 38:219–231. https://doi.org/10.1016/j.jmbbm.2013.11.022

Bursac P, Lenormand G, Fabry B, Oliver M, Weitz DA, Viasnoff V, Butler JP, Fredberg JJ (2005) Cytoskeletal remodelling and slow dynamics in the living cell. Nat Mater 4(7):557–561. https://doi.org/10.1038/nmat1404

Caille N, Thoumine O, Tardy Y, Meister J-J (2002) Contribution of the nucleus to the mechanical properties of endothelial cells. J Biomech 35(2):177–187

Crow A, Webster KD, Hohlfeld E, Ng WP, Geissler P, Fletcher DA (2012) Contractile equilibration of single cells to step changes in extracellular stiffness. Biophys J 102(3):443–451. https://doi.org/10.1016/j.bpj.2011.11.4020

Dahl KN, Engler AJ, Pajerowski JD, Discher DE (2005) Power-law rheology of isolated nuclei with deformation mapping of nuclear substructures. Biophys J 89(4):2855–2864. https://doi.org/10.1529/biophysj.105.062554

Dailey HL, Ghadiali SN (2010) Influence of power-law rheology on cell injury during microbubble flows. Biomech Model Mechanobiol 9(3):263–279

Desprat N, Richert A, Simeon J, Asnacios A (2005) Creep function of a single living cell. Biophys J 88(3):2224–2233. https://doi.org/10.1529/biophysj.104.050278

Engler AJ, Sen S, Sweeney HL, Discher DE (2006) Matrix elasticity directs stem cell lineage specification. Cell 126(4):677–689. https://doi.org/10.1016/j.cell.2006.06.044

Espinha LC, Hoey DA, Fernandes PR, Rodrigues HC, Jacobs CR (2014) Oscillatory fluid flow influences primary cilia and microtubule mechanics. Cytoskeleton 71(7):435–445

Fabry B, Maksym G, Butler J, Glogauer M, Navajas D, Taback N, Millet E, Fredberg JJ (2003) Time scale and other invariants of integrative mechanical behavior in living cells. Phys Rev E 68 (4):1–18. https://doi.org/10.1103/PhysRevE.68.041914.

Fletcher DA, Mullins RD (2010) Cell mechanics and the cytoskeleton. Nature 463(7280):485–492. https://doi.org/10.1038/nature08908

Gardel ML, Shin JH, MacKintosh FC, Mahadevan L, Matsudaira P, Weitz DA (2004) Elastic behavior of cross-linked and bundled actin networks. Science (New York, NY) 304 (5675):1301–1305. https://doi.org/10.1126/science.1095087.

Hecht FM, Schierbaum N, Rheinlaender J, Goldmann WH, Fabry B, Schaffer TE (2015) Imaging viscoelastic properties of live cells by AFM: power-law rheology on the nanoscale. Soft Matter 11(23):4584–4591. https://doi.org/10.1039/C4SM02718C

Hemmer JD, Nagatomi J, Wood ST, Vertegel AA, Dean D, Laberge M (2009) Role of cytoskeletal components in stress-relaxation behavior of adherent vascular smooth muscle cells. J Biomech Eng 131(4):041001. https://doi.org/10.1115/1.3049860

Hoey DA, Downs ME, Jacobs CR (2012) The mechanics of the primary cilium: an intricate structure with complex function. J Biomech 45(1):17–26

Khayyeri H, Barreto S, Lacroix D (2015) Primary cilia mechanics affects cell mechanosensation: a computational study. J Theor Biol 379:38–46

Lim CT, Zhou EH, Quek ST (2006) Mechanical models for living cells – a review. J Biomech 39 (2):195–216. https://doi.org/10.1016/j.jbiomech.2004.12.008

Lim YC, Cooling MT, Long DS (2015) Computational models of the primary cilium and endothelial mechanotransmission. Biomech Model Mechanobiol 14(3):665–678. https://doi.org/10.1007/s10237-014-0629-x

Mazzag B, Barakat AI (2011) The effect of noisy flow on endothelial cell mechanotransduction: a computational study. Ann Biomed Eng 39(2):911–921. https://doi.org/10.1007/s10439-010-0181-5

Mccoy RJ, O'Brien FJ (2010) Influence of shear stress in perfusion bioreactor cultures for the development of three-dimensional bone tissue constructs: a review. Tissue Eng Part B Rev 16 (6):587–601. https://doi.org/10.1089/ten.teb.2010.0370

Moreno-Flores S, Benitez R, Vivanco M, Toca-Herrera JL (2010) Stress relaxation and creep on living cells with the atomic force microscope: a means to calculate elastic moduli and viscosities of cell components. Nanotechnology 21(44):445101. https://doi.org/10.1088/0957-4484/21/44/445101

Mui KL, Bae YH, Gao L, Liu S-L, Xu T, Radice Gl L, Chen CS, Assoian RK (2015) N-cadherin induction by ECM stiffness and FAK overrides the spreading requirement for proliferation of vascular smooth muscle cells. Cell Rep 10(9):1477–1486. https://doi.org/10.1016/j.celrep.2015.02.023

Ofek Gi WDC, Athanasiou KA (2009) Contribution of the cytoskeleton to the compressive properties and recovery behavior of single cells. Biophys J 97(7):1873–1882. https://doi.org/10.1016/j.bpj.2009.07.050

Ofek G, Natoli RM, Athanasiou KA (2009) In situ mechanical properties of the chondrocyte cytoplasm and nucleus. J Biomech 42(7):873–877. https://doi.org/10.1016/j.jbiomech.2009.01.024

Pajerowski JD, Dahl KN, Zhong FL, Sammak PJ, Discher DE (2007) Physical plasticity of the nucleus in stem cell differentiation. Proc Natl Acad Sci U S A 40(104):15619–15624

Peeters EAG, Bouten CVC, Oomens CWJ, Bader DL, Snoeckx LHEH, Baaijens FPT (2004) Anisotropic, three-dimensional deformation of single attached cells under compression. Ann Biomed Eng 32(10):1443–1452

Peeters EAG, Oomens CWJ, Bouten CVC, Bader DL, Baaijens FPT (2005) Viscoelastic properties of single attached cells under compression. J Biomech Eng 127(2):237. https://doi.org/10.1115/1.1865198

Rosenbluth MJ, Lam WA, Fletcher DA (2008) Analyzing cell mechanics in hematologic diseases with microfluidic biophysical flow cytometry. Lab Chip 8(7):1062–1070. https://doi.org/10.1039/b802931h

Shih W, Yamada (2012) S. N-cadherin-mediated cell-cell adhesion promotes cell migration in a three-dimensional matrix. J Cell Sci 125(15):3661–3670. https://doi.org/10.1242/jcs.103861

Vaughan TJ, Mullen CA, Verbruggen SW, McNamara LM (2014) Bone cell mechanosensation of fluid flow stimulation: a fluid-structure interaction model characterising the role integrin attachments and primary cilia. Biomech Model Mechanobiol 2:703–718. https://doi.org/10.1007/s10237-014-0631-3

Vaziri A, Xue Z, Kamm RD, Kaazempur Mofrad MR (2007) A computational study on power-law rheology of soft glassy materials with application to cell mechanics. Comput Methods Appl Mech Eng 196(31–32):2965–2971. https://doi.org/10.1016/j.cma.2006.11.019

Weafer PP, Ronan W, Jarvis SP, McGarry JP (2013) Experimental and computational investigation of the role of stress Fiber contractility in the resistance of osteoblasts to compression. Bull Math Biol 75(8):1284–1303. https://doi.org/10.1007/s11538-013-9812-y

Zhou EH, Quek ST, Lim CT (2010) Power-law rheology analysis of cells undergoing micropipette aspiration. Biomech Model Mechanobiol 9(5):563–572. https://doi.org/10.1007/s10237-010-0197-7

Zhou EH, Xu F, Quek ST, Lim CT (2012) A power-law rheology-based finite element model for single cell deformation. Biomech Model Mechanobiol. https://doi.org/10.1007/s10237-012-0374-y

Chapter 11
The Future of Tissue Engineering Design for Bioreactor Stimulation

Scaffold biomaterials for tissue engineering can be produced in many different ways depending on the applications and the materials used. Most research into new biomaterials is based on an experimental trial-and-error approach that limits the possibility of making many variations to a single material and studying its interaction with its surroundings. Instead, computer simulation applied to tissue engineering can offer a more exhaustive approach to test and screen out biomaterials. In this chapter, current perspectives will be presented to indicate that more efforts need to be put into the development of such advanced studies, and a new workflow including the use of computer modelling for the development of new tissue engineering product is presented.

11.1 Towards Good Manufacturing Practice in Tissue Engineering

Most of the research in biomaterial science has been driven by a trial-and-error approach where a combination between material science and biochemistry has enabled to derive porous materials that are targeted to enhance a given cell response. However, this quest for the "ideal" or optimum material for a given application or a given biological response has produced materials with great variability and little control over the micropore architecture. With the development of additive manufacturing (AM) techniques, there were a lot of expectations to circumvent all the limitations from previous scaffold designs. And indeed almost any kind of geometry could be produced. Due to the different kinds of techniques available (see Chap. 3 for a detailed description), almost any materials, whether polymers, ceramics or metals, can be produced with a given architecture. The greatest limitation is still the resolution available for each technique. Some techniques have very high resolution enabling to include features on the order of a few micrometres, while others are limited to around hundred micrometres which is usually not enough for tissue engineering applications. The high-resolution technique has the drawback to be slow so a large scaffold takes time to manufacture and therefore is difficult to justify in a commercial application. Nonetheless there are wide ranges of additive

© Springer Nature Singapore Pte Ltd. 2019

D. Lacroix et al., *Multiscale Mechanobiology in Tissue Engineering*,
Frontiers of Biomechanics 3, https://doi.org/10.1007/978-981-10-8075-3_11

manufacturing techniques that finally enable to produce at ease the design of a scaffold that one has come up with. However, there are two main drawbacks that are not well discussed in the literature. First, very few studies have actually verified that the scaffolds that they have produced and used in vitro or in vivo using AM technique corresponds to the CAD scaffold that was intended to be produced. In other words they have not checked the accuracy of their method. This is of significant importance since the results of an experiment with cells are reported based on the design of the scaffold which may not correspond to the real test. Second, many samples are being used within the same in vitro or in vivo experiment. Yet, no study actually checks whether the samples are identical. In other words, there is no check on the precision of the manufacturing process. This is of significance importance as the variability in the manufacturing process can introduce some experimental noise that translates into less reliable results from a statistical point of view. Thus, those two essential criteria in scaffold manufacturing for tissue engineering (accuracy and precision of manufacturing) should come part of good manufacturing practice whenever one uses a newly produced scaffold in order to provide a quantification of the accuracy and precision of the scaffolds used.

11.2 Computational Modelling As Part of the Experimental Process

In order to provide a quantification of the actual architecture of a given scaffold, a reliable method should be used to assess the architecture of the scaffold over many samples, and the output should be comparable with the parameters that define the ideal scaffold in the design process. One method of choice, as described in Chap. 3, is the use of microCT which enables to obtain a 3D representation of the scaffold with a high precision (on the order of a few micrometres). Once the method has been validated on a known structure, it can easily be used in a systematic manner for any kind of study. The quantification of variability from one sample to another enables to characterize the variability found in the material architecture, and it can be used when error analysis is being performed in the whole study.

In addition to microCT characterization, computational modelling can also be used. As demonstrated in Chap. 4, the simulation of fluid flow passing through the scaffold can be an effective way to assess the variability of a scaffold at the microscopic level. Any irregularities within the architecture of the pores will produce some irregular fluid flow which will induce an inhomogeneous shear stress along the surface of the pores. The setup of computational fluid dynamic analysis is relatively simple and can benefit easily of parallel computing so it can produce a solution in a quick turnaround.

In addition to the use of computational modelling to check scaffold integrity before it is being used experimentally, it is also possible to use computational modelling after the experiment to assess the scaffold degradation or tissue formation

within the scaffold. For example, in Chap. 3 it was shown how osmium was used to stain collagen in order to enhance contrast in microCT and therefore be able to characterize the collagen distribution within the scaffold. There is potential for using many different markers that would enable identification in 3D of the tissue formation over time in a scaffold. In addition subsequent fluid or solid analysis can be performed to assess the change of permeability or porosity within the scaffold, as well as its change of stiffness. The combination of modelling techniques with the experimental input and output opens the door to a whole set of in vitro characterization that was not thought of before.

11.3 Quantification of Experimental Variability

As found in many studies and also in this book (Chaps. 1, 3, 6, and 7), a large source of variability in in vitro testing is found whether cells are included or not. There are several reasons to this. First we are dealing with a biological system that has some stochastic process, and therefore some randomness happens at all spatial and temporal levels inducing some variability at the end of the chain. All cells are not behaving in the same manner and this introduces some "noise". Second there are a lot of material, biological and experimental condition parameters that are interlinked and participate in the final outcome. Therefore, any variation of one or more parameters within a single experiment will produce some variation that is difficult to predict. Third, there is a lot of human handling in preparing, culturing and assessing the cell and tissue assays which inevitably result in small to large errors. As a result it is always recommended to perform the same experiment on at least three samples and in triplicates. This can give rise to quite a large range of analysed samples and yet it can be difficult to find statistical significance. Therefore, computer modelling is an interesting tool to design a scaffold or analyse the effect of one parameter over another by keeping all the other parameters fixed. This has been used very frequently in the past in order to optimize a design or to determine the sensitivity of a given parameter. But we can go further and actually model the variability encountered in vitro or in vivo by using stochastic tools that would introduce some "controlled noise" in the system and produce a range of outputs. In particular the creation of multiscale studies where the stochastic molecular events are combined with the more deterministic Newton's law at the macroscopic level is a good approach to provide a modelling framework that produces a stochastic result close to the one seen experimentally. We can even think of modelling the variability introduced by human errors when handling the scaffold and tissues in all steps of the tissue engineering process. It will be soon possible to replace a major part of the in vitro experimental tests with a suite of computational tests that evaluate the combination of many experimental parameters together to determine which combination is best to test in vitro. This will lead to the faster development of tissue engineering products and a safer evaluation for an in vivo or clinical trial study.

11.4 A New Workflow for Tissue Engineering Product

Throughout this book it has been shown how scaffold design could be checked against its CAD specification using computer modelling (Chaps. 4 and 8), how a bioreactor chamber could be optimized for fluid flow and cell seeding (Chap. 5) and how a multiscale approach can enable the calculation of mechanical stimuli at the macroscopic level and at the cell level (Chaps. 2, 9 and 10). This new approach for the design of scaffold and bioreactor conditions is particularly useful when checking the manufacturing process of the scaffold and before doing any in vitro test. We can therefore propose a new workflow for the development of tissue engineering products (Fig. 11.1) where computational modelling would be introduced at various time points in this workflow. The traditional workflow shown in blue in Fig. 11.1 shows that for the development of a product, the sequential following steps are needed: scaffold design, manufacturing, in vitro testing, in vivo testing, clinical trial and commercial scale-up. This is a long and costly process evaluated to more than $1 billion and where many products fail to see the market light due to unsuccessful clinical results at stage 3 of clinical trial. Some of the in vitro testing approaches using a bioreactor were presented in Chaps. 1, 3, 6 and 7. Therefore, there is a need for the development of more reliable computational and in vitro approach that can screen out better unsuccessful product design and reduce the number of products to be tested in vitro and in vivo. The investment made in the preclinical phase is rather small compared to the investment needed to perform the three phases of the clinical trials. Therefore, the computer modelling approach detailed in Chaps. 2, 4, 5, 8 and 9 can successfully be implemented to improve product performance before it is being

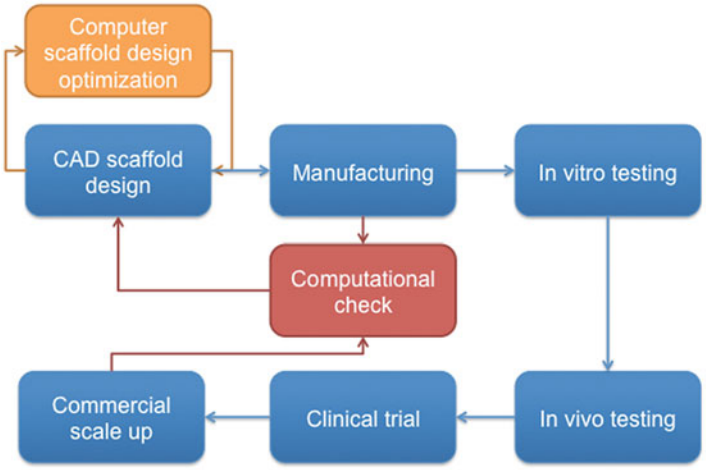

Fig. 11.1 Workflow for the design and testing of a new tissue engineering product. In addition to the traditional workflow (blue) from scaffold design to commercial scale-up, it is proposed to introduce various computational modelling tools to optimize and check the design and manufacturing processes

tested clinically. Another step where computational modelling will be useful in this workflow is when the new product has successfully passed the clinical trials and needs to be produced en masse for market production. When such scale-up is required, it is often the case that the manufacturing process changes slightly in order to increase throughput. As we have seen in Chap. 4, even a well-controlled manufacturing process can lead to significant variability from one sample to another. Therefore, a similar approach as the one used in Chap. 4 can be used to check whether the scale-up process still fulfils the design specifications.

11.5 Conclusion

In this chapter and in this book, a holistic approach was suggested where a combination of experimental and computational techniques is used to provide complementary data that are used together to inform on the design of scaffold and bioreactors in order to produce the desired tissue-engineered product. A research purely based on trial-and-error basis is unlikely to lead to an efficient product in the market or at a very high developmental cost. Computational modelling can provide an engineering-based rationale for screening out deficient designs and to ensure that good manufacturing practice is met.

Index

© Springer Nature Singapore Pte Ltd. 2019

D. Lacroix et al., *Multiscale Mechanobiology in Tissue Engineering*,
Frontiers of Biomechanics 3, https://doi.org/10.1007/978-981-10-8075-3